

**MICROSCOPY AND SURFACE CHEMICAL  
INVESTIGATIONS OF DYED CELLULOSE  
TEXTILES**

**SATINDERJEET KAUR CHETTRA    BSC (HONS)**

THESIS SUBMITTED TO THE UNIVERSITY OF NOTTINGHAM  
FOR THE DEGREE OF DOCTOR OF PHILOSOPHY

MARCH 2006

# CONTENTS

---

Abstract		<i>i</i>
Glossary		<i>iii</i>
<b>CHAPTER ONE</b>	<b>Introduction</b>	<b>1</b>
1.1	Introduction	1
1.2	Cellulose	2
1.2.1	Macromolecular structure	3
	<i>1.2.1.1 Crystalline versus amorphous</i>	4
	<i>1.2.1.2 Modification of crystal structure</i>	8
	<i>1.2.1.3 Regenerated cellulose</i>	9
1.2.2	Characterisation of cellulose	11
	<i>1.2.2.1 Bulk characterisation of cellulose</i>	13
	<i>1.2.2.2 Surface characterisation of cellulose</i>	14
1.3	Cotton	15
1.3.1	Cotton fibres	16
1.3.2	Cotton plant and fruit growth	16
	<i>1.3.2.1 Cotton fibre structure</i>	18
	<i>1.3.2.2 Mercerisation of cotton</i>	20
	<i>1.3.2.3 Applications of cotton</i>	21
1.3.3	Characterisation of cotton	22
1.3.4	Other studies on cotton fibres	26
1.4	Dyes	28
1.4.1	Dyeing Theories	29
1.4.2	Investigations of dye-uptake in cellulose	31

1.5	Aims & Outline of Research	33
<b>CHAPTER TWO</b>	<b>Instrumentation &amp; Experimental methods</b>	<b>36</b>
2.1	Atomic Force Microscopy	36
2.1.1	Instrumentation	37
2.1.2	Operational modes	40
	<i>2.1.2.1 Contact mode</i>	40
	<i>2.1.2.2 Non-contact mode (NC)</i>	41
	<i>2.1.2.3 Tapping mode (TM)</i>	42
	<i>2.1.2.4 Force-distance measurements</i>	44
	<i>2.1.2.5 Phase imaging</i>	46
	<i>2.1.2.6 Amplitude and phase versus distance curves</i>	47
2.1.3	Applications of AFM	49
	<i>2.1.3.1 Application of AFM in textile studies</i>	51
2.1.4	AFM analysis	52
	<i>2.1.4.1 Hydrophilic tips</i>	52
	<i>2.1.4.2 Hydrophobic tips</i>	53
	<i>2.1.4.3 Preparation of cotton sample for AFM analysis</i>	53
2.2	Time-of-Flight Secondary Ion Mass Spectrometry	
	<i>studies</i> 59	
	2.2.3	ToF-SIMS analysis
2.3	X-ray Photoelectron Spectroscopy	61
2.3.1	Instrumentation	62
2.3.2	Applications of XPS	63
	<i>2.3.2.1 Applications of XPS in textile studies</i>	64

2.3.3	XPS Analysis	67
	<i>2.3.3.1 Preparation of cotton samples for XPS analysis</i>	67
2.4	Scanning Electron Microscopy	68
2.4.1	Instrumentation	69
	<i>2.4.1.1 Energy dispersive X-ray analysis (EDAX)</i>	70
2.4.2	Applications of SEM	72
	<i>2.4.2.1 Applications of SEM in textile studies</i>	72
2.4.3	SEM and ESEM analysis	73
2.5	Differential Scanning Calorimetry	73
2.5.1	Instrumentation	74
2.5.2	Applications of DSC	76
	<i>2.5.2.1 Applications of DSC in textile studies</i>	76
2.5.3	DSC analysis	77
<b>CHAPTER THREE Cellophane – Surface Characterisation of a Model Cellulose System</b>		<b>78</b>
3.1	Introduction	78
	3.1.1 Characterisation of cellophane	79
3.2	Experimental	81
	3.2.1 Samples	81
	3.2.2 Sample preparation and analysis	81
3.3	Results and Discussion	82
	3.3.1 AFM analysis of cellophane	82
	3.3.2 ToF-SIMS analysis comparison	95
	3.3.3 DSC analysis comparison	104
3.4	Conclusions	110

<b>CHAPTER FOUR</b>	<b>Surface Characterisation of Cotton Fibres</b>	<b>114</b>
4.1	Introduction	114
4.1.1	Greige fibres	115
4.1.2	Undyed fibres (mercerised/processed)	116
4.1.3	Dyed fibres	116
4.2	Experimental	117
4.2.1	Samples	117
4.2.2	Sample preparation and analysis	117
4.3	Results and Discussion	119
4.3.1	Surface characterisation of greige cotton fibres	119
	<i>4.3.1.1 SEM Analysis</i>	119
	<i>4.3.1.2 AFM Analysis</i>	122
4.3.2	Surface characterisation of undyed cotton fibres	133
	<i>4.3.2.1 SEM Analysis</i>	133
	<i>4.3.2.2 AFM Analysis</i>	139
	<i>4.3.2.3 ToF-SIMS Analysis</i>	149
4.3.3	Surface characterisation of dyed cotton fibres	154
	<i>4.3.3.1 SEM Analysis</i>	154
	<i>4.3.3.2 AFM Analysis</i>	164
	<i>4.3.3.3 ToF-SIMS Analysis</i>	173
4.3.4	Surface characterisation of fibre cross-sections	178
	<i>4.3.4.1 AFM Analysis</i>	178
	<i>4.3.4.2 ToF-SIMS Analysis</i>	183
4.4	Conclusions	186

<b>CHAPTER FIVE</b>	<b>Dye-Uptake Mechanisms</b>	<b>189</b>
5.1	Introduction	190
5.2	Experimental	191
5.2.1	Samples	191
5.2.2	Sample preparation and analysis	192
5.3	Results and Discussion	192
5.3.1	XPS Analysis of dyed cotton	192
5.3.2	DSC comparison analysis	206
5.3.3	AFM dye-fibre interaction analysis	211
5.4	Conclusions	217
<b>CHAPTER SIX</b>	<b>Final Conclusions</b>	<b>220</b>
References		227
Acknowledgements		249

## *Abstract*

---

Cotton is a vital material for the textile industry, providing the fundamental raw component for the manufacture of numerous and varied garments. It has been thoroughly characterised both in terms of its constitution; behaviour under a variety of environmental and manufacturing conditions; and several mechanisms by which it takes up dyestuffs. Recently the availability of a range of high-performance surface analysis tools has allowed researchers to begin to assess the contribution of the surface interface to the overall properties of cellulose in cotton. In particular, these approaches offer considerable potential to address the current lack of fundamental experimental data in support of the proposed dye-uptake mechanisms in cotton fibres. The absence of a detailed molecular model for the process makes it difficult to predict dye performance and to identify the key characteristics of the cotton which influence dyeing. For example, the existence and location of dye binding sites is still unclear. It has been postulated that the occurrence of crystalline or amorphous regions in cotton may play a role in such binding and in dye uptake. A deeper understanding of the dyeing mechanisms therefore requires knowledge of the interplay between the physical chemistry of the dye, its adsorption/diffusion onto the surface of and within cotton fibres, and the related physical and chemical characteristics of the cotton itself.

Here we begin to address these broad questions through the application of atomic force microscopy (AFM) and other complimentary surface analytical techniques, to analyse a range of dyed and undyed cellulose based textiles. We provide high-resolution surface morphological image data, which show nanometre scale detail of the surface of dyed and undyed cotton fibres. It is believed that the dyeing process induces an increase in crystallinity, due to breakages in hydrogen bonds between cellulose chain molecules during swelling of fibres within the dye bath, thus allowing dye molecules to enter the

and become entrapped within the fibre matrix. We provide evidence in the form of image data that suggest a difference in the crystal structure between undyed and dyed cellulose fibres to support this theory. We also reveal possible crystalline and amorphous regions within the substrate through AFM phase imaging using modified tips and successfully fingerprint regions of dyed and undyed cellulose fibres.

Complimentary surface chemical analysis of dyed and undyed fibres, provide qualitative and quantitative data to show the presence of dye molecules on the surface of dyed cellulose textiles. Novel investigations of dyed fibres through X-ray photoelectron spectroscopy (XPS), determine the amount of dye present at the surface of cotton fibres. Using the N 1s atomic orbital region as a diagnostic peak, the level of dye loading could be directly attributed to the concentration levels of dye within the dyebath. The XPS data also provided strong evidence for possible dye-uptake mechanisms. We observed that certain stages of the dyeing process directly influenced the amount of dye entering cotton fibres. XPS showed that an increase in salt (NaCl) content within the dyebath produced dyed fibres with increased presence of dye compound at the surface.

The knowledge obtained from these studies will help to improve the dyes and dyeing mechanisms for cotton and other textiles, thus improving the quality of dyed garments offered to the consumer.

## GLOSSARY

---

%RH	percentage of relative humidity
AFM	atomic force microscopy
AMU	atomic mass unit
A-p-d	amplitude-phase-distance
ATR-IR	attenuated total reflectance infra-red spectroscopy
BE	binding energy
BTCA	butanetetracarboxylic acid
<sup>13</sup> C NMR	carbon-13 nuclear magnetic resonance
CS <sub>2</sub>	carbon disulphide
DCA	dynamic contact angle
DSC	differential scanning calorimetry
EDAX	energy dispersive X-ray analysis
EM	electron microscopy
ESCA	electron spectroscopy for chemical analysis
FT-IR	Fourier-transform infra-red spectroscopy
FT-Raman	Fourier-transform Raman spectroscopy
FWHM	full-width half-maximum
KE	kinetic energy
MD	molecular dynamics
NC	non-contact mode
OH	hydroxyl
OTS	octadecyltrichlorosilane

QSAR	quantitative structure-activity relationship
QSPR	quantitative structure-property relationship
RMS	root-mean-square
SAM	self-assembled monolayer
SEM	scanning electron microscopy
STM	scanning tunnelling microscopy
SPM	scanning probe microscopy
TEM	transmission electron microscopy
TM	tapping mode
ToF-SIMS	time-of-flight secondary ion mass spectrometry
UHV	ultra-high vacuum
XPS	X-ray photoelectron spectroscopy
XRD	X-ray diffraction

## CHAPTER ONE

---

### Introduction

There is little information known about how dyes and textile materials truly interact. There are some models that explain dye-uptake mechanisms within certain fibres such as cotton, and these mechanisms have been detailed within this thesis. However, these mechanisms are hypotheses and have not been proven to be correct or otherwise. The key aim of this study was therefore to provide surface morphology and physiochemical data to aid the development of dye-uptake models, to enable the future development of better dyes by understanding which factors in dye-uptake for cotton materials are important. Although cotton fibres have been examined previously, no other study has utilised atomic force microscopy (AFM) together with other complimentary surface science techniques to examine the surfaces of dyed and undyed cotton fibres to draw direct comparisons, and further explore dye-uptake mechanisms.

#### 1.1 INTRODUCTION

This introductory chapter is intended to highlight the importance of cotton textile fibre surfaces to a range of applications and hence the importance of their effective characterisation. Previous studies on cotton textile fibres are described within this chapter, and are followed by an outline of the main aims for this thesis.

## 1.2 CELLULOSE

Cellulose is the most abundant of all naturally occurring organic polymers, with thousands of millions of tonnes being produced by photosynthesis annually throughout the world<sup>1</sup>. As a material it has been widely used for centuries in all kinds of practical applications, such as textiles, papermaking and construction purposes. However, its chemical composition, structure and morphology remained unknown until the 19<sup>th</sup> century. The modern history of cellulose chemistry began in 1837 when Anselme Payen chemically identified cellulose as the main structural constituent in plants<sup>2</sup>. It was the first polymer on which X-ray investigation was performed<sup>3</sup>, a year after the discovery of diffraction of X-rays on crystalline materials in 1912. However, it was not until the 1930s that chemical structure of cellulose was established. Cellulose has an empirical formula of  $(C_6H_{10}O_5)_n$ , but it may be most conveniently described as a polydispersed linear polymer (polysaccharide) of 1,4- $\beta$ -D-glucan (see Figure 1.1), that is, a condensation polymer of  $\beta$ -D-glucopyranose with 1, 4-glycosidic bonds<sup>4</sup>.

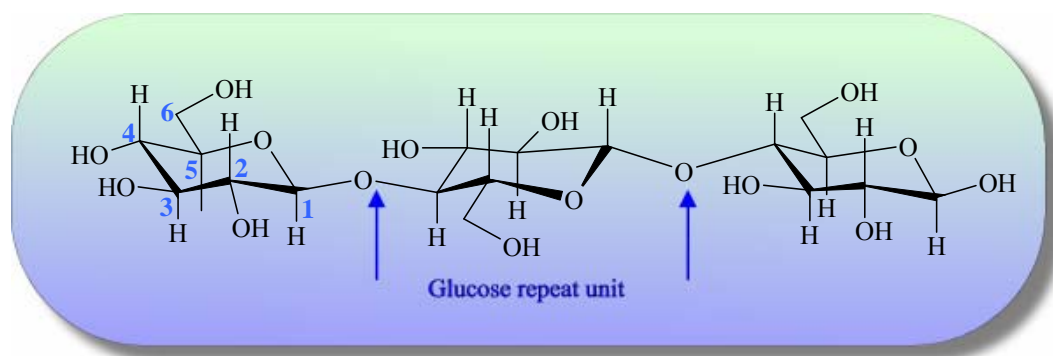


**Figure 1.1** Cellulose polymer chain in fully extended chair conformational formula.

The three hydroxyl groups (-OH) present in each glucose residue repeat unit can participate in hydrogen bond formation with other cellulose polymer chains, resulting in high intermolecular forces that combined with a regular structure, lead to a high degree of crystallinity<sup>5</sup>.

### **1.2.1 Macromolecular structure**

Cellulose is a highly *crystalline* material, but it does not form discrete crystals like those of glucose from which it is derived. The morphology and crystalline structure of cellulose are continuing areas of research and review<sup>6</sup>. X-ray diffraction (XRD) studies on crystallised cellulose have shown that cellulose chains form fairly straight and flat ribbons with a syndiotactic conformation<sup>7</sup> (alternating enantiomeric configurational base units). Transitions between chair and boat forms are possible, although steric hindrance and potential barriers from strongly polar groups make them unlikely<sup>8</sup>. Cellulose fibres from plant materials (such as cotton) consist of crystalline '*elementary fibrils*', named by Frey-Wyssling and Mühlethaler<sup>9</sup>, with a width of 35nm, and which are formed through the aggregation of cellulose polymer chains into partially crystalline bundles of molecules stabilised laterally through the hydrogen bonding<sup>10</sup>. Elementary fibrils vary in length and complexity and appear to be crystalline along their entire length<sup>11</sup>. These fibrils aggregate further to form *microfibrils*, which align themselves side-by-side to form concentric cylindrical lamellas with diameters in the order of tenths of a micron<sup>12</sup>.

### 1.2.1.1 Crystalline versus amorphous

Many theories and models exist about the crystalline or *amorphous* nature of cellulose. The ‘crystalline-fibril’ concept of the fine structure of cellulose in materials such as cotton has been refined by Rowland and Roberts<sup>13</sup>. They proposed that the microfibril consisted of a completely crystalline structure in which the irregularities were accounted for by various types of surface imperfections, such as distorted surfaces and twisted or strained regions of the crystalline elementary fibrils (see Figure 1.2).

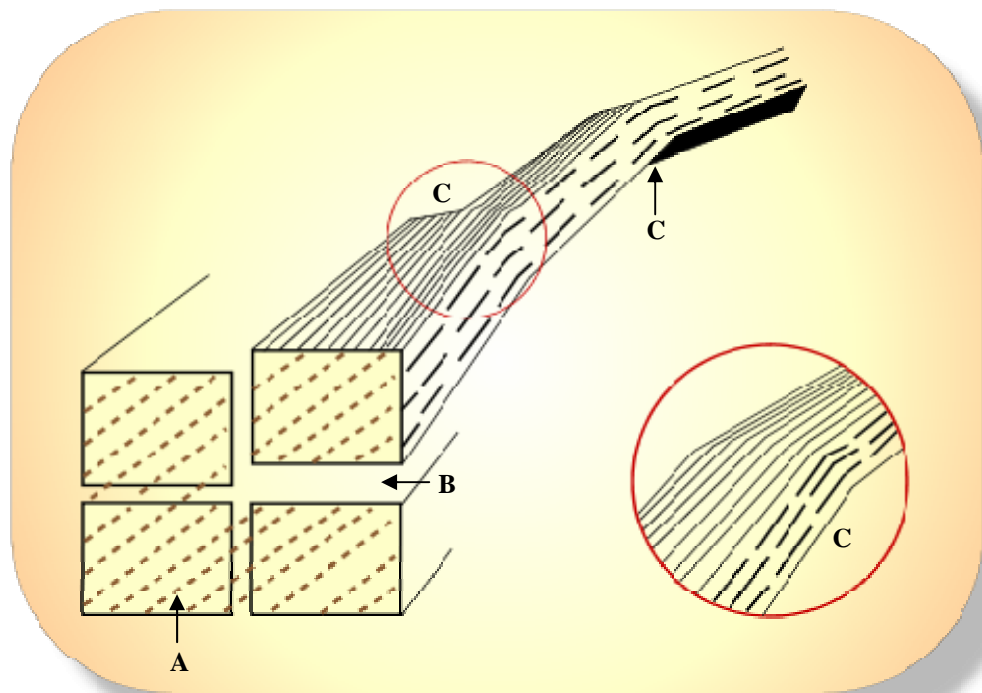


**Figure 1.2** Schematic representation of the elementary fibril as proposed by Rowland and Roberts showing: (A) coalesced highly ordered surfaces; (B) readily accessible disordered surfaces; (C) readily accessible surfaces of tilt/twist regions.

However, many studies based on a variety of physical and chemical methods have indicated that the microfibrils are not completely crystalline, but instead contain two distinctly different regions that are crystalline and amorphous<sup>14,15</sup>. For example Kondo and Sawatari<sup>16</sup>, who characterised hydrogen bond formation in methylcellulose polymer, using Fourier transform infra-red (FT-IR), revealed that while the hydroxyl groups at the C(2) and C(3) positions in the glucose repeating unit were isotropically involved in intermolecular hydrogen bonding in amorphous cellulose, the hydroxyl group at the C(6) position was favourably engaged in an inter-chain hydrogen bonding that resulted in the formation of a crystalline state. They proposed, therefore that amorphous cellulose might be composed, at least to some extent, by randomly distributed domains formed by intermolecular hydrogen bonds.

Howsmon and Sisson<sup>17</sup> hypothesised that there was a range of degrees of order in the packing of chain molecules within a cellulose fibre (see Figure 1.3), with a continuous transition from perfectly crystalline to completely amorphous material.

Another theory for degrees of crystallinity within cellulosic fibres is the *fringed-micellar* theory<sup>18,19,20</sup> in which crystalline micelles are embedded in an amorphous matrix (see Figure 1.4) with individual chain molecules extending through several crystalline and amorphous regions.

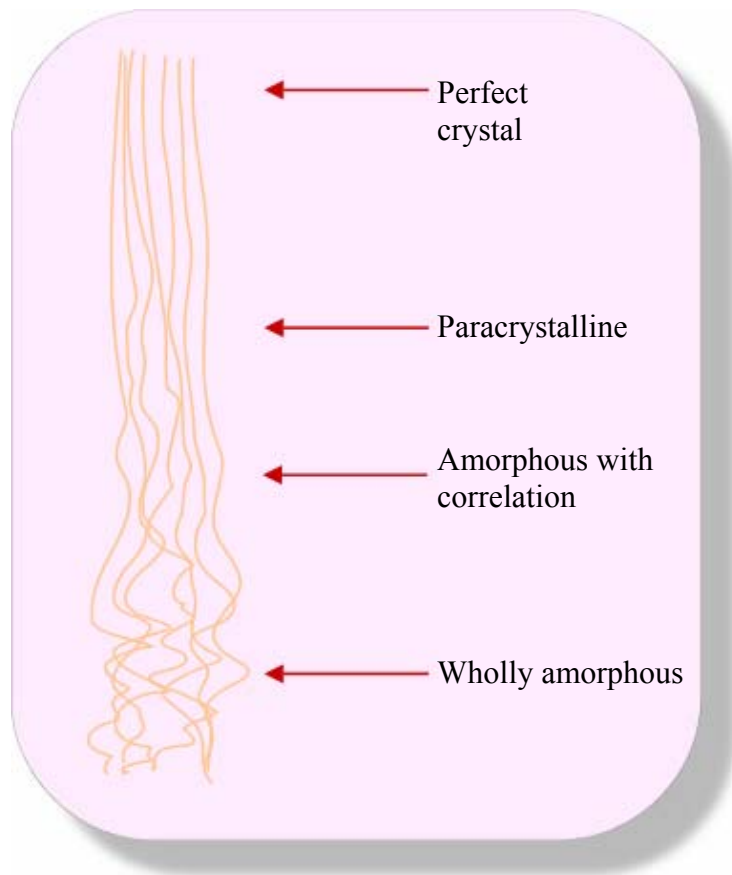


**Figure 1.3** Diagram of packing of chain molecules (crystalline to amorphous), as hypothesised by Howson and Sisson.

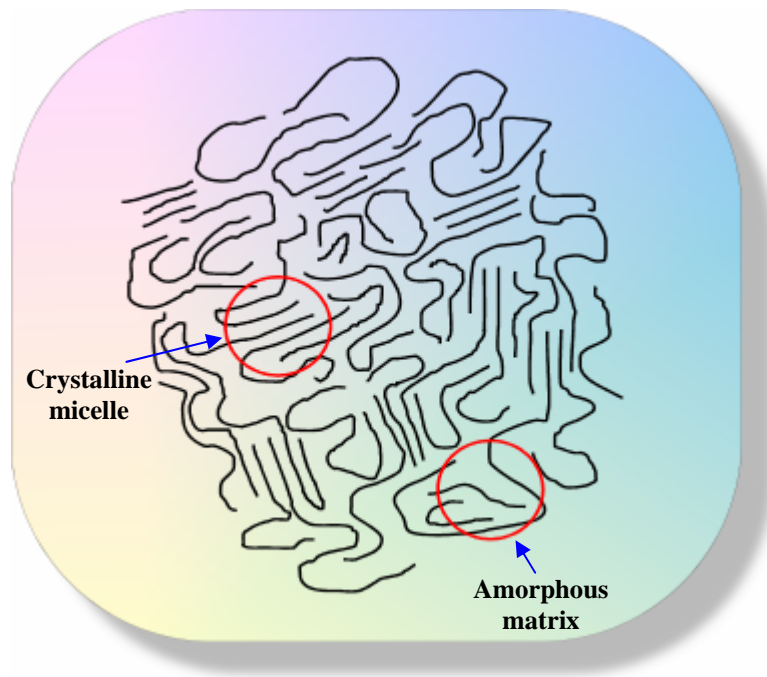


**Figure 1.4** Fringed micelle model displaying crystalline micelles within an amorphous matrix<sup>16,21</sup>.

A development of the fringed micellar theory was proposed by Fengel<sup>22</sup> (see Figure 1.5), who stated that the elementary cellulose fibrils from wood material, were surrounded by monolayers of hemicelluloses (a matrix polysaccharide with a lower molecular weight than cellulose), with the large units enveloped by hemicellulose and lignin (aromatic macromolecule found in wood).

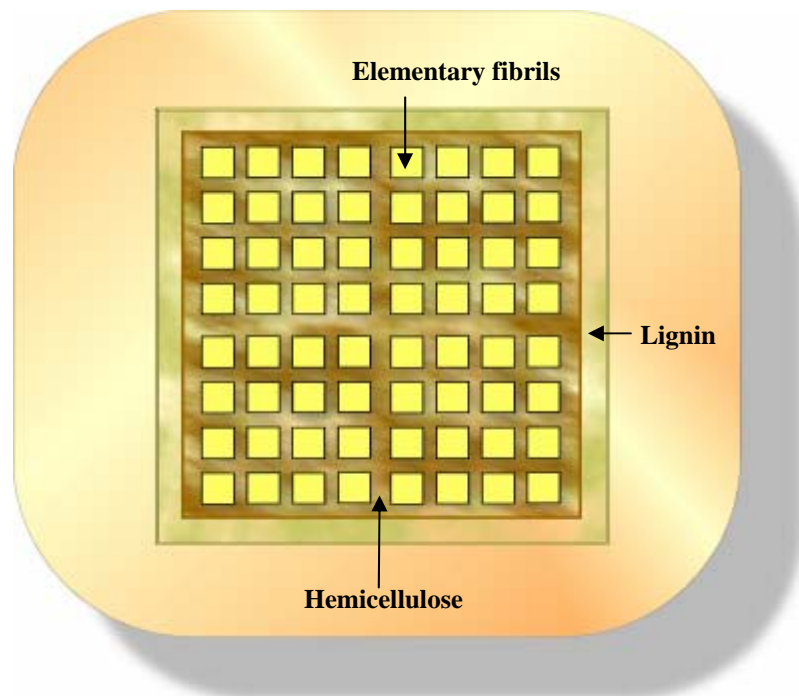


**Figure 1.5** Model of ultrastructural organisation of elementary fibrils lined within a hemicellulose and lignin matrix, as proposed by Fengel<sup>22</sup>.

However the various theories on crystalline and amorphous regions in cellulose are still speculative subjects. In 1967, Statton<sup>23</sup> pointed out that “theories and models of the crystalline/amorphous structure of cellulose are no more than theories and models. Very little is definitely known about the presence of

amorphous regions within cellulose macromolecular structure”. It can be said that the same is still true today, nevertheless, these concepts are helpful in considering the dyeing mechanisms of fibres, which are also key to the aims of this thesis.

#### *1.2.1.2 Modification of crystal structure*

The crystallisation behaviour of cellulose is influenced not only by chain conformation but also by the packing of adjacent chains<sup>24</sup> and the multiple possibilities of inter- and intramolecular hydrogen bonding. Chemical treatments and processing of cellulose can also generate a variety of polymorphic forms, and five have been identified<sup>25</sup> using XRD patterns<sup>26,27</sup> and FT-IR spectra<sup>28</sup>, but only cellulose I and cellulose II are believed to be important in textile processing. The other polymorphs (III, IV, and the fifth designated X)<sup>29</sup> can be formed after cellulose I along with cellulose II are subjected to treatments by heat or chemicals, but these are less important for the purpose of this thesis.

Cellulose I, *native cellulose* (to distinguish it from regenerated cellulose), is most commonly abundant in nature, whereas cellulose II is the most thermodynamically stable form, produced when cellulose is regenerated from solution or subjected to the process of *mercerisation* (see section 1.3.2.2). Transformation of cellulose I to cellulose II is irreversible which implies that cellulose II is the more stable form and native cellulose I is a metastable structure. This is thought to be due to the cellulose polymer chain strands in cellulose I, which lie parallel to each other but have no inter-sheet hydrogen

bonding. However, it is thought that within cellulose II the structure has an anti-parallel arrangement with some inter-sheet hydrogen bonding, making it more stable (see Figure 1.6), assumed through molecular dynamics (MD) simulations based on XRD data<sup>30</sup>.

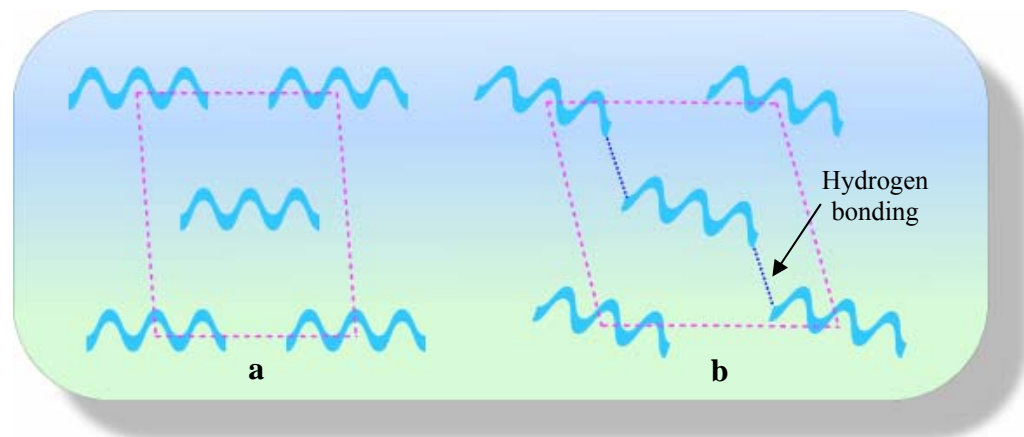


**Figure 1.6** Schematic showing cross section of cellobiose (2 glucose repeat units) unit cell, looking along the fibre axis: (a) cellulose I in parallel formation without hydrogen bonding; and (b) cellulose II in anti-parallel arrangement with inter-sheet hydrogen bonding.

### 1.2.1.3 Regenerated cellulose

Some important commercial products are prepared from cellulose by first dissolving the polymer, and then precipitating it from solution. As previously mentioned, cellulose may be regenerated by mercerisation or by acidification of the solution. The most widely used regeneration method is called the *xanthate* or *viscose process*<sup>31</sup>. *Alkali-cellulose*, (cellulose that is swollen with concentrated base) usually prepared from wood pulp, is allowed to age for 2–3 days, after which carbon disulfide ( $\text{CS}_2$ ) is added to convert the cellulose into the xanthate salt, (see Figure 1.7). Not all the hydroxyl groups are converted

within the polymer chain, but just enough to make the polymer more soluble in aqueous alkali. The basic solution known as viscose is further processed in a series of reactions with acids to convert the xanthate back in to cellulose (see section 1.3.2.2). Filaments extruded from the solution are stretched out to orient the molecules and increase crystallinity; these filaments are known as *viscose rayon*, which are an important textile fibre<sup>32</sup>. The technique is also applied for the production of continuous cellulose-derived films, called *cellophane*.

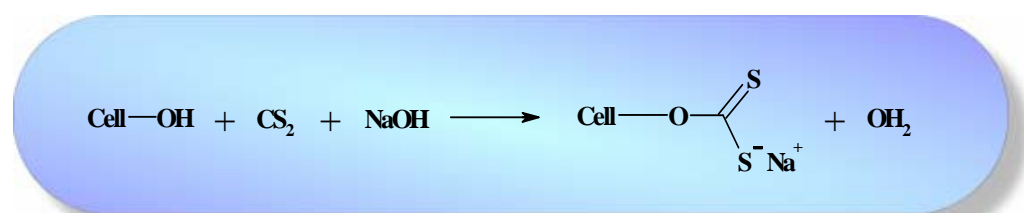


**Figure 1.7** Conversion of cellulose (Cell-OH) into xanthate, where some hydroxyl groups are replaced by xanthate ester groups. Upon treatment with acids, the xanthate returns to a more crystalline cellulose form (cellulose II).

A large number of other cellulose derivatives<sup>33,34,35</sup> have also been synthesised, including esters of inorganic acids<sup>36</sup>, ethers<sup>37</sup>, acetates<sup>38</sup>, and graft copolymers<sup>39</sup>, although relatively few have achieved commercial importance.

### **1.2.2 Characterisation of cellulose**

There is a large body of literature concerning the bulk and surface characterisation of cellulose and its derivatives by a variety of chemical, physical and theoretical methods, which is described in reviews by Rowland and Bertoniere<sup>40</sup>, Kamide and Saito<sup>41</sup>, Bayer et al.<sup>42</sup> and an editorial by Jarvis<sup>43</sup>. Some common techniques that are employed for characterisation of cellulose and its derivatives are summarised in Table 1.1. In the following sections of this chapter and chapter 2, the particular application of such characterisation techniques to cellulose textile materials, such as cotton will be discussed in further detail.

<b>Technique</b>	<b>Information</b>	<b>Reference</b>
<i>Bulk</i>		
XRD	Crystallinity - crystallite size and crystallinity index	Gümüřkaya & Usta <sup>44</sup> Koyama et al. <sup>45</sup>
Raman spectroscopy	Crystallinity – polymorphs	Atalla <sup>46</sup>
<sup>13</sup> C NMR	Crystallinity – hydrogen bonding	Viętor et al. <sup>47</sup>
Synchrotron X-ray & neutron diffraction	Crystal structure	Nishiyama et al. <sup>48</sup>
FT-IR & FT-Raman	Chemical degradation;	Proniewicz et al. <sup>49</sup>
FT-IR	Chemical composition;	Cao & Tan <sup>50</sup> Oh et al. <sup>51</sup>
DSC	Thermal degradation; Vaporisation of bound water	Jandura et al. <sup>52</sup> Hatakeyama et al. <sup>53</sup>
Theoretical modelling	Chain conformations, molecular dynamics	Pizzi & Eaton <sup>54</sup> Gessler et al. <sup>55</sup>
EM & electron diffraction	Crystallinity phases	Sugiyama et al. <sup>56</sup>
TEM	Crystallite dimensions	Wang & Ding <sup>57</sup>
<i>Surface</i>		
AFM	Frictional properties; Surface topography; Surface interactions	Zauscher & Klingenberg <sup>58</sup> Kuutti et al. <sup>59</sup> Nigmatullin et al. <sup>60</sup>
ATR-IR, ESCA & SEM EDAX	Surface chemistry	Krämer et al. <sup>61</sup>
FT-IR	Crystallinity	Hishikawa et al. <sup>62</sup>
ESCA & DCA	Surface interactions	Felix & Gatenholm <sup>63</sup>
AFM & TEM	Surface topography, microfibril dimensions	Hanley et al. <sup>64</sup>
EM	Fibrillar dimensions	Boylston & Hebert <sup>65</sup>
AFM & ESEM	Fibrillar dimension after swelling	Karlsson et al. <sup>66</sup>
ToF-SIMS	Surface chemistry	Baiardo et al. <sup>67</sup>

**Table 1.1** Summary of methods that have been used for the characterisation of cellulose and cellulosic materials (see Glossary page for terms).

### *1.2.2.1 Bulk characterisation of cellulose*

A number of comprehensive studies employing XRD have been carried out to distinguish the crystalline structure of cellulose. These include studies by Gümüşkaya & Usta, who examined the crystallite size of cellulose in wheat straw powder. They found that crystallite size increased when non-cellulosic material (such as lignin and hemicellulose) was removed from the powder. However, this was thought to be due to the chemicals that were used to remove these products, which caused the cellulose crystals to swell as well as reducing contaminants. Koyama et al. studied the crystalline features of algal celluloses and in particular the allomorphs of cellulose I, cellulose I<sub>α</sub> and cellulose II<sub>β</sub>. They were able to determine the dimensions and the orientation behaviour of the allomorphs within the cell wall surface of the algae. The group also discovered that one form of the allomorph, namely I<sub>α</sub> occurred mainly in primitive species of algae compared with II<sub>β</sub>. Atalla also examined the polymorphs I and II, but utilised Raman spectroscopy to do so. He confirmed that Raman data was consistent with existing infrared and X-ray data on the crystal structure and conformations.

In a more recent study, Proniewicz et al. utilised FT-IR and Fourier-transform Raman (FT-Raman) spectroscopy to examine the changes in cellulose structure after degradation processes, caused by acids, pollution and light. They found that the degradation processes irreversibly changed the hydrogen bond formation between molecular chains, due to loss of water in the form of a by-product. Similarly, Cao and Tan<sup>50</sup> examined hydrogen bonding energies with FT-IR, after native cellulose was treated with a series of microbial enzymes.

They found that through enzymatic treatment, the cellulose samples displayed changes in crystal structure through band shifts of –OH vibrations in FT-IR spectra. Hatakeyama et al. employed differential scanning calorimetry (DSC, see section 2.5) to examine the vaporisation of bound water associated with cellulose fibres in cellulose I and regenerated cellulose II. They showed that desorption of bound water (vaporisation split over two peaks observed at 60°C and 120°C) caused a structural change of the amorphous chains of cellulose, as the water molecules were directly attached to the hydroxyl groups within amorphous regions in cellulose I and II.

#### *1.2.2.2 Surface characterisation of cellulose*

Zauscher and Klingenberg examined the sliding frictional properties between cellulose surfaces in aqueous systems, using an extension of atomic force microscopy (AFM, see section 2.1), known as colloidal probe microscopy<sup>68,69</sup>. They attached a regenerated cellulose bead onto a silicon nitride cantilever, and then examined the surface forces between the probe and a cellulose flat film surface, at a scale that was appropriate for individual fibre-fibre contacts in a cellulose pulp suspension. They determined that friction was independent of surface roughness, but when polyelectrolytes were added to the beads, the sliding frictional forces were significantly lowered between the cellulose surfaces. Previous to this study, Hanley et al., used the AFM to image and characterise the surface topography of cellulose microfibrils, isolated from plant cell walls, however the topography of the microfibril surfaces showed a rounded profile due to convolution with the shape of the AFM cantilever tip.

The spectroscopic techniques of attenuated total reflectance infrared spectroscopy (ATR-IR), and X-ray photoelectron spectroscopy (XPS, see section 2.3) were utilised by Krämer et al. in their characterisation of modified cellulosic dialysis membranes. They were able to correlate surface chemistry with haemocompatibility by this approach. Felix and Gatenholm explored the surface properties of cellulose fibres (from wood pulp) in polymer composites, using electron spectroscopy for chemical analysis (ESCA, see also XPS) and dynamic contact angle (DCA) measurements. They were able to successfully resolve that surface chemistry, in the form of covalent bonding, was the defining factor for adhesion within the composites.

### **1.3 COTTON**

The main aim of this thesis was to establish a greater understanding of the surface characteristics and interactions of cotton textile materials through the use of AFM, time-of-flight mass spectrometry (ToF-SIMS), XPS, and other complimentary surface sensitive techniques.

Cotton, the purest form of cellulose found in nature, is the most used textile fibre in the world. The earliest evidence of using cotton as a textile fibre came from India, with a date assigned to 3000 B.C.<sup>70</sup>. There were also excavations of cotton fabrics of a comparable age in Southern America. Cotton cultivation first spread from India to Egypt, China and South Pacific<sup>71</sup>. Wild cotton is a perennial plant of tropical origin with an indeterminate fruiting habit, as it can continue to produce new foliage even after it begins to create seed. However cotton is most successfully cultivated in temperate climates with well-

distributed rainfall; hence today cotton is grown in more than 80 countries worldwide<sup>72</sup>. Despite its inherent perennial growth habit, cotton is managed as an annual crop plant, as continued vegetative growth after flowering diverts the plant's energy away from *lint* (fibre) and seed production<sup>73</sup>.

### **1.3.1 Cotton fibres**

Cotton fibres are the seed hairs of plants from the genus *Gossypium*<sup>74</sup>. Many species are grown commercially, but botanically, there are three principal groups of cotton that are of commercial importance. Type 1 fibres, known as *long* fibres, have *staple* (average fibre lengths) lengths varying from 25 to 60mm, this include the high quality fine cottons, such as Egyptian (*Gossypium barbadense*). Type 2, known as *medium*, are coarser species with shorter staple lengths (about 13-33mm), such as American Upland cotton (*Gossypium hirsutum*), and type 3 species are of even shorter staple lengths, (about 9-25mm, *G. herbaceum* and *G. arboretum*), and are usually from Asian countries such as India. These are also known as *short* fibres<sup>75</sup>.

### **1.3.2 Cotton plant and fruit growth**

Cotton is a shrubby plant with broad three-lobed leaves and seeds within capsules, or *bolls*. After pollination of the flowers occurs, the boll begins to develop (see Figure 1.8), and under optimum conditions the cotton plant would require approximately 50 days for a boll to 'open' (known as *dehiscence*, the opening of a blossom) after pollination. Within the boll each seed is surrounded with downy fibres (cotton fibres), which are white or creamy in colour<sup>76</sup>. The fibres have a fibrillar structure and the development of these

consists of four overlapping stages; (i) fibre initiation, (ii) cell elongation, (iii) secondary wall deposition and (iv) maturation.

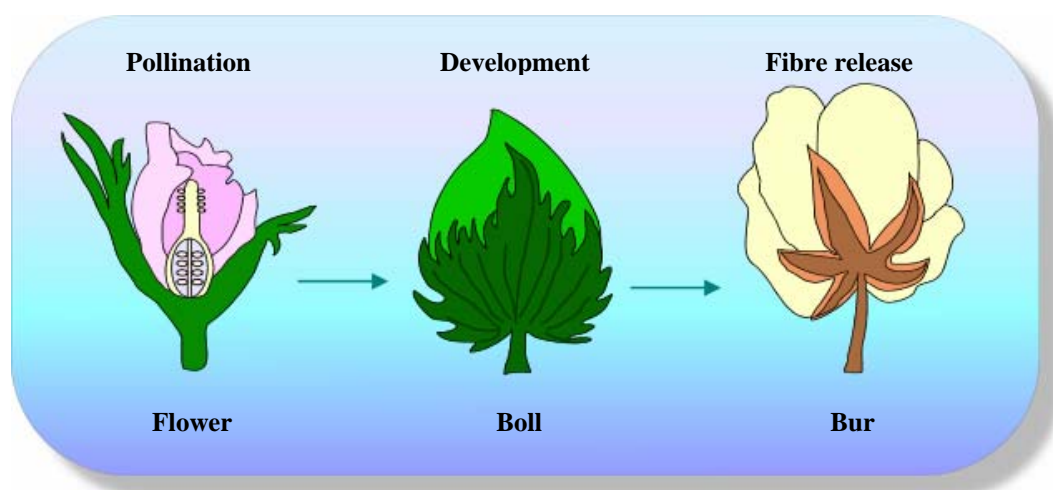


**Figure 1.8** Developmental stages of cotton fruit, from pollination of the flower, to development and maturation of fibres within the boll until the bur is formed through dehiscence.

Each fibre develops from a single epidermal cell on the surface layer of the cotton seed coat. During the early stages of fibre growth, (through boll development), the fibres elongate to their full length as thin-walled tubes. After slightly more than 2 weeks of lengthening, fibre cells synchronously enter the third stage of development, termed *secondary wall* deposition. During this time, the 1,4- $\beta$ -D-glucan chains that form the cellulose microfibrils of the secondary wall are synthesized, thickening the fibre wall by deposition inside the tube, leaving a hollow area at the centre. The boll maturation phase begins as the boll reaches its full size and maximum weight, and then boll dehiscence occurs, resulting in the release of cotton fibres, with the fruit now referred to as a *bur*.

### 1.3.2.1 Cotton fibre structure

The cotton fibre itself is composed of concentric layers. The cuticle layer of the fibre is separable from the fibre and consists of wax, fats and pectin materials. The primary wall, P1, the most peripheral layer of the fibre (see Figure 1.9), is thought to be composed of cellulosic crystalline fibrils<sup>77</sup>. The secondary wall of the fibre consists of three distinct layers, designated S1, S2 and S3. All three layers of the secondary wall include closely packed parallel fibrils with a spiral winding and represent the majority of cellulose within the fibre. The innermost part of cotton fibre is known as the lumen, and is filled with liquid containing cell nuclei and protoplasm material. The twists and convolutions of a dried fibre are due to the removal of this liquid at the end of the growth period. This mature fibre in the form of a flat ribbon varies in width between 12 and 20 $\mu\text{m}$ . Cotton fibres are also illustrated in cross-section within Figure 1.10. Their bean-shaped appearance is sometimes described as a *bilateral structure*, which indicates that the density of packing of cellulose chains is not uniform across the fibre. Hence the accessibility of the chain segments to various reagents varies across the fibre. For example, the three main zones (A, B, C in Figure 1.10) have been identified by means of enzymatic degradation<sup>78</sup>. The rate of degradation was found to increase from A to C, the order of decreasing density of packing, with zone N an area even more accessible than zone C (with an increased rate of degradation).

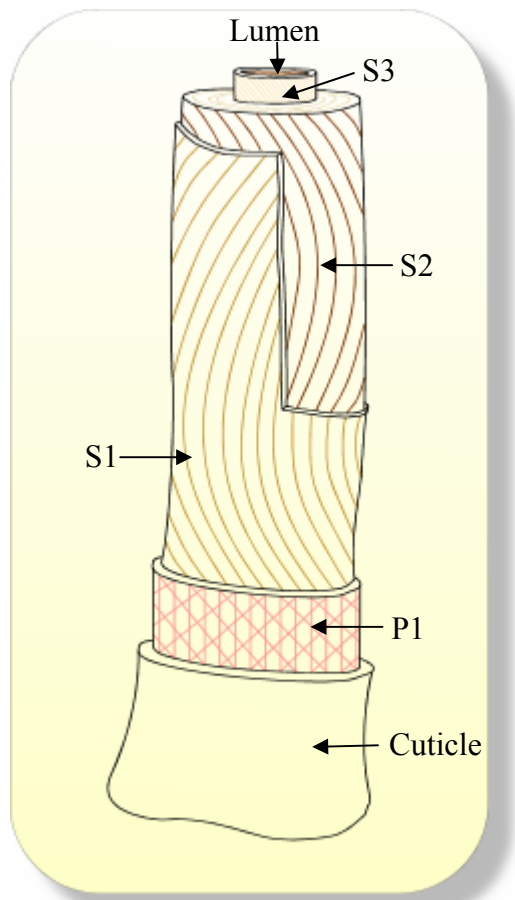


**Figure 1.9** Schematic to show layered structure of cotton fibre.

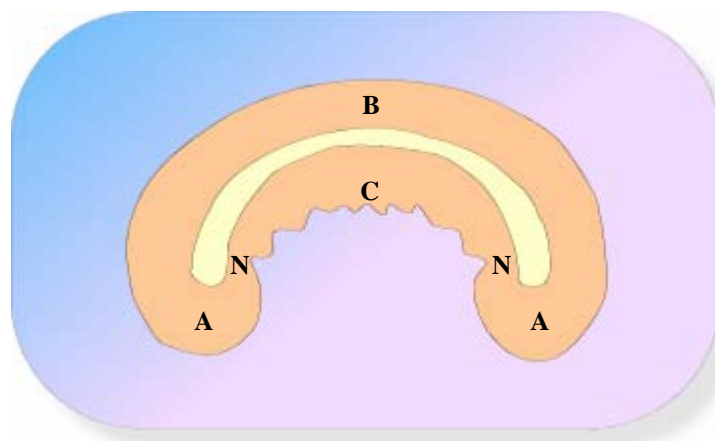


**Figure 1.10** Bilateral structure (cross-section) of mature cotton, zones A, B, C, and N differ in fibrillar packing density.

### 1.3.2.2 Mercerisation of cotton

An aim of this thesis was to improve the understanding of cotton interaction with dyes. It is already widely known within the dyeing industry that pre-treatment of cotton improves the dyeability and dye-uptake of the fibres. This was first discovered by John Mercer in 1877<sup>79,80</sup>. He suggested that using reagents, such as 25-30% sodium hydroxide (NaOH) or 62% sulphuric acid at room temperature on cotton yarn caused the fibres to swell in diameter and shrink in length, thus making the fabric denser and increasing its tensile strength<sup>81</sup>. About 40 years later Horace Lowe<sup>82</sup> discovered that if cotton cloth was stretched to its original dimensions during subsequent washing, or if it was held under tension to prevent it from shrinking during treatment, it acquired a much improved lustre and smoothness. Eventually this process became known as *mercerisation*, after Mercer, and is still widely practiced in the textile industry using entirely NaOH solutions<sup>83</sup>.

Within the actual process, the cotton fibres are thought to swell, causing breakage of the hydrogen bonds between adjacent cellulose chain molecules. With water and dilute aqueous solution this is proposed to occur in accessible (amorphous) regions of the fibres, located between fibrillar surfaces, and not in crystalline regions. However, NaOH solution is thought to penetrate the crystallites and only partially disrupt the solid structure of cellulose without causing complete disruption, as it displays no effect on the van der Waals forces which act at right angles to the hydrogen bonds between the cellulose chains<sup>84</sup>. Consequently, the cellulose acts as countless sheets held together by van der Waals forces that are capable of being pushed apart by NaOH

molecules, therefore causing the natural crystalline structure of the cellulose to relax. An intermediate step occurs with this process involving the initial conversion of cellulose I to Na-cellulose I<sup>85</sup>, an ionic association of Na<sup>+</sup> with the crystal which results in a change in the orientation of the crystals. Hence under an appropriate tension (as performed by Lowe), the crystalline dimensions can be set by the conditions. Rinsing with water while these conditions are maintained, removes the alkali along with ions associated with the crystals, thus completing the final conversion of cellulose to a new crystalline structure<sup>86</sup>, (cellulose I to cellulose II), fixing the dimensions within the cellulose molecule.

Raw cotton consists of 90-95% cellulose<sup>87</sup>, but also consists of waxes, pectins, and other plant material. It is these minor constituents which are removed during mercerisation to give a soft, clean, white and absorbent fibre. The cuticle layer in cotton fibres is impermeable to water and aqueous solutions, therefore it is removed during processing to aid the uptake of solutions and dyes. Mercerisation loosens the waxy cuticle layer, containing the pectins and other non-cellulosic materials to allow it to be rinsed away. After mercerisation, the fibres are normally bleached to remove their natural colour.

### *1.3.2.3 Applications of cotton*

In recent times, the cotton plant has not only been utilised for textile production, but also within other industries. As cotton cultivation has declined since the appearance of synthetic fibres, new markets have developed (see

Table 1.2). Such as the use of cotton plant residue as a supplemental fuel source for a power-generating plant in southern Arizona in U.S.A.<sup>88</sup>.

Main constituents	Uses
Lignocellulosic substances	Energy Pulp and paper Chemicals
Linters	Foods Chemicals Textiles Pulp and paper
Short fibres	Chemicals Textiles Pulp and paper Pharmaceuticals
Staple fibres	Textiles Furniture
Cuticles	Chemicals Pharmaceuticals Energy

**Table 1.2** Traditional and innovative uses of cotton plant<sup>89</sup>.

### 1.3.3 Characterisation of cotton

The observation and characterisation of cotton fibres is important for describing, defining and refining some questions in the paper and textile industries, and in particular to this thesis the application of dyes to textiles. The following text provides an overview of the existing literature relevant to the contents of this thesis.

Weis et al.<sup>90</sup> characterised through optical microscopy, the cell wall cytochemistry of motes (unfertilised ovules or aborted seeds) and compared them with normally developing seeds from the cotton plant. Mote fibres were

used as a model for non-dyeing fibres, as it was known within the industry that they might set as a contributor to poor quality textiles. The primary and secondary fibre walls were stained for cellulose, pectin, cutin and other non-cellulosic materials and viewed using conventional optical microscopy. After 25 days post-anthesis (DPA, the process of budding and unfolding of a blossom, refer to section 1.3.2) the mote fibres displayed primary walls that were rich in pectins with a thin layer of cellulose, which in normally developing fibres is indistinguishable from primary walls. Within the secondary walls, cellulose was found to be irregularly deposited, in contrast to the normally developing fibres which displayed thick cellulosic layers. At 29 DPA and the later stages of development, Weis et al. were able to show that fibres on normal seeds had well-developed secondary walls but the mote fibres were proportionately less developed. As most industrial dyes are specific for cellulose, these studies supported the theory that mote fibres made poor quality textiles, with mote fibres displaying a lack of cellulose and thus contributing to dye imperfections in fabrics.

In more recent times Maxwell et al.<sup>91</sup> investigated the morphological, nano-mechanical, and moisture absorption properties of transverse sections of mature and immature cotton fibres using scanning probe microscopy (SPM, see section 2.1). They examined the samples within resin blocks and cut away sections to reveal; growth bands, the lumen, and discrete fibrils with variations in the fibril density across the fibre cross-sections.

Takács et al.<sup>92</sup> studied the effect of  $\gamma$ -radiation and alkali treatment on cotton cellulose. They found that the irradiation of the sample resulted in the degradation of cellulose, which they characterised (using FT-IR) by the decrease in the degree of polymerisation and an increase in the carbonyl content. NaOH treatment after irradiation had no significant effect on these characteristics. But through XRD and SEM the group were able to show that the transformation of the crystalline structure from cellulose I to cellulose II occurred at lower alkaline concentrations when irradiation pre-treatment was applied. As small molecules such NaOH were able to access the crystal defects caused by the irradiation more easily.

In an earlier study to examine cotton fibre interaction with an aqueous medium for paper production, Siffert and Metzger<sup>93</sup> studied the adsorption of titanium oxide ( $\text{TiO}_2$ ) to cellulose fibres and found that adsorption was dependent on van der Waals and electrostatic forces. More precisely the interaction was dependent on the size of the  $\text{TiO}_2$  particle (particle aggregates) and its surface charge, which were strongly influenced by the pH. For successful adsorption to cellulose, the  $\text{TiO}_2$  particles needed to be small and have a surface charge close to that of the cellulose fibre itself.

Gilbert and Kokot<sup>94</sup> presented their characterisation work on processed cotton fabrics. They used FT-IR and FT-Raman to distinguish between cotton samples from each fabric processing stage, and found that the IR and Raman spectra from each processing stage appeared very similar for all cotton samples, with only minor variations. However, once a principle component

analysis (using a commercially available computer analysis program) was applied to all the spectra, it was observed that sample discrimination was possible for the Raman spectra, with some slight differences observed for the IR study. By using the two techniques and applying spectral data analysis the group were able to successfully discriminate cotton fabric samples from specific processing stages.

In more recent times, studies have focussed on improving the quality of cotton fibres produced by means of genetic modification and biotechnology. Ji et al.<sup>95</sup> isolated complimentary DNA (cDNA), that was expressed specifically in cotton fibres and found that once it was translocated into fission yeast cells (*Schizosaccharomyces pombe*), it induced longitudinal growth of the host cells with no effects on other aspects of the host cells. Ji et al. concluded that the sequence of cDNA played an important role in cotton fibre elongation and showed that further elucidation of the control mechanisms was necessary in the future improvement of cotton fibre quality. At the same time Harmer et al.<sup>96</sup> also characterised six  $\alpha$ -expansin (cell wall proteins which facilitate cell wall extension by disruption of non-covalent bonds between wall components) genes associated with cotton fibre elongation. They found that four of the genes were expressed within multiple tissues of the cotton plant but only two gave rise to transcripts that were specific to the developing cotton fibre. Other types of genetic modification have improved the resistance of cotton plants to pests and diseases, and the reader is directed to specific reviews on cotton biotechnology and cotton fibres, by John<sup>97</sup> and Wilkins et al.<sup>98</sup>.

#### 1.3.4 Other studies on cotton fibres

Other studies on cotton have included experiments on its wetting ability, particularly the degradation of cotton fabrics<sup>99,100</sup> by perspiration<sup>101</sup> and its prevention through fibre modification<sup>102,103,104</sup>. Fabrics used in tropical climates are of mainly cotton types, because of their ability to absorb moisture and perspiration away from the body. However cotton fabrics degrade after prolonged exposure to various stresses, including acid hydrolysis by perspiration. Many studies<sup>105,106</sup> have examined this in detail including Bhat et al.<sup>107</sup>, who considered the effect of lactic acid on cotton fibres, as it is found to be a component of human perspiration. They carried out the hydrolysis of cotton fibres using lactic acid for different durations and their studies revealed the mechanism for the degradation and partial dissolution of cellulose, as the 1,4- $\beta$ -glycosidic bonds within cellulose had been broken. This resulted in an extension of the crystallite zones involving longer chain segments; the increase in crystallinity was observed by XRD and IR spectroscopic studies. However the breakage of the 1,4- $\beta$ -glycosidic bonds also resulted in a decrease in the tensile strength of the fabric, and this change was reflected in the characteristic surface morphology of the cotton fibres, viewed by SEM, through degradation cracks that were observed on the cotton fibre surface.

Pongprayoon et al.<sup>108</sup> studied the wettability of cotton fabric in order to develop water repellent clothing that at the same time would allow water vapour to be transported through the fabric (to allow the wearer to feel more comfortable by keeping dry). They modified the cotton surface by coating it with admicellar polymerisation of styrene, and then tested the fabric's

hydrophobicity by taking contact-angle measurements and characterising the surface by AFM, (see section 2.1). They examined a series of coating strengths to find the optimal coating which would fit the criteria of water repellence, and a ratio of 1:5 of LAS/styrene (LAS is a linear alkylbenzene sulphonate, an anionic surfactant) was deemed to provide the optimum condition for the production of cotton with a hydrophobic character, as fabric with this coating exhibited higher contact angles and best coverage of cotton fibres, viewed by AFM. Pongprayoon et al.<sup>109</sup> later went on to improve their method for cotton fibre coating by thin film polystyrene with the help of cross-linking agents and judged its suitability by XPS. By using XPS the group were able to perform quantitative analysis on their fabric samples and determine percentage film coverage. They utilised the oxygen peak signal as a marker for cellulose within the fibres, as oxygen had no signal for pure polystyrene, and found that when optimal coverage of the fibres was reached the oxygen signal weakened. The group concluded that the use of cross-linking agents aided better coverage of the polystyrene on the fibre surfaces.

Cotton fibres have also been modified for use as sustained release drug carriers. Liu et al.<sup>110</sup> prepared cotton fibres with a chitosan coating (the *N*-deacetylated form of chitin, a naturally occurring polysaccharide), and observed through fluorescence microscopy and SEM that the coated fibre surface was more coarse than the usual cotton fibre surface, and suggested that this would increase drug absorption to the fibre. They obtained promising results with a herb medicine called *Shikonin*, and found cotton fibres to be suitable as a drug carrier. The group discovered that the chitosan treatment of

the cotton caused the tensile properties of the fibres to weaken. This was attributed to the oxidation of the fibres by potassium periodate (KIO<sub>4</sub>) which was applied to the fibres, prior to chitosan coating. The group believed this damaged the crystal structure of the cellulose in the cotton fibre, thus producing an unsuitable textile material but a useful drug carrier.

## 1.4 DYES

Dyes are substances used to colour textiles, paper, hair, or food. Unlike paints, which remain on the surface, dyes are dispersed into, or chemically bonded to the material they colour. Dye pigments contain chemical groups, known as *chromophores* or *chromogens*, which confer colour onto the material of interest. The occurrence of dyes has been known for many thousands of years. For example, *Indigo* the oldest known dye, was used by the ancient Egyptians to dye mummy cloths<sup>111</sup>. Before synthetic dyes, most dyes were obtained from natural sources. William H. Perkin (the founder of the synthetic dye industry) discovered the first synthetic dye, *Mauveine*, in 1856<sup>112</sup>. Since this time many thousands of synthetic dyes have been made, and the active ingredients of many natural dyes have been chemically synthesised.

Important characteristics of dyes, include hue, strength, and brightness, these can be explained in terms of wavelength and absorption energy. Dyes are characterised in accordance with their capacity to absorb the energy of electromagnetic radiation to which the human eye is sensitive. The dye compound wavelength of maximum absorption ( $\lambda_{\text{max}}$ ) within the visible band is thought to indicate its hue. The intensity of the visible band is a measure of the

strength of dye and the width of the visible band determines the brightness of a dye, hence the narrower the band of wavelength, the brighter the shade of the dye<sup>113</sup>. Dyes can also be grouped according to two different principles; chemical structure, or application of dyeing methods. However, these two areas overlap, as there is hardly a chemical class of dye that occurs solely in one colouristic group and vice versa. The main chemical types of dye compounds are azo, anthraquinone and aza annulene structures. When classified according to dyeing method, they may be known as *direct*, *reactive* or *disperse* dyes, depending on whether they are intended for use on protein, cellulose or polyamide fibres. However for the purposes of this thesis we shall concentrate on reactive dyes only as they have the most affinity for cellulose. Reactive dyes are thought to enter into chemical combination with cellulose structure and therefore give an excellent fastness property, such as resistance to fading. They contain groups (for example, sulphonic acid group – SO<sub>3</sub>H) that are capable of reacting with the substrate to form covalent bonds.

#### **1.4.1 Dyeing Theories**

Dye molecules must be firmly attached to textile fibres to which they are applied in order to resist removal, for example by washing. However, there is no single interpretation of the interaction of dyes with fibres. The most well established models describe limiting cases; such as when the dye and substrate are in thermodynamic equilibrium, which only partially reflect the practical dyeing processes.

Dye molecules of many chemical structure classes are designed to activate attractive forces within the polymer molecules of the fibre. As mentioned before, in reactive dyeing, the dye molecules combine chemically with the polymer forming covalent bonds. Whatever the proposed method of dyeing, the dye must distribute itself evenly throughout the material to give uniform colour, a process known as level dyeing<sup>114</sup>.

The process of fibre dyeing for some dyes can be considered to occur in three stages; the diffusion of dye molecules from the solution to the surface of a fibre, the adsorption of dye molecules on the surface, and the diffusion of the dye to the fibre centre. Of the three stages, diffusion of dye molecules inside the fibre is considered to be the rate-determining step, therefore making the study of dye diffusion in fibres extremely important.

The absence of a molecular model for the dye sorption process on cellulose fibres makes it difficult to exact a location of dye binding sites in cotton fibres that is if it occurs in crystalline or amorphous regions<sup>115</sup>. Much research has been directed towards increasing the dyeability of cotton<sup>116,117,118</sup> and in particular dye binding in the possible crystalline regions of cellulose<sup>119,120</sup>. Although dyeing is believed to be more difficult within the crystalline regions of the cellulose fibre, it is not confined to the external surface. Accessible internal surfaces include the voids between microfibrils and the space between elementary fibrils<sup>121</sup>, are thought to afford entry for dye molecules<sup>122</sup>, provided they are not prevented from entering by their physical size. Therefore, it is

considered that the application of many dyes to cotton is accompanied by a minimum of chemical change within cellulose of the fibre.

#### **1.4.2 Investigations of dye-uptake in cellulose**

Ferreira et al.<sup>123</sup> studied the emission spectra of the fluorescent dye Auramine O, after exposure to microcrystalline cellulose. They concluded that the dye in its monomeric form was strongly entrapped and rigidly held between polymer chains of cellulose, which were prepared with solvents that had swollen the substrate efficiently. Kai et al.<sup>124,125</sup> have studied effects of dyes on microbial cellulose by X-ray diffraction and <sup>13</sup>C-NMR and concluded that the dyes formed a crystalline complex with the microbial cellulose from the diffraction patterns. In contrast Daescu et al.<sup>126</sup> have focussed upon the sorption of dyes in the amorphous regions of cellulose by utilising correlations of azotol affinity with computed hydrophobicity and steric azotol parameters. They considered the hypothesis of the existence of multi-layered microcrystalline micelles at the surface of cellulose fibre, as regions of potential azotol sorption.

Application of QSAR techniques to dye-cellulose binding is based on the hypothesis of specific dye-fibre interaction<sup>127</sup>. Electrostatic interactions act between the ionic centres of the dyes and ionise polymers, such as cellulose (at the hydroxyl groups, refer to Figure 1.1). It is the charge properties of the exterior fibre surface, which are responsible for the kinetics and thermodynamics of the surface sorption of ions and molecules of dyes<sup>128</sup>. Van der Waals interactions between dye molecules and the substrate help in the sorption of dyes in fibres if the distance between the dye and polymer molecule

is very small, as for dyes with large planar structures<sup>129</sup>, due to less steric hindrance of the dye molecule. Dye-fibre hydrogen bonds are controlled by the presence of hydrogen bonding functional groups in the fibre and the dye which is true for cellulose (hydroxyl groups). The importance of hydrogen bonding in dyeing is shown by the fact that most dyes contain nitrogen and/or oxygen atoms. It is the availability of lone pair of electrons on these atoms that appears to greatly influence the dye affinity for cellulose. Timofei et al. used qualitative and quantitative studies carried out by QSAR/QSPR (quantitative structure-activity/property relationships) techniques to investigate industrial dye adsorption on cellulose fibres. They concluded from their studies that there were many similarities between dye-fibre interactions and biological receptor-ligand interactions. Comparisons of the results showed that these methods usually agreed with their predictions of structural features of dyes and fibre substrates, favourable for dyeing.

Gooding et al.<sup>130</sup> studied the kinetics and mechanism of azo dye-uptake in cotton and nylon cloths. They found that the variation in dyeing with flow rate proceeded via a mechanism in which the flux of dye entering the cloth relative to the flux of dye at the cloth surface, decreased with increasing flow rate. They deduced a mechanism, in which the dye passed from the bulk solution through a porous surface layer within the cloth, before passing into the bulk cloth, and adsorption onto surface sites in this porous layer blocked the passage of further dye into the cloth (see Figure 1.11).

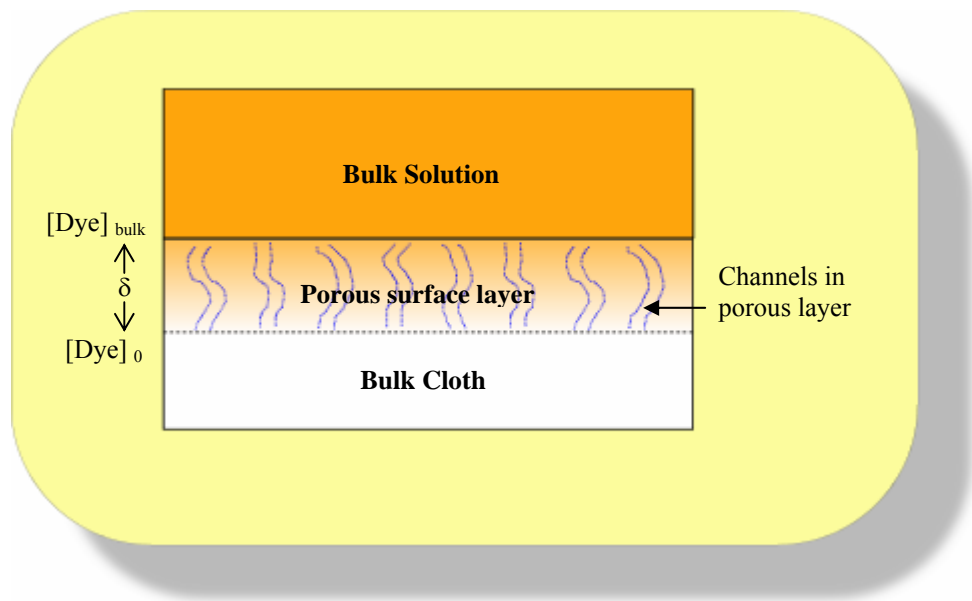


**Figure 1.11** Schematic of the model describing the dyeing mechanism with azo direct dyes as hypothesised by Gooding et al. .

The group found that the rate of dye crossing the surface layer/bulk cloth interface was dependent on the difference between the concentration gradient and the dye concentration at this interface.

## 1.5 AIMS & OUTLINE OF RESEARCH

Through the previously discussed literature, it is evident that there is only limited existing information about how cotton cellulose and dyes truly interact. The mechanisms detailed in the previous sections are likely models for the interactions that take place, but lack data that is supportive or otherwise. It is the aim of this project to utilise AFM, with other surface sensitive techniques, to investigate the surfaces of both undyed and dyed cellulose based textiles in order to provide this much needed information. Although previous studies of cotton fibres using surface sensitive techniques exist, none have tried to

investigate the cellulose and dye at the point of interaction, so that the dye-uptake mechanism can be further elucidated. The advantage of using the AFM is that it allows the user to view both dyed/undyed cellulose fibres at the nanometer scale, potentially enabling the user to identify and image crystalline and amorphous regions within cellulose, and gain an understanding of dye-uptake into cotton fibres. Here I test this hypothesis with a view to improving the existing knowledge on dye-uptake mechanisms, and providing a basis for future research on manufacturing more sophisticated dyes to advance dyeing techniques.

Chapter 2 provides background information on the techniques employed within this thesis, with specific details of instrumentation on AFM, ToF-SIMS, XPS, SEM and DSC. A review of the limited existing literature on textiles materials investigated using the techniques mentioned and the main experimental methods used through this thesis are also outlined.

The studies presented within chapter 3 focuses on characterising cellulose within a model system, cellophane film, specifically with AFM. Experimental protocols for sample imaging were optimised and the investigations within this study also discerned through other surface sensitive techniques, similarities and differences between undyed and dyed cellophane samples. This chapter explains an understanding of the cellulosic structure within the model system, which then leads into the analysis of cotton fibres.

Chapter 4 concentrates on cotton fibre characterisation using the same techniques employed in chapter 3 and discerns differences between dyed and undyed fibres. It also studies the structural differences of mercerised and non-mercerised (greige) cotton fibres, through the use of AFM and phase imaging, which highlights the cuticle layer and possible underlying crystalline structure.

The studies presented in chapter 5 displays data from XPS analysis which was employed to quantitatively determine dye coverage of cotton fibres at the surface and to determine whether dye concentration affected the percentage amount of dye attached to the cotton surface. This chapter also contains results obtained from DSC and highlights crystallinity of cotton cellulose fibres, as well as preliminary AFM studies of undyed cellophane using dye-functionalised tip. Chapter 6 is the final chapter; it states the final conclusions and discusses the work undertaken with the long-term implications and objectives of this research.

### **Instrumentation & Experimental Methods**

Described within this chapter are the techniques and instruments used to analyse and investigate dyed and undyed cellulose samples for this thesis. The following literature will also review the existing studies on various textile materials, which have been performed already using these specific techniques. However it will become evident to the reader that there is a lack of investigation for dyed cellulose fibres using these particular analysis methods.

#### **2.1 ATOMIC FORCE MICROSCOPY**

The atomic force microscope (AFM) was developed by Binnig, Quate and Gerber in 1986<sup>131</sup>, following its predecessor, the scanning tunnelling microscope (STM)<sup>132</sup>. Both instruments belong to a family of microscopes broadly known as scanning probe microscopes (SPM) that rely upon interactions between a proximal probe and a sample surface in order to derive surface sensitive data. The AFM is an invaluable high-resolution imaging technique that is used in a wide variety of disciplines, including surface science, surface roughness analysis and three-dimensional (3-D) imaging. An important feature of AFM is that data can be acquired in a range of dynamic environments such as air and liquids, without the need of prior surface treatment for samples. This is in contrast to the STM which required the sample surface to be conductive and it was this drawback that led to the

successful development of the AFM. The AFM critically allows samples to be analysed close to or within their natural state, and for these studies it is proposed that these abilities could provide significant information on the fibrillar assembly and ultra-structure of cellulose fibrils within cotton fibres.

### 2.1.1 Instrumentation

The primary use of AFM is to quantitatively determine surface morphology at the nano-scale, by virtue of the forces of interaction between a sharp probing tip, which is attached to the free end of a deflecting cantilever spring, and the sample surface. The cantilever acts as a soft spring of known spring constant that obeys Hookes Law (Equation 2.1):

$$F = -kz \quad (2.1)$$

Where  $F$  is the force acting on the cantilever,  $k$  is the cantilever spring constant and  $z$  is the vertical displacement of the end of the cantilever. The micro-fabricated cantilever, typically composed of silicon nitride ( $\text{Si}_3\text{N}_4$ ), has dimensions of 50-200 $\mu\text{m}$  in length and with a tip located at the apex with a radius of 5-20nm<sup>133</sup> (see Figure 2.1) with a point of contact area<sup>134</sup> equating to 10nm<sup>2</sup>. The sharpness of the tip is the key determinant in the resolution of AFM imaging, hence efforts have been made in the manufacture of probes which incorporate carbon nanotubes as their tips, as these are much sharper than conventional tips<sup>135,136,137</sup>.

The tip is raster scanned in the  $xy$ -plane over the specimen either by moving the sample beneath a fixed tip or by moving the tip over the sample area (see

Figure 2.2). A diode laser is focused onto the back of the cantilever and reflected onto a position sensitive (photo) diode. The detection system measures the angle of reflection of the laser from the cantilever through the photodiode. During scanning the laser beam is deflected off the cantilever as it moves up and down with the contour of the sample surface, into a four quadrant photodiode. A feedback loop connects the photodiode to a piezoelectric scanner, which controls the  $z$ -position of the tip or sample, depending on instrument. The  $z$ -movement of the piezo-scanner is plotted against lateral probe position producing a 3-D image of the surface.

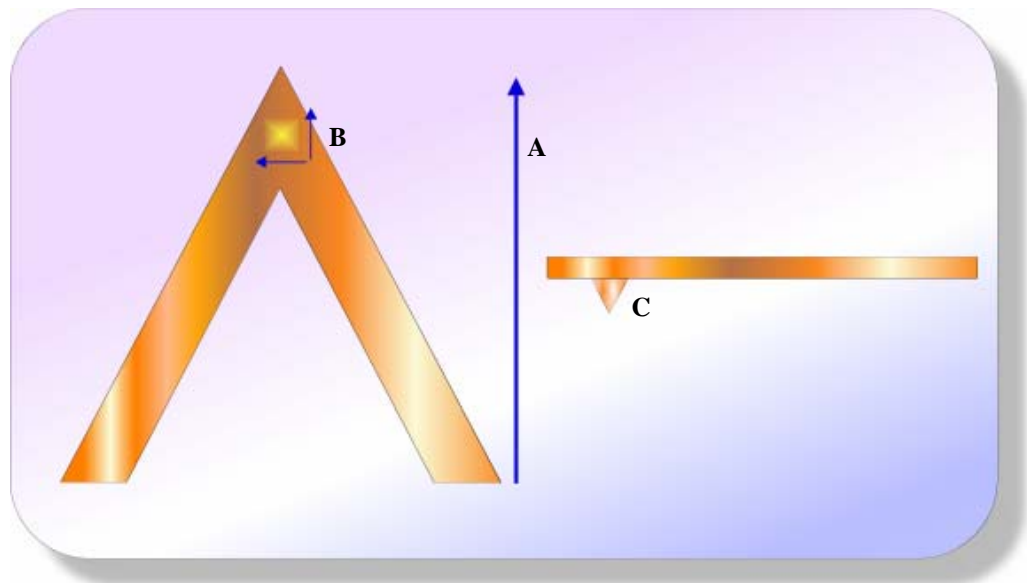


**Figure 2.1** Schematic of typical silicon nitride ( $\text{Si}_3\text{N}_4$ ) cantilever with approximate dimensions; (A) 50-200 $\mu\text{m}$  in length, (B) square-based pyramid tip with base measurements from 4x4 $\mu\text{m}$ , and (C) tip apex with 10-50nm radius.

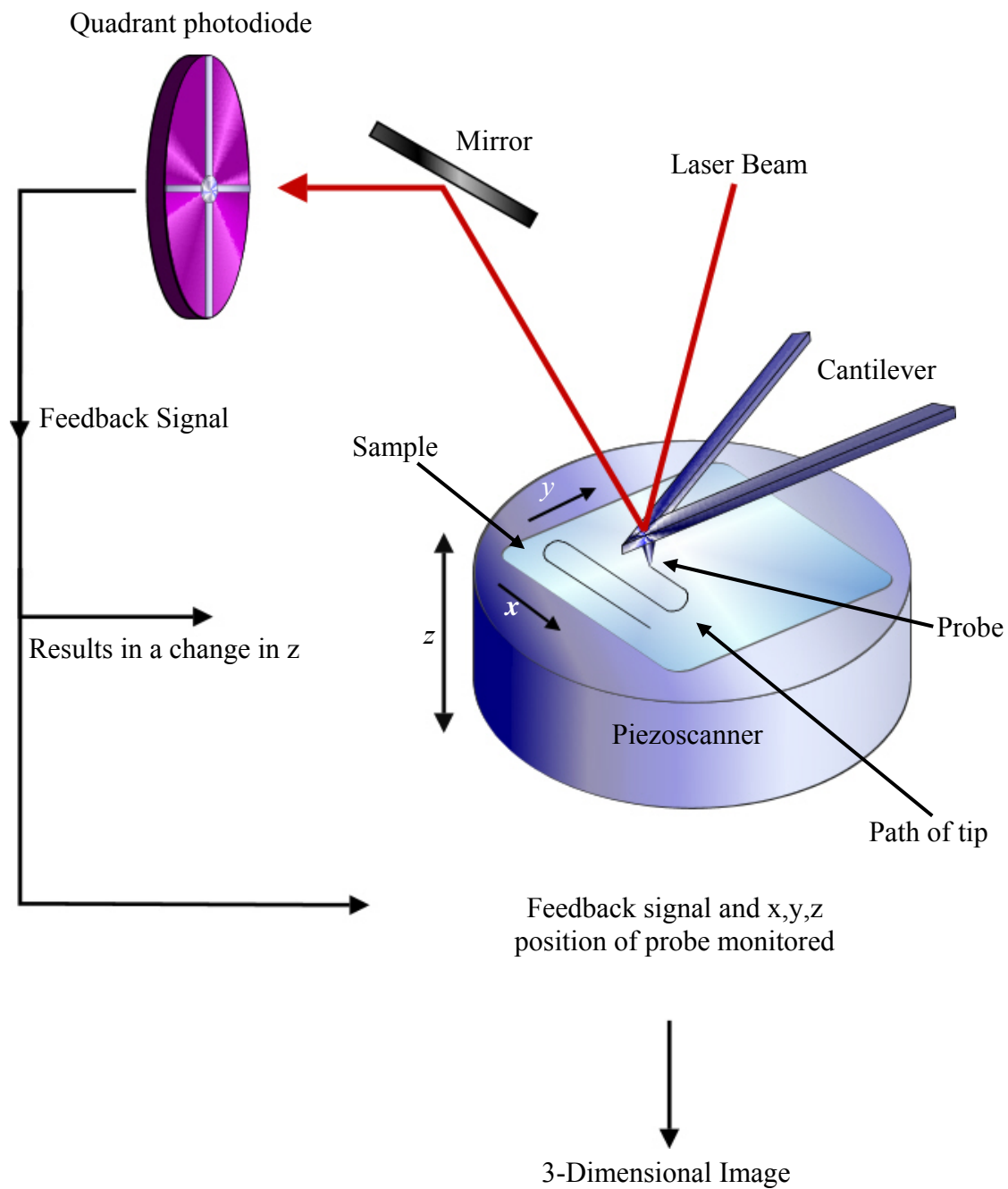


**Figure 2.2** Adapted schematic illustration of the atomic force microscope (AFM)<sup>138</sup>.

## 2.1.2 Operational modes

Several forces typically contribute to the deflection of an AFM cantilever and form the basis of differing operational modes for AFM. Three modes of operation are utilised depending on the sample under interrogation:

### 2.1.2.1 Contact mode

Regarded as the original imaging mode developed for the AFM (Figure 2.3 (a)), here the cantilever tip apex is in continuous contact with the sample surface and incurs repulsive and lateral forces, due to nano-Newton forces (usually in the pN to nN range) that exist between sample atoms and probe atoms<sup>139</sup>, the electron orbital of the atoms of the probe and sample overlap (Born repulsion). The AFM can be operated in either *constant force* or *constant height (deflection)* mode during contact mode. Constant force mode utilises an electronic feedback loop to constantly regulate the probe-sample separation (depending on the AFM set-up) to maintain a constant force on the sample whilst the tip is raster scanned across the surface. The system then monitors changes in the piezo height and uses this information to produce the 3-D image of the sample surface. In constant height mode, the z-piezo remains fixed whilst the deflection data from the movement of the laser in reaction to variations in topography are recorded and an image is constructed from the deflection information.

Contact mode is almost always preferred when imaging hard, stable samples in air or liquid sampling environments, as it involves applying a relatively high

force to the sample. This generally achieves higher resolution images, due to the continuous contact between probe and sample surface. Therefore this mode is more sensitive to variations in height, as forces differ greatly with small changes in distance occurring between sample and tip. However, the disadvantage in applying high force to a sample increases the likelihood of damage, through unwanted lateral tip-sample effects such as frictional forces or enhanced adhesion to the sample surface. This causes an overall effect of ‘sweeping’ and deformation across the sample surface,<sup>140,141</sup> as a result damage to ‘softer’ samples from this type of imaging led to the further development in other types of imaging within AFM, specifically non-contact and tapping modes.

#### *2.1.2.2 Non-contact mode (NC)*

This mode was developed to allow non-invasive sampling (for soft, easily damaged samples). In this mode the tip oscillates at its resonant frequency at a finite distance from the surface, at which long-range attractive interaction forces typically exist between the probe and sample<sup>142,143</sup> (Figure 2.3 (b)). The tip does not come into physical contact with the sample surface<sup>144</sup>, but is able to detect changes in the force gradients as it is raster scanned across the surface, either by observing shifts in the resonant frequency or oscillation amplitude of the cantilever. This type of imaging is desirable if it is necessary to completely eliminate potential sample damage through probe-sample contact. However images in this mode usually display a lower spatial resolution, due to the interaction forces which in this regime are typically less sensitive to the probe-sample separation<sup>145</sup>.

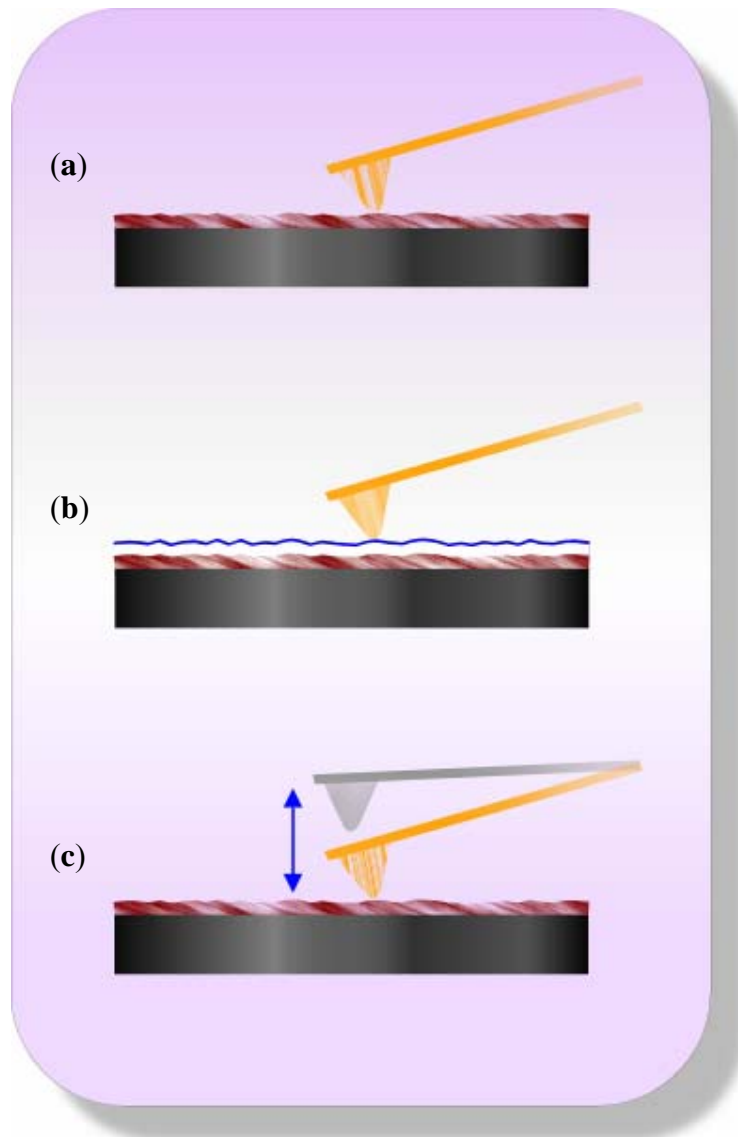


**Figure 2.3** The basic imaging modes for AFM: (a) Contact mode, (b) non-contact mode, the tip responds to long-range interaction forces during scanning, in order to generate an image. (c) Tapping mode, the probe ‘taps’ the surface at its low-point during scanning. Probe-sample interaction causes variations in the oscillation frequency, generating an image.

### 2.1.2.3 Tapping mode (TM)

Tapping or intermittent contact mode, was also developed to alleviate sample damage problems associated with destructive lateral forces caused during contact mode imaging<sup>146,147</sup>, but also to retain the higher resolution imaging

associated with contact mode. As in this mode the cantilever tip has a higher oscillation amplitude than NC mode. The tip is then brought closer to the sample surface until it gains intermittent contact with the surface as it scans (Figure 2.3 (c)). During contact with the sample the oscillation amplitude of the cantilever lowers, these changes in amplitude are monitored and are used to produce images of sample topography. The main benefit of TM is that it reduces the lateral forces resulting from frictional interactions, which can often damage and displace soft and weakly immobilised samples. This mode can be effectively applied in air or liquid environments. Figure 2.4 highlights the average probe-sample separation in all the three modes.

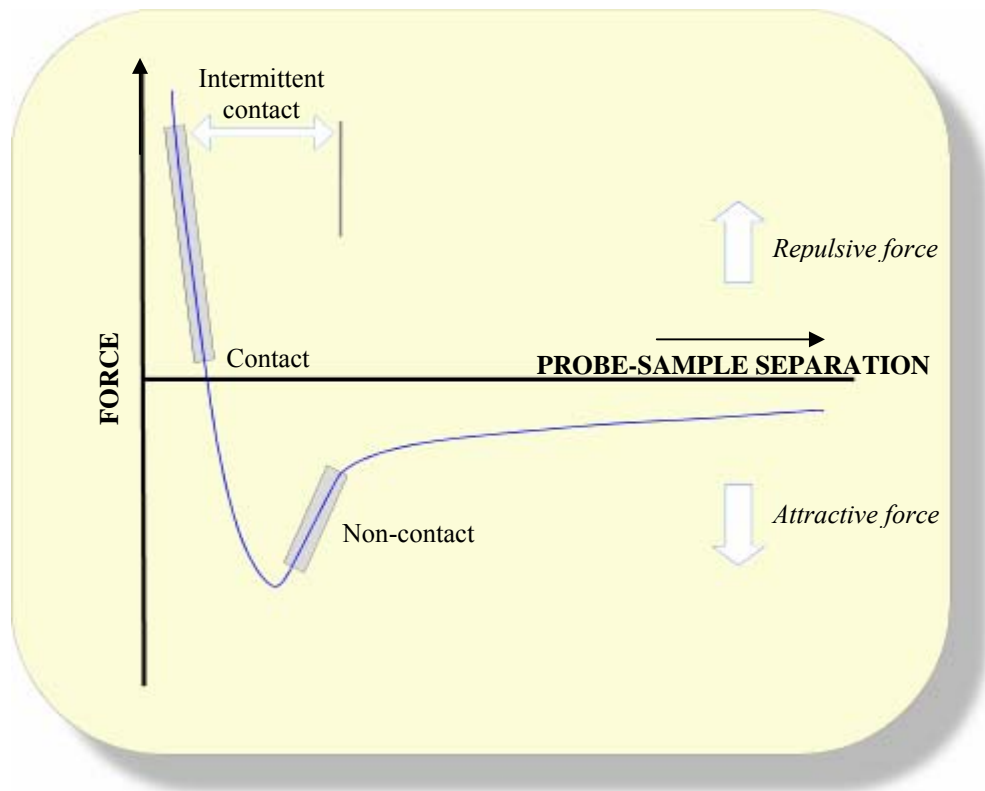


**Figure 2.4** Probe-sample separation and variance of forces between the three main AFM imaging modes<sup>148</sup>.

#### 2.1.2.4 Force-distance measurements

In addition to its imaging functions, AFM is also able to quantitatively measure the attractive and repulsive forces that exist between the sample and probe, as the cantilever is brought into contact with and then pulled away from the sample surface. Generally referred to as force-distance measurements<sup>149</sup>, they are recorded by monitoring the deflections of the cantilever probe as it is first brought into contact (approach trace) with the sample at a constant z-piezo velocity and then separated (retract trace) from the sample. The resultant plot of cantilever deflection versus distance is shown in Figure 2.5.

At **(a)** the probe-sample distance is significant enough that there is no cantilever deflection. From this position the probe advances towards the sample at a constant velocity until it is close enough to begin experiencing discrete adhesive forces (attractive regime), first highlighted by Hoh et al.<sup>150</sup>. When the level of these forces exceeds the rigidity of the cantilever spring, the probe then ‘jumps’ into contact with the sample surface, this is predominantly due to van der Waals forces **(b)**, progression of the probe towards the sample results in repulsive forces between the two, resulting in an upwards deflection of the cantilever. This forward motion continues until **(c)**, which represents a preset point of maximum load. At this point the direction of the probe is reversed and it begins to retract from the surface. During the retraction phase the tip often remains engaged to the sample due to adhesion forces between the probe and sample **(d)**. The force required for disengagement, typically exceeds that obtained at jump-to-contact, but eventually the tip detaches fully and returns to its original rest position out of range of any surface forces.

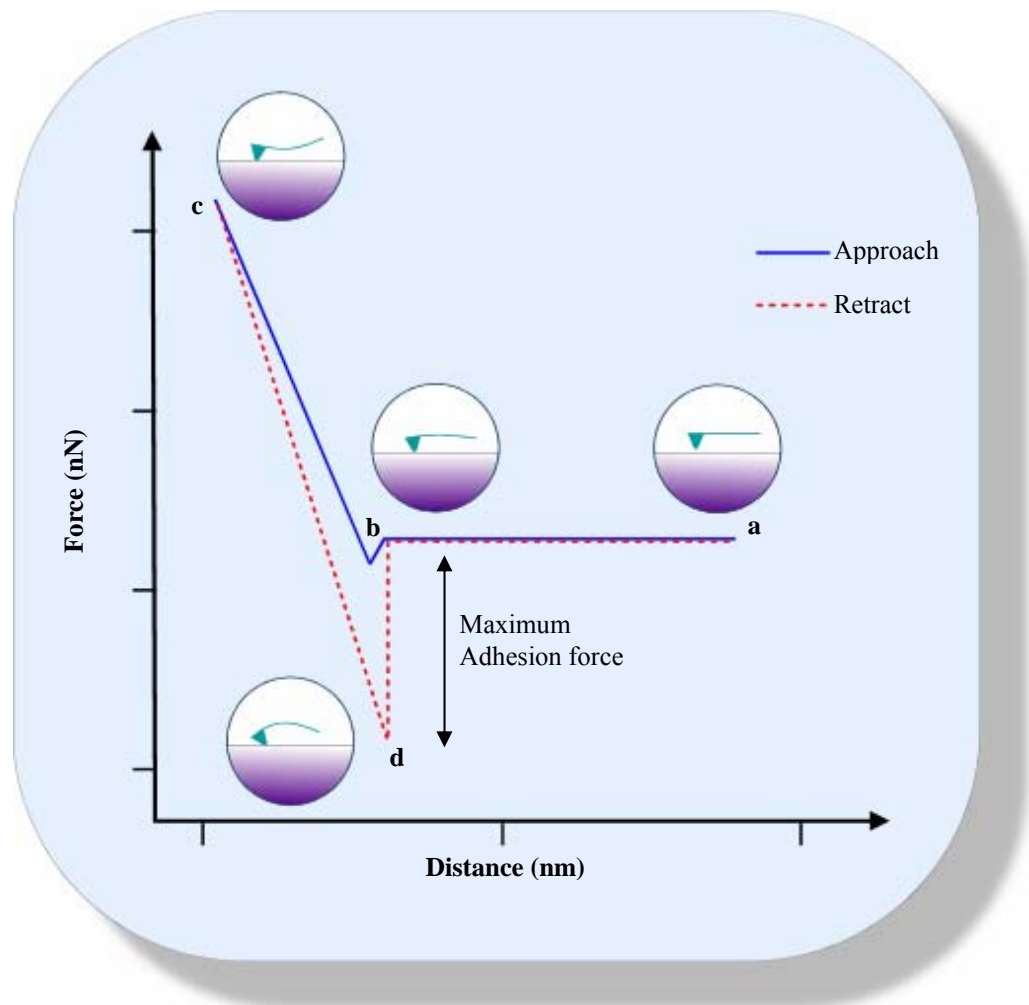


**Figure 2.5** Adapted representation of a typical force-distance curve, (a) Probe moves towards the sample surface, (b) ‘jump’ to contact due to long range attractive forces, (c) point of maximum load, set by the user, (d) detachment of the cantilever tip as it is retracted from surface and probe returns to its rest position.

This type of interaction can reveal local chemical and mechanical properties including adhesive and elastic properties, surface charge densities, and degrees of hydrophobicity<sup>151,152,153</sup>. Experiments are often carried out in aqueous environments to minimise or eliminate the level of capillary forces acting between the probe and sample surface, which could otherwise interfere with the interaction of interest within a particular experiment.

#### *2.1.2.5 Phase imaging*

An extension of TM, phase imaging provides nanometer-scale information about surface properties often not revealed by other SPM techniques<sup>154</sup>. In TM, the cantilever is excited to its resonance oscillation by the piezoelectric driver. Phase imaging refers to the monitoring of the phase lag between the signal that drives the cantilever oscillation and the cantilever oscillation output signal. The phase signal changes when the probe encounters regions of increased adhesion or viscoelasticity (hard or soft regions), this cause an increase in energy dissipation which in turn increases the phase lag, as shown in Figure 2.6. Phase shifts are registered as bright and dark regions of contrasts in phase images, similar to the way height changes are indicated in height images. By mapping the phase of the cantilever oscillation during the TM scan, the AFM can be utilised to detect variations in composition, adhesion, visco-elasticity, and other properties, as phase lag is very sensitive to variations in material properties.

Once the AFM is engaged in TM, phase imaging is enabled simply by displaying a second image and selecting the phase data type in the AFM software. Both the TM topography and phase images are viewed side-by-side in real time. The resolution of phase imaging is comparable to the full resolution of TM imaging. However, phase imaging can also act as a real-time contrast enhancement technique, because it can highlight edges and is not affected by large-scale height differences. Similar to the error signal used during contact mode imaging<sup>155</sup>. It can therefore, provide for a clearer observation of fine features, such as fibril striations, which can be obscured by rough topography, and hence is utilised for this purpose in this thesis.

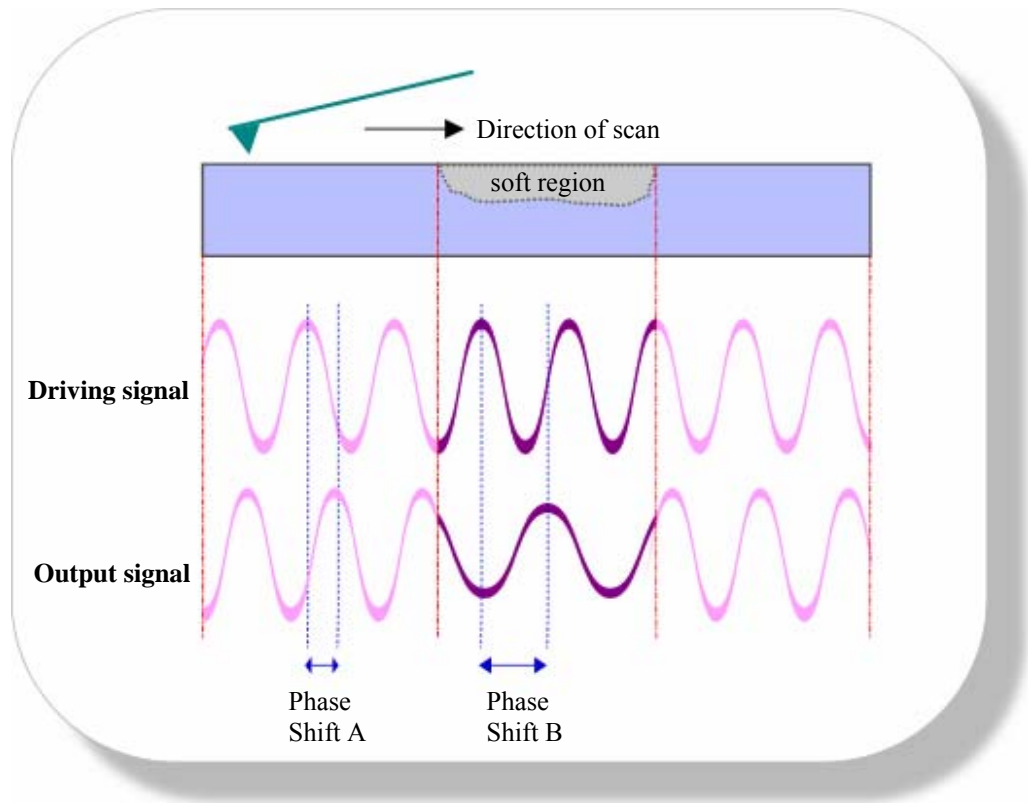


**Figure 2.6** The phase lag changes depending on the viscoelastic properties of the sample surface.

#### 2.1.2.6 Amplitude and phase versus distance curves

Collectively known as *a-p-d curves*, these two curves are simultaneously acquired and can be employed as a useful tool to complement phase imaging, they are analogous to force distance curves shown in Figure 2.5. The curves allow the user to select parameters for optimal imaging, or determine which regime (attractive or repulsive) the curves of a particular image are acquired in. In Figure 2.7, the blue line represents the tip approach and the red line is the tip retraction. Curve (A) shows the amplitude versus distance (the *z*-position of the piezo) and displays the variations in the oscillation amplitude of the cantilever as a function of the probe-sample separation. It allows the user to

determine the force required to image a surface successfully. Therefore from this information it is possible to alter the setpoint (the value of the root-mean-square (RMS) of the cantilever oscillation amplitude that the feedback loop maintains and is directly proportional to the force applied to the sample surface). Curve **(B)** provides information about variations of phase lag of the tip, due to adhesive forces working between the tip and sample surface. In the case of the example shown, the tip is in an attractive regime in relation to the sample surface. A-p-d curve measurements have been previously utilised to distinguish between two drug polymorphs, as each polymorph would display a ‘fingerprint’ a-p-d curve measurement, supporting image data obtained of the drug in question<sup>156,157</sup>.

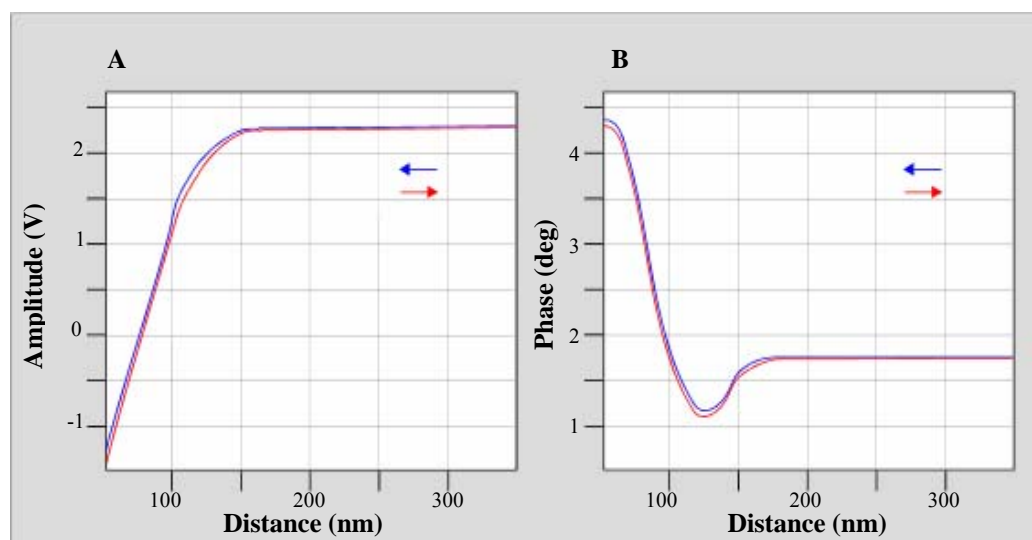


**Figure 2.7** (A) amplitude versus distance and (B) phase versus distance curves displaying an attractive force on the cantilever.

### 2.1.3 Applications of AFM

Due to the ability of AFM to image surfaces in any environment and without the need for elaborate sample pre-treatment, the applications of AFM within the areas of materials and surface science has grown significantly in recent years. As previously discussed the AFM is able to explore not only topography but many other surface characteristics. For example, it can determine the frictional properties of a sample by monitoring the twisting of the AFM probe<sup>158</sup> on thin films of liquids between two smooth solid surfaces. It is also able to measure the elasticity of a sample<sup>159</sup> by imaging soft samples such as endothelial cells or human platelets. Also the adhesion forces between probe and surface from force-distance curves<sup>160</sup> using such materials as cleaved mica. Several comprehensive reviews exist detailing the extensive use of AFM for the analysis and characterisation of organic systems,<sup>161</sup> such as early studies performed on the surfaces of the polymer, polyethylene (PE)<sup>162</sup>, to map the crystallographic positions of end methyl groups and molecular folds. Also biological systems<sup>163,164</sup> imaged not only in air but also in liquid environments, where the AFM was utilised to image immunoglobulins in near native conditions using buffers. Or frozen biological specimens such as DNA imaged within an ambient pressure chamber containing the AFM instrument using a technique now known as cryo-AFM<sup>165,166</sup>.

Allen et al. reviewed the AFM as a tool for the study of biomolecular interaction forces. Such measurements can be achieved between individual receptor-ligand complexes, by functionalising the AFM probe with a biomolecule of interest and its complimentary molecule immobilised onto a

sample surface. Similarly inter-particle forces in cohesive powders have also been studied by AFM<sup>167</sup>. In that study different commercially available powders were attached to the AFM probe and force-distance curves were studied for particle-particle and particle-wall contacts as a function of relative humidity (10-90%RH).

The AFM is the ideal tool for single particle studies because it can provide information on both the fundamental surface forces (via force curves) and on particle geometry through topographic images. Gunning et al.<sup>168</sup> also developed a method of immobilising oil droplet to cantilever tips and sample surface to monitor droplet-droplet interaction. The study demonstrated the ability of the AFM based measurements to determine the structure and stability of dispersed systems, such as emulsions.

There are many detailed studies on the use of TM and phase imaging within AFM. These include, Chen et al.<sup>169</sup> who used a-p-d measurements to interpret topography and phase images acquired of gelatine (in water-propanol mixtures) absorbed onto polystyrene and mica surfaces, using TM. Scott et al.<sup>170</sup> who examined viscoelastic contrast in polymer nanocomposites using phase imaging and Möller et al.<sup>171</sup> who used TM to image delicate protein surfaces. Various factors during the process of imaging have been taken into account within many studies to examine phase imaging. These studies have included tip wear process<sup>172</sup>, where the condition of the tip is shown to not only compromise image resolution but also introduces artefacts. The influence of

volume and surface properties on phase contrast<sup>173</sup> has also been examined, by showing that when the imaging parameters remained constant (frequency, vibration amplitude), then the changes of the phase value could be directly attributed to changes of sample properties. Also the optimisation of phase imaging using dynamic force curves (a-p-d)<sup>174</sup>, by imaging mica and polystyrene surfaces with stiff or weak cantilevers. The study highlighted how the state of the vibrating tip during TM was affected by drive frequency, cantilever stiffness and oscillation amplitude and therefore allowed the user to directly control phase imaging.

In contrast to textile material, studies of surface topography of crystalline cellulose isolated from plant cell walls have been investigated using AFM<sup>175,176</sup>. In addition, the imaging of collagen fibrils with AFM<sup>177</sup> was used to determine the fibrillar assembly and ultra-structure within bone tissue.

#### *2.1.3.1 Application of AFM in textile studies*

A number of groups have undertaken studies to image various textile fibres by AFM. For example, Titcombe et al.<sup>178</sup> imaged the internal cellular structure of merino wool fibres using AFM. They embedded the fibres in LR (London Resin) White resin<sup>TM</sup> and sectioned with an ultramicrotome. This yielded a sufficiently flat surface for imaging and they found that their results were consistent with previous transmission electron microscopy (TEM) data. Treated and untreated wool fibres were analysed by Gibson et al.<sup>179</sup>, and they were able to image the native surface lipid layer of untreated fibres, which is known to be absent in treated fibres. Lee et al.<sup>180</sup> investigated the mechanism

of cellulase action on cotton fibres using AFM in TM in air. They were able to image the physical effects of cellulases on the surface of cotton fibres and found a degree of surface disruption. Other groups have investigated surfaces of silk, Kevlar<sup>®</sup>, human hair and wool<sup>181,182,183,184</sup>.

#### **2.1.4 AFM analysis**

Images of the cotton samples throughout this thesis were produced using three different AFMs; Dimension (DI) 3000 (Veeco Digital Instruments, Santa Barbara, U.S.A); DI Multimode (Veeco) atomic force microscope both of these instruments were equipped with a Nanoscope IIIa controller; an Explorer AFM (Veeco). All samples were either imaged in air or liquid (water), unless otherwise stated, using contact or TM, and at a scan rate in the range of 2-8 Hz. Silicon cantilevers, TESP (Veeco), were used for TM imaging, with nominal spring constant of 20-100 Nm<sup>-1</sup> and tip radii of 5-10nm. Silicon nitride cantilevers were employed for contact mode imaging, with nominal spring constants of 0.1-0.3 Nm<sup>-1</sup> and tip radii of 20-60nm (Veeco) (all figures quoted are as stated by the manufacturer).

##### *2.1.4.1 Hydrophilic tips*

Cantilevers were plasma etched using a Bio-Rad RF Plasma Barrel Etcher (Polaron Equipment Ltd, Watford, UK), for 20 seconds at 100W in an oxygen atmosphere at a pressure of  $2 \times 10^{-2}$  mbar. The ion bombardment cleaned the surface of the cantilever physically and chemically, a method adapted from Ton-That et al.<sup>185</sup>. Oxygen radicals absorb and react on the cantilever surface to form volatile products with the hydrocarbon contaminants (as well as carbon

dioxide and water by-products), which in turn desorb and are then pumped away by a vacuum system. The oxygen plasma then further oxidizes silanol groups onto the cantilever surface, thus making it hydrophilic.

#### *2.1.4.2 Hydrophobic tips*

These were manufactured by process of silanisation<sup>186</sup> using octadecyltrichlorosilane (OTS –  $\text{CH}_3(\text{CH}_2)_{17}\text{SiCl}_3$ , Sigma-Aldrich, Gillingham, UK) in a mixture of chloroform (Sigma-Aldrich) and hexane (Sigma-Aldrich) (7:3 ratio) to produce a 1mM concentration (adapted from a method by Wei et al.<sup>187</sup>). The silane adsorbs to the surface of the cantilever by reacting with silanol groups, and then polymerises by self-assembly, (self-assembled monolayer (SAM), see review article by Kajiyama et al.<sup>188</sup>), from the dilute solvent mixture onto the surface of the tip, by forming covalent bonds with the silicon substrate making it hydrophobic. The tips were first plasma-etched to clean off any contaminants, and then placed in a glass petri dish inside another glass dish containing the OTS mixture, and then left covered for 1 hour under ambient conditions. This was done to promote vapour deposition inside the petri dish and to minimise excess polymer assembly. After this period the cantilevers were then washed with chloroform to remove any excess polymer from the surface and oven-dried at 50°C for 30 minutes.

#### *2.1.4.3 Preparation of cotton sample for AFM analysis*

DyStar UK, (DyStar UK, Cheadle Hulme, UK) kindly supplied the cotton and cellophane samples used in all experiments contained in this thesis. A range of knitted cotton cloth (brand type – CP20) types were supplied, these included

greige cloths, undyed cloths, and various dyed samples. With the exception of greige, all samples had undergone a series of scouring, bleaching and mercerisation processes before being knitted into cloth for dyeing purposes.

A protocol for sample mounting/fibre immobilisation was devised, to enable the imaging of single extracted strands of cotton fibres from the samples. This would in turn minimise the opportunity for tip entangled with the cotton fibres, which would otherwise cause tip damage during imaging. The method was achieved by pulling the strands from the woven cloth using fine tipped tweezers. Tempfix, (Agar Scientific, Stansted, UK) a thermoplastic waxy glue, was then used as an embedding medium for the extracted cotton strands. Samples were prepared by embedding the cotton fibres into Tempfix, adapting a previously reported method by Baldwin et al.<sup>189</sup> and Shakesheff et al.<sup>190</sup>. The Tempfix was softened onto a hot magnetic sample stub that had been placed on a hotplate. The strands were held taught in the medium until it dried which took approximately 20-30 seconds. A number of adhesives and embedding media were utilised in the preparation the cotton fibres for imaging including Tempfix. However, most proved to be problematic and did not aid in the imaging of the cotton fibres (see Table 2.1 and Figure 2.8). Cellophane samples (100µm thickness; 30g/m<sup>2</sup> weight) were mounted on magnetic sample stubs using adhesive tape. Cross-sections of cotton fibres were prepared by embedding the fibres within Vitralit<sup>®</sup> (Panacol-Elosol GmbH, Oberursel, Germany), a rapid UV curable resin, and then cutting away a section using a RMC MT7 microtome (Boeckeler Instruments Inc., Tucson, Arizona), to leave

a flat smooth surface for examination. These samples were prepared by Dr. Steven Ebbens at Molecular Profiles, Nottingham, UK.

Type of adhesive or embedding medium	Problem encountered for AFM imaging
Double-sided adhesive tape	Caused tip to stick to the sample stub and did not hold the fibres stable for imaging.
Spray Mount	Encountered similar problems as double-sided tape.
Araldite Glue	Soaked into the fibres causing them to become brittle.
Nail Varnish	Adhesive took a long time to dry. Fibres were laid onto the sample stub applied with varnish. This would cause fibres to become coated in the adhesive. If fibres were applied late onto the stub, then adhesive became too dry to adhere.
Tempfix	Allowed sufficient time to apply the fibres onto mounting stub and did not cause soaking of fibres or brittleness.

**Table 2.1** Types of embedding media used in the sample preparation of cotton samples for AFM imaging.

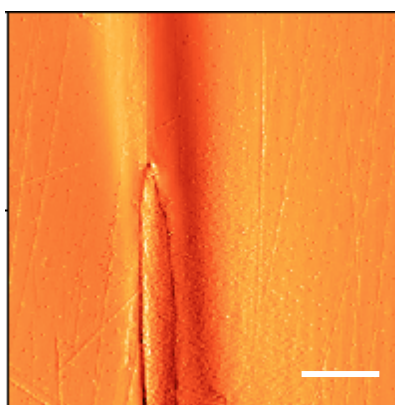


**Figure 2.8** Partially covered undyed cotton fibre in nail varnish, imaged in contact mode with Z-range 2 $\mu$ m and field of view 50 $\mu$ m x 50 $\mu$ m with scale bar 10 $\mu$ m.

## 2.2 TIME-OF-FLIGHT SECONDARY ION MASS SPECTROMETRY

Secondary ion mass spectroscopy (SIMS) is a surface sensitive method for analysing the chemical composition of a material<sup>191</sup>. The technique is based on the mass spectrometric analysis of secondary ions, generated by the interaction of a primary ion beam with the outermost 10 Å of a samples surface. In conjunction with time-of-flight (ToF) analysis, ToF-SIMS provides several advantages over other mass spectrometry and surface specific techniques. It offers a unique combination of wide mass range (0-10000 atomic mass units), high mass resolution >10000 m/z (mass to charge ratio), and detection of atomic concentrations as low as 10ppm<sup>192</sup>. In addition, all ion masses can be recorded in parallel and mass spectra can be reconstructed from any image area<sup>193</sup>.

### 2.2.1 ToF-SIMS Theory & Instrumentation

ToF-SIMS is an ultra high vacuum technique employing a pulsed primary ion beam, for example, Ga<sup>+</sup> or Cs<sup>+</sup> (Figure 2.9). The mass and energy of the primary ion determines the energy transferred to the sample during bombardment. Therefore, in general, larger atomic mass ions donate greater energy to the site of bombardment, which in turn increases secondary ion yield. The larger mass primary ions also increase the ratio of higher mass secondary ions relative to the lower mass secondary ions. Ultra high vacuum (10<sup>-9</sup> torr) is needed within the sample chamber to minimise scattering of primary and secondary ions by residual gas molecules.

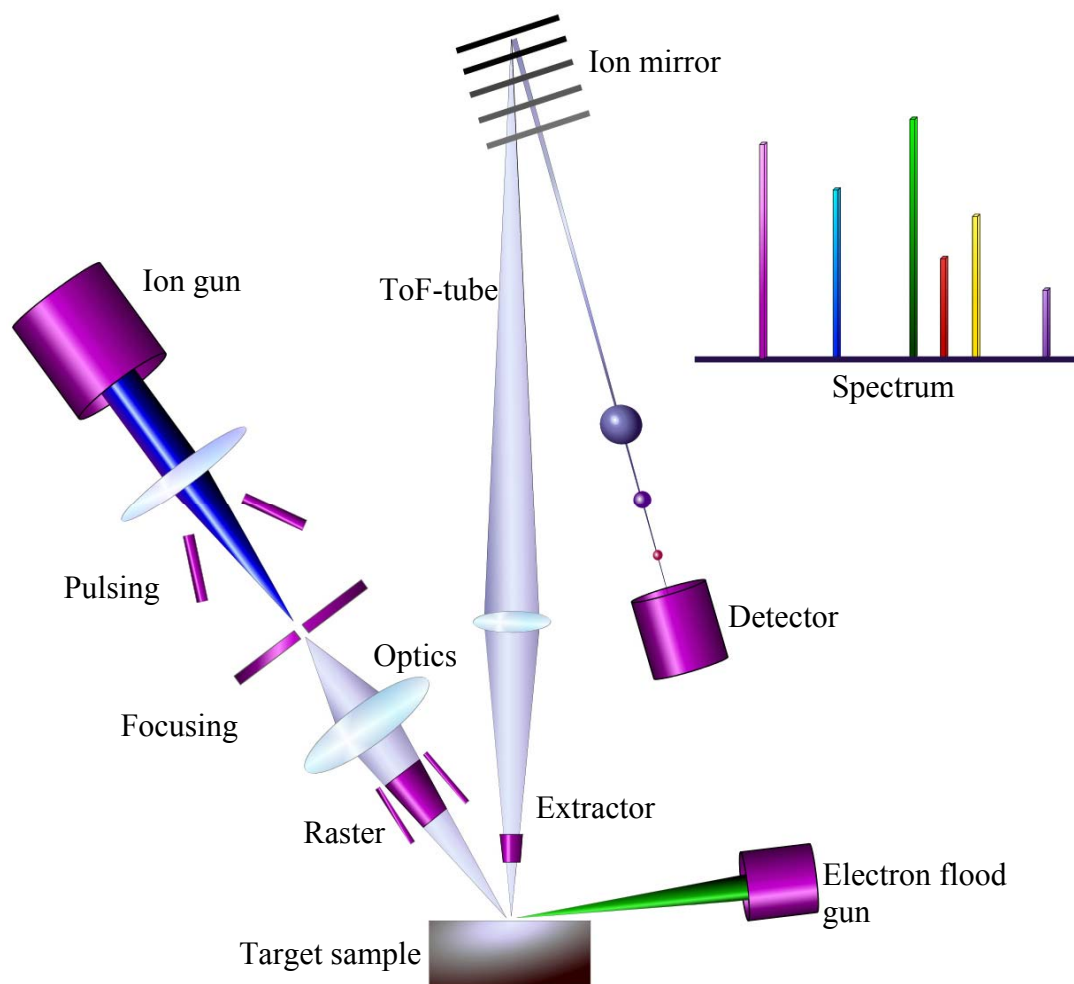


**Figure 2.9** Adapted schematic illustration of the time-of-flight secondary ion mass spectroscopy (ToF-SIMS) instrument<sup>194</sup>.

The primary ion beam is initially accelerated through a potential difference before being focussed onto the sample causing a dissipation of energy resulting in the ejection of secondary ion fragments, or sputtering of the outermost surface. The majority of material is emitted as neutral atoms and molecules. However, a certain amount of the material is emitted as either positively or negatively charged ions<sup>195</sup>. Once lifted from the sample surface, these secondary ions will have slightly differing energies depending on the distance from the site of impact. The ToF tube electro-statically collects and accelerates the fragments to a constant kinetic energy, KE, (3kV), which allows separation due to:

$$KE = \frac{1}{2}mv^2 \quad (\text{Eq.2.2})$$

Where  $m$  represents the mass of the moving particle and  $v^2$  represents the velocity of the particle squared. Upon entering the field-free reflectron drift tube, the difference between individual mass fragments results in their separation according to different velocities acquired by the accelerating kinetic energy, with smaller ions travelling along the tube faster. The fragments are reflected into a second portion of the tube by means of an ion mirror, where they continue to be separated. The measured flight times can easily be converted to their corresponding masses by monitoring the time at which the ions reach the mass detector. The data is then displayed as secondary ion signal intensity versus atomic mass units (amu) to charge ( $z$ ) ratio. Chemical images can be generated by collecting a mass spectrum at every pixel as the primary ion beam is raster scanned across the sample surface. Since all ions are detected, the images of all the ions are detected in parallel.

## 2.2.2 Applications of ToF-SIMS

Many studies have been undertaken using the ToF-SIMS as the analyser's technique of choice and the reader is directed to review articles<sup>196,197</sup> which highlight this with more detail.

### 2.2.2.1 Application of ToF-SIMS within textile studies

ToF-SIMS is not always considered the method of choice for examining textile fibres, due to its destructive nature of sample surfaces by the ion gun (but this damage is kept to the absolute minimum by bombardment of only 1% of the top surface layer of atoms or molecules with primary ion impact<sup>198</sup>). However it has been used in many studies as a complimentary method to other surface science techniques, by providing important information about the chemical composition, with depth resolution at the nanometre level and sensitivities at the parts per million levels. SIMS was utilised by Sokhan et al.<sup>199</sup> to examine artefacts from three London museums, to ascertain any surface damage from laser cleaning during restoration of many materials, including ancient silver threads in silk textiles. Brack et al.<sup>200</sup> examined non-ionic surfactants on the surface of wool fibre using ToF-SIMS and demonstrated that many treatments during processing altered the surface properties of the fibres by reducing its hydrophobic nature and enhancing dye-uptake. The resulting spectra showed peaks attributed to the surfactants of interest and wool surface lipids, on different parts of the wool fibre, therefore displaying various degrees of wettability. Bletsos et al.<sup>201</sup> first reported the detection of high mass fragments for nylons by mass spectrometry. They observed fragmentation of the backbone produced ions smaller than one monomer unit of nylon, and

attachment of  $\text{Ag}^+$  to low mass fragments. Protonation and cationisation of the repeat unit with  $\text{Ag}^+$ ,  $\text{K}^+$ , and  $\text{Na}^+$  produced high mass ions characteristic of the polymer and the repeat unit sequence in the polymer chain.

Arunyadej et al.<sup>202</sup> investigated the effect laundering had on cotton fibres which had been finished with a fluorochemical treatment (to increase water repellency), which was achieved by employing ToF-SIMS (and XPS, see section 2.3) to characterise the nature of surface adsorbents arising from laundering. The group noted that after approximately 20 washes the cotton fabric lost its repellency towards water and oil due to the formulation of the commercial detergent used in to wash the fabrics. The ToF-SIMS analysis was able to characterise the nature of the fluoropolymers and the anionic/non-ionic surfactants at the fibre surface. The group found that initial laundering caused only the anionic surfactants of the washing powder to adsorb onto the cationically charged fluorocarbon-treated surface. However, when samples which had been subject to extended laundering were analysed, they noted that only the non-ionic surfactants were adsorbed to the cotton fibre surface. Both techniques displayed a large loss of surface fluorine, which in turn reflected a loss in repellency. They concluded that the loss of repellency was due to a combination of fluorocarbon loss and surfactant adsorption during laundering.

### **2.2.3 ToF-SIMS analysis**

SIMS analysis was undertaken using a ToF-SIMS IV (Ion-ToF GmbH, Muenster, Germany), ion microanalyser utilising a  $\text{Ga}^+$  liquid metal ion source operated at 15kV, with a spot size of approximately 100 to 200 $\mu\text{m}$ . An

electron flood gun was used to neutralise surface charge, with care taken not to exceed the static limit for the area analysed. Both positive and negative spectra were obtained, with the calibration and peak assignment of the mass spectra based on the built-in library, Static SIMS Library, version 3, (Surface Spectra Ltd, Manchester, UK). Instrumental operation was carried out by Dr. Frank Rutten within the Laboratory of Biophysics and Surface Analysis, in the School of Pharmacy, University of Nottingham.

#### *2.2.3.1 Preparation of samples for ToF-SIMS analysis*

Samples were prepared by mounting cut-sections of the various cloth samples approximately 1cm<sup>2</sup> in size into the specially designed sample clamp. This held the samples taut and level for the instrument to take measurements. The cross-sections of cotton fibres which were prepared for examination by AFM were also used in ToF-SIMS.

### **2.3 X-RAY PHOTOELECTRON SPECTROSCOPY**

X-ray photoelectron spectroscopy (XPS), also known as electron spectroscopy for chemical analysis (ESCA), is a technique which can be used to probe the surface structure of materials, as the signal obtained is typically from a few nm of the surface of the material. The phenomenon is based on the *photoelectric effect* outlined by Einstein in 1905, where the concept of the photon was used to describe the ejection of electrons from a surface when photons impinge upon it. Its uses are highlighted within this thesis as a complimentary technique to ToF-SIMS, as it provides quantitative elemental analysis of the surface composition of sample. X-rays are used to excite photoelectrons on the sample

surface, which result in the ejection of inner shell electrons with a ‘binding energy’ (BE) characteristic of the atom the electron originated from<sup>203</sup>, a process known as *photoionisation*. The photoelectron emitted has a kinetic energy,  $KE$  (Eq. 2.3) which is related to the X-ray energy ( $h\nu$ , where  $h$  is Planck’s constant and  $\nu$  is the frequency of the radiation) and the  $BE$  of the electron emitted by the Einstein relation (Eq. 2.4):

$$KE = h\nu - BE \quad (\text{Eq.2.3})$$

$$E = h\nu \quad (\text{Eq.2.4})$$

By measuring this kinetic energy it is possible to characterise the surface layer composition<sup>204</sup>. The bonding state of species present in a material can result in a *shift* in the binding energies compared with those expected from the pure element, known as ‘chemical shift’. The emitted electron signal is plotted as a spectrum of binding energies and the spectral information can be collected from a depth of 2-20 atomic layers, depending on the material under investigation and angle of analysis. Different information on chemical states resulting also from chemical reaction is contained in the photoelectron peak position and shape. The peak areas can thus be used (with appropriate sensitivity factors) to determine the elemental and chemical composition of the sample surface.

### **2.3.1 Instrumentation**

XPS involves the irradiation of a sample with soft X-rays and the energy analysis of photoemitted electrons which are generated close to the sample surface. An XPS instrument therefore consists of an ultra high vacuum (UHV) analysis chamber, sample introduction/manipulation system (load lock), an X-

ray source, an electron energy analyser (the hemispherical mirror analyser), an electron detection system (multi-channel detector) and a computer which controls both the instrument operation and the acquired data processing (see Figure 2.10).

The photoelectrons are irradiated from the sample surface by the x-ray source, which was placed in the chamber using the load lock. The energy of the ejected photoelectrons are analysed by the combination of an electron lens and hemispherical mirror analyser. They are dispersed according to their kinetic energy and therefore measure the flux of emitted electrons of a particular energy within the high vacuum environment, to enable the emitted photoelectrons to be analysed without interference from gas phase collisions. A computer-based data system scans the electron energy and accumulates counts of the detected electrons, generating the photoelectron spectrum. Photoelectron peaks are labelled according to the quantum numbers of the level from which the electron originated from. The data system is then also used for subsequent manipulation of spectra, for example elemental identification, quantification, curve fitting and plotting.

### **2.3.2 Applications of XPS**

XPS has been used to characterise heterogeneous catalysts<sup>205</sup>, in particular to determine the chemical and physical changes of the catalysts upon exposure to gaseous molecules. There have also been studies which use XPS as a complimentary technique alongside other surface techniques. Gustafsson et al.<sup>206</sup> studied the surface properties and ultrastructure of spruce (*Picea abies*)

kraft pulps. They established that a rough correlation existed between the increasing relative amount of fibrillar surface structure in the AFM images and the increasing O/C atomic ratio in the XPS spectra, as the delignification (the process by which lignin is removed from cellulosic material by chemical treatment) proceeded.

The two techniques complimented each other in this particular study as the XPS gave the chemical composition of the surface and therefore helped to interpret the morphological components observed in the AFM images. However AFM probes the actual surface revealing not only the surface morphology and local adhesion properties but also the thin structural layers covering the fibre surface, which will also be further discussed in this thesis.

#### *2.3.2.1 Applications of XPS in textile studies*

Pongprayoon et al. characterised the surfaces of cotton fibres coated by a thin film of polystyrene; a process used to make the fibres water repellent. They employed XPS to establish whether an even coating had been achieved, as XPS could quantitatively measure the surface components and distinguish between the polystyrene and the underlying cotton structure. As with ToF-SIMS (see section 2.2.2.1), XPS has also been utilised for the examination of tarnished silver and copper threads in museum textiles<sup>207</sup>. The textiles were examined using XPS before and after laser cleaning, and the work was focussed on optimising the cleaning process to control the side effects of discolouration of the threads. XPS highlighted which cleaning method removed enough of the tarnish without damaging the metal underneath.

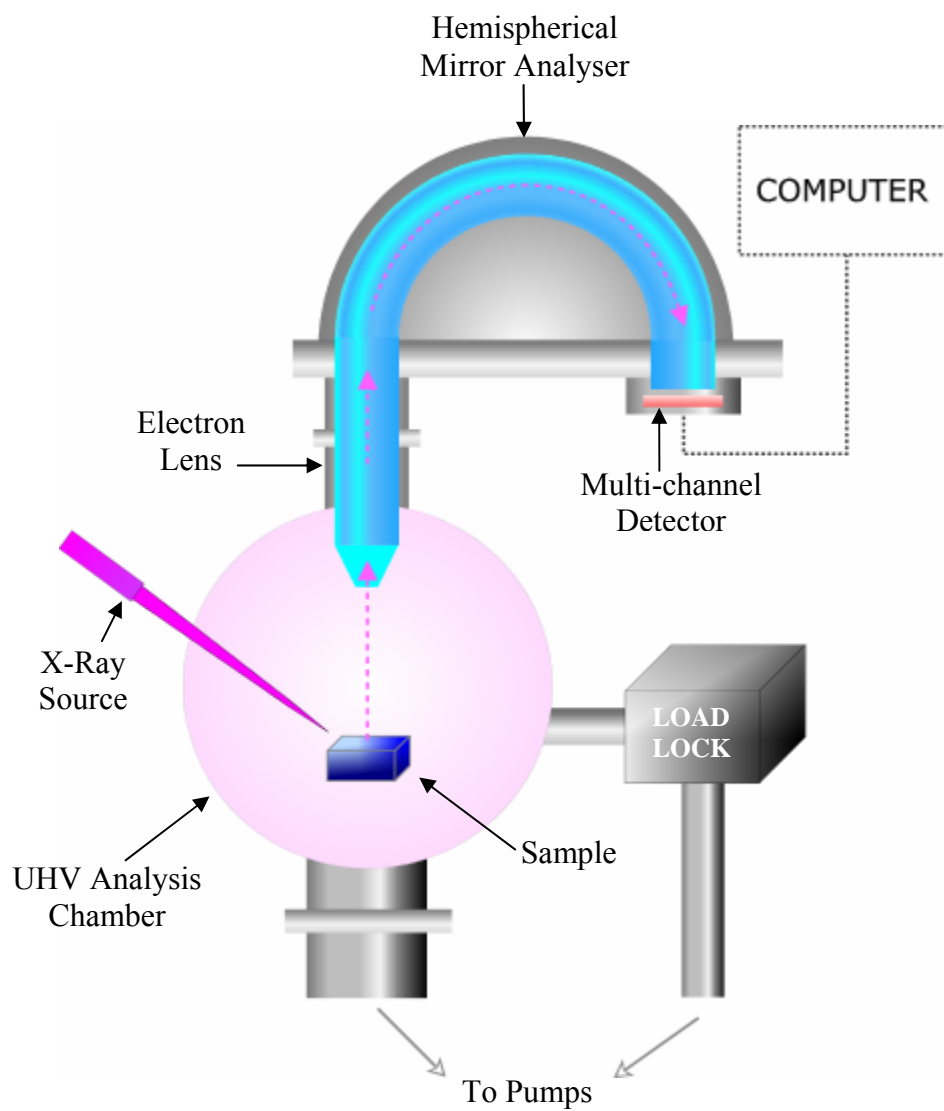


**Figure 2.10** Schematic illustration of X-Ray Photoelectron Spectroscopy (XPS) instrument.

Shao et al.<sup>208</sup> examined the surface of silk fibres and more closely fibroin, a component of silk. XPS was utilised to probe the nature of the silk fibroin surface and in particular the tyrosine content and the sulphur species. XPS has also been utilised alongside ToF-SIMS in a study to investigate and characterise butanetetracarboxylic acid (BTCA) powder and BTCA modified cotton fibre surface<sup>209</sup>. BTCA is used in the textile industry to add crease resistance to the cotton textile. The two techniques demonstrated the enhanced binding of sodium cations in the BTCA to the carboxyl-rich cotton fibre surface. Similarly an increased affinity of copper ions to the polycarboxylic acid treated cotton was also observed.

Fras et al.<sup>210</sup> analysed the oxidation of cotton fibres by titration and XPS, the purpose of their study was to evaluate the effect of selective oxidation on the surface properties of cotton cellulose fibres. They found that their combination of methods appeared to be a very useful tool to identify the formation and distribution of ionic groups in cotton fibres and their surfaces. The combined techniques displayed two processes taking place when the oxidation process was applied; the elimination of low molecular mass non-cellulosic compounds and the formation of new acidic groups within the cellulose chains. XPS analysis showed that the surface concentration of acidic groups was significantly lower than the bulk concentration, due to the oxidation step which decreased the content of carboxyl groups in the surface region. However the group suggested that this increased in amorphous regions. They reasoned that decrease was due to the dissolution of low molecular weight compounds and the increase due to formation of new acidic groups.

### 2.3.3 XPS Analysis

Analysis was carried out using an AXIS ULTRA XPS (Kratos Analytical Ltd, Manchester, UK), with a monochromated Al  $\kappa\alpha$  source (1486.6eV) operated at 10mA emission current and 15kV anode potential. The detector (ULTRA) was used in fixed analyser transmission (FAT) mode, with pass energy of 80eV for wide scans, and 40eV for high resolution (or narrow) scans. The dwell time for wide scans on each step-size of 1eV were 0.5 seconds; and 3 seconds on a step-size of 100meV for narrow scans, with single sweeping on each region. The magnetic immersion lens system used a slot aperture of  $300 \times 700\mu\text{m}$  for wide and high resolution scans. The take-off angle the photoelectron analyser was  $90^\circ$ , and acceptance angle  $30^\circ$  (in magnetic lens mode). A charge neutraliser was used for the samples and it provided a flux of low energy electrons providing uniform charge neutralisation. The analysis chamber pressure was typically better than  $1.3 \times 10^{-9}$  mbar ( $1.3 \times 10^{-7}$  Pa). The background was corrected using the Linear or straight-line method<sup>211</sup>. Data generated was analysed using CasaXPS software with Kratos sensitivity factors (for glass samples) to determine the atomic percentage values from the peak areas. Instrumental operation was carried out by Ms. Emily Smith, in the Centre for Surface Chemical Analysis, within School of Chemistry, University of Nottingham, UK, under the guidance of Prof. David Briggs.

#### *2.3.3.1 Preparation of cotton samples for XPS analysis*

DyStar UK (DyStar UK, Cheadle Hulme, UK) kindly supplied the cotton samples which were used in this study. These were a series of dyed cloths, with either increasing dye concentration, or increased salt content within the

dyebath when the cloths were produced. All cloth samples were cut and stretched under the constant height bar by clamping into place (see Figure 2.11). The ends of the cut samples were trimmed to minimise the pumping-down times, as the samples were left to pump overnight (12 hours) in the instrument. All the samples were handled using nitrile gloves to minimise any surface contamination.



**Figure 2.11** Displays the series of undyed and dyed cloths (from left to right – undyed, 4%, 1% and 9% w/v dyed cloths) clamped into position prior to analysis by XPS.

## 2.4 SCANNING ELECTRON MICROSCOPY

The scanning electron microscope (SEM) as its name suggests, is a microscope that utilises electrons instead of light waves. Conventional light microscopes use a series of glass lenses to refract light waves and create a magnified image.

In contrast the SEM creates magnified images by using electrons instead of light waves<sup>212</sup>. It allows a large amount of the sample to be in focus at one time and produces images of high resolution, which means that closely spaced features can be examined at a high magnification (with a resolving power of approximately 3nm)<sup>213</sup>. The combination of higher magnification, greater resolution, and ease of sample observation makes SEM one of the most heavily used instruments in research areas today.

### **2.4.1 Instrumentation**

The SEM works by scanning an electron beam across a specimen. Samples have to be prepared carefully to withstand the vacuum inside the microscope, and biological specimens are normally dried to prevent vaporisation within the vacuum, which would otherwise cause deformation of sample. Samples are made conductive for imaging by coating with a very thin layer of gold (5 – 50nm thickness<sup>214</sup>) by sputter coating and are placed inside the microscope's vacuum column through an airtight door. After the air is pumped out of the column, an electron gun at the highest part emits a beam of high-energy electrons. This beam descends through a series of magnetic lenses designed to focus the electrons to a very fine spot and is held under a high vacuum to allow a free path for the electrons, and to prevent high voltage discharge. Near the base, a set of scanning coils moves the focused beam back and forth across the specimen. As the electron beam strikes each spot on the sample, secondary electrons are knocked free from its surface. A detector measures these electrons and sends the signals to an amplifier (see Figure 2.12). The final image is developed from the number of electrons emitted from each point on

the sample, unlike TEM where the electron beam passes through the sample and therefore an image is gained through transmitted electrons.

In recent times the development of environmental SEM (ESEM) has enabled the application of SEM to biological and wet samples<sup>215</sup>. This technique allows the investigation of samples in their natural state, under environmental conditions. ESEM operates without coating the sample, and is non-destructive. Sample preparation is kept at the minimum because samples containing liquids can be examined under elevated pressure within the environment as it reduces vaporisation.

#### *2.4.1.1 Energy dispersive X-ray analysis (EDAX)*

Compositional analysis of a specimen may also be obtained by monitoring secondary X-rays produced by the electron-specimen interaction, a process known as energy dispersive X-ray analysis (EDAX), the information can illustrate the surface elemental composition of the sample (at approximately 1µm depth). Detailed maps of elemental distribution can be produced from multi-phase or complex biologically active materials. Characterisation of fine particulate matter in terms of size, shape, and distribution as well as statistical analyses of these parameters, may be performed.

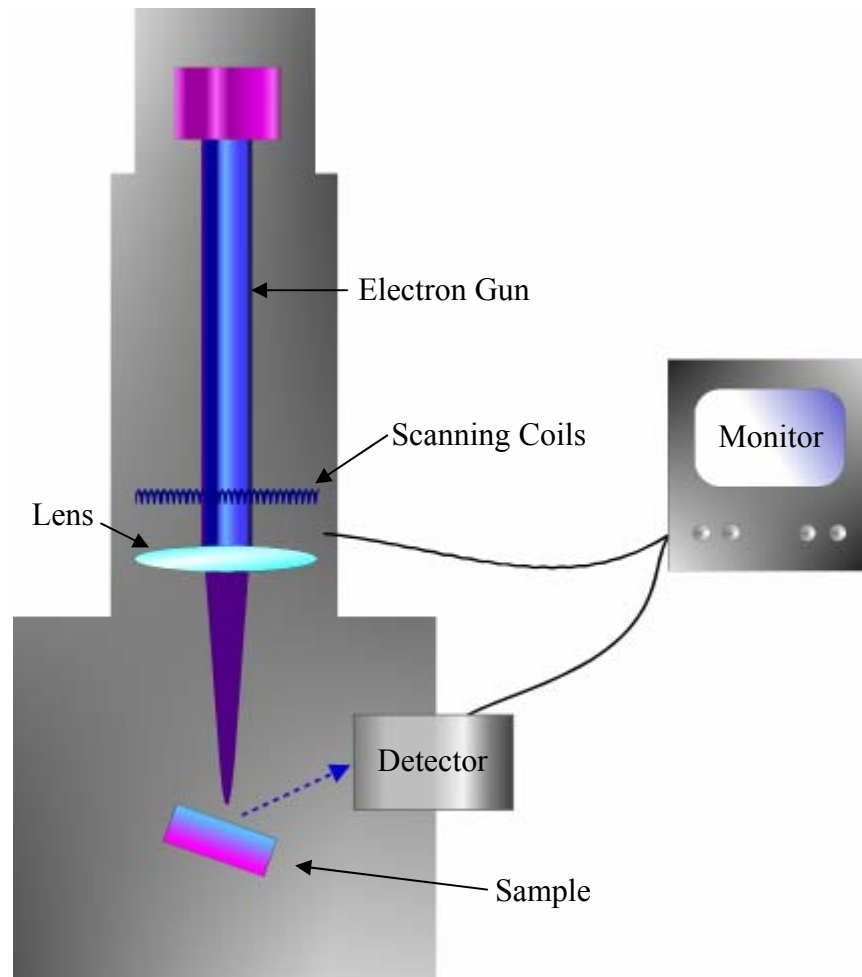


**Figure 2.12** An adapted schematic diagram of Scanning Electron Microscope (SEM).

## 2.4.2 Applications of SEM

Felix et al.<sup>63</sup> studied the surface topography of cellulose-polymer composites and Annadurai et al.<sup>216</sup> investigated cellulose-based wastes (banana and orange peels) and adsorption of dyes from aqueous solutions. They found that the cellulose wastes were promising materials for adsorption removal of dyes from aqueous solutions.

### *2.4.2.1 Applications of SEM in textile studies*

Previous investigations involving textile fibres have been analysed using SEM. Zhang et al.<sup>217</sup> studied and characterised the ultrastructure of cotton fibres using scanning tunnelling microscopy (STM) and compared the results with that obtained by SEM. The group found that with SEM, fibrils could be seen, however they found it difficult to further observe fine structures within the fibrils. This was the opposite when analysis was carried using the STM, the group were able to study the fibrils, and by making scan areas smaller, they could also observe microfibrillar structure, which were arranged in parallel.

Qin et al.<sup>218</sup> utilised field emission gun SEM to analyse polyethersulfone (PES) hollow fibre ultrafiltration membranes and pore structure in the outer membrane of the hollow fibres. Carrott et al.<sup>219</sup> investigated commercial acrylic textile fibres, where they studied the variations in surface texture and dimension during carbonisation and activation of three acrylic fibres, made of acrylonitrile (~90%) and vinyl acetate (~10%) monomers. SEM has been used in the analysis of silk membranes and fibres<sup>220,221</sup> to study the effects on

morphology after processing temperature and fracture surfaces of silkworm and spider silk.

### **2.4.3 SEM and ESEM Analysis**

Both types of SEM were employed within this research. For SEM analysis all samples were gold-coated using a Balzers SCD 030 Sputter Coater (Balzers Union Limited, Liechtenstein), operated at 0.1mbar with a sputtering current of 30mA for a duration of 2 minutes. A Philips 505 SEM (Philips Electron Optics, Eindhoven, Netherlands) was used to image all samples under a range of magnification settings at a voltage of 23kV, with a spot size of 50  $\mu\text{m}$ . For ESEM analysis a Philips FEI XL30 FEG-ESEM (Philips Electron Optics) was employed, under different magnifications at voltages of 10 or 15kV with a spot size of 3 or 4 $\mu\text{m}$ , with EDAX analysis. Instrumental operation was carried out by Mrs. Nicola Weston, in School of Mechanical, Materials and Manufacturing Engineering, University of Nottingham. Samples were mounted onto SEM stubs using adhesive carbon discs for analysis.

## **2.5 DIFFERENTIAL SCANNING CALORIMETRY**

Differential scanning calorimetry (DSC) is a thermoanalytical technique used to characterize the bulk thermal properties of a material. Whenever a material undergoes a change in physical state, such as melting or transition from one crystalline form to another, or whenever it reacts chemically, heat is either absorbed or liberated. The DSC determines the enthalpies of these processes, or transitions, by measuring the energy necessary to establish a nearly zero temperature difference between a substance and an inert reference material.

The temperature is usually programmed to scan a temperature range by increasing linearly at a predetermined rate. DSC can provide information about both 1<sup>st</sup> and 2<sup>nd</sup> order transitions these include; the melting temperature ( $T_m$ ), glass transition ( $T_g$ ) and crystallization temperature ( $T_c$ ).

### **2.5.1 Instrumentation**

Within DSC instrument the two specimens, the reference and sample materials are placed inside aluminum (Al) pans and are enclosed in an environmentally controlled chamber. The pans are then heated at a constant pre-determined rate within the chamber; as the thermal energy is applied to the sample pan, the amount of energy required to heat the sample at that given rate in comparison to the reference pan is measured, see Figure 2.13. The sample material undergoes thermal transitions during heating which are then measured by the instrument. As the material passes through thermal transitions, the amount of energy required to maintain a constant heating rate alters in some way depending on the type of transition event. The data is then fed into a computer which plots the rate of heat flow against temperature or time. A shift in the DSC curve baseline results from the change in heat capacity of the sample. The curve can be used to measure the enthalpy involved in polymer transitions. The peak area between the curve and the baseline is proportional to the enthalpy change ( $\Delta H$ ) in the sample; therefore the enthalpy change can be determined from the area of the curve peak. Figure 2.14 shows typical thermal transitions within a DSC curve which can be observed for a polymer sample, the transitions can provide information on the crystallinity of sample material.

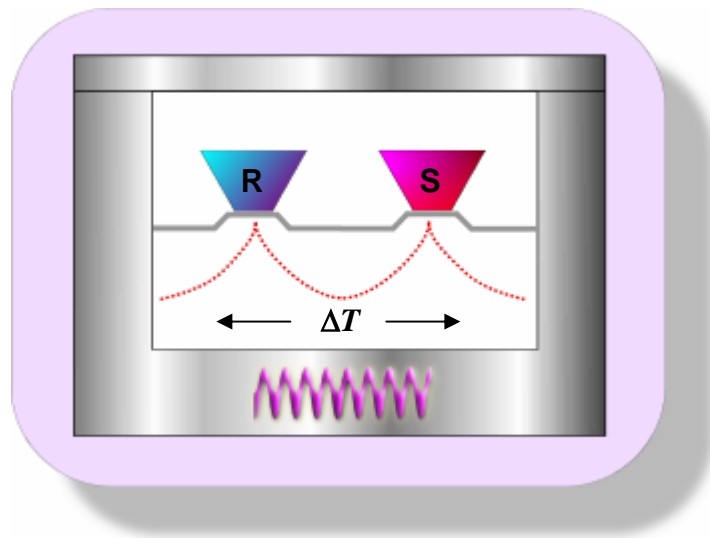


**Figure 2.13** Illustration of heat-flux DSC assembly enclosed in single furnace chamber with one heat source, (R) inert reference and (S) sample,  $\Delta T$  is change in temperature.

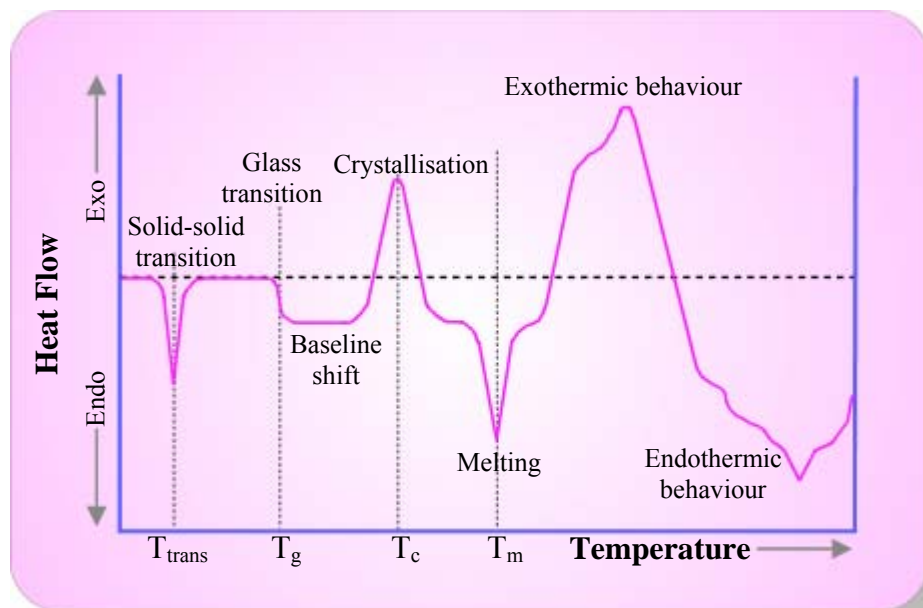


**Figure 2.14** A typical DSC curve obtained for a polymer sample<sup>222</sup>, which highlights the transitions a material undergoes, either endothermic or exothermic behaviour.

## 2.5.2 Applications of DSC

Many studies have utilised the DSC to carry out thermal analysis of polymer compounds, therefore the reader is directed to excellent reviews on DSC by Vandooren and Muller<sup>223</sup>, Gmelin<sup>224</sup>, and Coleman and Craig<sup>225</sup>. Cellulose samples<sup>226</sup> have also been examined through DSC, Hirata and Nishimoto<sup>227</sup> compared untreated cellulose with cellulose treated with a flame retardant. Their results showed broad endothermic peak between 320-390°C for the untreated cellulose whereas the treated cellulose sample showed a very small and sharp endothermic peak at 220-260°C. Although the treated sample had an endothermic peak at a lower temperature than the untreated sample, the weight loss for the treated cellulose was insignificant compared with the untreated cellulose, as the peak within the treated samples was attributed to random chain scissions in the cellulose (due to the flame-retardant preventing complete pyrolysis of the sample). Tsujiyama and Miyamori<sup>228</sup> analysed wood through DSC and used the obtained thermograms to assign the exothermic peaks to specific components from the wood samples. They found cellulose within their Japanese wood sample showed two exothermic peaks at 336°C and 488°C, the peaks were attributed to crystalline and amorphous regions present in the sample; however the group did not assign which peak corresponded to which type of region.

### 2.5.2.1 Applications of DSC in textile studies

Studies on thermal degradation of cotton fibres have furthered the development of flame retardant fabrics within the textile industry. Dahiya and Rana<sup>229</sup> presented studies on cotton cellulose modified with arylphosphonate

compounds and subjected the fibres to thermal degradation using DSC and thermogravimetric (TG) techniques to study their potential flame retardancy. The treated fibres displayed high values of enthalpy of reaction (1016-1025J/g) for the decomposition and oxidation in their DSC thermograms, compared with normal cotton fibres, indicating a suppression of flammable components in cotton. Upon phosphorylation the cellulose exhibited a typical condensed phase flame-retardant activity, in the TG thermograms, thought to be due to the presence of phosphorous. They also utilised the SEM to examine the cotton fibre morphology more closely after treatment, and noticed that the surface morphology remained largely unchanged. They therefore concluded that this type of cellulose derivative would give rise to the production of flame-retardant cellulosic material. Zhu et al.<sup>230</sup> also carried out comparable investigations on flame-retardant cotton fibres and obtained similar results to Dahiya and Rana using the same analysis techniques.

### **2.5.3 DSC Analysis**

Thermal analysis was carried using a TA Instruments DSC Q10 (TA Instruments, New Castle, USA). The instrument was calibrated prior to analysis using an indium calibration sample. Each sample (cut sections of cellophane film, cotton fabric or powdered dye compound) was placed and weighed in an open Al pan, with the weight kept at a constant of 2mg. A blank Al pan was also used as a reference pan during all experiments which were carried out at a temperature ramp of 10°C/min in a nitrogen gas atmosphere.

### **Cellophane – Surface Characterisation of a Model Cellulose System**

A number of studies exist on the characterisation of cellulose film, cellophane; however these are mainly limited to the determination of the bulk construction, rather than local surface characteristics. Within this chapter, AFM has been applied to the surface characterisation of cellophane film as a model system for cellulose, with particular attention paid to dyed cellophane film. AFM and other surface sensitive techniques, such as ToF-SIMS were employed to investigate these surfaces as an introduction to further studies within chapter 4, which employs AFM to characterise the surface of cotton fibres before and after dyeing processes.

#### **3.1 INTRODUCTION**

The structure and characterisation of cellulose is discussed in detail within chapter 1. Cellulose is of great importance to the textile industry, because of the diversity of fibres and films that can be produced from the raw material, and this has lead to continued research and debate over its morphology and crystal structure. In this chapter we examine the morphology and structure of cellulose as cellophane film. Briefly mentioned in section 1.2.1.3, cellophane is a film of regenerated cellulose (from the words *cellulose* and *diaphane*, the later being French for transparent). Cellophane was discovered by J.E.

Brandenberger, a Swiss textile engineer, in 1908<sup>231</sup>. He realised that cellophane could be generated by adapting a process used in the production of *rayon*. Within Brandenberger's manufacturing process, the alkaline solution of cellulose fibres (usually wood or cotton, known as viscose) was extruded through a narrow slit, instead of a round hole, into an acid bath<sup>232</sup>. The acid regenerated the cellulose from the alkali, forming a thin film, and through further treatment of washing and bleaching the cellophane was yielded. Cellophane was originally invented to provide a waterproof coating to textile fabrics<sup>233</sup>, but now is employed for many uses; including the packaging<sup>234</sup> of meat products<sup>235</sup> and cigarettes<sup>236</sup>, ultrafiltration<sup>237,238</sup> membranes for dialysis machines<sup>239</sup>, a base for adhesive tapes<sup>240</sup> and mobile phone technology<sup>241</sup>.

### **3.1.1 Characterisation of cellophane**

Although many studies have been carried out on cellophane, these studies have mainly concentrated on the bulk analysis of the films. Such studies include the examination of cellophane films by XRD, which showed a typical cellulose II crystal structure in contrast to electron diffraction pattern which highlighted typical cellulose I crystal structure, indicating a presence of both polymorphs within the bulk material<sup>242</sup>. The surface morphology of cellophane was examined through the use of confocal laser scanning microscopy (CLSM)<sup>243</sup>, (by illuminating and collecting reflected light from a single focal plane of the sample). The analysis of cellophane films through CLSM by Furuta et al. displayed a presence of holes and irregularities on the surface, and the interior displayed a variety of reflections, consistent with heterogeneous materials (confirming presence of two polymorphs). They measured the diameters of the

depressions within the films to be 2-20 $\mu\text{m}$ , and the height of the depressions to be 1-6 $\mu\text{m}$ .

Other studies have examined the permeability properties of membrane films; for example Vazquez et al.<sup>244</sup> examined cellophane membranes after modification with gamma-irradiation. They paid particular attention to its permeability after treatment, which appeared to lower salt permeability, which was attributed to a reduction in free space within the membrane matrix. Wu and Yuan<sup>245</sup> examined the gas permeability of a novel cellulose film, which had been prepared using amine oxides. Preparation of the films in this way, improved the mechanical properties of the cellulose film overall and increased the permeability of CO<sub>2</sub> gas, easily separating it from other gases such as H<sub>2</sub> and N<sub>2</sub> compared with ordinary cellophane film. The group hypothesised that this was in part due to the crystallinity of the novel film and its spatial structure which improved the gas separation.

However a small number of studies have looked at the surface of cellophane using AFM<sup>246,247</sup> but these were performed on modified cellophane surfaces for the purposes of ultrafiltration. With the exception of Frazier<sup>248</sup>, a former member of the Laboratory of Biophysics and Surface Analysis, who examined the surface morphology of unmodified cellophane using AFM but not at high resolution as displayed in this chapter. Studies on dyed cellophane films have also been carried out in the past but only to utilise cellophane as a mimic for paper or cotton textiles<sup>249</sup>, to carry out studies on lightfastness<sup>250,251</sup> and hydrolysis<sup>252</sup> properties of the dyes used. Within this study, cellophane has

been used a model to investigate the surface morphology of cellulose in both dyed and undyed samples through the use of AFM, with complimentary analysis of surface chemistry by ToF-SIMS and thermal degradation by DSC. No other studies have employed these techniques together to examine the effects of dye-uptake in cellulose materials.

## **3.2 EXPERIMENTAL**

The experiments detailed here examined cellophane films through the use of AFM, ToF-SIMS and DSC analysis. Any experimental conditions which differ from ones previously discussed in chapter 2 are stated with the image in question.

### **3.2.1 Samples**

All cellophane films samples (100 $\mu$ m thickness and 30g/m<sup>2</sup> weight) examined within this study were supplied by DyStar UK (DyStar UK, Cheadle Hulme, UK). These samples included undyed and dyed cellophane; the dye used was a reactive dye (using exhaustive dyeing method), referred to within this chapter as Blue 1 for the purpose of commercial confidentiality, see Figure 3.1 for chemical structure.

### **3.2.2 Sample preparation and analysis**

All sample preparation and analysis method of cellophane films have been previously detailed within section 2.1.4 for AFM analysis, section 2.2.3 for ToF-SIMS analysis, and section 2.5.3 for DSC sample preparation and analysis.

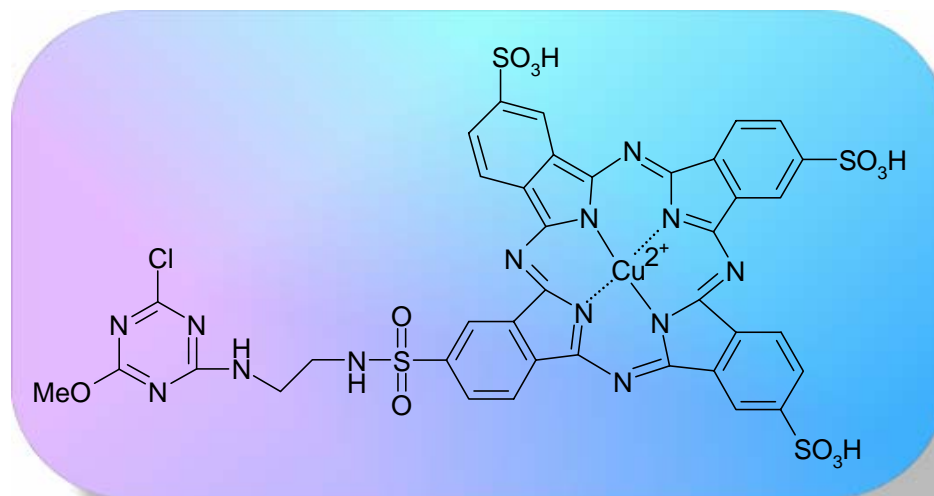


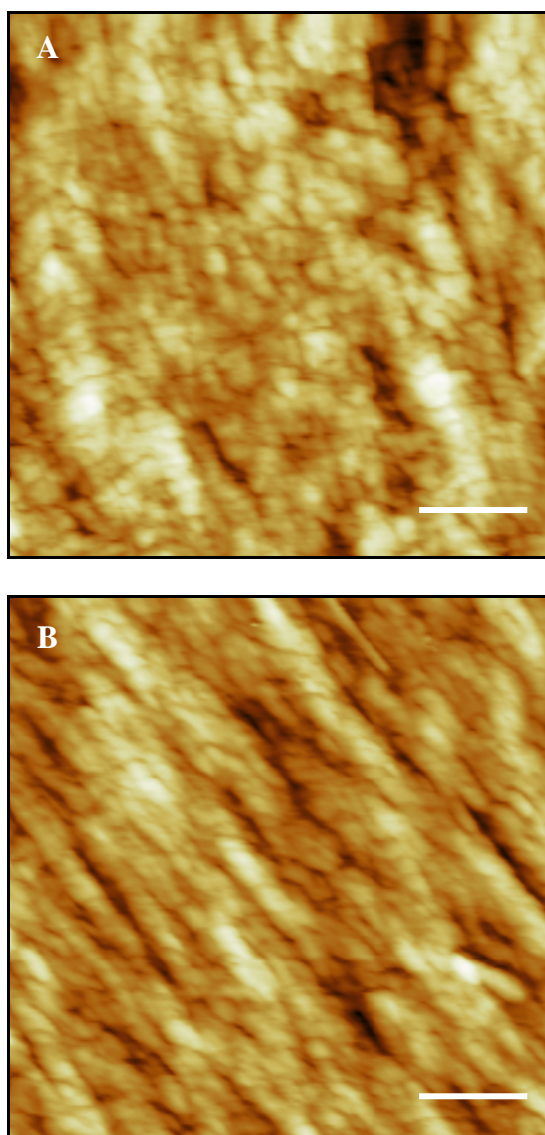
**Figure 3.1** Chemical structure of reactive dye used to dye cellophane sample, referred to as Blue 1 within this chapter for commercial confidentiality.

### 3.3 RESULTS AND DISCUSSION

Initially the undyed cellophane was examined and characterised using AFM, this was then compared to the dyed sample. ToF-SIMS analysis was carried out on both types of samples to determine the presence of dye within the surface layer of the dyed cellophane sample. Both cellophanes were also subjected to bulk thermal analysis via DSC, and a comparison between the two types of samples was made to determine any effects on thermal transitions due to dye compound.

#### 3.3.1 AFM analysis of cellophane

All samples were imaged in air using an Explorer AFM or DI 3000 AFM (see section 2.1.4) using TM (refer to section 2.1.2.3), unless otherwise stated.



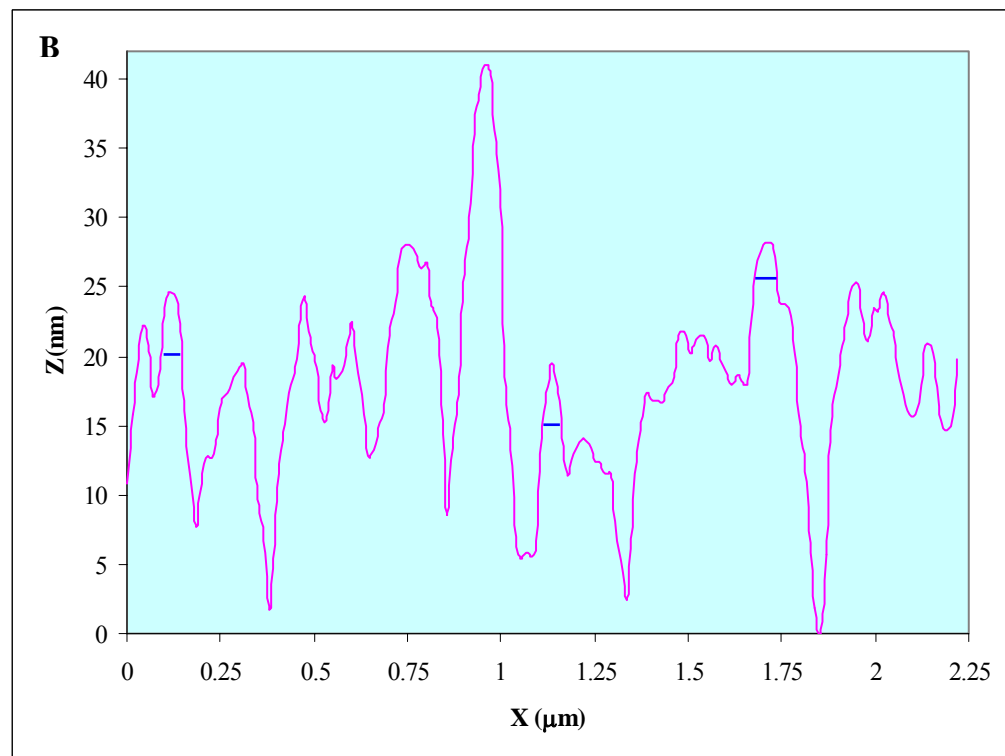
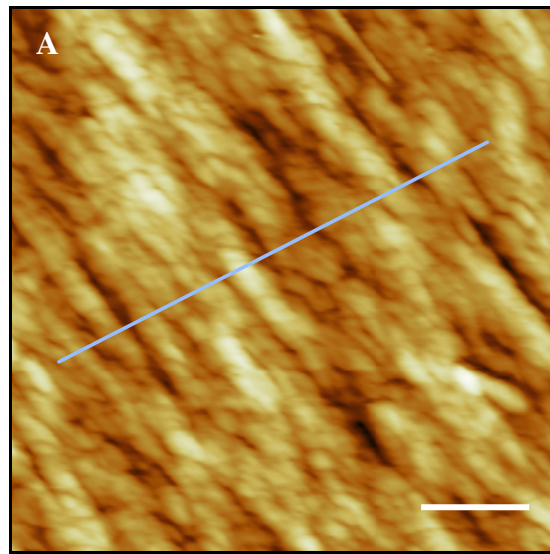
**Figure 3.2** Two  $2.5\mu\text{m} \times 2.5\mu\text{m}$  Explorer AFM images of undyed cellophane, displaying typical features obtained using an unmodified tip in contact mode, with Z-range 55.7nm for image (A), 61.9nm for image (B). (Scale bars 500nm). Image (A) shows globular features whereas (B) shows fibrillar structures.

Figure 3.2 displays typical Explorer AFM data topography images obtained for undyed cellophane film using an unmodified tip in contact mode. The two images display typical features for cellulose (closely packed fibrils<sup>253</sup> and globular surface, image (A) shows globular surface topography and image (B)

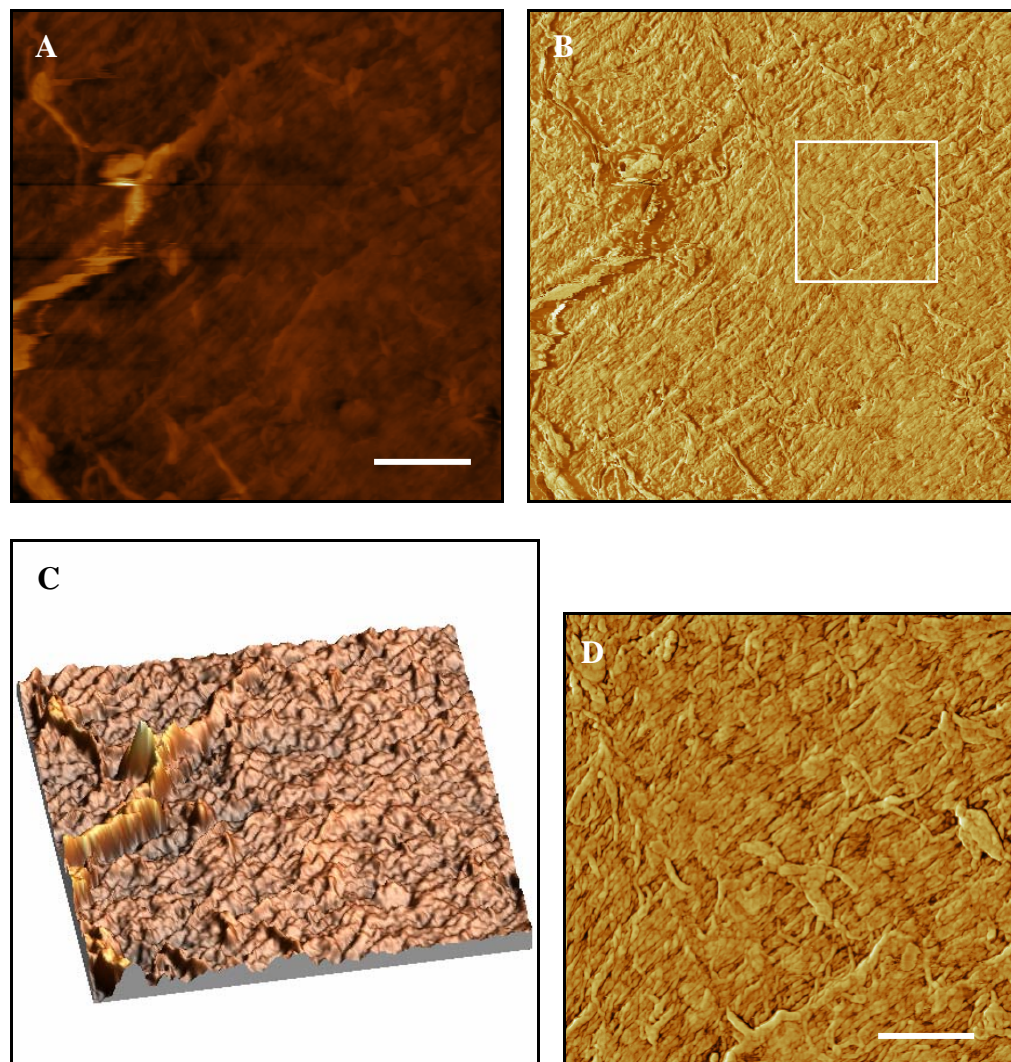
shows fibrillar striation pattern. Both types of features were observed on the cellophane sample, dependent on the area of the sample interrogated. The globular features represent a less-ordered surface topography than image (B) which shows tightly packed fibrils that are much more ordered; such observations suggest and are consistent with the presence of amorphous (globular) and crystalline (fibrillar) regions within the surface of the cellophane film.

Figure 3.3 shows a line profile measurement taken of the fibrillar striations from topography image (B) from Figure 3.2. The line profile measurement highlighted that the fibrils were in the region of 50-65nm wide (at FWHM, see glossary), which compares well with the figures cited in literature; however it should be noted that those figures were for cellulose within cotton plants, and not regenerated cellulose as in the cellophane films.

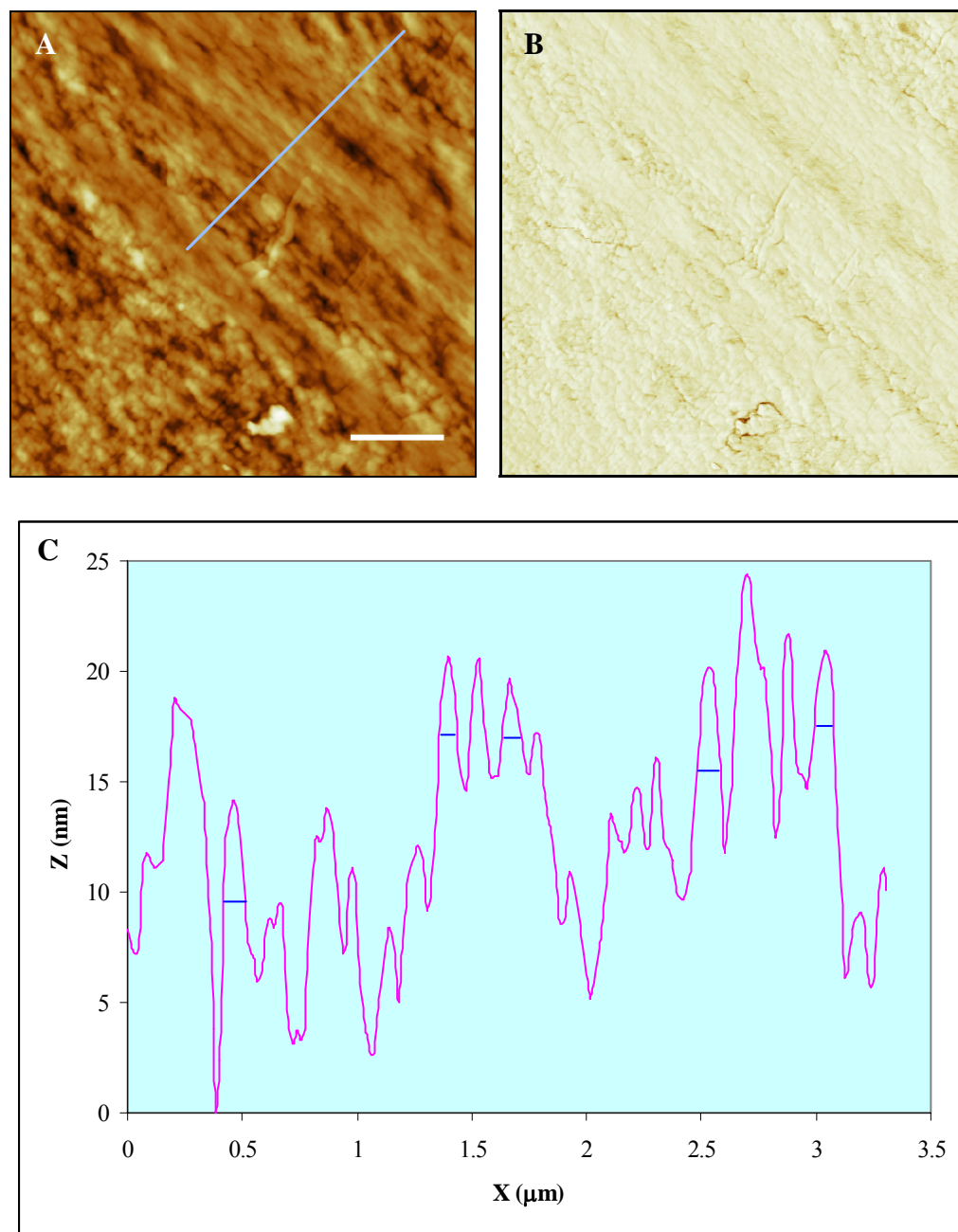
The undyed cellophane sample was also imaged in TM using a DI 3000 AFM, to utilise the phase imaging (see section 2.1.2.5) function of the instrument. Figure 3.4 displays a typical image of undyed cellophane using an unmodified tip in TM (see section 2.1.2.3). The phase image (B) in Figure 3.4 shows little contrast suggesting a homogeneous surface chemistry or material property, but the phase image does clarify the ultrastructure of the cellophane topography, which is difficult to see in image (A). Image (B) particularly highlights the edges of the microfibrils, which can be seen even more clearly in image (D), a zoomed-in section from (B) (highlighted by white square). The microfibrils appear ordered in a striation pattern and follow a particular line of direction.



**Figure 3.3** Line profile of undyed cellophane film, (topography image in Figure 3.2 (B)) with scale bar 500nm (white line), fibrils are a few tens of nanometres across, highlighted by blue lines. Fibrillar measurements were taken of single fibres from within the phase image, as opposed to thick bundles of fibres.

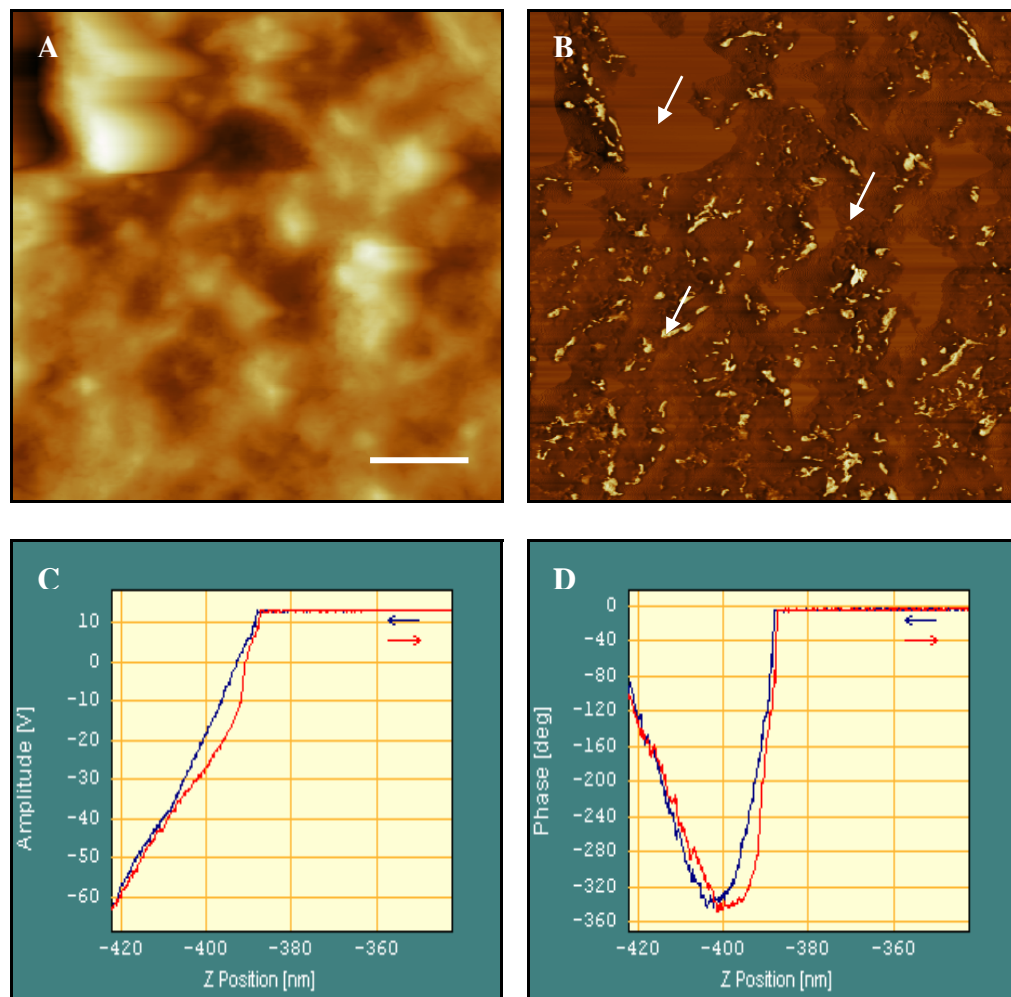


**Figure 3.4** Typical DI 3000 AFM  $5\mu\text{m} \times 5\mu\text{m}$  (A) topography, (B) phase and (C) 3D rendered topography images of undyed cellophane, imaged using an unmodified cantilever tip in TM, with Z-range 309.6nm and scale bar  $1\mu\text{m}$ . Image (D) is a  $1.9\mu\text{m} \times 1.9\mu\text{m}$  zoomed-in area from phase image (B), which clearly shows the microfibrils following a particular line of direction, (scale bar 400nm).



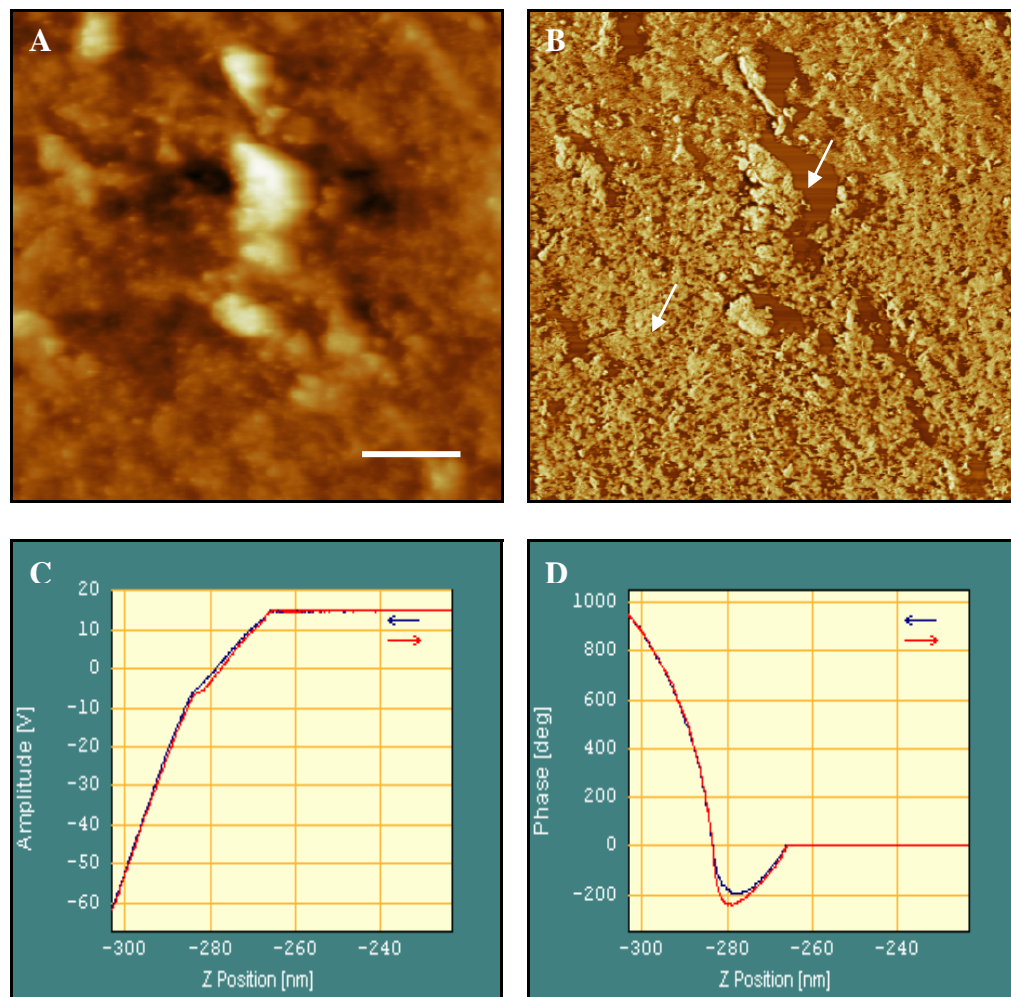
**Figure 3.5** A typical DI 3000 AFM  $5\mu\text{m} \times 5\mu\text{m}$  (A) topography, (B) phase image of Blue 1 dyed cellophane, imaged using an unmodified cantilever tip in TM, (with Z-range 66.2nm and scale bar  $1\mu\text{m}$  (white line)). The line profile (C) of fibrillar structure observed in topography image. Fibrillar measurements were taken of single fibres from within the phase image, as opposed to thick bundles of fibres.

Figure 3.5 displays a typical DI 3000 AFM image of Blue 1 dyed cellophane film obtained in TM using an unmodified tip. The topography in image (A) shows the familiar fibrillar structure that was also observed for the undyed cellophane sample. As in Figure 3.4 no contrast is also observed in the phase image (B), but it does further highlight the topographic detail within the sample surface. A line profile measurement (C) was also taken of the fibrils within topography image (A). The fibrils appeared to have widths of 90-100nm across, which is larger (almost double) than the fibrillar width within an undyed cellophane sample in Figure 3.3. The increase in the fibrillar dimensions in the cellophane samples may be attributed to the Blue 1 dye compound; as during the dyeing process the fibres would swell in the aqueous environment, causing hydrogen bond breakages between adjacent cellulose chain molecules (thought to be amorphous regions) but minimal swelling would occur in crystallite regions. The intrafibrillar swelling would allow the dye molecules to adsorb into the cellulose substrate. It could be hypothesised that this action causes the fibrillar structure to remain enlarged as after the dyeing process the dye remains fixed in the cellulose structure. Also within Figure 3.5, the two types of surface features are observed, (in a diagonal direction, from bottom-left corner to top-right corner in image (A)), globular and fibrillar patterns. These surface features may be linked to the surface crystallinity of the cellulose substrate, as the globular (amorphous) may provide easy access for dye molecules to enter the bulk fibre due to the uneven surface. Whereas the tightly packed fibrils (crystalline) may make this process difficult, due to the strong intermolecular hydrogen bonding within the crystallites regions.



**Figure 3.6** Displays a  $5\mu\text{m} \times 5\mu\text{m}$  typical AFM (A) topography and (B) phase images of undyed cellophane obtained using a hydrophilic tip in TM, (Z-range 173.6nm and  $1\mu\text{m}$  scale bar). Images (C) and (D) display typical a-p-d curves from the undyed cellophane sample. The data obtained highlights strong attractive regime acting between the cantilever tip and sample surface, suggesting a hydrophilic nature for the surface.

To further explore the nature of the probe-sample interaction during imaging, modified tips (see sections 2.1.4.1 and 2.1.4.2) were utilised to see if this had any affect on the image contrast. Figure 3.6 illustrates a DI 3000 image of undyed cellophane obtained in TM using a hydrophilic tip, under ambient conditions. The topography image (A) shows a globular surface, similar to that first observed in Figure 3.2 (A), and the phase image (B) displays some contrast. To further investigate the nature of the observed contrast, a-p-d measurements were taken from different areas within the phase image, such as regions which appeared light or dark within the image (white arrows in image (B) of Figure 3.6). However the a-p-d measurements appeared to display the same profile irrespective of the sample position. The a-p-d curves displayed in Figure 3.6 (images C and D) illustrate the typical profile that was observed across the whole sample surface, indicating strong attractive probe-sample interaction forces. As little variation was observed over the sample, the a-p-d curves suggested a very homogenous surface chemistry for the undyed cellophane sample. The large interaction forces may reflect the hydrophilic nature of the cellophane; which is due to an increased water layer (-OH groups (from the cellulose) on sample surface, these promote water vapour from the atmosphere to be attracted and become attached to the sample surface, producing a water layer), which increases the capillary forces acting between probe-sample causing strong adhesive interaction, hence an attraction of the sample surface to the modified hydrophilic tip. Therefore the phase contrast did not show 'true' contrast but displayed contrast due to topography.



**Figure 3.7** Displays typical  $5\mu\text{m} \times 5\mu\text{m}$  DI 3000 AFM (A) topography and (B) phase images of Blue 1 dyed cellophane obtained using a hydrophilic tip in TM, (Z-range 165.4nm and  $1\mu\text{m}$  scale bar). Images (C) and (D) display typical a-p-d curves from the dyed cellophane sample. The data obtained highlights a strong repulsive regime acting between the cantilever tip and sample surface, suggesting a hydrophobic surface (or less hydrophilic, than undyed cellophane surface).

Figure 3.7 displays a DI 3000 image of Blue 1 dyed cellophane obtained using a hydrophilic tip in TM in air. Similar to the undyed cellophane sample in Figure 3.6, the topography image (A) shows a globular surface, and the phase image (B) displays some contrast. Again a-p-d measurements were obtained from across the whole sample surface (white arrows) to determine the nature of the phase contrast within image (B). However, as in the undyed cellophane sample the a-p-d measurements appeared to display the same type of profile and which were not specific to any particular region within the phase image. The a-p-d curves displayed in Figure 3.7 (images C and D) demonstrate the typical profile that was observed across the whole sample surface which indicated strong repulsive forces acting on the tip. The a-p-d curves equally indicate a homogenous surface chemistry for the Blue 1 dyed cellophane sample. The sample displays a less hydrophilic (or hydrophobic) nature than the undyed cellophane, due to decreased water layer on sample surface (less –OH groups present at the surface because of dye molecules which are highly aromatic, see Figure 3.1, page 82), which in turn decreases the capillary forces working between probe-sample resulting in weak adhesive interaction; hence repulsion between the dyed sample surface and the modified hydrophilic cantilever tip.

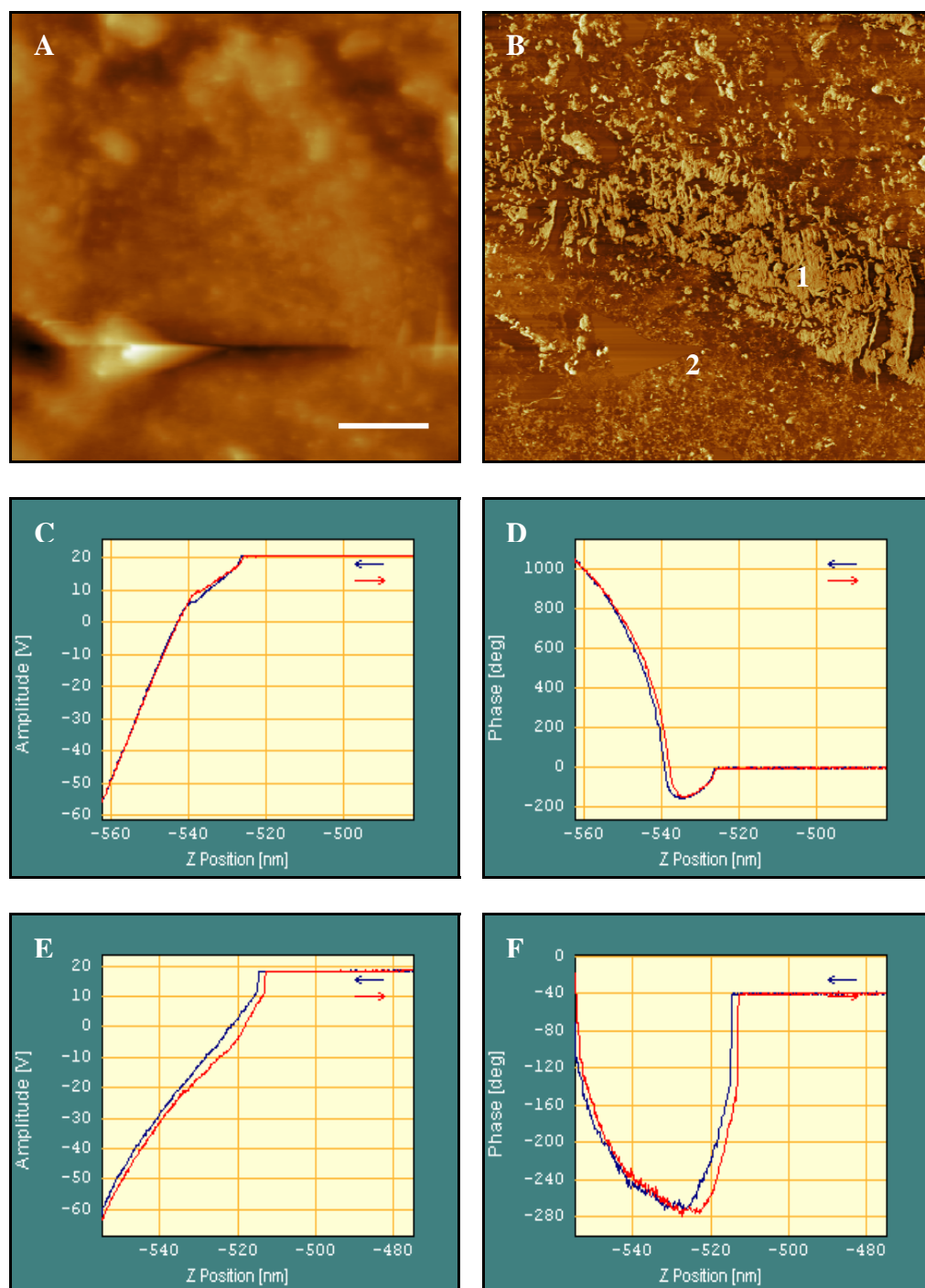


**Figure 3.8** Displays typical  $10\mu\text{m} \times 10\mu\text{m}$  (A) topography and (B) phase images of dyed cellophane border using a hydrophilic cantilever tip, (Z-range  $439.4\text{nm}$  and scale bar  $2\mu\text{m}$ ). A-p-d curves (C) and (D) correspond to the light area, point 1 within the phase image (B). Curves (E) and (F) correspond to dark area, point 2 within image (B).

AFM images were also achieved on a same dyed sample of cellophane which possessed an area of uneven dyeing that resulted in a border of undyed and Blue 1 dyed cellophane. The images were again obtained using the same modified hydrophilic tip as used in the previous images. Figure 3.8 displays this achievement clearly. Whilst the topography (A) shows the same globular features which have been observed in both dyed and undyed samples, this time (B) shows marked contrast within the phase image.

A-p-d curves can be used as a *fingerprint* to identify different components within a sample surface, by providing information on repulsive/attractive property of the probe-sample interaction. Therefore in Figure 3.8, a-p-d measurements were taken to identify (fingerprint) regions of dyed cellophane across the sample surface. Curves (C) and (D) in Figure 3.8 correspond to the light region from point 1 in phase image (B), and curves (E) and (F) correspond to the dark region from point 2 within the image. Curves (C) and (D) show strong repulsive profile, the behaviour is similar to the dyed cellophane sample in Figure 3.7. The profile suggests that the light region within the phase image corresponds to dye within the sample as it also displays a hydrophobic nature (repulsion to the hydrophilic tip) unlike the undyed cellophane sample. Curves (E) and (F) display an attractive profile, here the results appear to be very similar to the undyed cellophane sample in Figure 3.6; the profile suggests the dark regions within the image are undyed regions of the cellophane sample. The attractive profile suggests a hydrophilic nature due to its attraction to the tip. We can see that both sets of data from Figures 3.6 and 3.7 closely match the data sets within Figure 3.8. These previous images

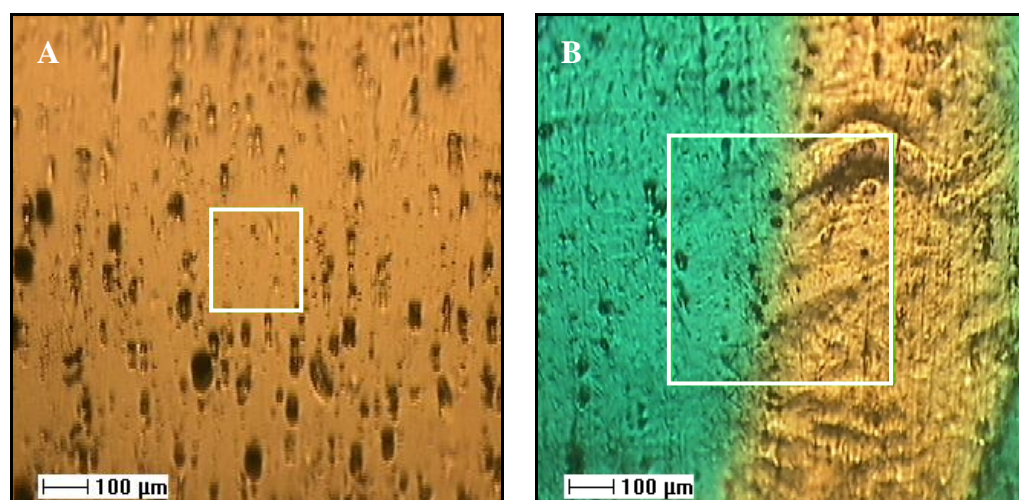
helped to fingerprint the different regions within Figure 3.8, which allowed identification of dyed and non-dyed areas within the sample. From the light and dark regions within image (B), it is possible to infer that the contrast within the image is due to difference in surface chemistry attributable to the presence of dye compound in varying quantities across different regions of the sample. Image (B) displays the inconsistent coverage of the dye clearly, as very little contrast is observed in the lower half of the image suggesting a completely undyed region (supported by the a-p-d curves). The middle section of the image displays an area of dyed cellophane (also supported by the a-p-d curves), but the top-half of the phase image displays an area which shows some contrast, suggesting an incomplete coverage of dye within that area.

### **3.3.2 ToF-SIMS analysis comparison**

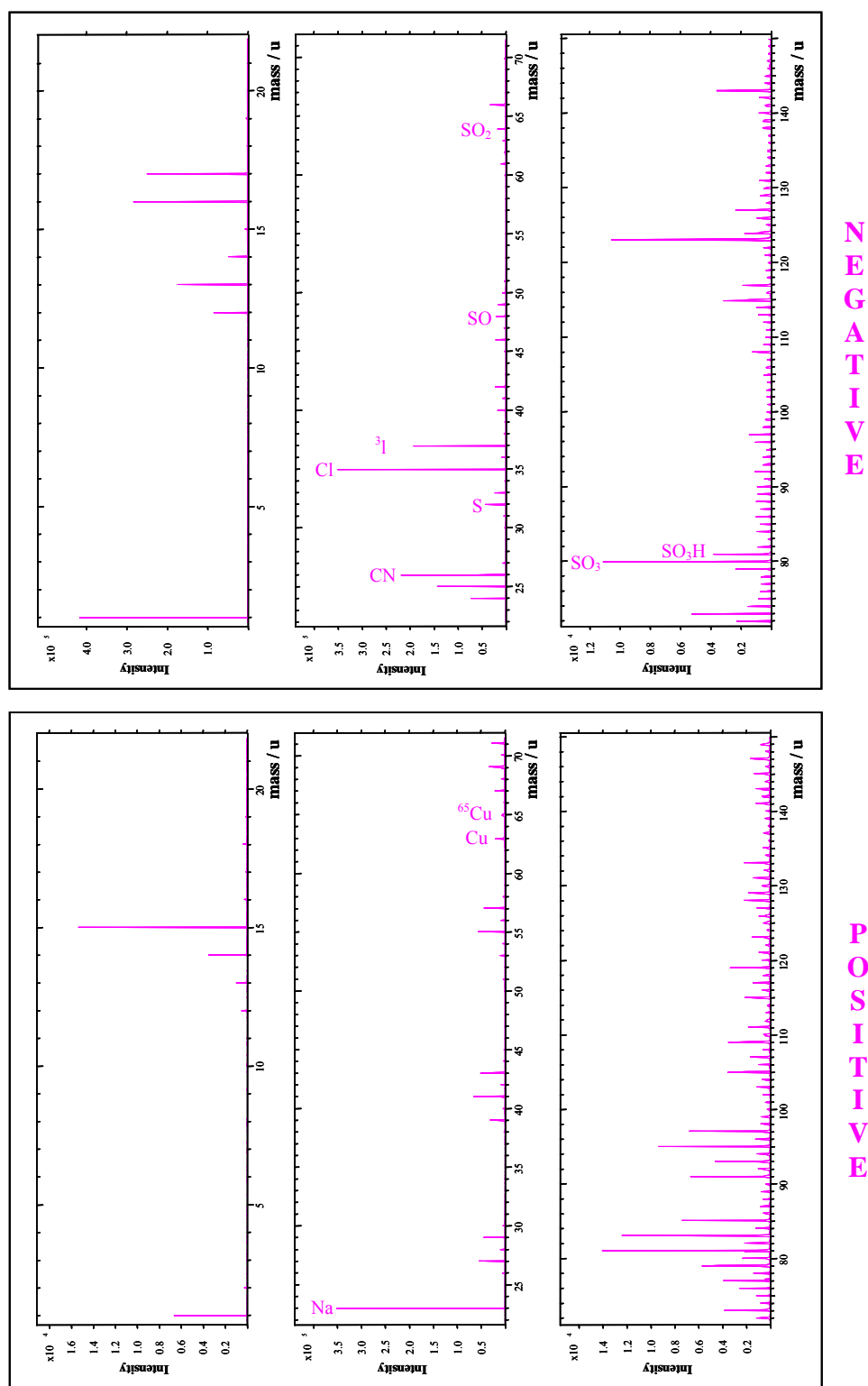
ToF-SIMS analysis was performed on the undyed and Blue 1 dyed cellophane film samples. Firstly the pure dye compound was analysed to produce control spectra and peak lists, in an attempt to distinguish the data obtained from ToF-SIMS spectra of Blue 1 dyed and undyed cellophane. This would allow identification of ion fragments indicative of dye molecules from the surface of the dyed cellophane (see section 2.2.3 for analysis method and peak assignment) compared with the undyed cellophane sample. The spectrum obtained from the undyed cellophane was used to produce characteristic negative and positive ion peak lists, indicative of the cellulose substrate.

Figure 3.9 displays the cellophane film samples that were imaged by the optical microscope camera attached to the ToF-SIMS instrument (which aids

the location of sampling areas). Image (A) shows the surface of the undyed cellophane film. Image (B) shows the Blue 1 dyed cellophane film, and also displays the dye border which was mentioned previously for Figure 3.8. Both images display ‘black holes’ within the surfaces of the samples, which most likely arise during the manufacturing process which can cause a ‘bubbling’<sup>254</sup> of the surface when the cellophane film is being extruded from the acid bath. These were not observed in the AFM images as they are to a much larger scale within these images.



**Figure 3.9** ToF-SIMS optical image of undyed (A) and Blue 1 dyed (B) cellophane films (displays dye border) showing ‘bubbled’ surface. White squares display the sampling area (100μm x 100μm for undyed sample and 200μm x 200μm for dyed cellophane sample).



**Figure 3.10** ToF-SIMS positive and negative ion spectra of Blue 1 dye compound, obtained using a  $\text{Ga}^+$  gun, with a scan area of  $200\mu\text{m} \times 200\mu\text{m}$ .

The Blue 1 dye compound was first analysed using ToF-SIMS to produce control spectra to aid the analysis of the dyed cellophane. Figure 3.10 displays the negative and positive ion spectra for the Blue 1 dye compound. The most important characteristic peaks have been identified and marked within the spectra. The positive ion spectrum highlights the presence of  $\text{Cu}^{2+}$  ions, at  $m/z$  63 ( $^{63}\text{Cu}$ ) and 65 ( $^{65}\text{Cu}$ ), a key component of the reactive dye. The negative ion spectrum displays the presence of Cl ions at  $m/z$  35 ( $^{35}\text{Cl}$ ) and 37 ( $^{37}\text{Cl}$ ), also a key component of the dye molecule, as well as a peak at  $m/z$  81 attributable to the  $\text{SO}_3\text{H}$  group. To enable ToF-SIMS analysis, the dye compound was spun-cast onto a hexane-cleaned (to remove contaminants) sample of silicon wafer at a 0.05% w/v concentration (in water), see Figure 3.11. Table 3.1 and 3.2 display the full positive and negative ion peak lists respectively for the Blue 1 dye compound, which were used in the analysis of the dyed cellophane sample.

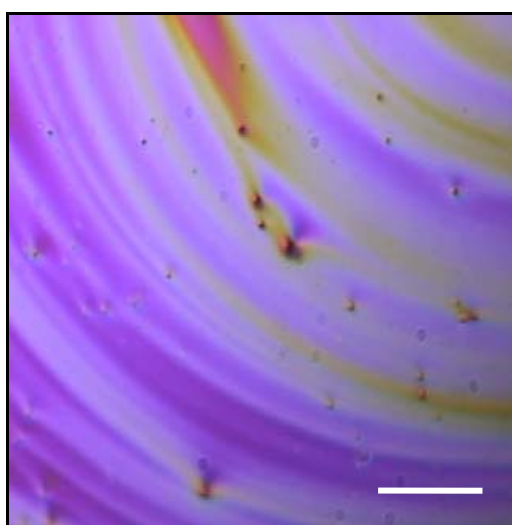


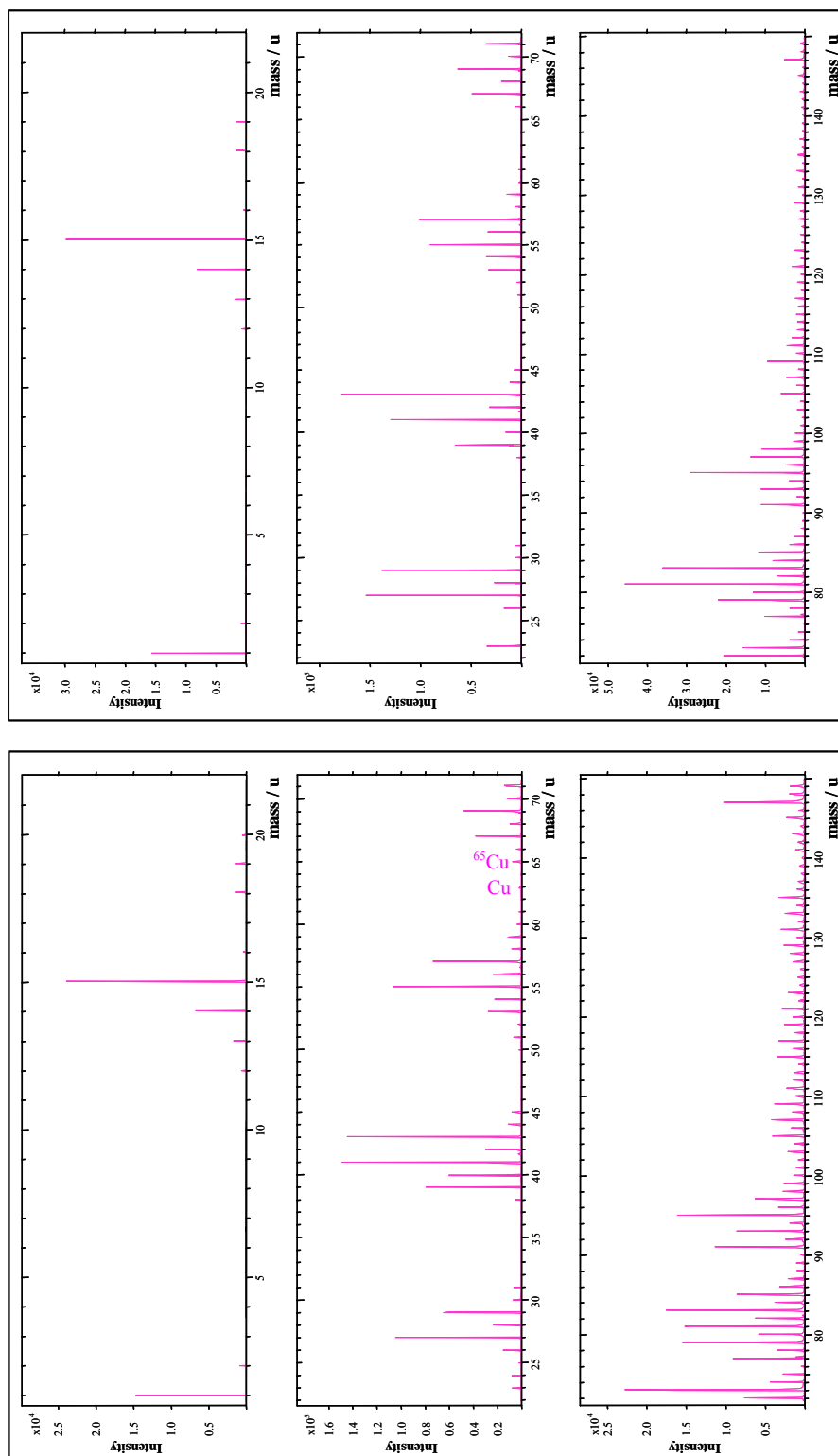
**Figure 3.11** A 320 $\mu\text{m}$  x 320 $\mu\text{m}$  ToF-SIMS optical microscope camera image of spun-cast Blue 1 dye compound on silicon wafer with scale bar 64 $\mu\text{m}$ .

m/z	Positive Ion Fragment
12	C
13	CH
14	CH <sub>2</sub>
15	CH <sub>3</sub>
23	Na
25	C <sub>2</sub> H
26	C <sub>2</sub> H <sub>2</sub>
27	C <sub>2</sub> H <sub>3</sub>
28	Si
28	C <sub>2</sub> H <sub>4</sub>
29	SiH
37	C <sub>3</sub> H
38	C <sub>3</sub> H <sub>2</sub>
39	C <sub>3</sub> H <sub>3</sub>
40	C <sub>3</sub> H <sub>4</sub>
41	C <sub>3</sub> H <sub>5</sub>
42	C <sub>3</sub> H <sub>6</sub>
43	C <sub>3</sub> H <sub>7</sub>
53	C <sub>4</sub> H <sub>5</sub>
55	C <sub>4</sub> H <sub>7</sub>
56	C <sub>4</sub> H <sub>8</sub>
57	C <sub>4</sub> H <sub>9</sub>
63	<sup>63</sup> Cu
65	<sup>65</sup> Cu
65	C <sub>5</sub> H <sub>5</sub>
67	C <sub>5</sub> H <sub>7</sub>
69	C <sub>5</sub> H <sub>9</sub>

**Table 3.1** Characteristic positive ion peak list for Blue 1 dye powder compound.

m/z	Negative Ion Fragment
12	C
13	CH
14	CH <sub>2</sub>
15	NH
16	O
17	OH
23	Na
24	C <sub>2</sub>
26	CN
31	CH <sub>3</sub> O
32	S
33	HS
35	Cl
36	C <sub>3</sub>
37	<sup>37</sup> Cl
40	CN <sub>2</sub>
41	CNO
46	NO <sub>2</sub>
48	SO
49	C <sub>4</sub> H
50	C <sub>3</sub> N
57	C <sub>2</sub> HS
60	C <sub>5</sub>
61	CNCl
64	SO <sub>2</sub>
66	C <sub>4</sub> H <sub>2</sub> O
79	CO <sub>2</sub> Cl
80	SO <sub>3</sub>
81	SO <sub>3</sub> H
123	C <sub>4</sub> H <sub>3</sub> N <sub>4</sub> O

**Table 3.2** Characteristic negative ion peak list for Blue 1 dye powder compound.

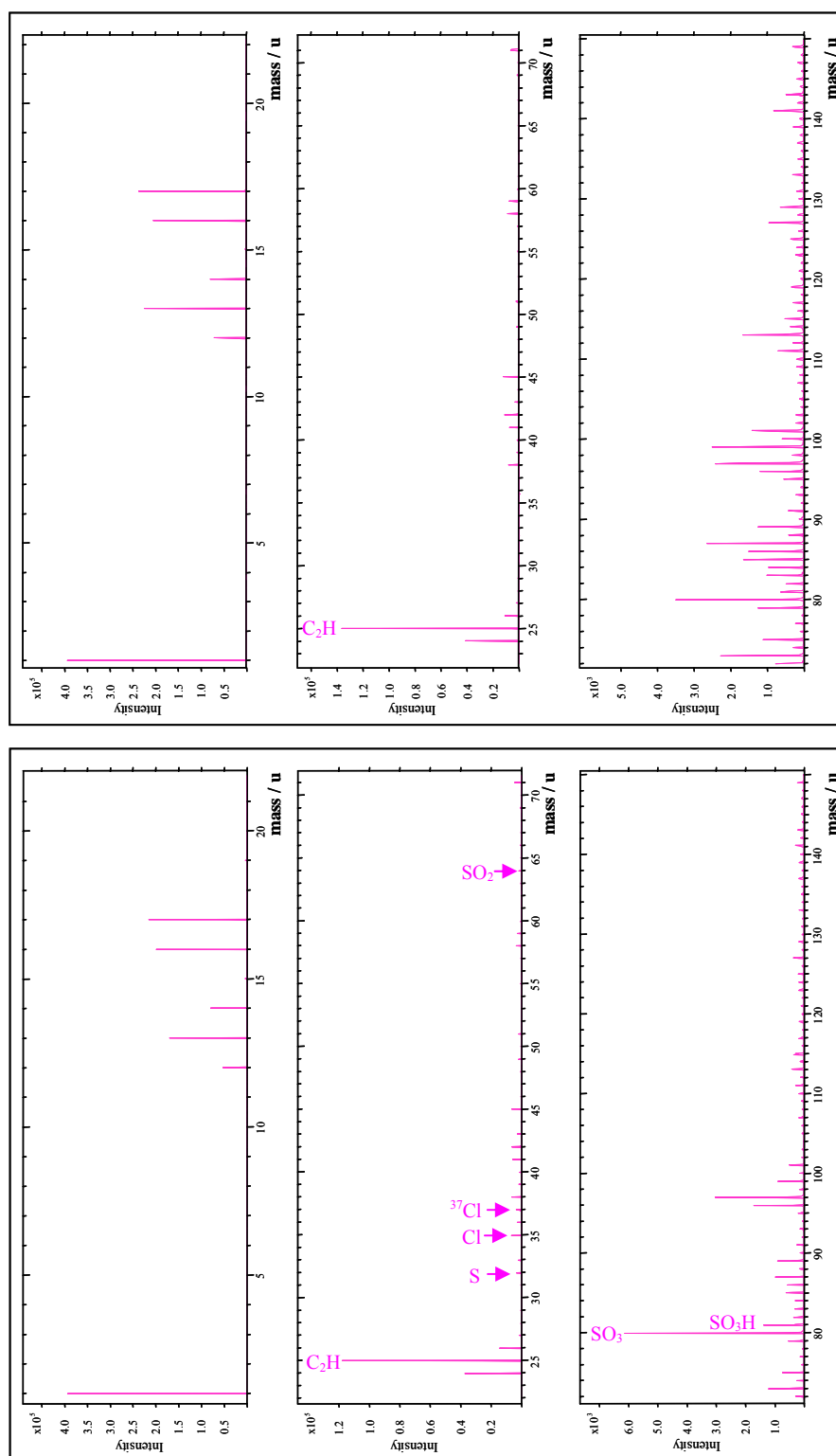


D  
Y  
E  
D

D  
Y  
E  
D

**Figure 3.12** ToF-SIMS mass spectra of positive ion peaks for undyed and Blue 1 dyed cellophane films obtained using a  $\text{Ga}^+$  gun, with a scan area of  $100\mu\text{m} \times 100\mu\text{m}$  for undyed sample and  $200\mu\text{m} \times 200\mu\text{m}$  for dyed sample.

Next the dyed cellophane film was compared with spectra obtained for the undyed material, to allow identification of ion fragments indicative of dye molecules from the surface of dyed cellophane film. The spectra appeared to be very similar for both of the cellophane samples, however on closer inspection there was evidence to support chemical differences based upon the presence of dye compound. The presence of  $\text{Cu}^{2+}$  ions, at  $m/z$  63 and 65, were found within the dyed sample spectra, but were absent from the undyed sample spectra. The presence of these ion fragments from the dyed sample highlight the sensitivity of the instrument to provide qualitative data to show differences in chemical composition between the two samples. Both positive ion spectra for the cellophane samples did however display traces of siloxane contaminants at  $m/z$  28, 29, 73 and 147, but it should be noted that the sensitivity of the instrument will often highlight such minute contaminants (ppm), despite cleaning of samples within hexane and careful sample preparation, as siloxane contaminants are known to present within the atmosphere<sup>255</sup>. For this reason it is difficult to attribute the siloxane to one particular sample preparation or handling stage. However, its presence does not mask the peaks which are important for this study, and a comparison of the spectra highlights chemical differences between the two samples due to the presence of the dye.



UNDYED

DYED

**Figure 3.13** ToF-SIMS mass spectra of negative ion peaks for undyed and Blue 1 dyed cellophane films obtained using a Ga<sup>+</sup> gun, with a scan area of 100µm x 100µm for undyed sample and 200µm x 200µm for dyed sample.

Figure 3.13 displays the corresponding negative ion fragment peak spectra for the dyed cellophane and undyed cellophane. Again both spectra appear to be very similar, but some differences are observed. The undyed cellophane spectrum displays the repeat ion fragmentation pattern characteristic of small hydrocarbon chains, which are associated to cellulose from  $m/z$  80 to 150. The dyed cellophane negative ion spectrum displayed the presence of dye indicative peaks at  $m/z$  35 and 37 for Cl and  $^{37}\text{Cl}$ , as well as fragments ions  $\text{SO}_3$  and  $\text{SO}_3\text{H}$  at  $m/z$  80 and 81, (refer to Figure 3.1). The negative ion fragment at  $m/z$  25, for  $\text{C}_2\text{H}$ , is the most intense peak in both of the samples, this would be due to its presence within the dye compound and the cellulose structure itself, and therefore would present itself to be the most common and abundant fragment produced from the primary ion bombardment during ToF-SIMS analysis.

Tables 3.3 and 3.4 display the undyed cellophane negative and positive ion peak lists respectively.

m/z	Negative Ion Fragment
12	C
13	CH
14	CH <sub>2</sub>
15	NH
16	O
17	OH
24	C <sub>2</sub>
25	C <sub>2</sub> H
26	CN
27	C <sub>2</sub> H <sub>3</sub>
31	CH <sub>3</sub> O
32	O <sub>2</sub>
36	C <sub>3</sub>
37	C <sub>3</sub> H
38	C <sub>3</sub> H <sub>2</sub>
39	C <sub>3</sub> H <sub>3</sub>
40	C <sub>2</sub> O
41	C <sub>2</sub> HO

**Table 3.3** Characteristic negative ion peaks selected for the analysis of undyed cellophane film.

m/z	Positive Ion Fragment
12	C
13	CH
14	CH <sub>2</sub>
15	CH <sub>3</sub>
23	Na
26	C <sub>2</sub> H <sub>2</sub>
27	C <sub>2</sub> H <sub>3</sub>
28	Si
28.9	SiH
29	C <sub>2</sub> H <sub>5</sub>
38	C <sub>3</sub> H <sub>2</sub>
39	C <sub>3</sub> H <sub>3</sub>
40	C <sub>3</sub> H <sub>4</sub>
41	C <sub>3</sub> H <sub>5</sub>
42	C <sub>3</sub> H <sub>6</sub>
43	C <sub>3</sub> H <sub>7</sub>
44	C <sub>3</sub> H <sub>8</sub>
53	C <sub>4</sub> H <sub>5</sub>
54	C <sub>4</sub> H <sub>6</sub>
55	C <sub>4</sub> H <sub>7</sub>
56	C <sub>4</sub> H <sub>8</sub>
57	C <sub>4</sub> H <sub>9</sub>

**Table 3.4** Characteristic positive ion peaks selected for the analysis of undyed cellophane film.

### 3.3.3 DSC analysis comparison

Thermal analysis of the cellophane samples was carried out to determine any thermal transitions, which might be characteristic of crystalline or amorphous structure (and any change in these following dyeing), as the AFM data suggested the presence of both types of structure (due to density of fibrillar packing) in the surface morphology.

It is known that cellulose can be heated for many hours up to 120°C without any adverse effects. However in dry air, at higher temperatures, considerable depolymerisation takes place, accompanied by the; formation of carbonyl and carboxy groups in the solid material, the evolution of water, carbon monoxide and carbon dioxide, and a loss of tensile strength<sup>40,256,257</sup>. The pyrolysis of cellulose is a very complex chemical process and is commonly believed to involve two different mechanisms<sup>258</sup>. One of the processes is the dewatering and charring of cellulose which produces the H<sub>2</sub>O, CO<sub>2</sub> and solid residues. The second mechanism produces the non-volatile liquid L-glucose (CH<sub>2</sub>OH occurring at C4 instead of C5, refer to Figure 1.1, section 1.2) by depolymerisation, and the L-glucose cleavage is thought to continue, producing low molecular weight products, which are more flammable. The competition of these two reactions exists throughout the thermal decomposition of cellulose<sup>259</sup>.

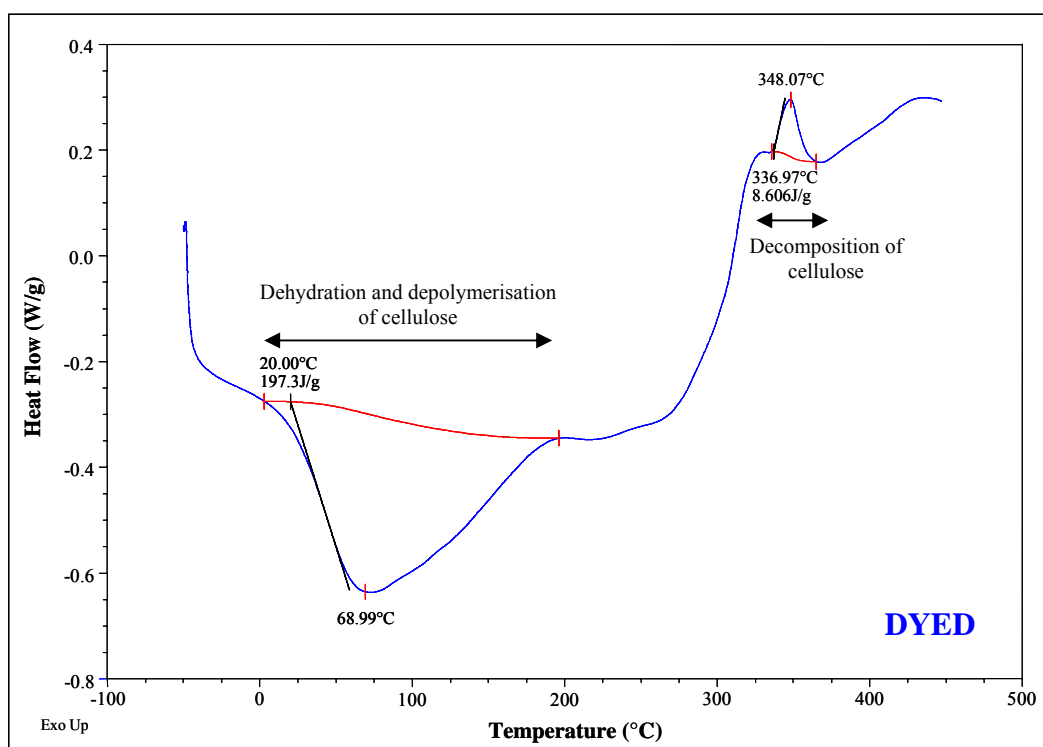
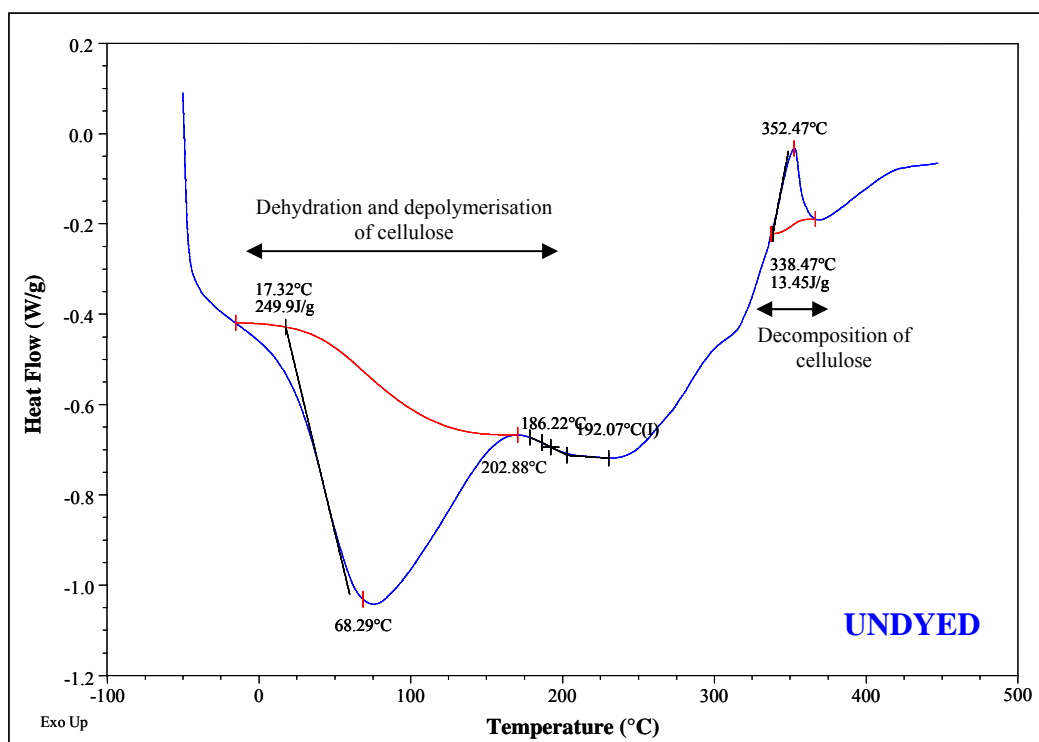


**Figure 3.14** Typical DSC curves for undyed and Blue 1 dyed cellophane samples displaying thermal transitions.

The DSC curves presented in Figure 3.14 display the typical results which were obtained for the undyed and dyed cellophane samples. Within the undyed cellophane sample in Figure 3.14, the DSC curve displays many thermal transitions which include a broad endothermic peak ranging from 0 to 175°C, which reaches a maximum at approximately 70°C. This confers well with figures cited within the literature, which attribute an endotherm peak of 80°C to the evolution of adsorbed moisture, and another endotherm peak at 160°C to dehydration and depolymerisation of cellulose. Within this particular sample, we see only one large endotherm; however its broad size would suggest that both these thermal actions occurred within the sample. The size of the endotherm peak may have been due to the experimental conditions such as the temperature ramp used (10°C/min), which may not have separated these thermal actions causing an overlap of transitions.

A small exothermic peak also occurs, ranging from 335°C to 370°C with a peak maximum at 353°C. This also agrees well with figures cited within the literature, as Dahiya and Rana observed exothermic transition at this temperature range. However they observed two exotherms; one small peak at 315°C and one large peak at 345°C. These were attributed to the decomposition of cellulose (from cotton origin) which leads to the formation and volatilisation of L-glucose and other volatile products. Within the undyed sample in Figure 3.14, we observe only one exotherm, again this may be attributed to the experimental conditions or it may be due to the different cellulose material (cellophane) being analysed but does occur within the expected temperature range.

In comparison to the undyed cellophane film, the DSC curve for the Blue 1 dyed cellophane in Figure 3.14 displays a slightly broader but similar endothermic peak ranging from 0 to 190°C, with a peak maximum at 70°C. Again this is attributed to the evolution of adsorbed water and subsequent dehydration and depolymerisation of cellulose. There is also the presence of a small exothermic peak, observed at peak maxima 348°C, which is comparable to the undyed sample; this similarity is suggested by literature to be attributed to the cellulose structure, (rather than the dye compound), a decomposition of the cellulose substrate to L-glucose.

The only difference between the two thermograms is displayed in the undyed DSC curve, an endothermic shift from the baseline is observed at around 192°C. Its presence suggests a glass transition ( $T_g$ ), however as the exothermic peak which follows it is identified as a decomposition peak (from literature values), and not a crystallisation temperature  $T_c^{260}$  (where the molecules obtain freedom of motion to spontaneously arrange themselves into a stable crystalline form), it is difficult to assign this shift in the baseline to a  $T_g$ , due to a lack of the  $T_c$  transition. (A  $T_c$  would also present itself as an exothermic peak due to release of energy from amorphous solid to crystalline solid). Within the dyed cellophane sample there is a small shift in the baseline to the exothermic, which does not signify any actual phase transition. The lack of shift in the baseline to the endothermic ( $T_g$ ) within the dyed sample may be due to the presence of dye molecules within the sample, as they could mask any transitions occurring at around this temperature.

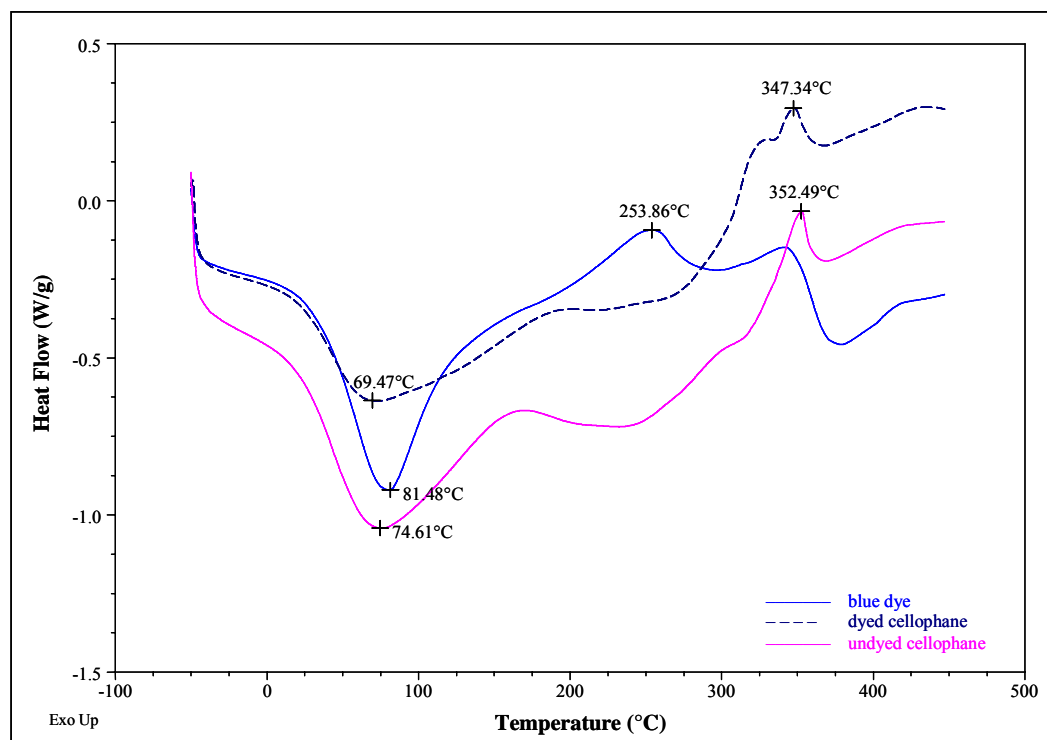
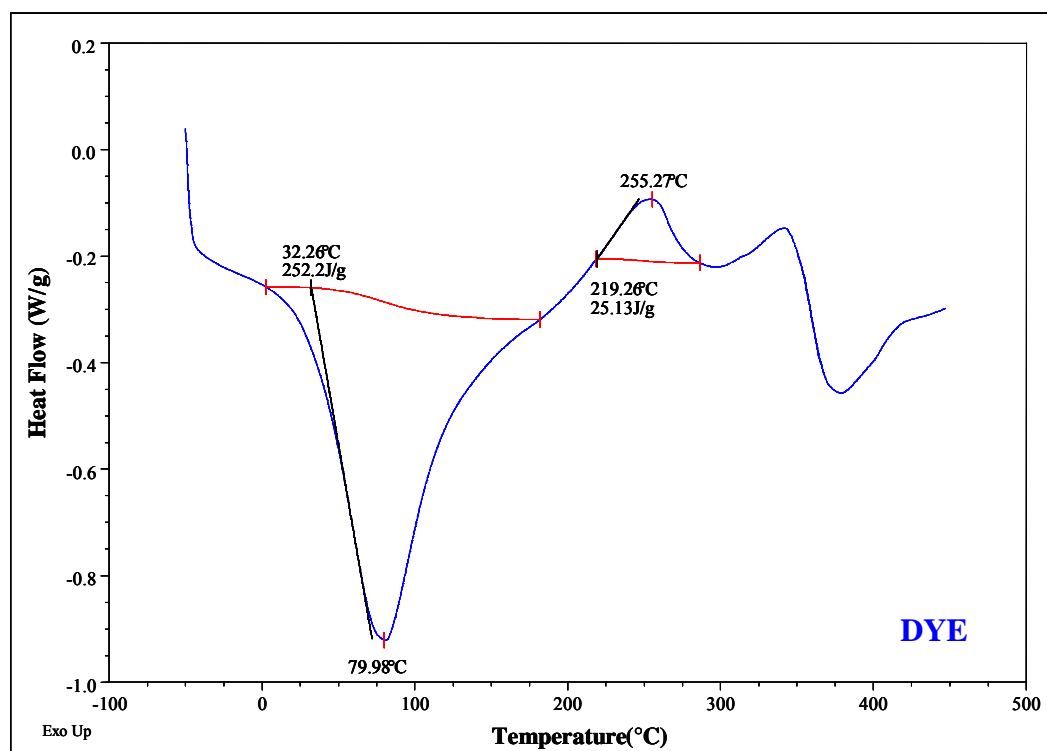


**Figure 3.15** Typical DSC curves for Blue 1 dye compound and DSC curve displaying all three DSC curves overlaid, highlighting specific points of interest.

Figure 3.15 displays the DSC curve for the dye compound, to provide a comparison to the dyed cellophane DSC curve. An endothermic peak is observed with peak maxima at 80°C, 10°C higher than both cellophane samples with a narrower peak. This is assigned to the dehydration of the sample. Also two exothermic peaks were observed within the dye compound, with peak maxima at 255°C and 340°C, these can also be attributed to decomposition of the dye compound and combustion of volatile products. The DSC curve for the dye compound is very distinctive and has many thermal transitions occurring between 200°C and 400°C which could easily hide/mask any transitions occurring from the cellulose substrate within the dyed cellophane sample. The transitions which were observed within the dye compound occurred at nearly the same temperatures as the transitions observed in both cellophane samples, which are highlighted by overlaying all three DSC curves, (see Figure 3.15). This would in part help to explain why little differences could be analysed between the undyed and dyed cellophane samples.

### **3.4 CONCLUSIONS**

The analysis of the cellophane samples through AFM showed many similarities in surface morphology between dyed and undyed cellophane samples. Both types of samples displayed the same typical features; globular and fibrillar patterns. However differences between undyed and dyed cellophane samples were also highlighted by the line profile measurements obtained from the fibrillar widths in both samples. The dyed samples showed a fibrillar width dimension that was almost doubled that from the undyed sample. This suggested that the process of dyeing permanently altered the physical structure

of the cellulose substrate; through the breakages of hydrogen bonds between the cellulose chain molecules, by the process of swelling within the dyebath, thus allowing entry of dye molecules into the substrate. The adsorbed dye molecules within the cellulose substrate may have caused the fibre matrix to remain enlarged after processing and hence the cellulose fibrillar width dimension was wider than would be expected for the undyed cellophane material.

A-p-d measurements obtained using an unmodified tip for both undyed and dyed samples suggested that they both possessed a homogenous surface chemistry, as little phase contrast was observed. However, by changing the tip chemistry, phase contrast was observed and this may have been due to the hydrophilic nature of the modified tip being more sensitive to differences in surface chemistry. The presence of hydroxyl groups at the surface of the samples would have induced more interaction between probe and sample, due to an increased water layer on the sample. This sensitivity allowed different regions on the cellophane to be successfully fingerprinted for the presence/absence of dye compound across the sample surface.

ToF-SIMS produced qualitative data, and showed the presence of dye compound at the surface of the dyed cellophane samples; this was assisted by the reference spectra gained of the undyed sample and dye compound material as the positive and negative ion fragments peak lists aided identification of dye-specific peaks within the dyed cellophane spectra. Crucially these indicative peaks were absent from the undyed sample surface. Therefore

successful chemical identification of the dye compound was obtained from the surface analysis of the cellophane samples.

The DSC thermograms displayed many similarities between the undyed and dyed cellophane samples, with the exception of what appeared to be a  $T_g$  thermal transition in the undyed sample. The broad endothermic peaks in both samples were attributed to a dehydration and depolymerisation of the cellulose within the samples. The exothermic peaks occurring at higher temperatures (353°C and 348°C, in the undyed and dyed samples respectively) than the endotherm were attributed to the decomposition of cellulose, leading to the formation and volatilisation of L-glucose and other volatile products. However, the dye compound DSC thermogram presented different thermal transitions occurring at similar temperatures to the transitions within the cellophane samples. This may have caused a masking of any small or overlapping transitions present within the dyed cellophane sample, (that were perhaps different to the undyed sample), which in turn could have aided the comparison to the undyed sample.

We could perhaps interpret the lack of the *possible*  $T_g$  transition in the dyed cellophane sample, as suggesting that the structure of the dyed cellophane had altered from the undyed cellophane. However, this would be difficult to determine without repeating the experiments using modulated DSC (where periodic temperature modulation is superimposed on the constant heating or cooling rate of a conventional DSC measurement), which would help to *tease-*

*out* any small or overlapping thermal transitions, which could otherwise be missed during a controlled temperature program in normal DSC mode.

### Surface Characterisation of Cotton Fibres

Within the previous chapter cellulose surface morphology and chemistry was characterised on a model system, cellophane. This allowed for many of the employed experimental approaches, such as AFM imaging, to be perfected before they were used for the analysis on cotton cellulose fibres. Presented within this chapter are the surface morphology and chemical investigations of cotton fibres, both before and after the dyeing process. The chapter commences by examining non-mercerised, undyed fibres known as *greige*, and then examines mercerised *undyed* fibres, and lastly studies processed *dyed* fibres. Comparisons involving the three types of fibres are made using the many different surface analytical techniques employed within this chapter. The results highlight similarities and differences between all of the cotton fibre types.

#### 4.1 INTRODUCTION

The limited availability of information on the surface characteristics of untreated and treated cotton fibres makes the application of AFM for their investigation at high resolution an attractive prospect. Previous AFM studies of cotton include those already discussed in section 2.1.3.1, also by Shen and Parker<sup>261</sup> who examined cotton lint fibres, for paper manufacture by AFM and the spread of alkyl ketene dimers (AKD) on the fibres. Through the use of

AFM the group were able to show the surface capillary structures of cotton lint fibres, and the finding that capillary structures in the form of either inter-fibre pores in a paper sheet or V-shaped grooves on the surface of single fibres were essential for the spreading of molten AKD on a cellulose substrate to occur. Henriksson and Gatenholm<sup>262</sup> used the AFM to visualise a micron-sized particle coating applied to cellulose fibres to improve its water repellency. Juhue et al.<sup>263</sup> also used AFM to examine the surface roughness of cotton fibres coated with a fluorinated polymer to increase water repellency.

Unfortunately, the previous studies do not boast particularly high resolution images. Nor do they concentrate on the actual characterisation of the cotton cellulose fibres, but instead focus on wood derived cellulose fibres or surface-modified cotton fibres, with the main purpose of improving the finishing properties of the fibre, (with the aid of further chemical treatment), within the product in question. However, presented within this chapter are high resolution AFM images of; unmodified, undyed, and dyed cotton cellulose fibres. The purpose of this study is to understand the type of dyeing mechanism that takes place by examining possible *dye-entry* or *dye-binding* sites within all the cotton fibre types.

#### **4.1.1 Greige fibres**

Greige fibres can be simply described as fibres which have not been finished/processed (mercerised, section 1.3.2.2), and are unbleached and undyed. These fibres are quite important to the textile industry, as cotton fibres are graded<sup>264,265</sup> on their colour (cream to yellowish brown) and quality whilst

in their greige or raw state before being sold on to the textile, paper or other manufacturing industries. Today there is an increased demand for greige fabrics<sup>266</sup> and clothes by the 'green' consumer, in order to combat the impact to the environment<sup>267</sup> from effluents<sup>268,269</sup> and waste<sup>270</sup> products which result from textile manufacture, for example, through the mercerisation and dyeing of cotton fibres. However, the textile and paper industries are taking steps to reduce<sup>271</sup> dye effluents and its effect on the environment, through the use of nanofiltration membranes<sup>272</sup> and agricultural waste<sup>273</sup> to absorb the effluents.

#### **4.1.2 Undyed fibres**

Throughout this thesis some fibres are referred to as undyed fibres, these equate to mercerised cotton fabrics which are bleached white but are undyed. Knitted cotton fabrics are prepared for dyeing through many stages, including mercerisation, but also include de-sizing using natural starch from potatoes or organic polymers<sup>274</sup> (de-sizing reduces the frictional properties of yarns by coating them with film-forming polymers), scouring with hot alkaline solutions or solvents<sup>275</sup> to remove non-cellulosic materials and bleaching the natural fibre colour out with sodium chlorite<sup>276</sup>.

#### **4.1.3 Dyed fibres**

All the dyed fibres used in this thesis were *reactive*-dyed fabrics, (prepared at DyStar UK, Cheadle Hulme, UK). Reactive dyes utilise a chromophore containing a substituent that is capable of chemically reacting with the cellulose fibre substrate. The covalent bonds that attach reactive dyes to natural fibres make it among the most permanent of dyes.

## **4.2 EXPERIMENTAL**

The experiments detailed here examine the morphologies and surface properties of cotton cellulose fibres through the use of AFM, ESEM (with EDAX) and ToF-SIMS analysis. Any experimental conditions which otherwise differ from ones previously discussed in chapter 2 are stated with regards to the data in question.

### **4.2.1 Samples**

The cotton fabrics, from which all studied fibres were extracted by methods mentioned in section 2.1.4.3, were supplied by DyStar UK (DyStar UK, Cheadle Hulme, UK). These samples included greige fabrics, bleached undyed fabrics and a series of dyed samples, which were dyed with an orange ( $C_{51}H_{42}Cl_2N_{16}O_{16}S_4$ ), red ( $C_{48}H_{39}Cl_2N_{15}O_{20}S_6$ ), and fuchsia (2 components  $C_{75}H_{57}Cl_3N_{22}O_{30}S_9$  &  $C_{54}H_{46}C_{12}N_{16}O_{21}S_6$ ) dye. Where all dyes were manufactured by DyStar UK, and supplied without chemical structure for the purposes of industrial confidentiality. A further set of dyed fabrics were also utilised for experimentation, these were supplied with the chemical structures by DyStar UK, and for the purposes of confidentiality shall be referred to in this chapter as: Blue 1, Yellow 2 and Red 3 (see Figure 4.1).

### **4.2.2 Sample preparation and analysis**

All sample preparation and analysis methods of the cotton fibres have been previously detailed within section 2.1.4 for AFM analysis and instrumentation, section 2.2.3 for ToF-SIMS analysis and peak assignment, and section 2.4.3 for SEM sample preparation and analysis.

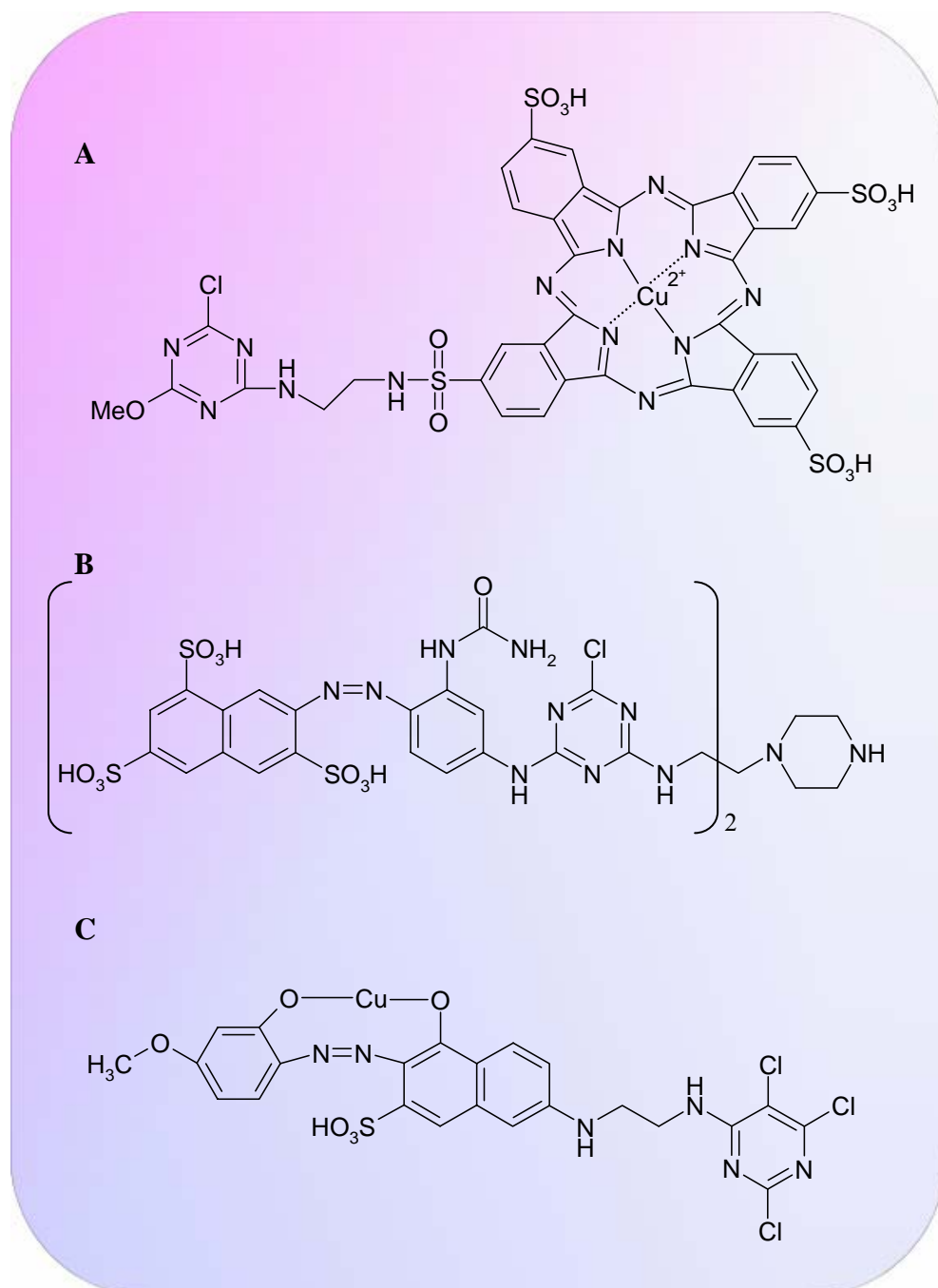


**Figure 4.1** Chemical structures of (A) Blue 1, (B) Yellow 2 and (C) Red 3.

## **4.3 RESULTS AND DISCUSSION**

### **4.3.1 Surface characterisation of greige cotton fibres**

Initial studies were carried out on greige fibres to enable comparisons with undyed processed fibres. SEM was employed to characterise the general morphology of the fibres and to visualise the microfibrillar structure as stated in literature (see section 1.2.1). The AFM was then employed to image these structural features to the nanometer level.

#### *4.3.1.1 SEM analysis*

SEM images of greige fibres were gained using Philips FEI XL30 FEG-ESEM (Philips Electron Optics, Eindhoven, Netherlands) under conditions listed in section 2.4.3. EDAX analysis was also performed to provide information on the elemental composition of the sample. Figure 4.2 displays an ESEM image of greige fibres in their natural state. From this image we were able to see that the sample followed general morphology (twisting and convolutions of the fibre) already described within the literature (refer to section 1.3.2). The ESEM was used to focus on an area from this image to further investigate the surface morphology at a higher magnification, as displayed in Figure 4.3, and the surface of the fibres appeared to be quite smooth. This may have been due to a uniformed covering of cuticle layer on the cotton fibre, which may smooth out/mask, any fine detail from the surface of the fibres. A corresponding EDAX spectrum was taken from the area, for later comparison with spectra from undyed and dyed fibres, and to highlight differences due to the cuticle layer present on the samples. Several EDAX spectra were acquired from various different areas on the sample to ensure reproducibility of results. The

spectrum illustrated the presence of carbon (C) and oxygen (O) from the cellulose structure. However, the results also exhibited trace amounts of potassium (K) and calcium (Ca), which could be attributed to the cuticle layer of the greige fibres, as these were elements not associated to pure cellulose. An artefact/contaminant feature on the central fibre within Figure 4.3 (within blue circle) was also observed, which was difficult to assign an origin to, i.e. as it was possibly attributable to the many solvents used during processes the fibre was subjected to until it was woven.

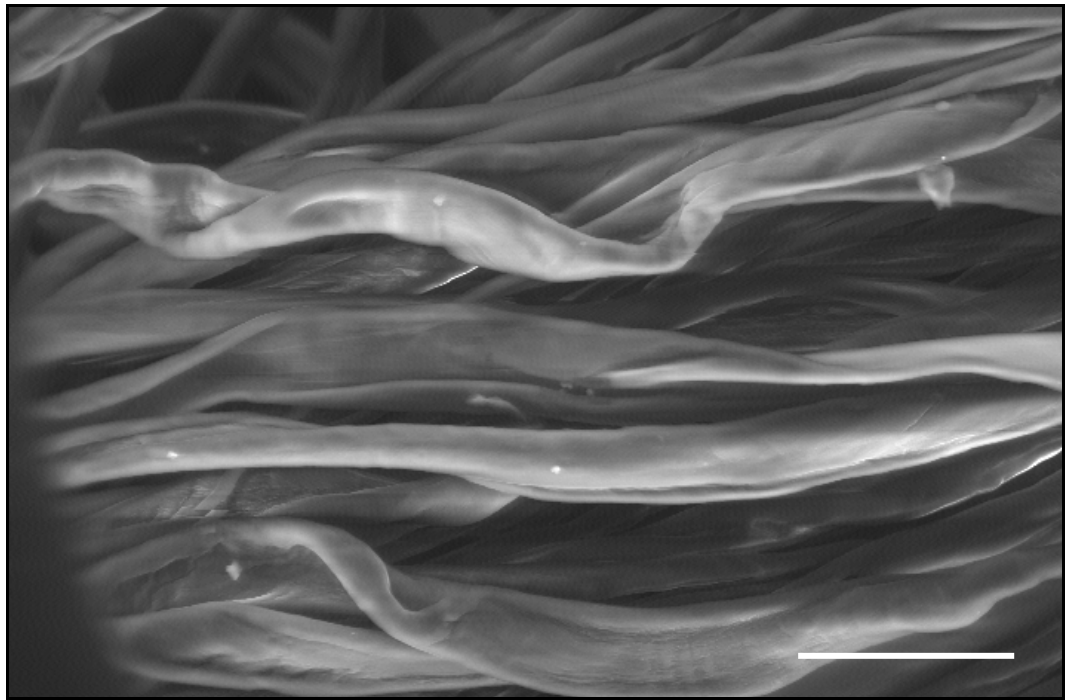


**Figure 4.2** Typical ESEM image of greige fibre at 500x magnification, spot size 4 $\mu\text{m}$ , with scale bar 50 $\mu\text{m}$ ; image displays the general morphology of long staple fibres with a twisted and convoluted shape (see section 1.3.2.1).

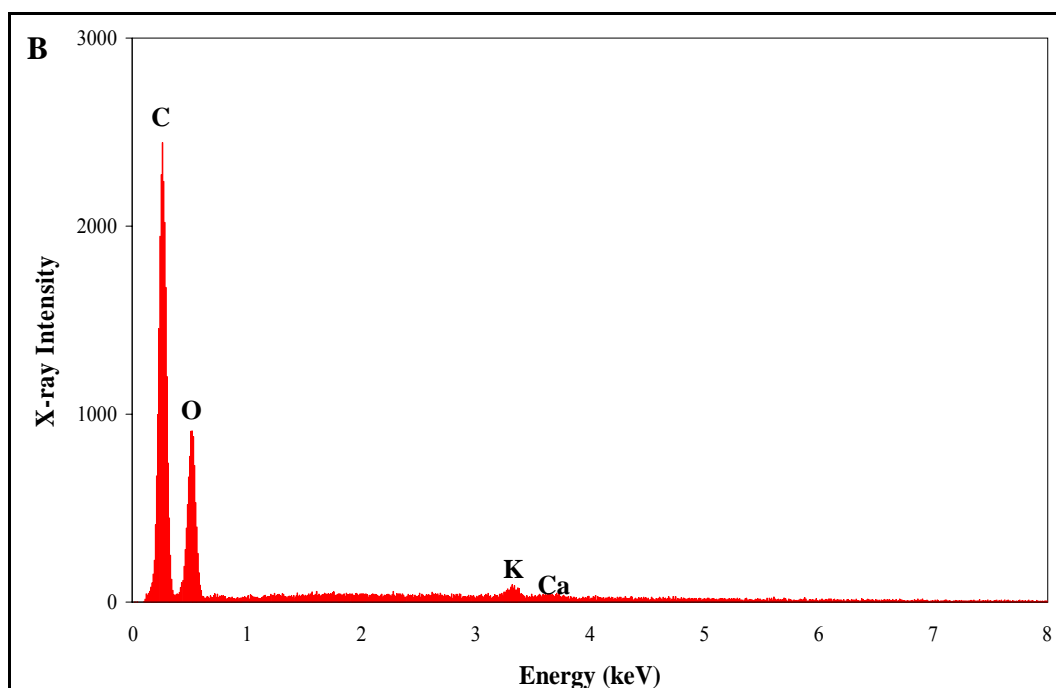
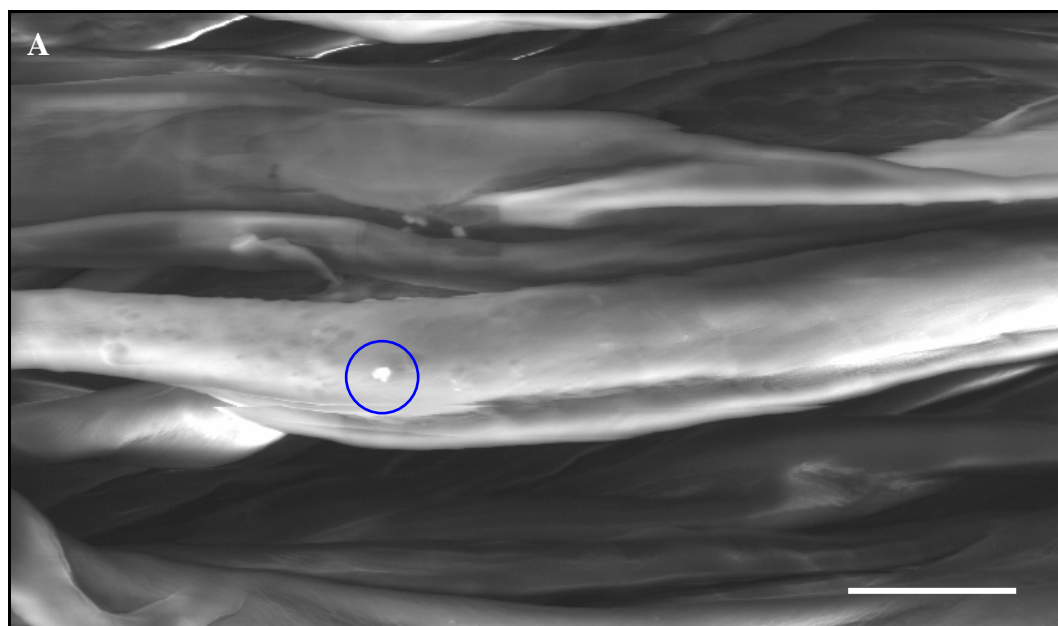


**Figure 4.3** (A) Typical ESEM image of greige fibre at 1000x magnification, spot size 4 $\mu$ m, with scale bar 20 $\mu$ m. (B) shows the corresponding typical EDAX spectrum, which shows chemical information about the surface elemental composition of the sample (at approximately 1 $\mu$ m depth). In this spectrum the greige fibre displays traces of K. Artefact in blue circle may be product of sample handling.



**Figure 4.4** ESEM image of greige fibre at 1000x magnification and spot size 4 $\mu$ m, with scale bar 20 $\mu$ m; displaying natural fibre end in a characteristic tapered shape.

The image displayed within Figure 4.4, shows a greige fibre with a characteristic tapered end shape. ESEM data therefore showed the general morphology of the greige fibres, which was consistent with literature, and the EDAX was able to provide chemical information on the surface elemental composition. (This provided some useful information for comparisons with other fibre types).

#### *4.3.1.2 AFM analysis*

AFM images were captured using the DI 3000 (see section 2.1.4) in TM (refer to section 2.1.2.3) under ambient conditions. Typical AFM topography (A) and phase (B) data obtained using an unmodified tip in TM for greige fibres,

are displayed in Figure 4.5, with topography showing finer surface features that were not observed within the previous SEM data, due to higher resolution imaging with the AFM. The phase image (refer to section 2.1.2.5) shows contrast, most likely indicating differences in the material or adhesive properties of the greige fibre. The typical ‘fibre’ features (ordered fibril features) are visible in the topography image, which become even more apparent in the three-dimensional (3D) rendered image (see Figure 4.5 (C)). However, *plate-like* features are also observed, which were not visible through SEM, but are reported in the literature as globular (or granular) and are a typical feature of cellulose, (due to the density of fibrillar packing). Of the features that can be seen in the phase image, two distinct regions can be identified; plate and fibril features, as well as a large featureless homogenous regions. This detail therefore most likely shows information about the cuticle layer on the greige fibre. A possible reason for the phase contrast could be that the cuticle layer which overlays the cellulose fibre structure underneath, has incomplete coverage on the fibres. On the other hand, phase contrast may be due to the cuticle layer components (wax/pectins) existing in dispersed quantities on the fibre surface. Phase imaging is sensitive to adhesive forces which exist between probe and sample; these can arise due to the existence of water layer on the sample surface, which increase capillary forces between the probe and sample resulting in adhesive interactions (see section 3.3.1). To further investigate the origin of the observed phase contrast, a-p-d curves (refer to section 2.1.2.6) were taken of the two area types to determine the reason for the observed contrast in Figure 4.6.

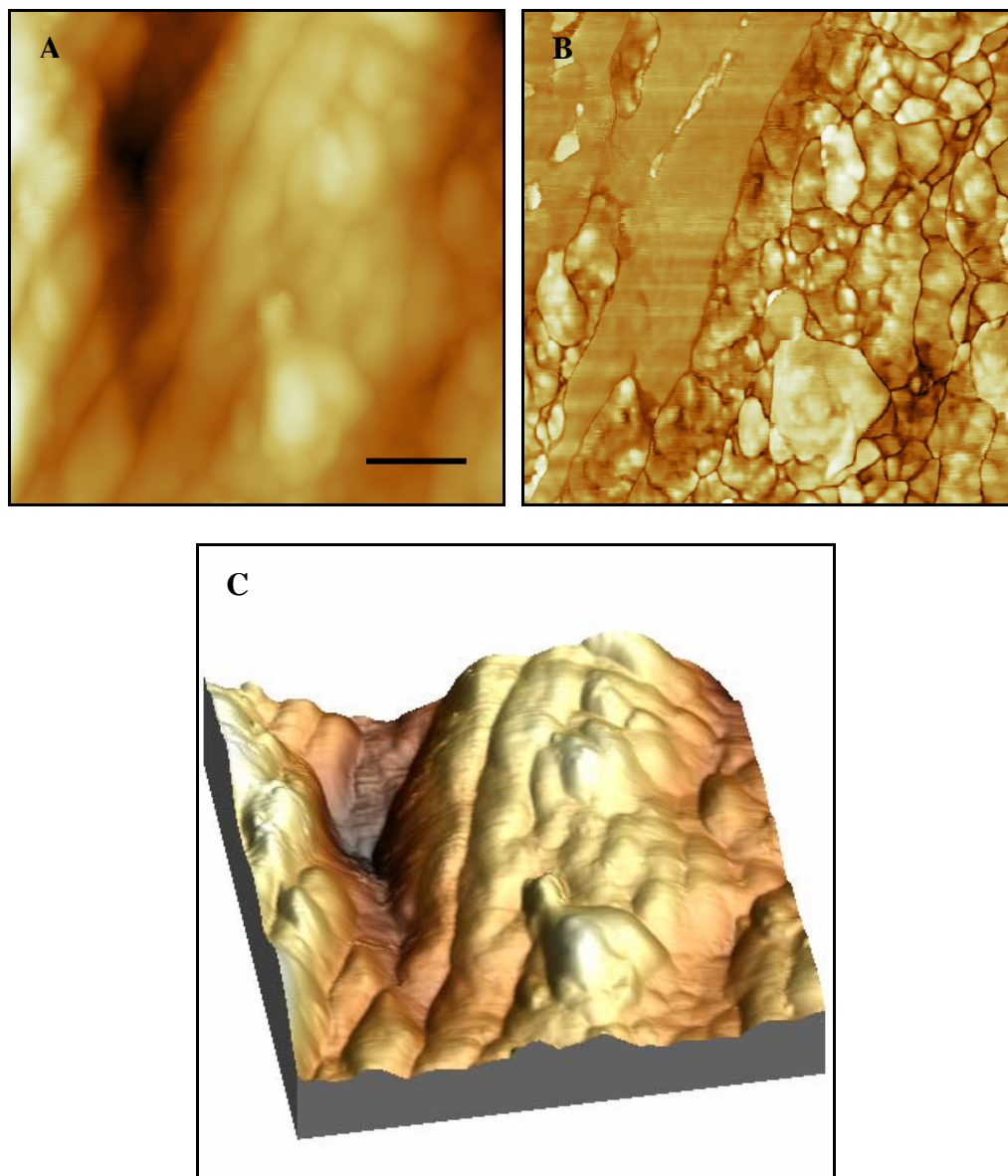


**Figure 4.5** A  $3.45\mu\text{m} \times 3.45\mu\text{m}$  image of greige fibre, topography (A), phase (B), and 3D rendering of topography (C) imaged using TM in air with an unmodified silicon tip, (Z-range 195.4nm, and scale bar 700nm).

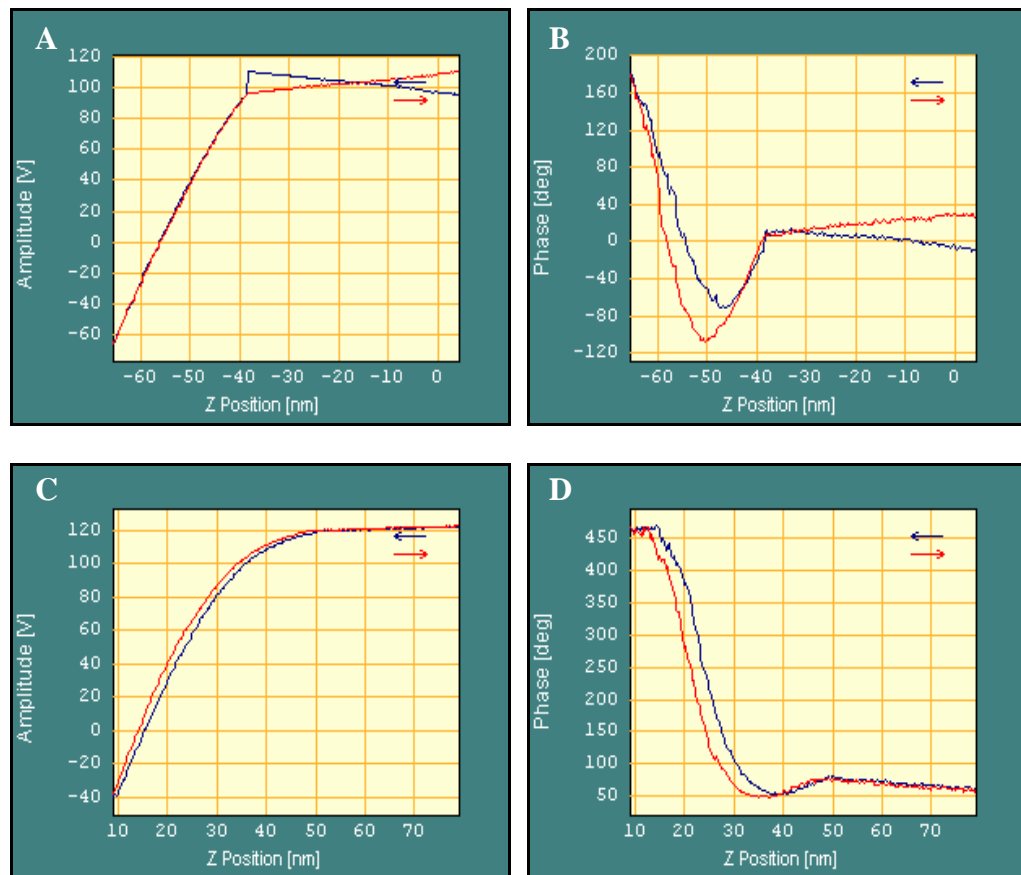
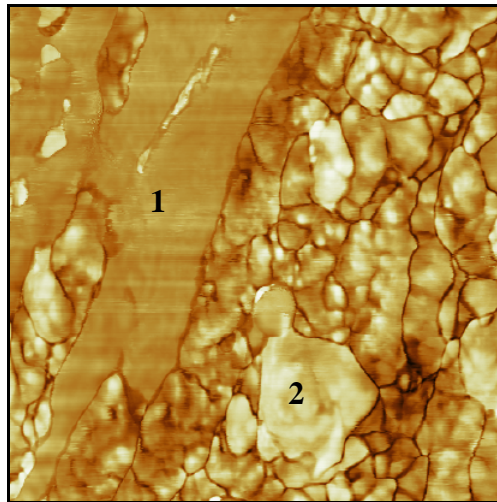
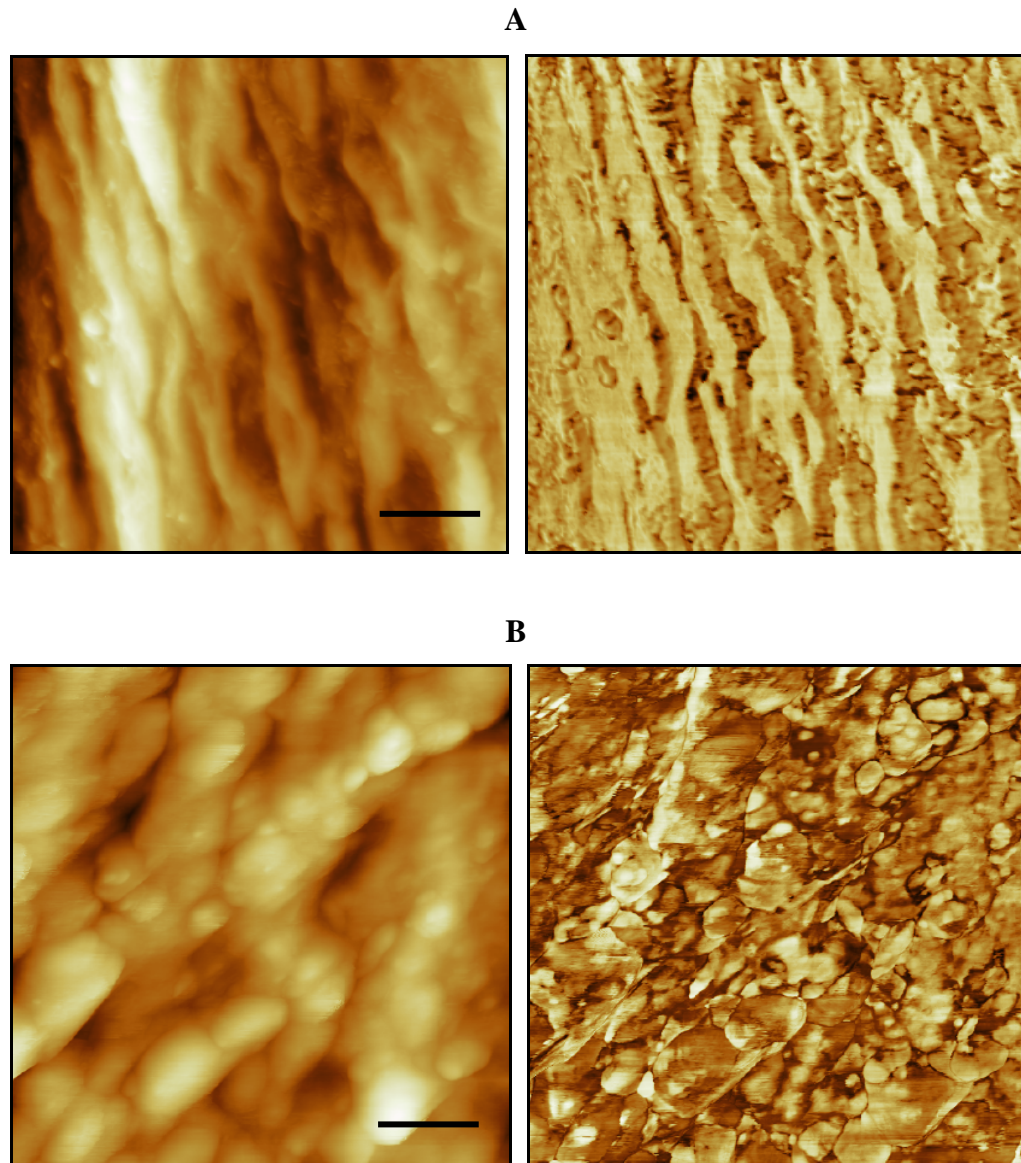


**Figure 4.6** The top image is the phase data (greige fibre obtained with unmodified tip) from Figure 4.5, below which are the corresponding a-p-d curves of the two areas of interest (points 1 and 2). Curves (A) and (B) correspond to point 1 in the phase image and curves (C) and (D) correspond to point 2 within the phase image.

In Figure 4.6 the images show a-p-d curves; curves A and C are amplitude versus distance and curves B and D phase versus distance. The upper set of curves (A & B) show measurements taken from a homogenous area (point 1 within the phase image of Figure 4.6). The large dip in curve B is typical of a strong attractive force working on the tip as it is moving towards and away from the surface. The lower set of curves (C & D) were measured from a plate area (point 2 within phase image), in curve D there is no sharp dip but a steep rise in the curve, such is a typical profile for a repulsive force acting between the probe and sample. The a-p-d curves show that the interaction between the tip and sample is different in each sampling areas, suggesting different composition. Either within the material (soft or hard region) or the adhesive properties of the cellulose sample. The curves provide characteristic profiles for each region (a fingerprint).

Greige fibres were also imaged using modified cantilever tips (see sections 2.1.4.1 and 2.1.4.2) to further probe the nature of the tip-sample interaction. Figure 4.7 shows two sets of topography/phase data images of greige fibres imaged using TM in air using a modified, hydrophilic tip. Results here show similar findings to the topography image in Figure 4.5. Image set (A) shows only fibrillar features, and image set (B) illustrates globular (plate-like) features similar to Figure 4.5, but this time without fibrillar features or any large areas of contrast within the phase image. It should be noted however, that the different features observed in (A) or (B) most likely reflect the particular points on the fibre the images were obtained. It was also difficult to obtain phase contrast when using a hydrophilic cantilever tip; this most likely

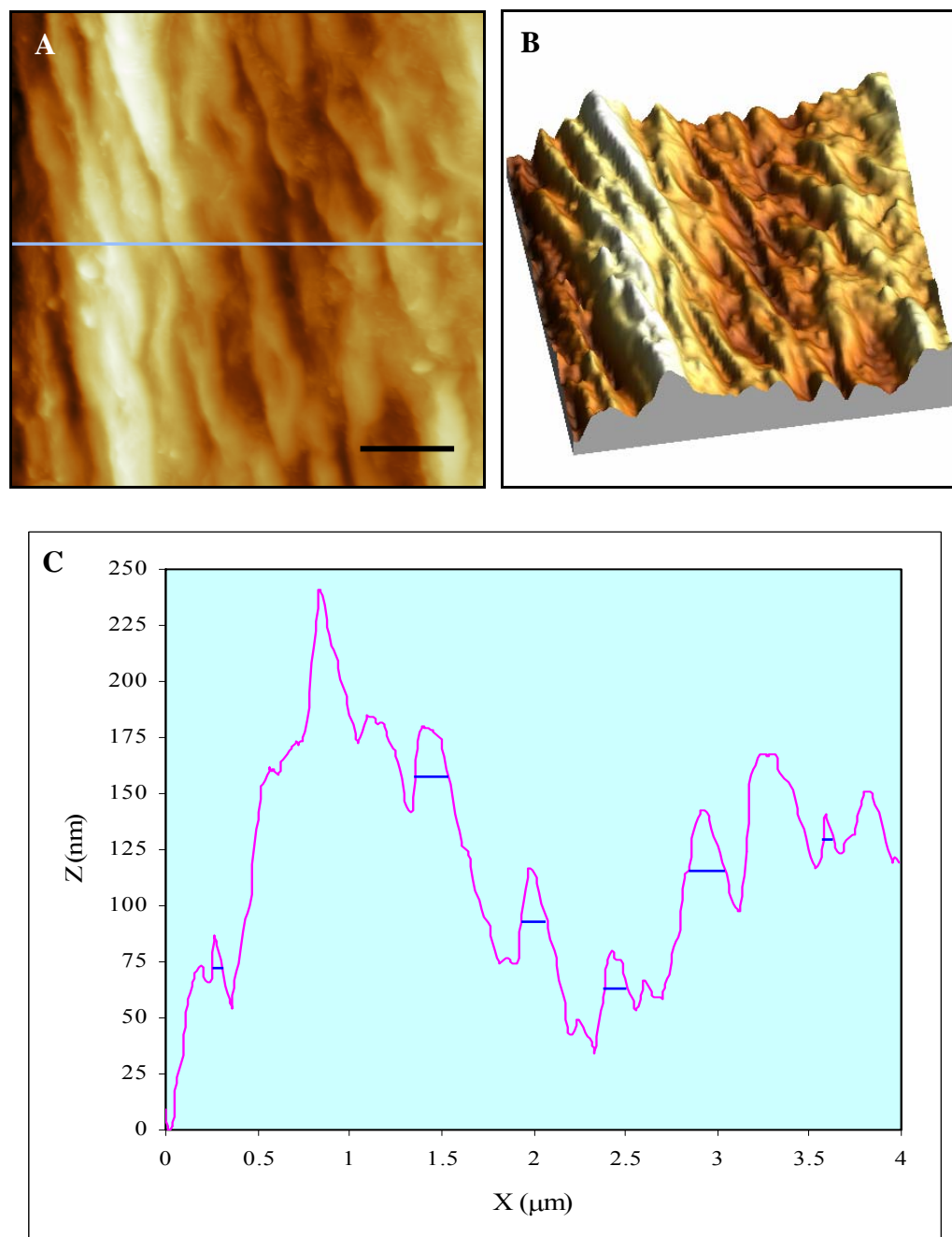
reflected the hydrophobic nature of the sample surface, due to the presence of the waxy cuticle layer.



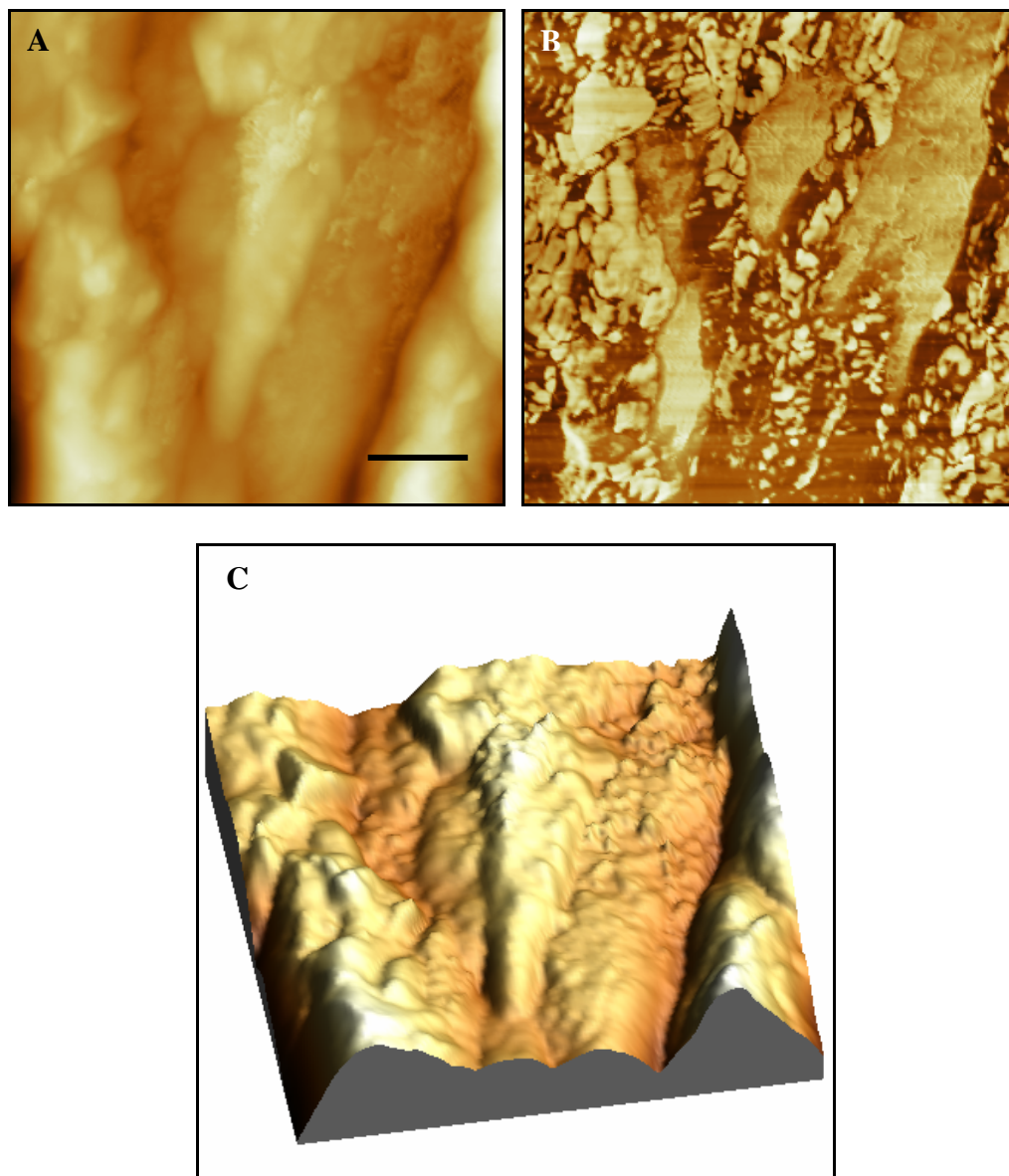
**Figure 4.7** AFM topography (left) and phase (right) images displaying two types of images obtained from greige fibres utilising a hydrophilic tip. Image set (A) shows a  $4\mu\text{m} \times 4\mu\text{m}$  image with Z-range of 228.4nm, and scale bar 800nm (fibrillar features). Image set (B)  $3.18\mu\text{m} \times 3.18\mu\text{m}$  image with Z-range of 210.8nm, and scale bar 630nm (globular features).

Figure 4.8 (A) shows the topography image from Figure 4.9, image set A, and (C) displays the line profile across the observed fibrillar structure. From this we are able to gather quantitative nanoscale measurements of the widths of individual fibrils. Some of the fibrils appear to be a few tens of nanometres across (at FWHM and highlighted by blue lines), which comply well with the figure already reported in literature, but others appear to be in the region of 150-200nm (also highlighted by blue lines). Such features may be bundles of fibrils or may be more likely due to the overlaying cuticle layer increasing the surface width of the fibrils, particularly as figures quoted in literature were of cellulose from mercerised cotton fibres.

Figure 4.9 shows topography and phase images of a greige fibre imaged in air using TM with a modified, hydrophobic tip. In contrast to the data obtained with a hydrophilic tip, the phase image shows great contrast and detail, which is not mirrored in the topography image. The hydrophobic tip has increased adhesion with the sample surface, as the cuticle layer on the greige fibres is hydrophobic in nature. Consequently acquiring a-p-d curves measurement also became difficult, due to the very strong interactions between probe and sample surface.



**Figure 4.8** AFM topography image (A), with 3D rendering (B) of greige fibre sample, and line profile of fibrillar structure (C); the profile displays fibrillar width at tens of nanometres to a few hundreds of nanometres (highlighted by blue lines). Fibrillar measurements were taken of single fibres as opposed to thick bundles of fibres in relation to the phase image.



**Figure 4.9** A  $3\mu\text{m} \times 3\mu\text{m}$  image of greige fibre, topography (A), phase (B), and 3D rendering of topography (C) imaged using TM in air with a hydrophobic cantilever tip, Z-range 239.9nm and scale bar 600nm.

Images displayed in Figure 4.10 show greige fibres that were imaged in a liquid environment (water), using TM with a hydrophilic tip. These images lack the visual clarity (fine topographical detail) when compared with images obtained in air environments, but they demonstrate that imaging in liquid environments is possible with such *non-ideal*, sample surfaces in terms of AFM substrate.

Within liquid environments cellulose fibres swell, this can increase the diameter of the fibres by up to 20%<sup>277</sup> and elongate the fibre by up to 13% its original (dry fibre) length<sup>278</sup> in mercerised fibres. With greige fibres we would expect to see minimum swelling due to the impermeable waxy cuticle layer. Using the line profile, we can obtain a width measurement of the fibrils and see that in this case the fibres were swollen by almost 100% (to about 500nm), compared with measurements from Figure 4.7. This may be explained by the sample preparation, as for the purposes of this particular experiment the entire sample stub was submerged in a liquid environment, so that the scissor-cut fibre sections could still swell from end to end. However, this measurement is not entirely accurate as it was not achieved using the same cantilever tip that was used to obtain images in Figure 4.7; also the images in Figure 4.10 were produced at a slower oscillation frequency to Figure 4.7, due to the liquid environment in which the images were obtained.

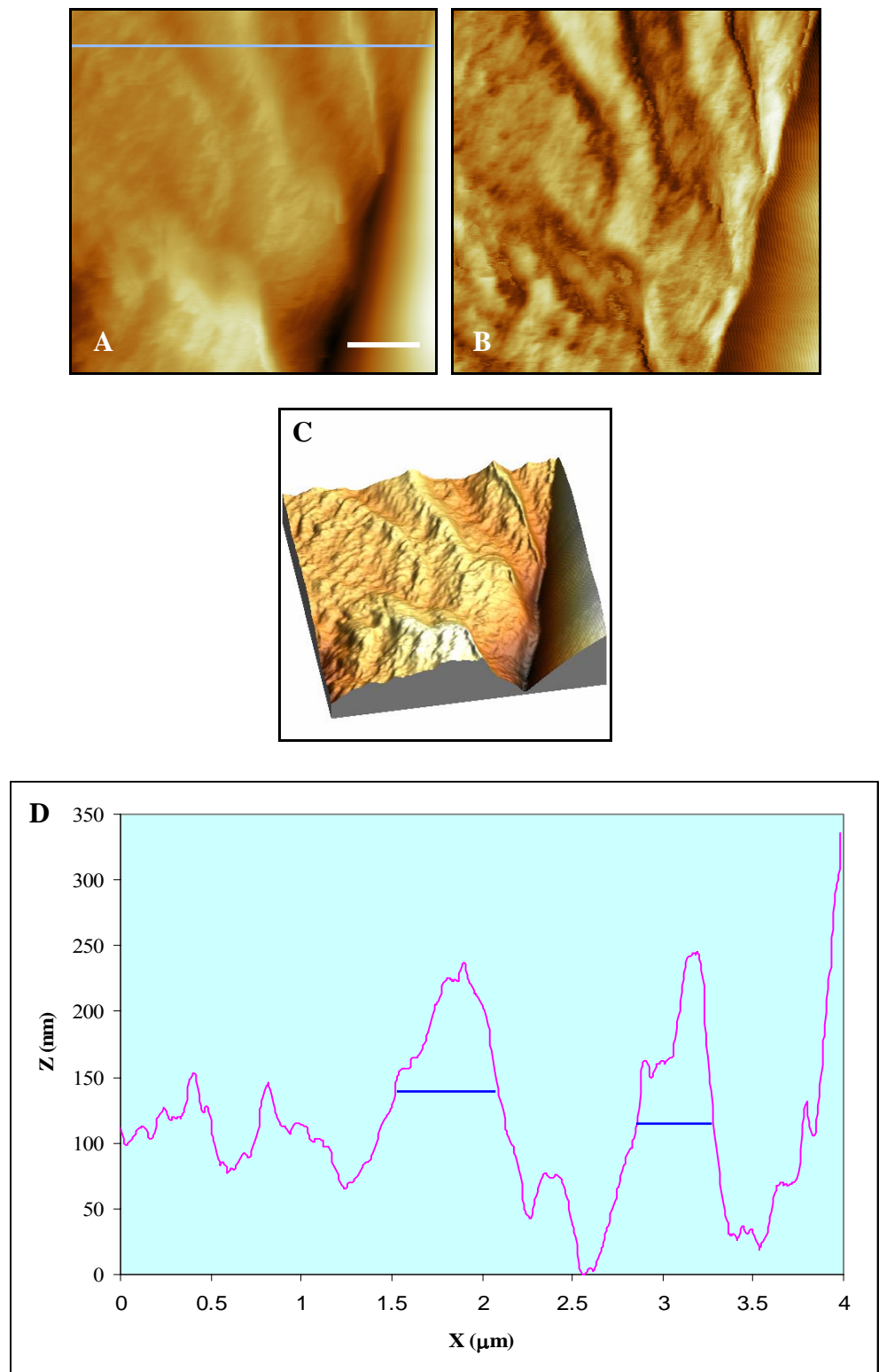


**Figure 4.10** AFM images of greige cotton fibre imaged in liquid environment; (A)  $4\mu\text{m} \times 4\mu\text{m}$  topography image with Z-range  $1.52\mu\text{m}$  and scale bar  $800\text{nm}$ . (B) phase contrast, (C) 3D rendering of topography and (D) line profile of fibrils observed in topography image, with fibrillar width (blue lines) at 100% compared line profile in Figure 4.8.

Greige fibres were therefore imaged in air and liquid environment using primarily TM, as this mode produced the most high resolution images of the fibres. Within the study we were able to successfully reproduce the AFM images under the various conditions. All AFM images displayed the typical fibre features, either fibrils or globular features (or both), within the topography. Phase image data showed enhanced contrast and detail using a modified hydrophobic tip. This may have been due to increased probe-sample interaction owing to the hydrophobic nature of the fibre cuticle layer. A-p-d curves measurement enabled distinct regions (globular plate features and large featureless homogenous areas) to be fingerprinted due to the different profiles produced from each area. Line profile measurements showed widths that were larger than figures cited within literature; however literature figures were for mercerised cotton fibres. The study also showed that imaging of greige fibres within liquid environments was possible, despite that difficult nature of the sample with respect to ideal (flat surface) AFM substrate.

#### **4.3.2 Surface characterisation of undyed cotton fibres**

The next focus within this study was the imaging of mercerised undyed fibres using the same techniques that were employed in analysing greige fibres. The subsequent results were therefore also compared with the information achieved for greige cotton fibres.

##### *4.3.2.1 SEM analysis*

Figure 4.11 shows a SEM image of undyed fibres at 500x magnification, gained through the use of a Philips 505 SEM (Philips Electron Optics,

Eindhoven, Netherlands, refer to section 2.4.3). Unlike the samples investigated by ESEM, this analysis required the samples to be gold coated prior to imaging. When compared to the ESEM image within Figure 4.2, Figure 4.11 illustrates the undyed cotton fibre surface appearance as much smoother than the greige fibres, with less twists and convolutions along the fibre length. This may in part, be due to the mercerisation of the cotton fibres which produces a more stable crystalline structure within the fibres as well as improving its lustre, but may also be due to gold-coating of samples.

Using the same sample area in Figure 4.11, and imaged at a higher magnification (5000x magnification), the image within Figure 4.12, highlights in great detail the fibrillar structure of the cotton cellulose fibre. It displays tightly packed and ordered microfibrils, which could not be clearly seen in the ESEM images of greige fibres, most likely reflecting the removal of the cuticle layer.

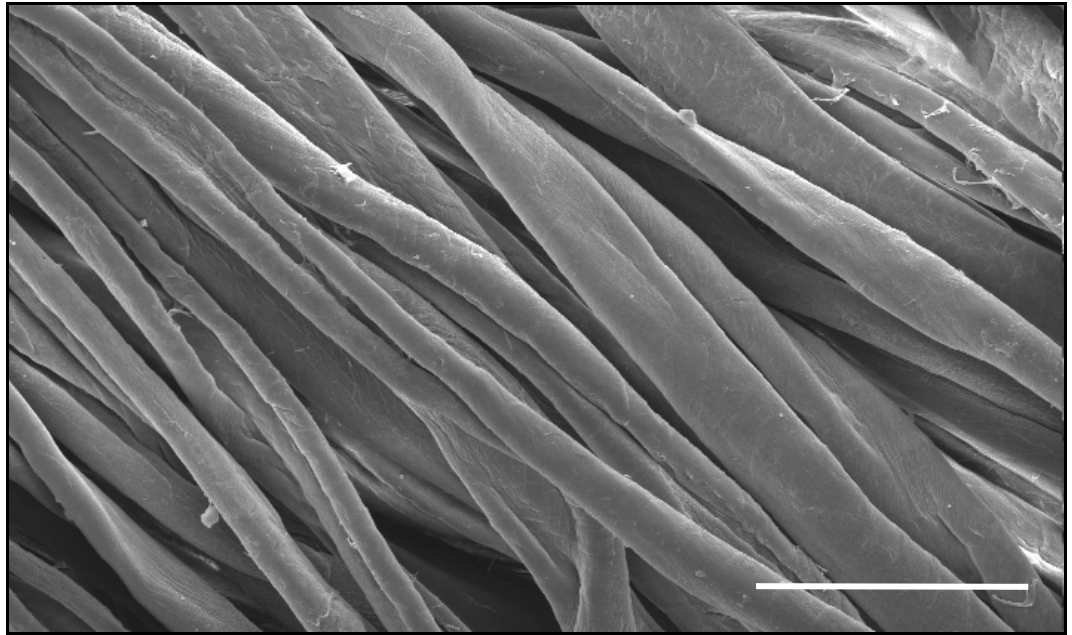


**Figure 4.11** A typical SEM image of undyed fibres at 500x magnification with spot size 3 $\mu$ m and scale bar 50 $\mu$ m.

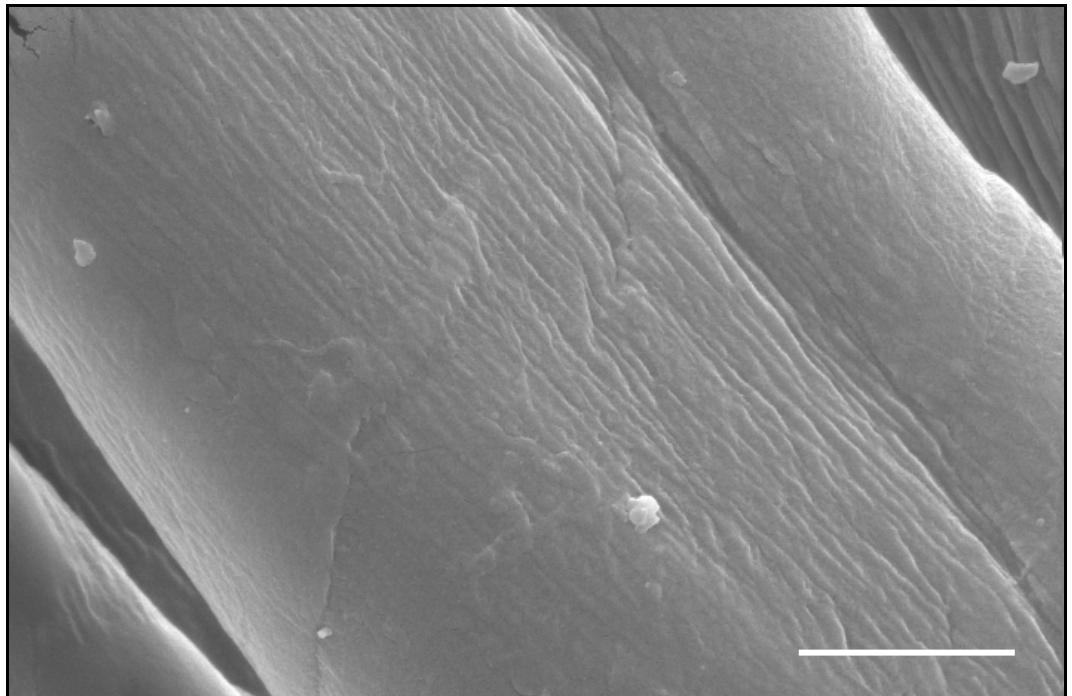


**Figure 4.12** A SEM image of undyed fibres displaying fibrillar structure at 5000x magnification with a spot size of 3 $\mu$ m and scale bar 5 $\mu$ m.

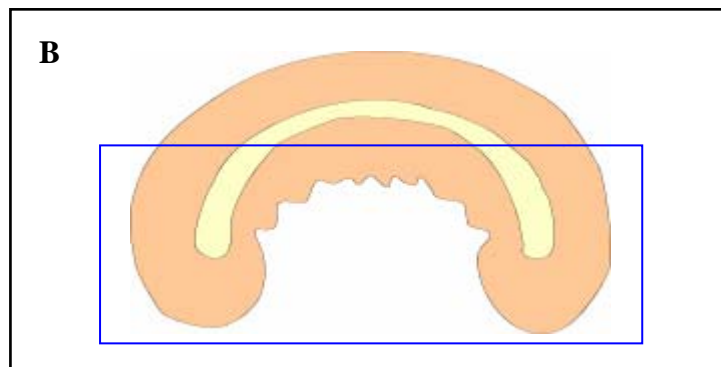
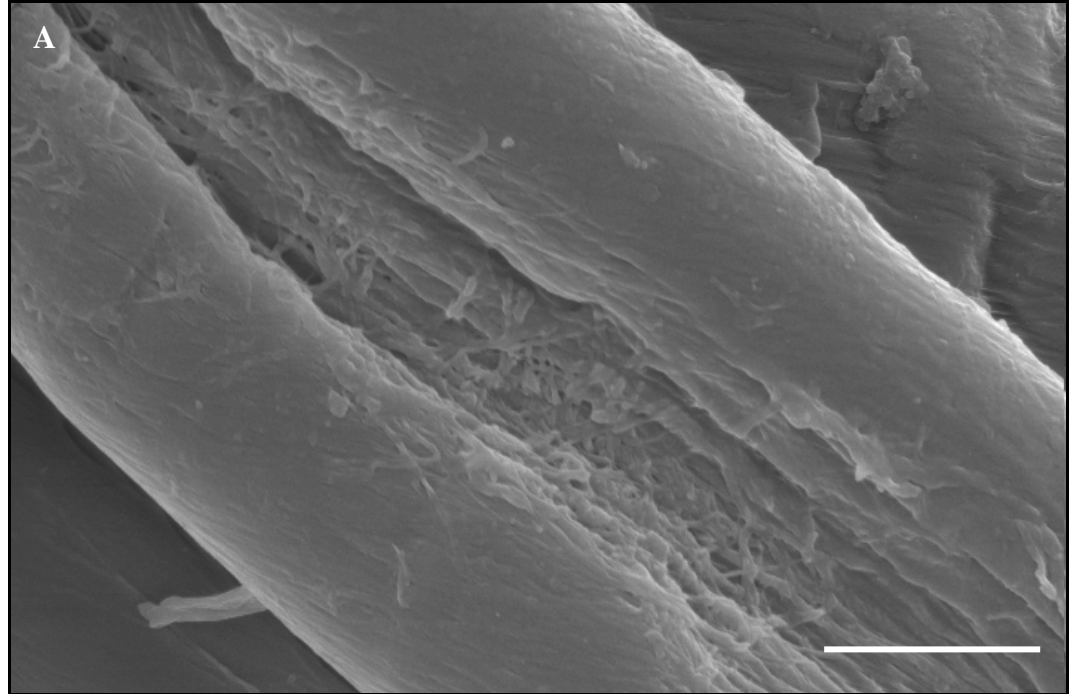


**Figure 4.13** (A) SEM image of undyed fibre at 5000x magnification, with spot size at  $3\mu\text{m}$  and scale bar  $5\mu\text{m}$ . This image (B) highlights the bilateral structure of cotton fibres; the blue box shows a likely representation of the imaging area.

Figure 4.13 shows a cotton fibre surface that appears to conform to the bilateral structure (see Figure 1.10, section 1.3.2.1) which has been highlighted in literature, as the middle section of the fibre appears less well-ordered as compared to the smoother, more ordered fibre outer edges (see images (A) and (B) for comparison).

It should be noted however, that as these images were obtained using gold coated samples, it was also deemed necessary to image the samples in their natural state to make comparisons with the greige fibres which were gained using ESEM. Therefore the image in Figure 4.14 shows an ESEM image and EDAX profile of undyed fibres, without the gold conductive layer. Several EDAX spectra were taken of the undyed fibre samples which displayed only C and O elements, confirming that most non-cellulosic components had been removed during mercerisation.

The presented SEM images of the undyed fibres exhibited a general morphology and fibrillar structure consistent with that reported in literature; the tightly ordered fibrillar packing density was visible across the fibre, as highlighted in Figure 4.13. A comparison of the EDAX spectral information of the greige fibre samples, which contained C, O and traces of K and Ca, against the EDAX spectra of the undyed fibres displayed only the pure elemental components found in cellulose.

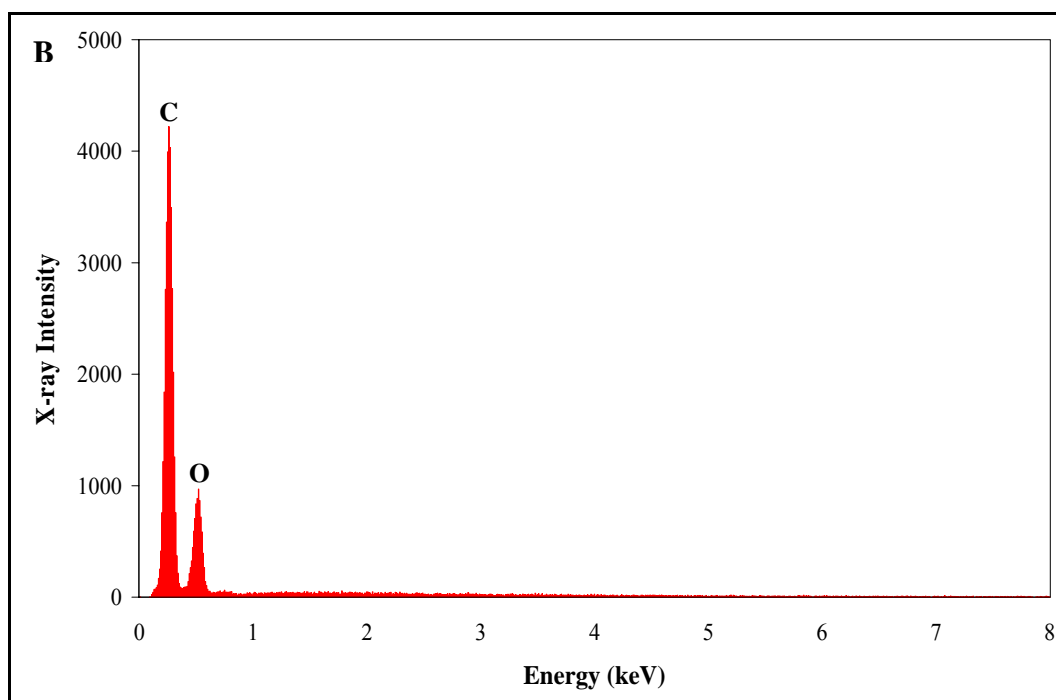
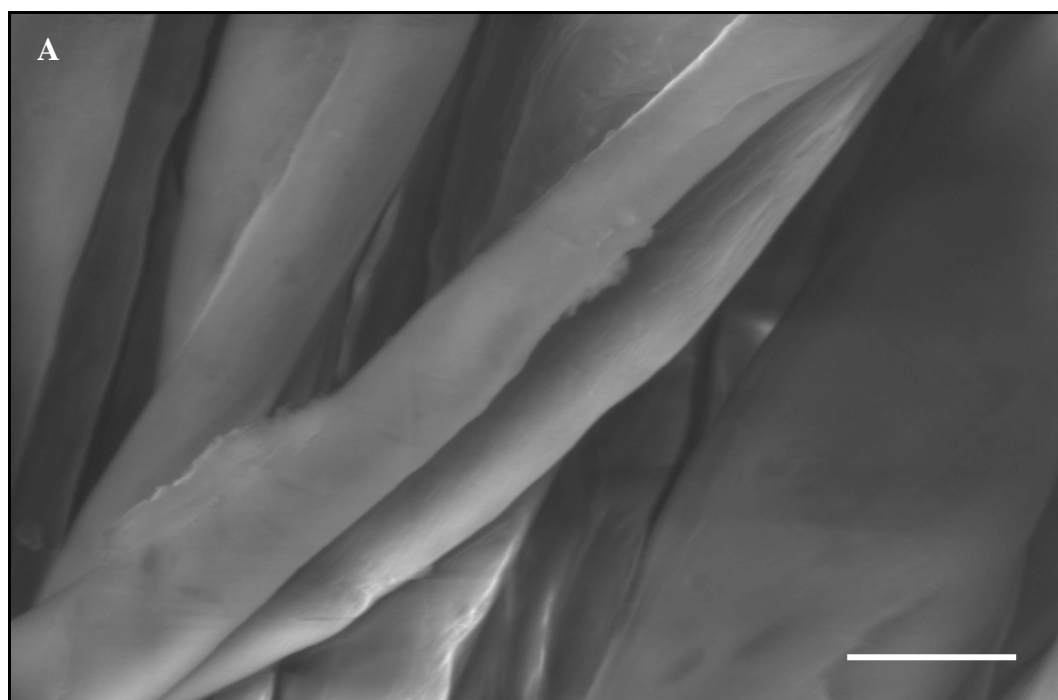


**Figure 4.14** (A) ESEM image of undyed fibre at 2000x magnification with spot size of 4 $\mu$ m and scale bar 10 $\mu$ m, (B) EDAX spectra displays the presence of C and O elements, due to the structure of cellulose.

#### 4.3.2.2 AFM analysis

The AFM images of undyed cotton fibres were imaged using an Explorer AFM (Veeco, refer to section 2.1.4) and DI 3000 using both contact mode (see section 2.1.2.1) and TM under ambient conditions.

The AFM images displayed in Figure 4.15 demonstrate a surface morphology that is disordered (A), however it also shows evidence of step edges or fibrillar striations which follow a particular line of direction. Figure 4.16 displays two sets of AFM images obtained using DI3000 AFM. Both  $2\mu\text{m} \times 2\mu\text{m}$  image sets show the two types of cotton fibre surface features typically observed, (as first detailed in the greige fibre samples); (i) uneven disordered (globular) surface and (ii) fibrillar features. Unlike the greige fibres however, the phase images in both sets show no contrast within the data obtained, signifying a homogenous surface chemistry and/or material property.

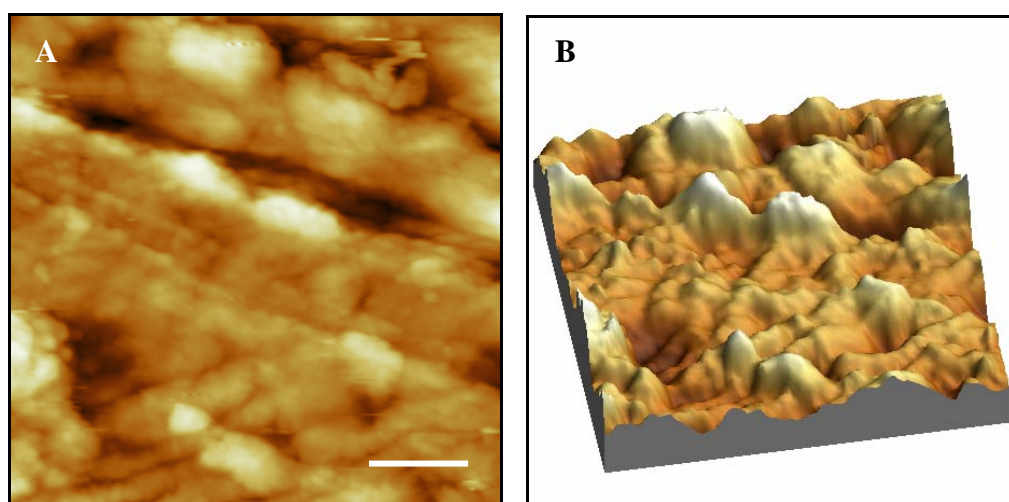


**Figure 4.15** A  $5\mu\text{m} \times 5\mu\text{m}$  Explorer AFM image of an undyed fibre obtained using an unmodified tip in contact mode. Image (A) displays topography and (B) displays 3D rendering of topography, (with Z-range 518.6nm, and scale bar  $1\mu\text{m}$ ).

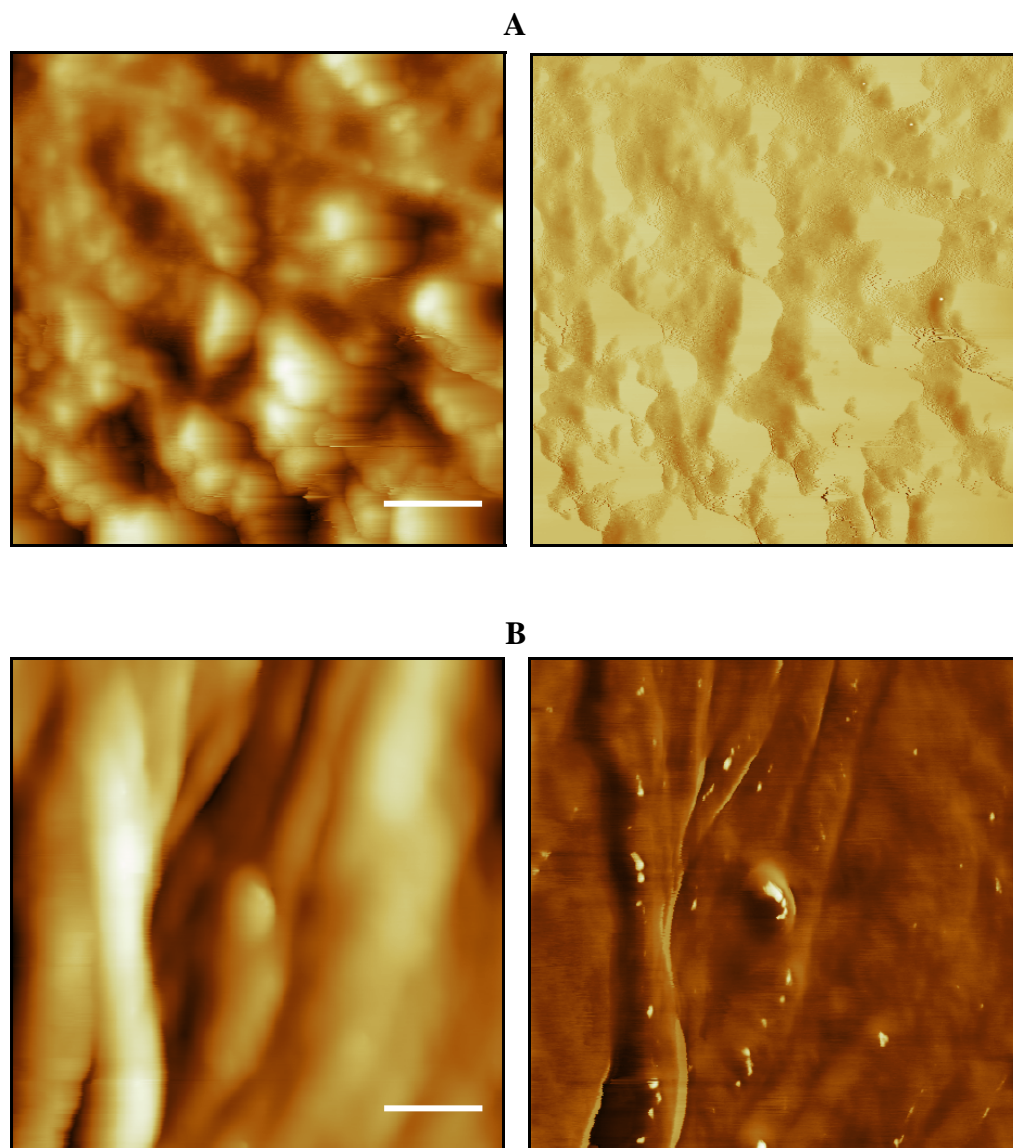


**Figure 4.16** Image set (A) displays  $2\mu\text{m} \times 2\mu\text{m}$  AFM images of an undyed fibre surface showing topography (left) and phase (right), with Z-range 141.6nm and scale bar 400nm. Image set (B) shows another  $2\mu\text{m} \times 2\mu\text{m}$  image of undyed fibre surface displaying topography and phase images, with Z-range 459.7nm. Both data sets obtained using unmodified tip in TM in air.

To further investigate the chemical/physical nature of the undyed cotton, the fibres were also subjected to imaging using chemically modified tips. Figure 4.17 shows undyed cotton fibres imaged using a hydrophilic tip on the DI 3000 AFM. The topography image (A) displays very tight fibrillar packing but once more there is a lack of contrast within the phase image, further supporting the argument that the undyed cotton fibre surface possesses a homogeneous surface chemistry. After mercerisation the fibre is nearly entirely cellulose based, due to the removal of the cuticle layer and other non-cellulosic material and hence the surface would be homogenous. In Figure 4.18, a line profile measurement of the topography image from Figure 4.17 is also displayed. The fibrils within the image appear to be a tens of nanometres across (at FWHM, highlighted by the blue lines within the graph (B)), which again conform well to figures cited in the literature<sup>279</sup> (see section 1.2.1). The larger widths within the line profile are most likely bundles of fibrils together.

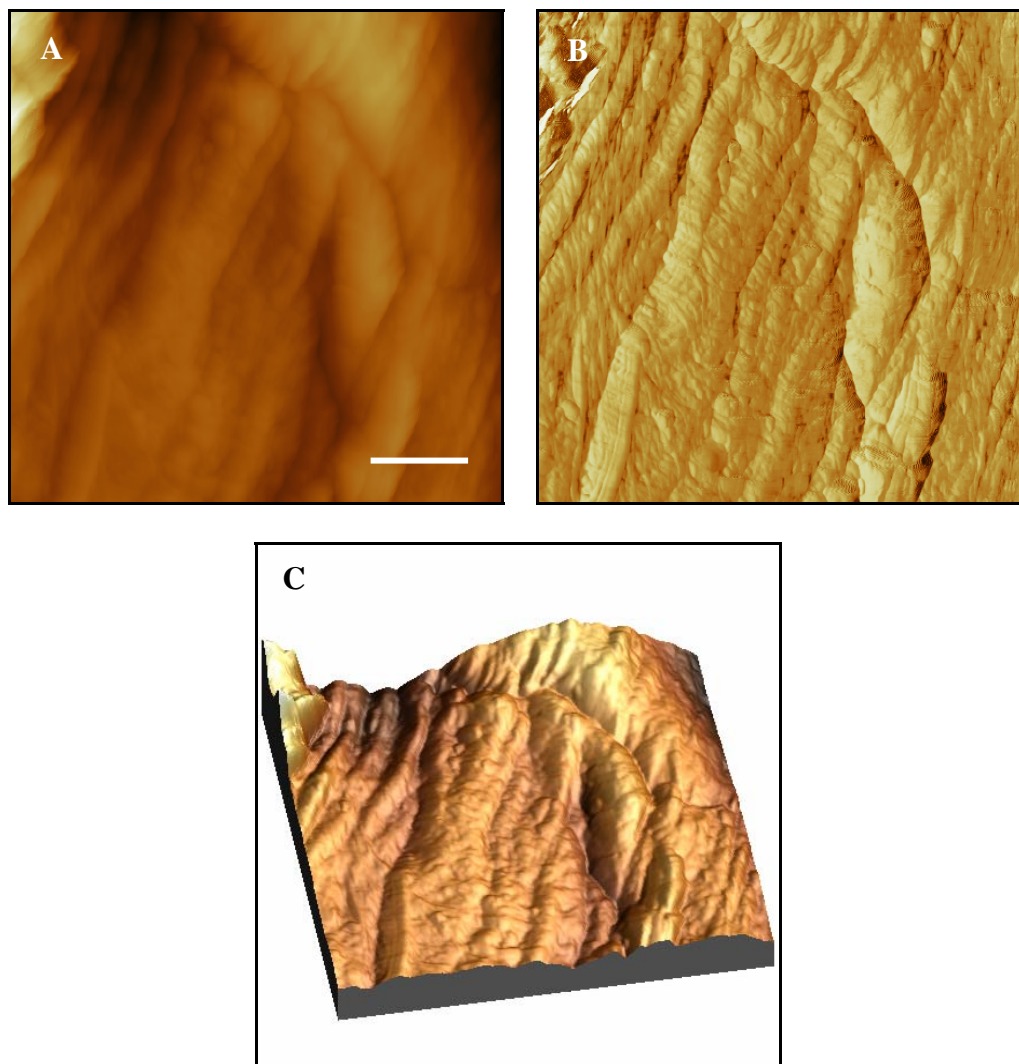


**Figure 4.17** A  $5.5\mu\text{m} \times 5.5\mu\text{m}$  image of undyed cotton fibres imaged using a modified hydrophilic tip: (A) topography, (B) phase and (C) 3D rendered topography, with Z-scale  $1.4\mu\text{m}$  and scale bar  $1.1\mu\text{m}$ .

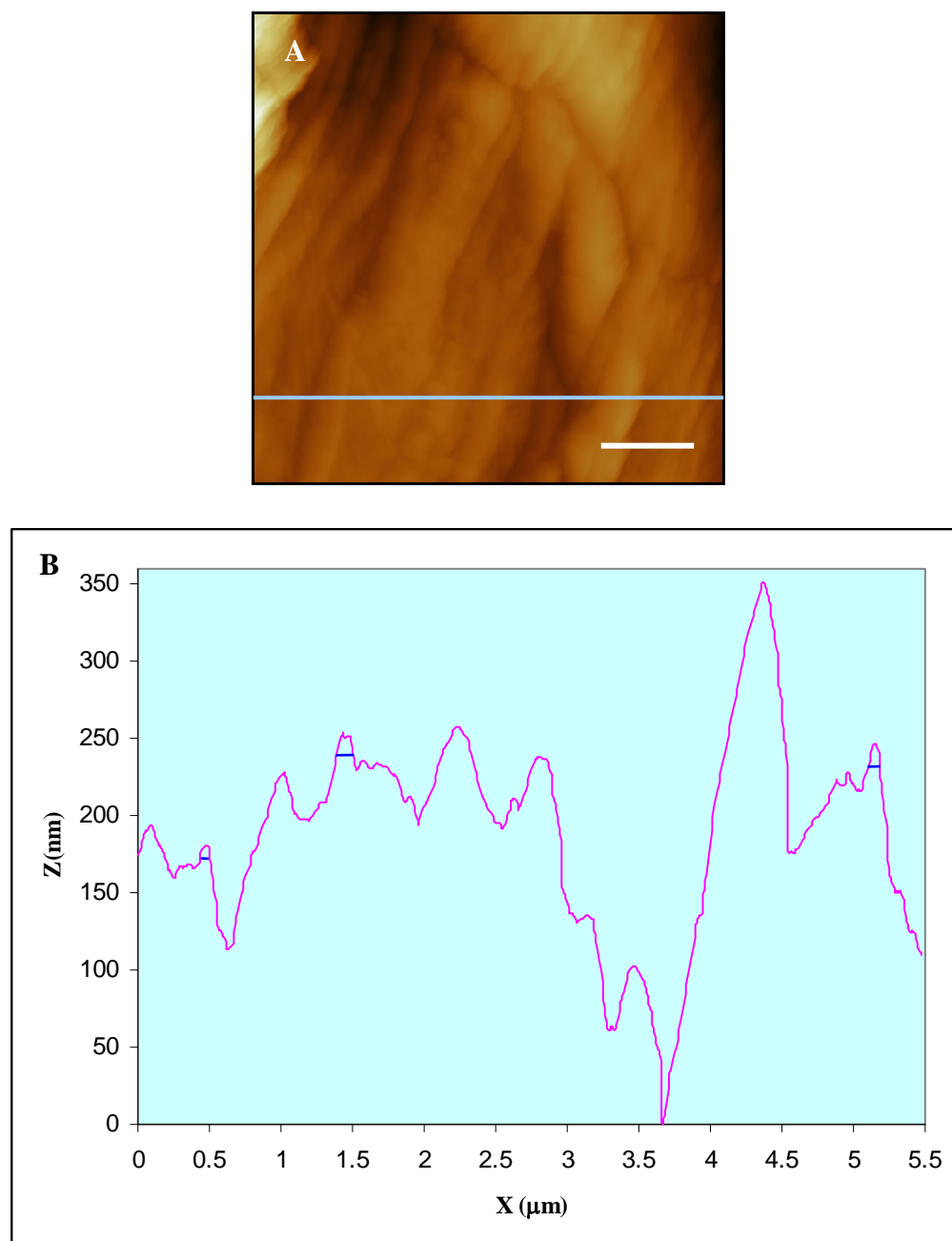


**Figure 4.18** Line profile of fibrillar pattern observed in topography (A) image of Figure 4.17. Fibrils appear to be a few tens of nanometres across (highlighted by blue lines). Fibrillar measurements were taken of single fibres from within the phase image, as opposed to thick bundles of fibres.

Figure 4.19 displays a  $5\mu\text{m} \times 5\mu\text{m}$  DI 3000 AFM image of undyed cotton fibres achieved using a modified hydrophobic tip. Again within the topography image (A) fibrillar striations can be seen in addition to some irregular features. However, the phase image in (B) now displays contrast. To further investigate the nature of the observed contrast, a-p-d curves measurements were obtained from the phase image, shown in Figure 4.20. Curves (A) and (B) display a strong repulsive profile within the light regions of the phase image highlighted by point 1. Curves (C) and (D) display what appears to be an attractive profile occurring within the dark regions of the phase image (point 2), however is difficult to judge this as the curve goes off-scale. The a-p-d curve data may reflect the crystallinity of the undyed cellulose fibres. As mentioned previously, phase imaging is sensitive to adhesive forces (as well as material properties) which exist between probe and sample, which arise from the water layer on the sample surface. It could be hypothesised, that regions of crystallinity within the undyed cellulose fibre, would present more –OH (from the cellulose molecule) at the surface and hence possess a hydrophilic nature. Than amorphous regions, which would present less –OH at the surface, resulting in a less hydrophilic (or hydrophobic) nature. Therefore the light regions from the phase image (displayed a strong repulsive profile) may be assigned to areas of increased crystallinity (hydrophilic nature) within the fibre surface, due to the interaction with the hydrophobic tip. The dark regions from the phase image, which displayed what appeared to be an attractive profile, could be assigned to areas of decreased crystallinity or amorphous (hydrophobic) regions, due to the interaction with the modified hydrophobic tip.

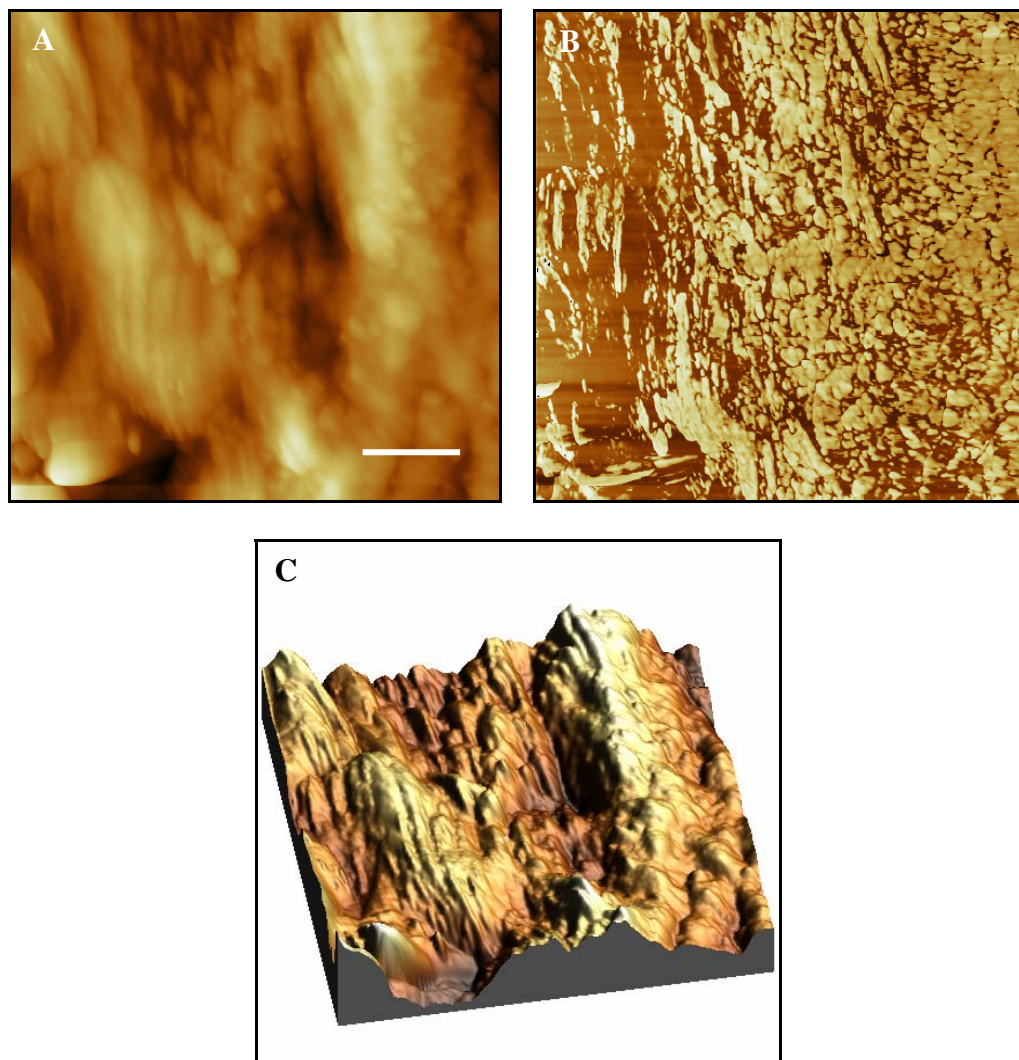


**Figure 4.19** A  $5\mu\text{m} \times 5\mu\text{m}$  image of undyed cotton fibres imaged using a modified hydrophobic tip: (A) topography, (B) phase and (C) 3D rendered topography, with Z-scale  $379.7\text{nm}$  and scale bar  $1\mu\text{m}$ .

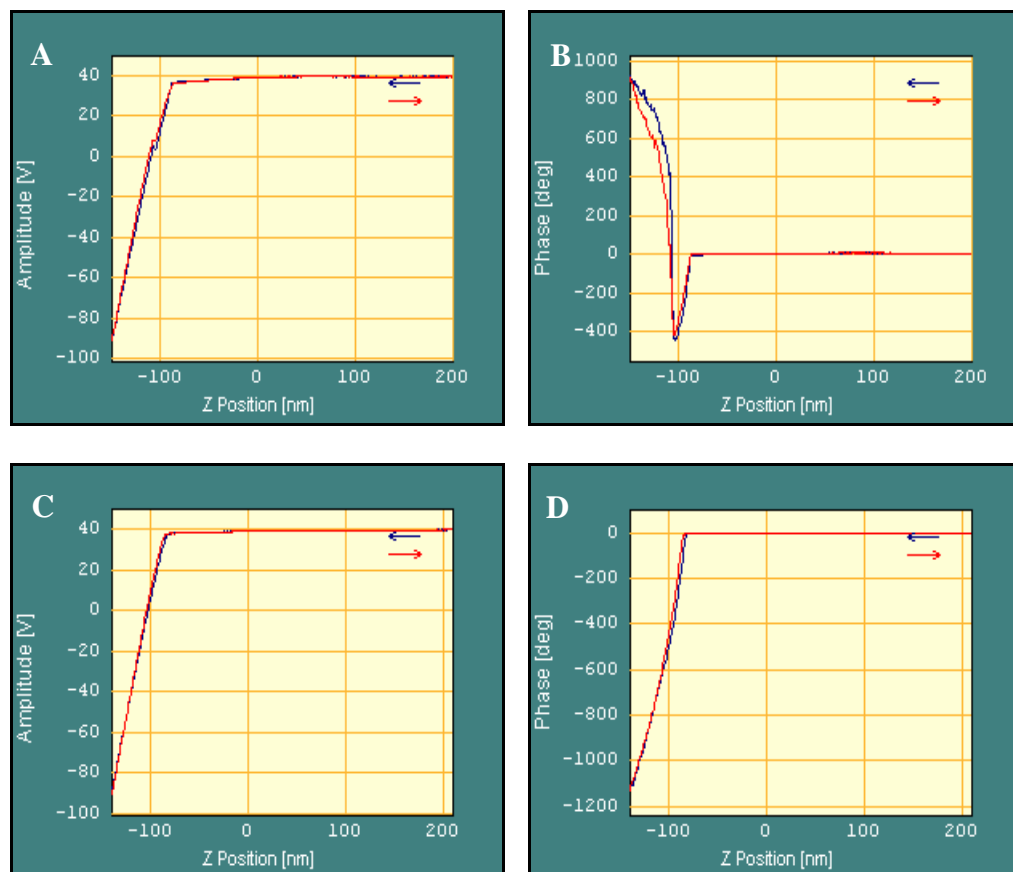
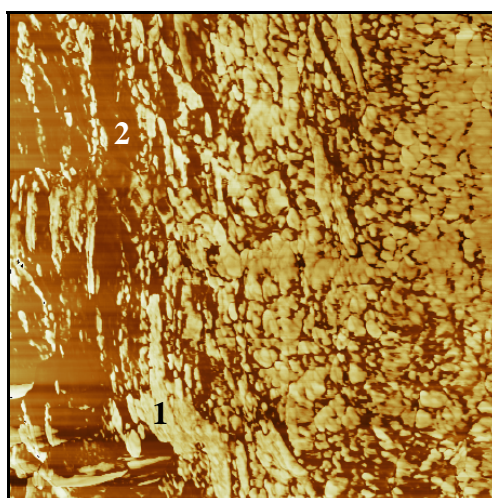


**Figure 4.20** The top image (undyed cotton fibres obtained with hydrophobic tip) is the phase data from Figure 4.19, below which are the corresponding a-p-d curves of the two areas of interest (points 1 and 2). Curves (A) and (B) correspond to point 1 within the phase image and curves (C) and (D) correspond to point 2 within the phase image. Curves (A) and (B) display a strong repulsive regime and what appears to be attractive regime on the cantilever tip within curves (C) and (D).

The results displayed within Figures 4.19 supports the *fringed micelle model* represented by Figure 1.4, section 1.2.1.1. The model described crystalline micelles within an amorphous matrix, which may describe the arrangement of crystallinity within the phase image. An alternative explanation could attribute the phase contrast to remnants of cuticle (oily) components existing on the surface of the undyed fibre in differing quantities<sup>280</sup>.

Undyed fibres were also imaged in liquid (water) environments using a modified hydrophilic tip (see Figure 4.21). Within the topography image (A) we can see a detachment of the tip from the sample surface due to an increase in the Z-range (see image (C)). Again it should be noted, that difficulties do arise from imaging in liquid environments with non-ideal samples, with respect to AFM, due to the physicality of the sample surface. However, despite the imaging environment, the now familiar uneven surface of the cotton fibre is also seen in the topography image. From this image and previous AFM data, it may be possible to assign these features to areas or regions from the bilateral structure of the cotton fibre, (areas C and N in Figure 1.10, section 1.3.2.1), due to varying degrees of fibrillar packing density. Within the phase data (B) no phase contrast is observed in the image, most likely due to the liquid (water) environment, which covers the tip and sample surface. It is known within SPM, that phase contrast is difficult to achieve in liquid environments<sup>281</sup>, as contrast occurs due to tip sensitivity/interaction with the sample surface through the water layer. Therefore by placing both the tip and sample within the same liquid environment (water), the sensitivity of the probe to sample interactions is greatly affected.

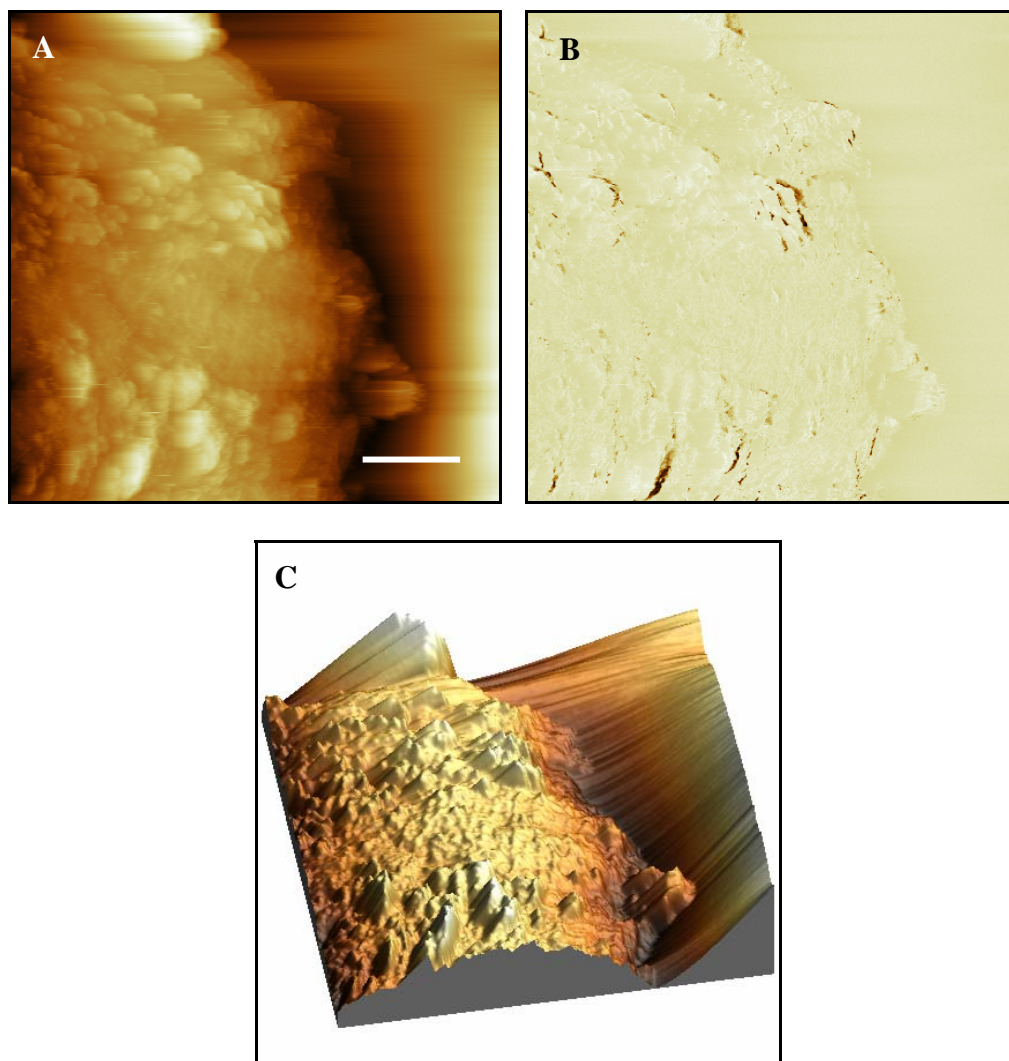


**Figure 4.21** A  $7.5\mu\text{m} \times 7.5\mu\text{m}$  image of undyed cotton fibres imaged using a modified hydrophilic tip in a liquid environment: (A) topography, (B) phase and (C) 3D rendered topography, (with Z-scale 100nm and scale bar  $1.5\mu\text{m}$ ).

The AFM data for the undyed samples has shown many similarities to the greige fibres, through the presence of typical fibre features (fibrils and globular areas), and by analysing these features it is possible to assign the AFM images to specific areas from the cotton fibre bilateral structure (due to fibrillar packing density). The fibrillar width dimensions within the undyed samples

were smaller than those observed within the greige fibres, but the measured values agreed well with figures cited within the literature. A-p-d measurements obtained using a modified hydrophobic tip highlighted the possible surface crystalline structure of the undyed fibre samples, as great contrast detail was observed within the images. This information may help to elucidate possible dye-entry/binding sites within the cellulose fibre.

#### *4.3.2.3 ToF-SIMS analysis*

Analysis of fibre samples with ToF-SIMS can provide qualitative chemical information on the surface composition of a sample material, and therefore within this study, it would allow for easy chemical comparisons to be made between undyed and dyed cotton fibres. ToF-SIMS analysis was performed on the undyed cotton fibres samples to produce control spectra for the surface chemistry of these fibres. These spectra would be used later to compare with dyed fibre spectra, to aid discrimination of any peaks indicative of dye molecules from the surface of the dyed fibres, (see section 2.2.3 for analysis method).

Figures 4.22 and 4.23 display the positive and negative ion spectra for the undyed cotton fibres, respectively. The most important peaks, assigned to the cellulose structure are highlighted within the spectra. Such as ion peaks for small hydrocarbon fragments at  $m/z$  41, 51, 55, and 56 within the positive ion spectra (see Table 4.1) and oxygen containing fragments at  $m/z$  16, 17, 28, 32, 71, 87, 113 and 221 within the negative ion spectra (see Table 4.2), which are characteristic of cellulose.

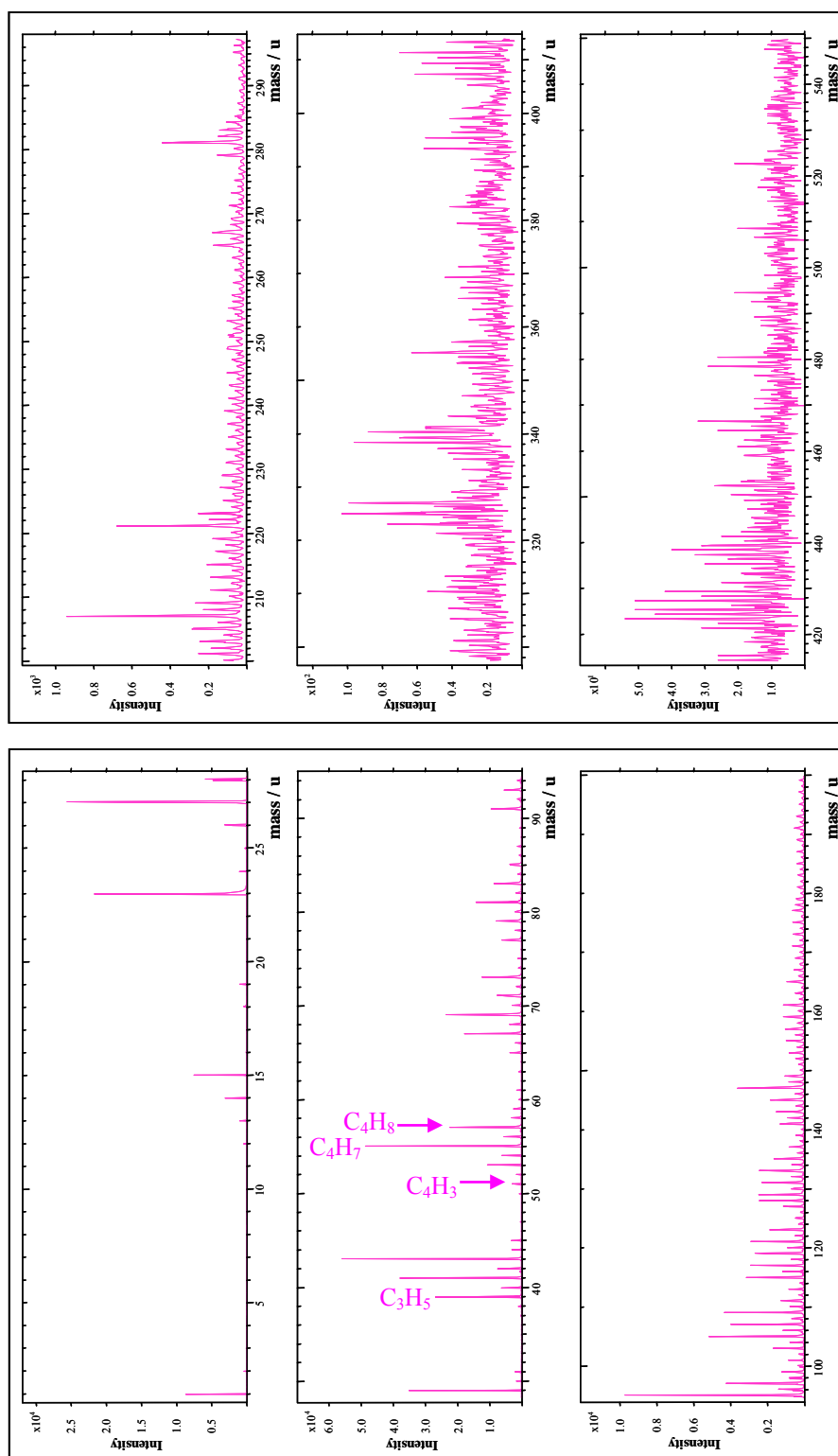


**Figure 4.22** ToF-SIMS mass spectra of positive ion fragments from undyed cotton fibre samples, using a Ga<sup>+</sup> gun, with a scan area of 100µm x 100µm, (displaying up to m/z 550).

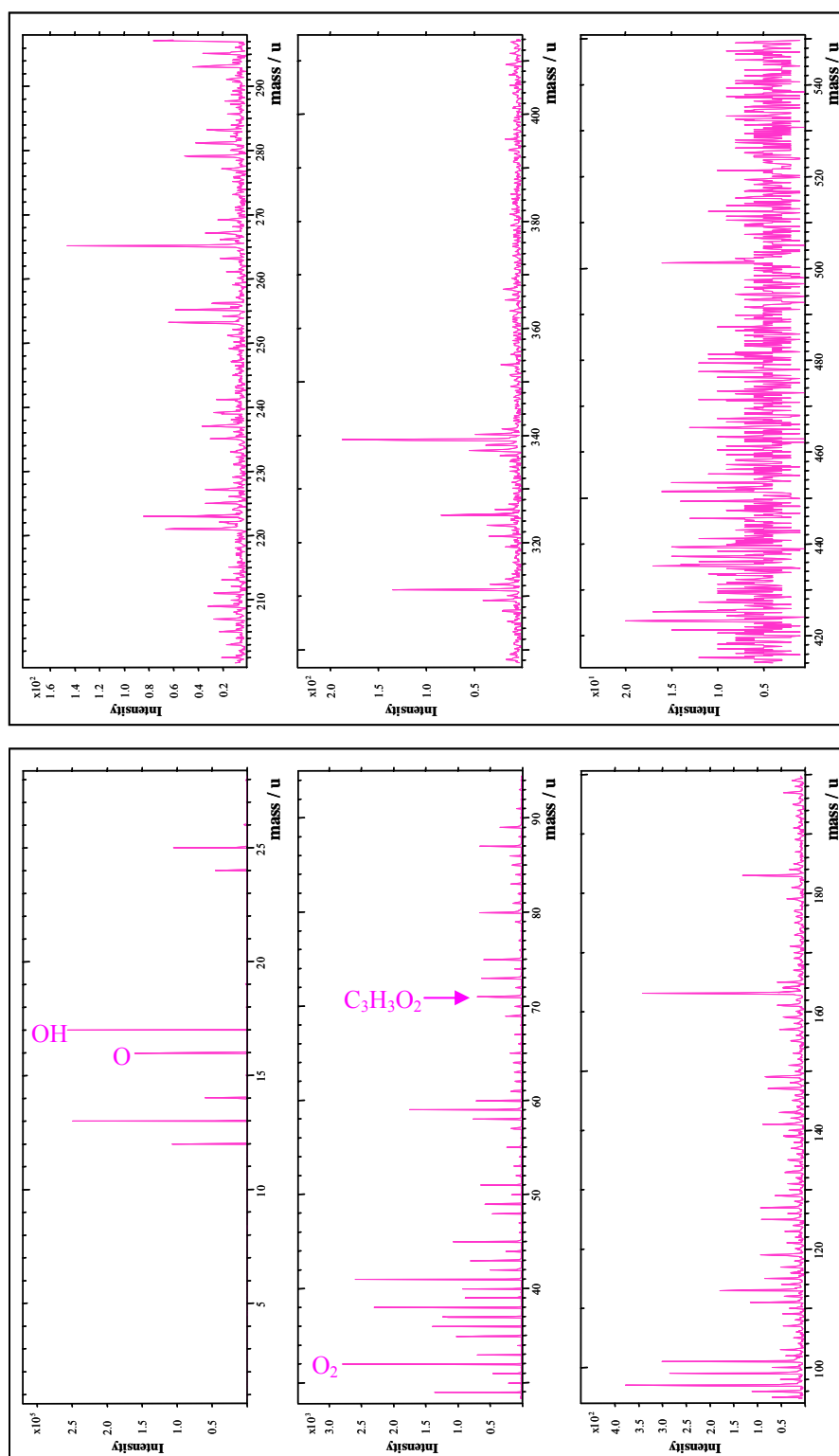


**Figure 4.23** ToF-SIMS mass spectra of negative ion fragments from undyed cotton fibre samples, using a Ga<sup>+</sup> gun, with a scan area of 100 $\mu$ m x 100 $\mu$ m, (displaying up to m/z 550).

However from this analysis it became evident that the spectra collected from the surface of undyed fibres were contaminated with siloxane, ion fragment peaks at  $m/z$  28, 29, 73 and 147 within the positive ion spectra. Siloxanes are a common contaminant detected in SIMS analysis<sup>282</sup>, and can arise from sample preparation or exposure to atmosphere contaminants. However, it was determined that the contamination of these particular samples would have occurred at the sample preparation stage, as the contamination was found to be present just at the surface of the fibre. This was determined through the use of a higher current density (beyond static limits for the sample) to etch (erode) a minimum amount of sample surface, this allowed the instrument to probe the chemistry of the material deeper into the fibre. The siloxane species were found to be superficial in nature, through its rapid disappearance under continuing primary ion bombardment by the ion beam. The siloxanes were attributed to the adhesive tape on which the extracted undyed fibre strands were mounted to during sample preparation, in order to immobilise the fibres onto the sample stub. A new sample preparation method was consequently later used, by mounting whole fabric sections directly into the sample holder clamp. However this method also had its disadvantages as it was discovered that the system took too long to pump down to a vacuum, and due to large height variations within the fabric, in turn lead to large charging effects of the sample which could not be charge compensated by the electron-flood gun.

Despite the presence of siloxane, peaks characteristic of the cellulose structure could still be observed. These are summarised and presented within Tables 4.1 (positive ion fragments) and 4.2 (negative ion fragments) and the undyed fibre

spectra would still aid in the comparison with spectra from dyed fibres samples.

m/z	Positive Ion Fragment
12	C
13	CH
14	CH <sub>2</sub>
15	CH <sub>3</sub>
23	Na
26	C <sub>2</sub> H <sub>2</sub>
28	Si
29	SiH
40	Ca
41	C <sub>3</sub> H <sub>5</sub>
42	C <sub>3</sub> H <sub>6</sub>
51	C <sub>4</sub> H <sub>3</sub>
52	C <sub>4</sub> H <sub>4</sub>
53	C <sub>4</sub> H <sub>5</sub>
54	C <sub>4</sub> H <sub>6</sub>
55	C <sub>4</sub> H <sub>7</sub>
56	C <sub>4</sub> H <sub>8</sub>
73	(CH <sub>3</sub> ) <sub>3</sub> Si
147	(CH <sub>3</sub> ) <sub>3</sub> SiOSi(CH <sub>3</sub> ) <sub>2</sub>

**Table 4.1** Characteristic positive ion peaks selected for the analysis of undyed cotton cellulose fibres.

m/z	Negative Ion Fragment
16	O
17	OH
18	<sup>18</sup> O
24	C <sub>2</sub>
25	C <sub>2</sub> H
28	CO
31	CH <sub>3</sub> O
32	O <sub>2</sub>
36	C <sub>3</sub>
71	CH <sub>2</sub> =CHCOO
87	HOCH=CHCOO
113	C <sub>5</sub> H <sub>4</sub> O <sub>3</sub>
221	C <sub>8</sub> H <sub>13</sub> O <sub>7</sub>

**Table 4.2** Characteristic negative ion peaks selected for the analysis of undyed cotton cellulose fibres.

ToF-SIMS analysis of the undyed fibres characterised cellulose ion fragments from the surface of the sample. Siloxane contaminants were observed within the spectra, but these were attributed to the adhesive tape that the undyed fibres were immobilised onto for analysis.

### **4.3.3 Surface characterisation of dyed cotton fibres**

Further analysis within this study was carried on examining the morphology and characteristics of dyed fibres in comparison to determine any physical differences to undyed cotton fibres.

#### *4.3.3.1 SEM analysis*

Figure 4.24 displays SEM images of undyed fibres, achieved by utilising the Philips 505 SEM and gold coating the samples, at 500x magnification using a spot size 3 $\mu$ m. The figure shows three fibre samples all dyed with different reactive dyes, referred to as fuchsia, orange and red within this thesis. The images revealed that it was difficult to see any differences, as the surface structure appeared to be the alike in all samples. This may have been due to the samples being gold coated, which could have potentially masked any differences on the sample surfaces due to dye molecules. However, the images did highlight slightly disrupted the fibre surfaces (see Figure 4.24 (A) and (B)), compared with the smooth undyed fibre surfaces (as in Figure 4.11). Through higher magnification (5000x magnification) imaging of the samples, the observed images illustrated the ultrastructure of the dyed cotton fibres more clearly, in Figure 4.25. The images displayed similar tightly ordered fibrillar packing as seen in the undyed fibre samples (Figure 4.12).

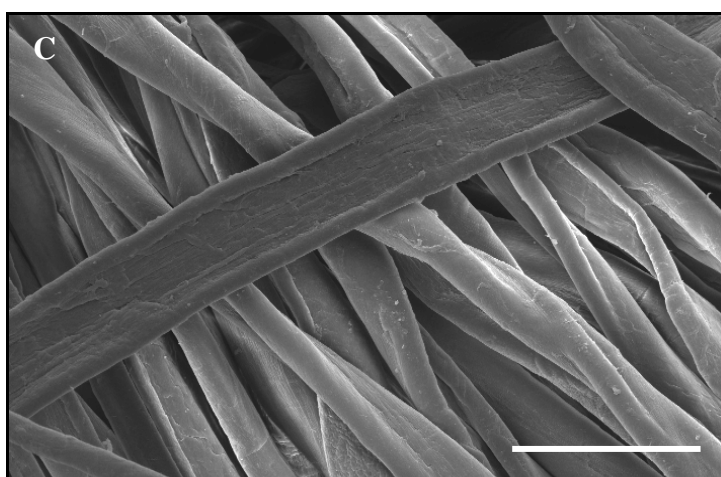
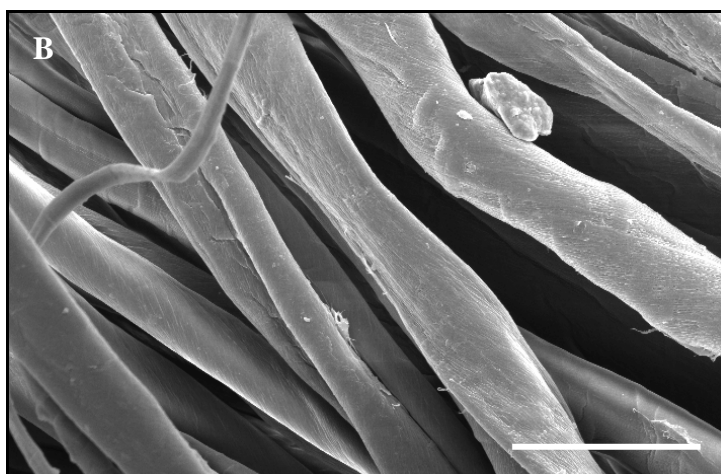
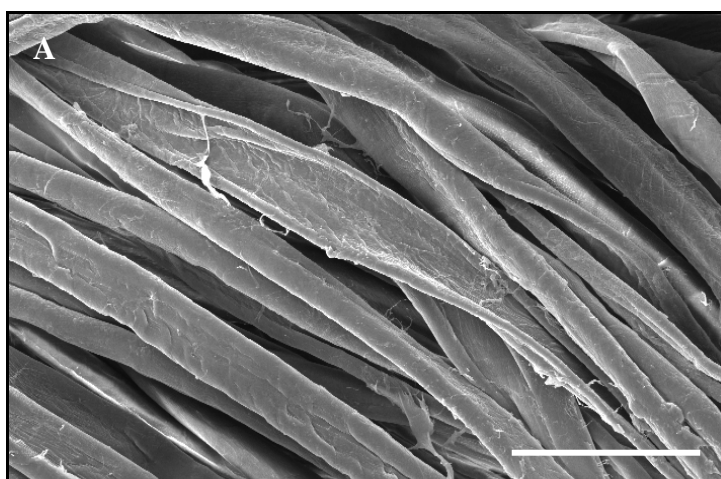


**Figure 4.24** Typical SEM images of dyed cotton fibre samples, (A) fuchsia, (B) orange and (C) red, all imaged at 500x magnification with spot size 3 $\mu$ m and scale bar 50 $\mu$ m.

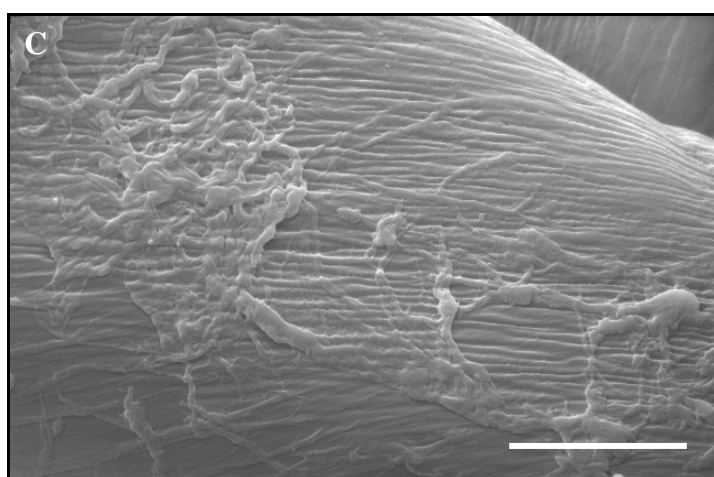
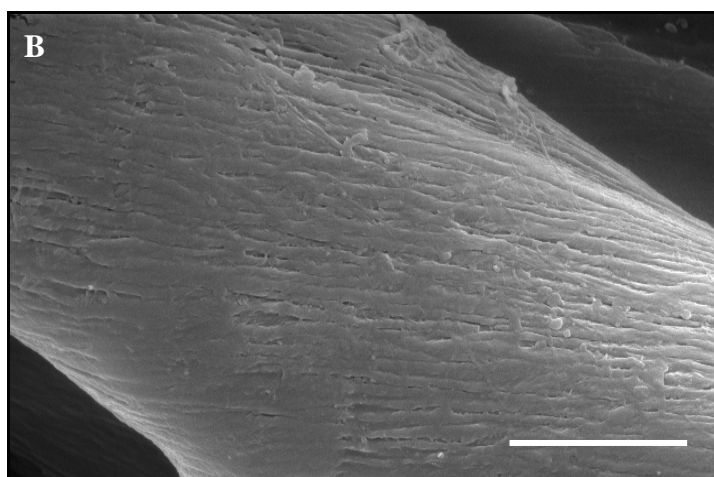
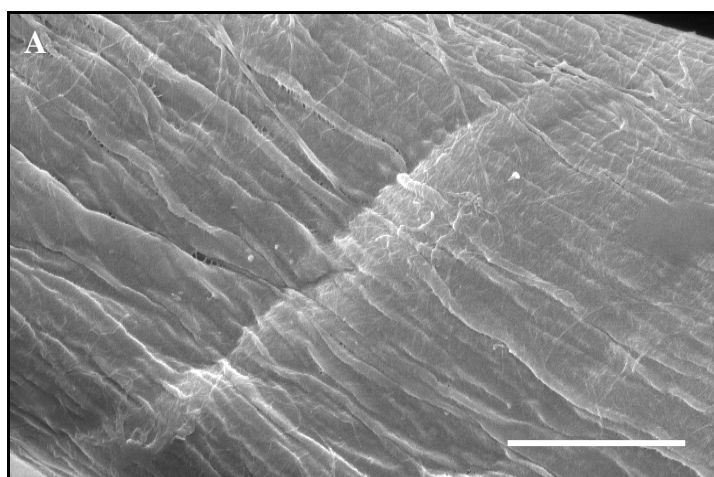


**Figure 4.25** SEM images of dyed cotton fibre samples displaying microfibrillar structure. (A) fuchsia, (B) orange and (C) red, all imaged at 5000x magnification with spot size 3 $\mu$ m and scale bar 5 $\mu$ m.

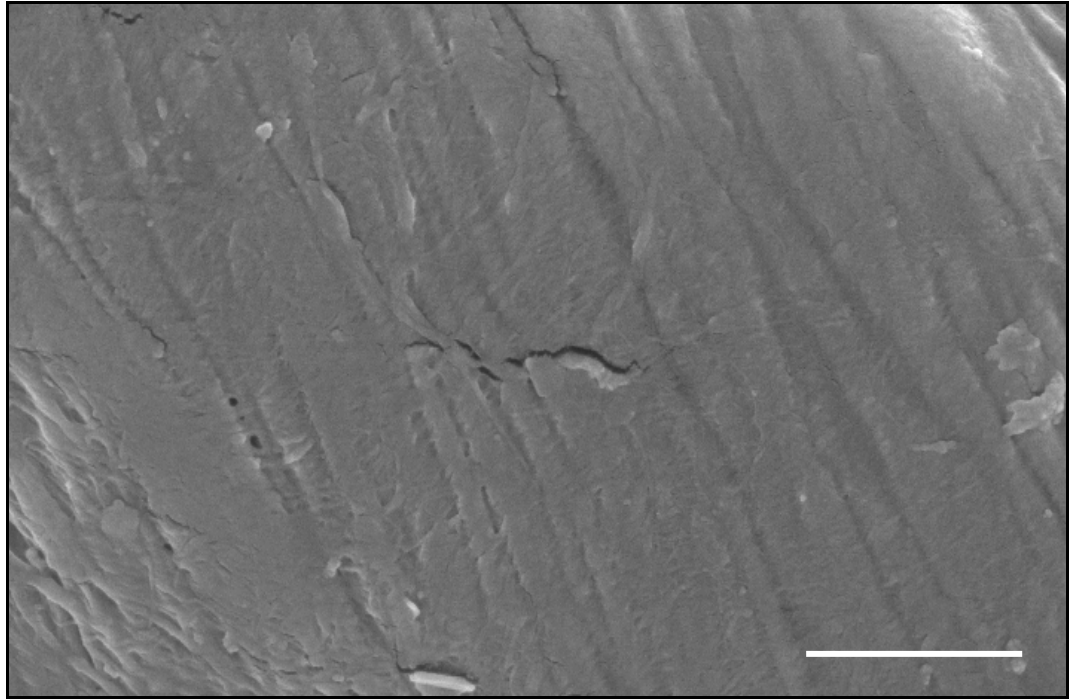


**Figure 4.26** SEM image of orange dyed fibre at 10,000x magnification with 3 $\mu$ m spot size and 2 $\mu$ m scale bar, image displays damage to surface.

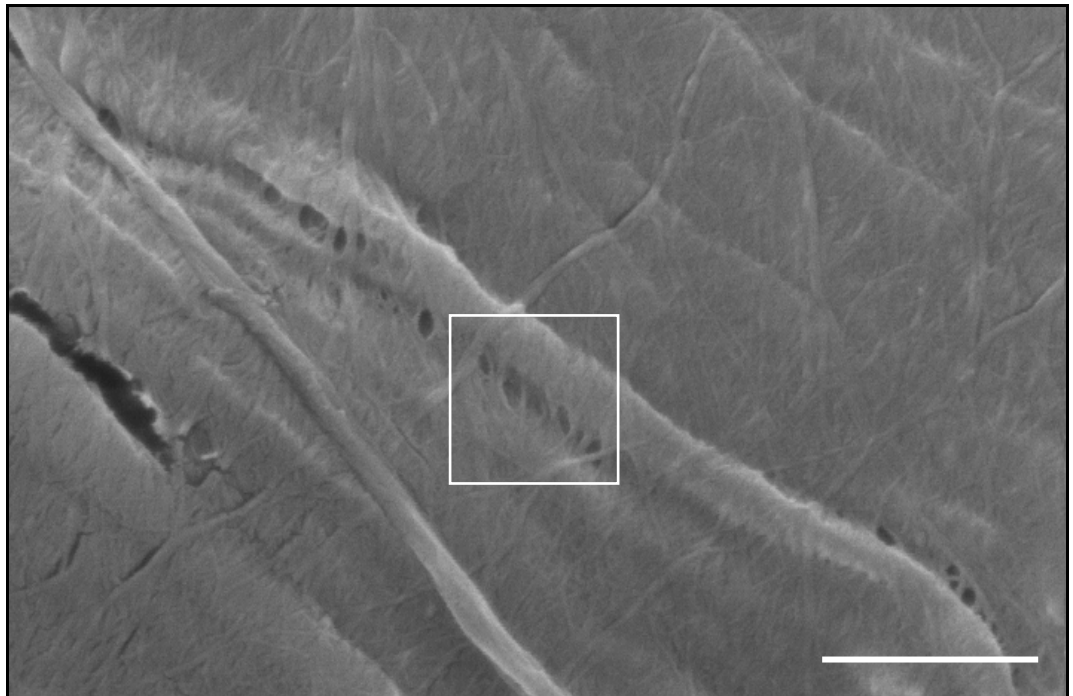


**Figure 4.27** SEM image of fuchsia dyed cotton fibres at 20,000x magnification with spot size 3 $\mu$ m and 1 $\mu$ m scale bar; image displays elementary fibrils.

Figure 4.26 exhibits an SEM image obtained at higher magnification (10,000x magnification) than Figures 4.24 or 4.25. Within the centre of image we can see a crack in the surface of the fibre most likely due to the gold-coating drying-out the sample within the SEM vacuum column. In Figure 4.27, the SEM image was obtained at 20,000x magnification, and although difficult to achieve, we can see evidence of surface features that show the presence of *elementary* fibrils (refer to section 1.2.1) within the image (highlighted by white square). These fine features have not been previously observed with the SEM in literature, due to imaging difficulties.

SEM imaging did not draw attention to any physical differences between the surfaces of dyed and undyed cotton fibres. Therefore ESEM and EDAX analysis was also carried on dyed fibres (a different set); blue 1, yellow 2 and red 3, as these samples had been dyed using reactive dyes that contained characteristic components such as metals or sulphonic acid groups which would be distinguishable in EDAX spectral analysis.

Figure 4.28 shows an ESEM image of Blue 1 dyed cotton fibres, observed at 2000x magnification with a spot size of 4 $\mu$ m. The corresponding EDAX spectra (B) displayed elemental information, and showed the presence of C and O from the cellulose structure and also trace peaks for Cu and S, which could be attributed to the dye molecule (see inset molecular structure), as they are present within the chemical structure. Traces amounts of Ca and iron (Fe) are also observed within the spectra, Ca was also previously observed in the greige fibre sample (not in undyed fibres) and was attributed to the cuticle layer.

However these samples are unmercerised fibres, suggesting that origin of the Ca and Fe may be from other than the cellulose fibre and dye compound, such as the dyeing process the sample was subjected to prior to analysis.

Figure 4.29 displays an ESEM image of Yellow 2 dyed cotton fibres, these were observed at 1000x magnification with a spot size of 4 $\mu$ m. The EDAX analysis carried out on the fibre sample showed the presence of cellulose as well dye specific peaks for S and Cl, see inset diagram in Figure 4.29 (B). Again the Na peak may be attributed to the dye molecule, as during the dyeing process, the sulphonic acid groups from the dye compound become sodiated (H replaced with Na) (due to salt with the dyebath), these groups then react with the cellulose substrate. However, the fibres are subjected to washing, which normally removes Na from the surface. The results suggest in this case that not all of Na was removed from the surface during the dyeing process.

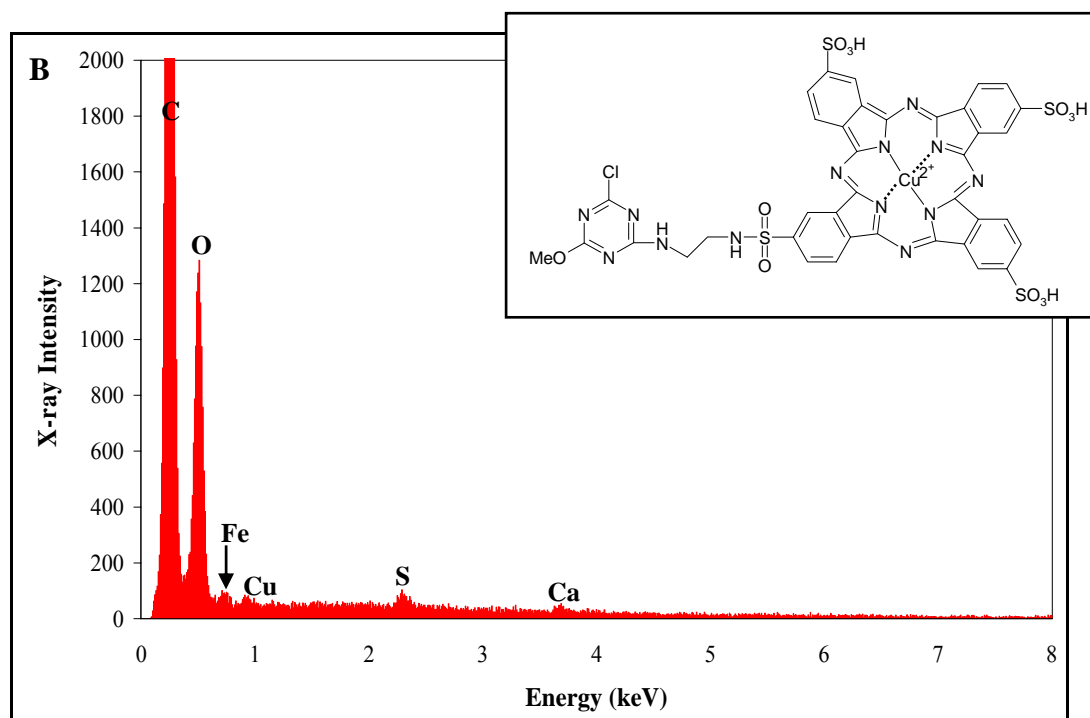
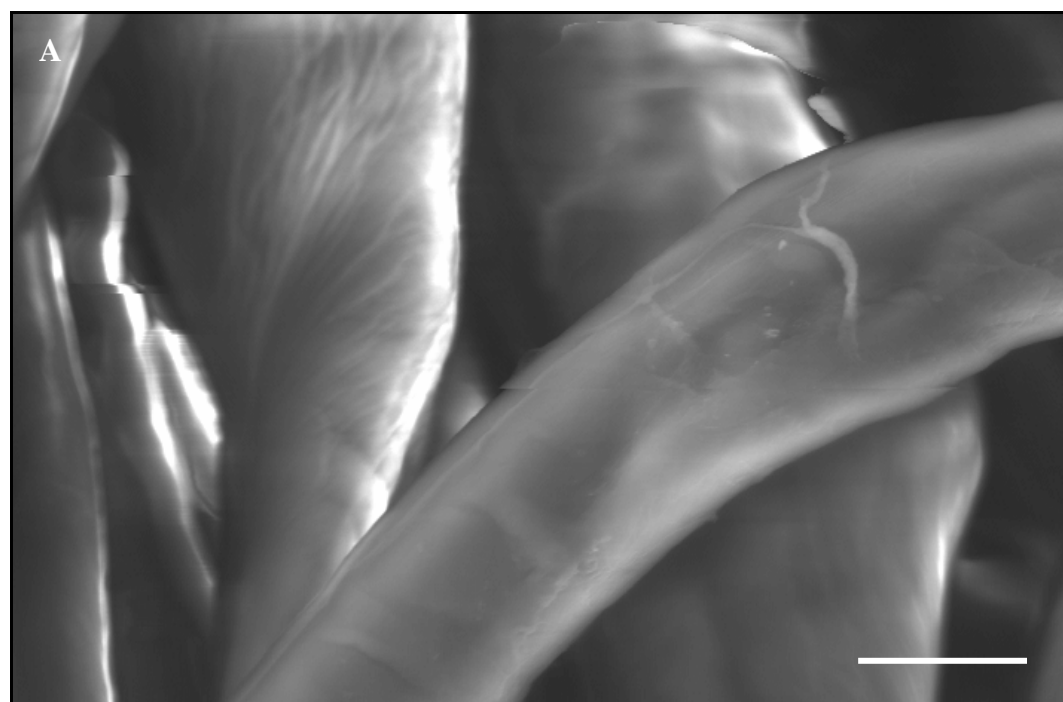


**Figure 4.28** ESEM image (A) of Blue 1 dyed cotton fibre at 2000x magnification, with spot size 4 $\mu$ m and scale bar 10 $\mu$ m. EDAX spectra (B) of the sample area show traces of C, O, Cu, S, Fe and Ca. (C peak exceeds Y scale, with peak maxima at 5277 counts (X-ray intensity)).

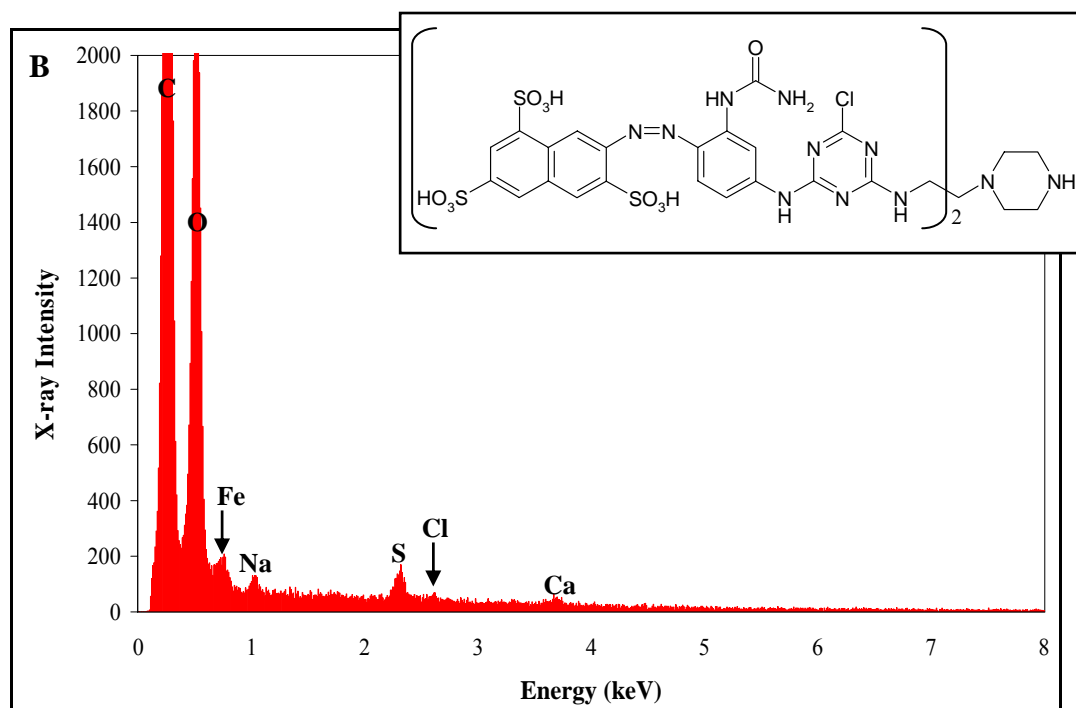
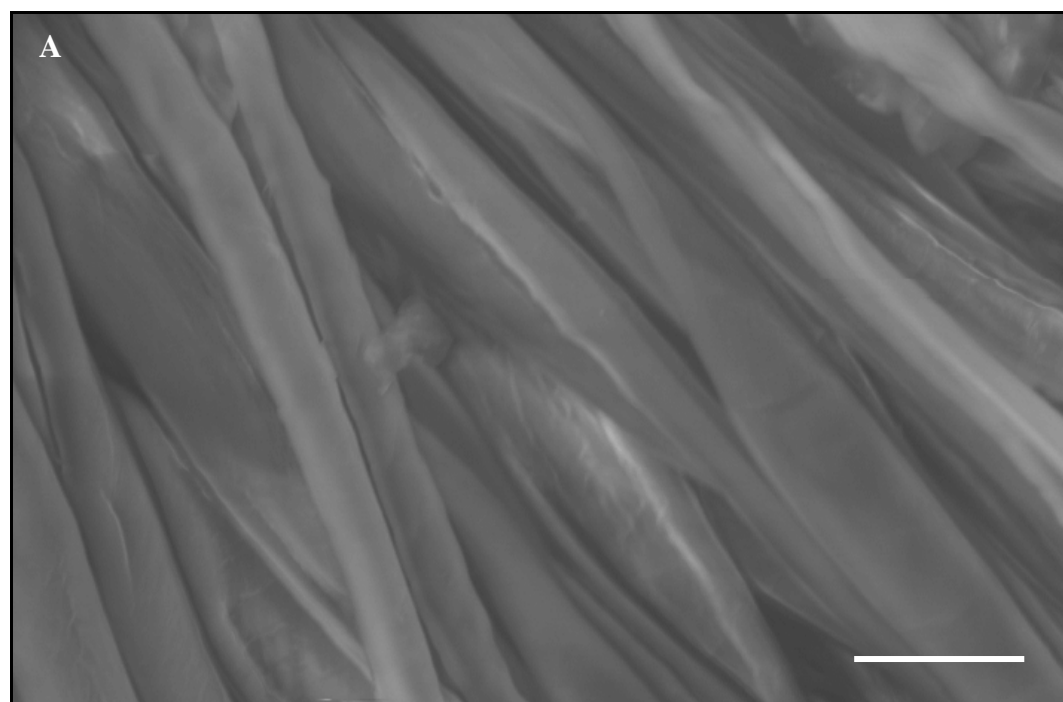


**Figure 4.29** ESEM image (A) of Yellow 2 dyed cotton fibre at 1000x magnification with spot size 4 $\mu$ m and scale bar 20 $\mu$ m. EDAX spectra (B) of the sample area show traces of C, O, Fe, Na, S, Cl and Ca. (C and O peaks exceed Y scale, with peak maxima at 5936 and 2492 counts (X-ray intensity) respectively).

The ESEM image in Figure 4.30 is of Red 3 dyed fibres at 1000x magnification, the corresponding EDAX spectra does not show any peaks that are characteristic to the dye molecule (see inset), but does display Na, which would have been present during dyeing. While the dye molecule itself is N-rich, unfortunately the peak for N which occurs between the C and O peaks is swamped by the signals for these two peaks, and so is difficult to observe.

Through the use of SEM, the dyed fibre images obtained showed no large differences within the surface morphology compared with the undyed fibres, as both sets of data displayed the microfibrillar ultrastructure. Also the SEM images did not show any differences due to the dye compound used to dye the cotton fibres. However through the use of ESEM within this study, chemical information was achieved on the elemental make-up on the dyed fibre surfaces, and in most cases the dye compound was detectable from all the dyed fibre surfaces.

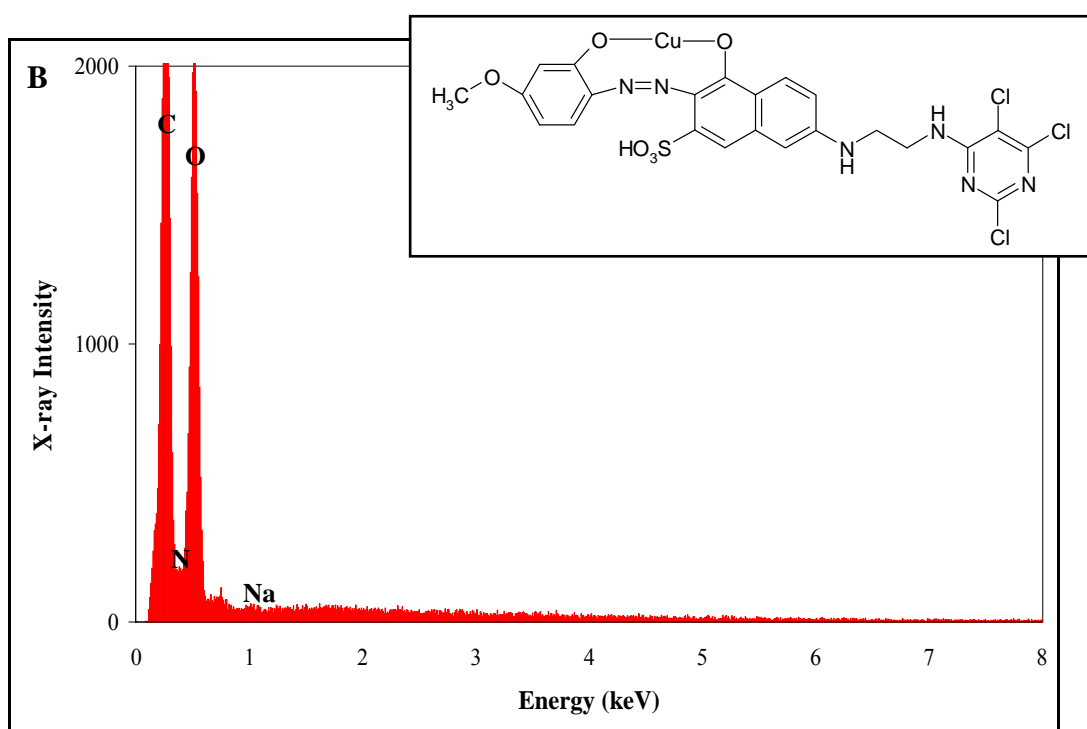
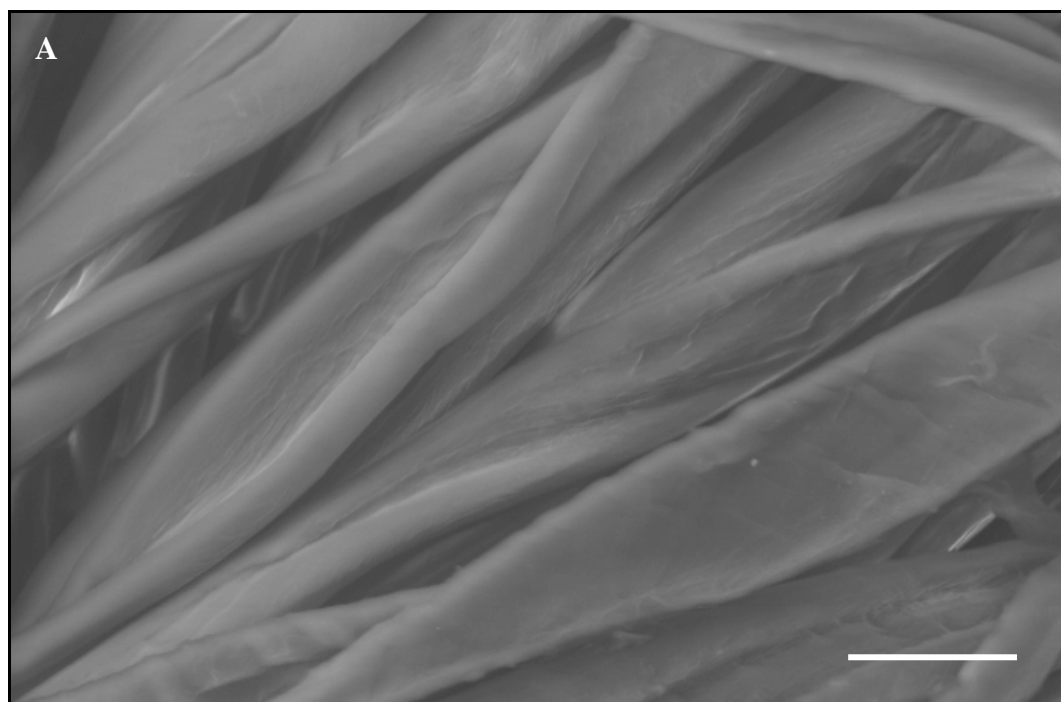
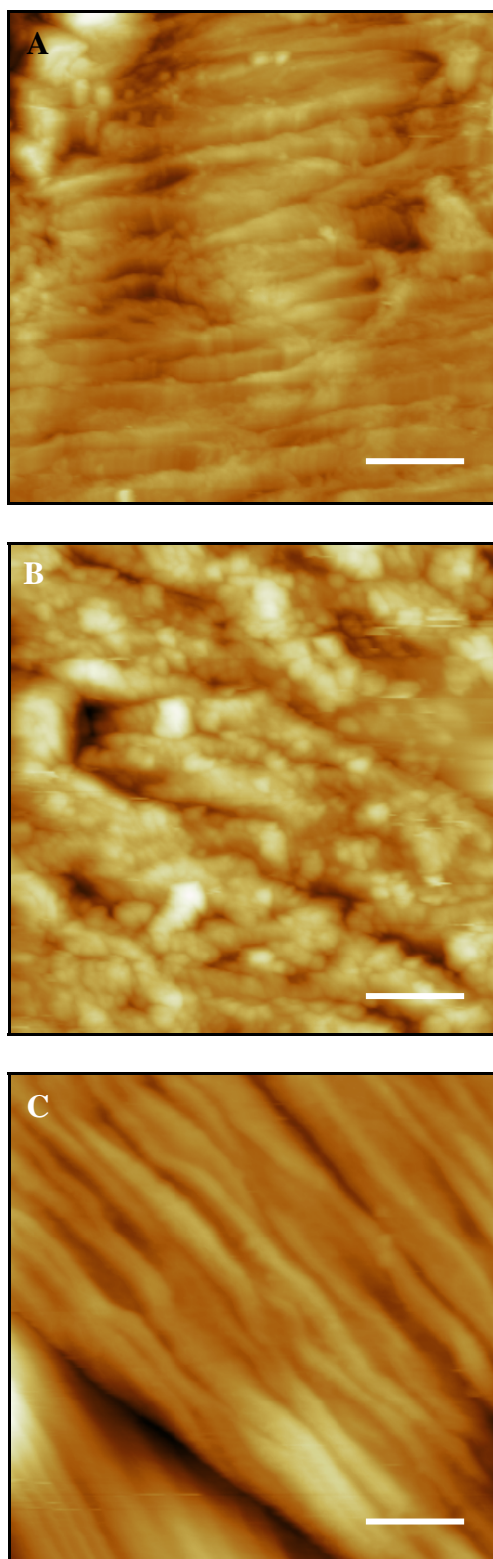


**Figure 4.30** ESEM image (A) of Red 3 dyed cotton fibre at 1000x magnification with spot size 4 $\mu$ m and scale bar 20 $\mu$ m. EDAX spectra (B) of the sample area show traces of C, O, N (swamped by C and O), and Na. (C and O peaks exceed Y scale, with peak maxima at 2958 and 2133 counts (X-ray intensity) respectively).

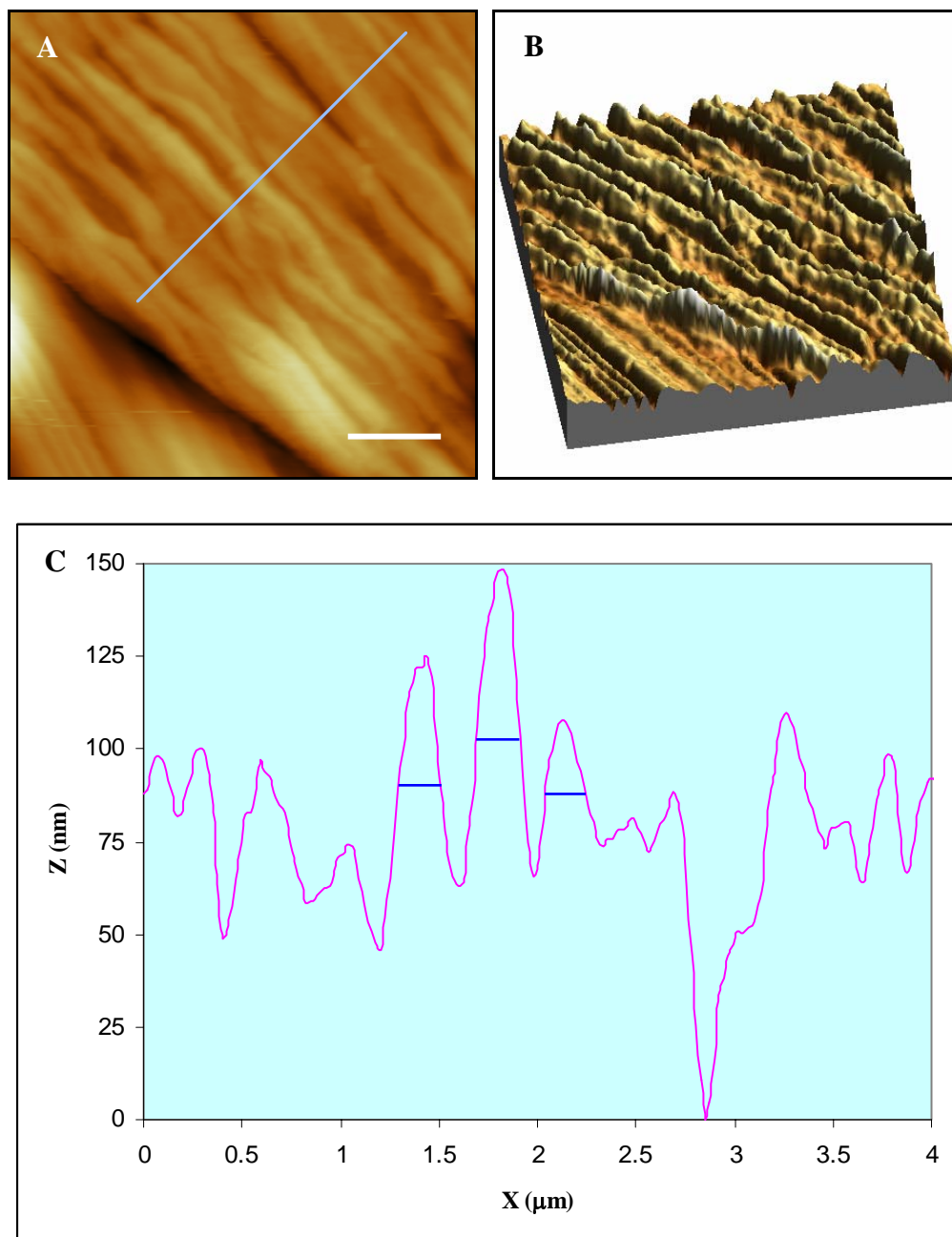
#### 4.3.3.2 AFM analysis

AFM analysis was carried out on dyed cotton fibres using Explorer and DI 3000 AFM in air ambient conditions using either contact mode or TM. Figure 4.31 displays Explorer AFM images of red, fuchsia and orange dyed cloths; the images were all achieved using an unmodified tip using contact mode in air. Similarly to the SEM data, the AFM data here exhibits no obvious differences in the surface morphology of the fibres, however the sampling areas are clearly different due to the types of features observed in each image; i.e. the images show either microfibrillar packing or the uneven surface characteristic of the fibrillar packing density due to the bilateral structure, depending on the sampling position (see Figure 4.13).

Figure 4.32 displays a line profile measurement carried out on the fibrillar pattern within the topography image (C) of Figure 4.31. Here the line profile showed the fibrillar width measurements to be 200-250nm across, which were much larger in dimension to the figures cited within literature for mercerised undyed fibres, but this time comparable to greige fibres which displayed similar measurements (see Figure 4.8). The increase in the fibrillar dimensions may be attributed to the dye itself, as during the dyeing process the fibres would swell in the aqueous environment, causing hydrogen bond breakages between adjacent cellulose chain molecules (intramolecular structure, thought to be amorphous regions). The intrafibrillar swelling would allow the dye molecules to adsorb into the cellulose fibre. It could be hypothesised that this action causes the fibrillar structure to remain enlarged, as the dye becomes entrapped within the cellulose structure.



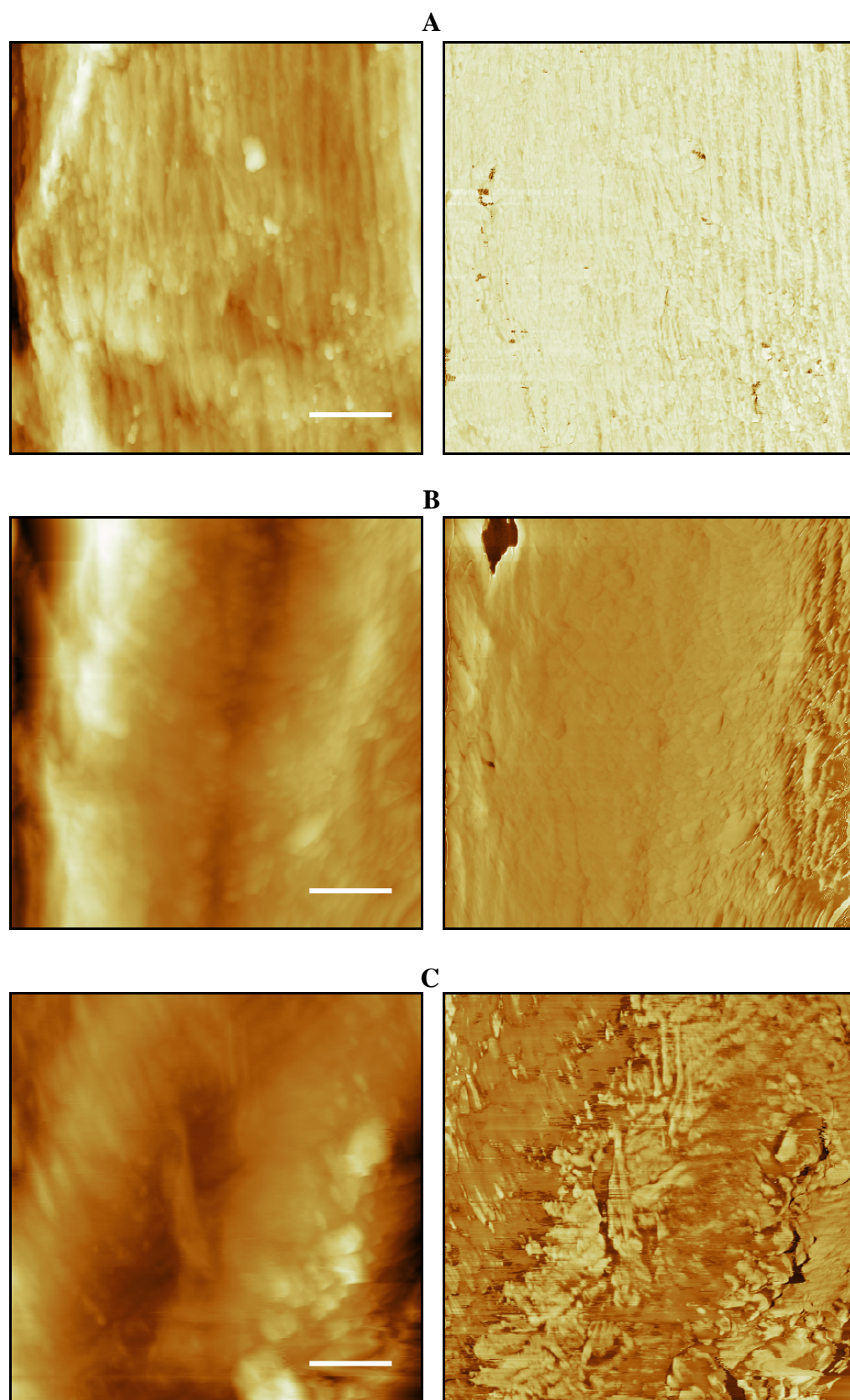
**Figure 4.31** Three Explorer AFM images displaying dyed cotton fibres (A) red with Z-range 762.3nm, (B) fuchsia with Z-range 625.7nm, and (C) orange with Z-range 1.38μm. All images are 5μm x 5μm with scale bar 1μm.



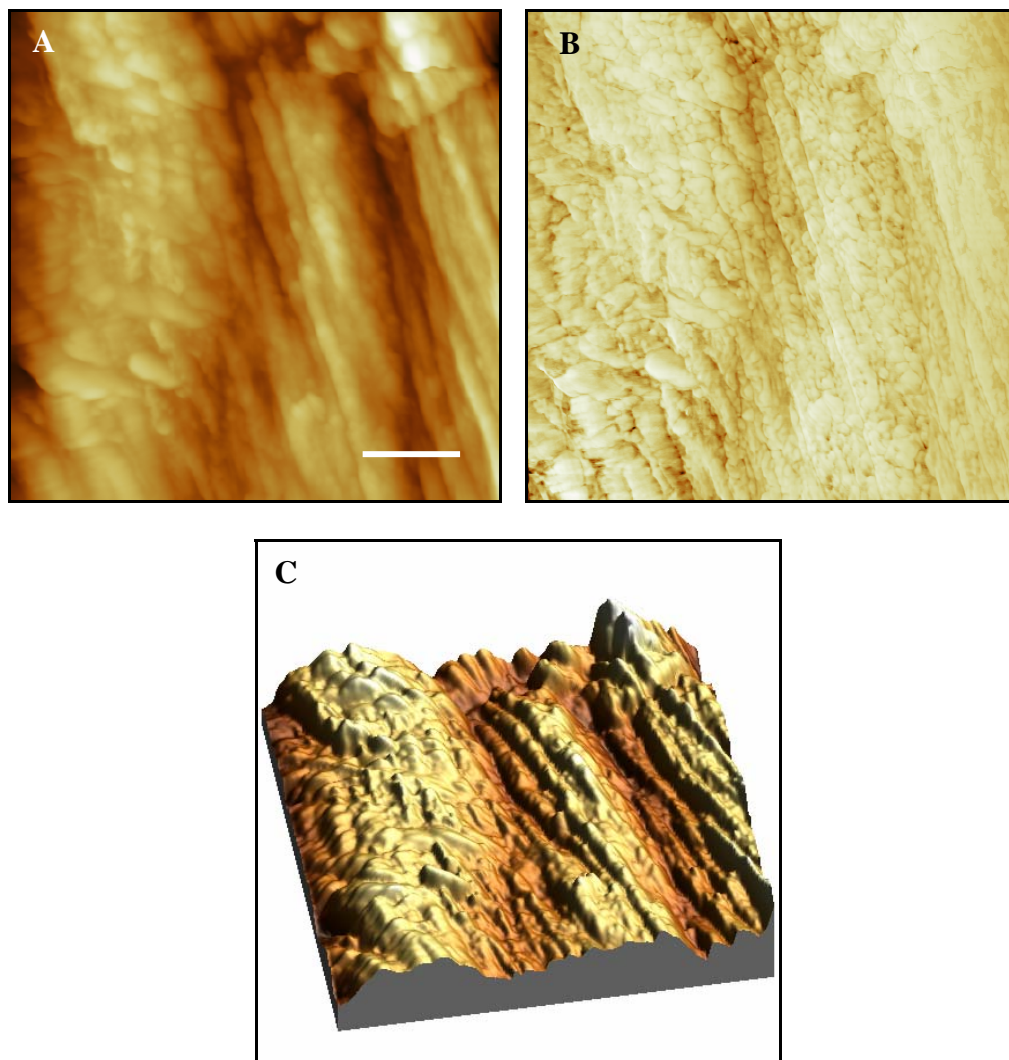
**Figure 4.32** Line profile (C) of orange dyed fibre microfibrillar pattern (A) (observed in topography (C) of Figure 4.31) and (B) 3D rendered topography. Fibrils appear to be 200-250nm across (at FWHM, highlighted by blue lines), similar to greige fibre samples. Fibrillar measurements were taken of single fibres from within the phase image, as opposed to thick bundles of fibres.

Figure 4.33 shows three sets of DI 3000 AFM images of dyed fibres using an unmodified tip in TM under air ambient conditions, (in Figure 4.31). Here the images display topography (left images) and phase (right images) data for red, orange and fuchsia dyed fibres. In all the image sets the phase data does not show any significant contrast detail, this may reflect a homogenous surface chemistry due to uniformed distribution of dye across the sample surface, or a homogenous material property (hard/soft or adhesive). Or it may be simply that the unmodified tip is not sensitive to any changes within the surface chemistry/material properties.

The samples were subsequently imaged using modified tips to further explore the nature of the sample surface chemistry. Figure 4.34 displays a DI 3000 AFM image of orange dyed cotton fibre, obtained utilising a hydrophilic tip in TM under air ambient conditions, the imaging conditions were identical as the data obtained in Figure 4.33 with the exception of the modified tip, and the phase data (Figure 4.34 (C)) still displayed no contrast.



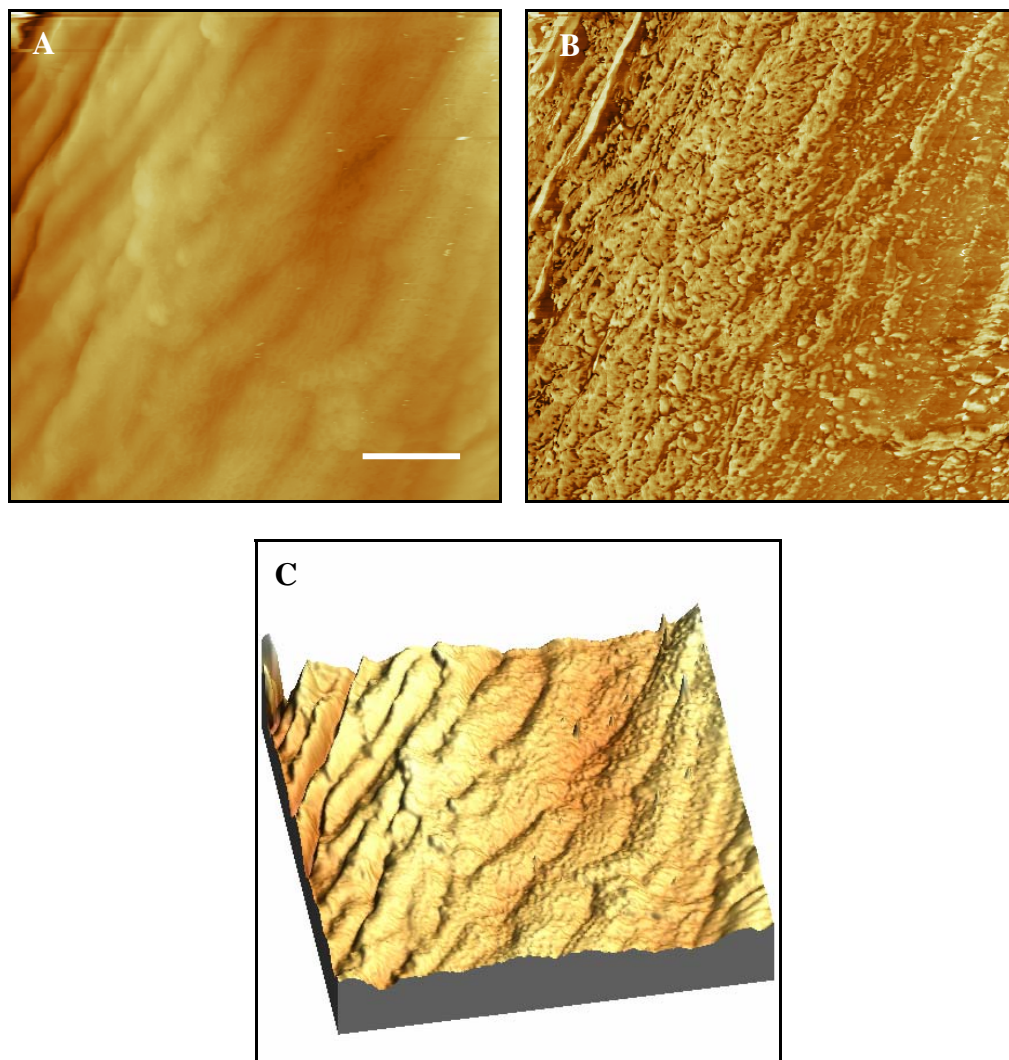
**Figure 4.33** Three DI 3000 AFM image sets showing topography (left) and phase (right) of dyed cotton fibres (A) 10 $\mu\text{m}$  x 10 $\mu\text{m}$  image of red (Z-range 1.26 $\mu\text{m}$  and scale bar 2 $\mu\text{m}$ ). (B) 5 $\mu\text{m}$  x 5 $\mu\text{m}$  image of orange (Z-range 1.03 $\mu\text{m}$ , scale bar 1 $\mu\text{m}$ ), and (C) 9 $\mu\text{m}$  x 9 $\mu\text{m}$  fuchsia (Z-range 787.8nm and scale bar 1.8 $\mu\text{m}$ ).



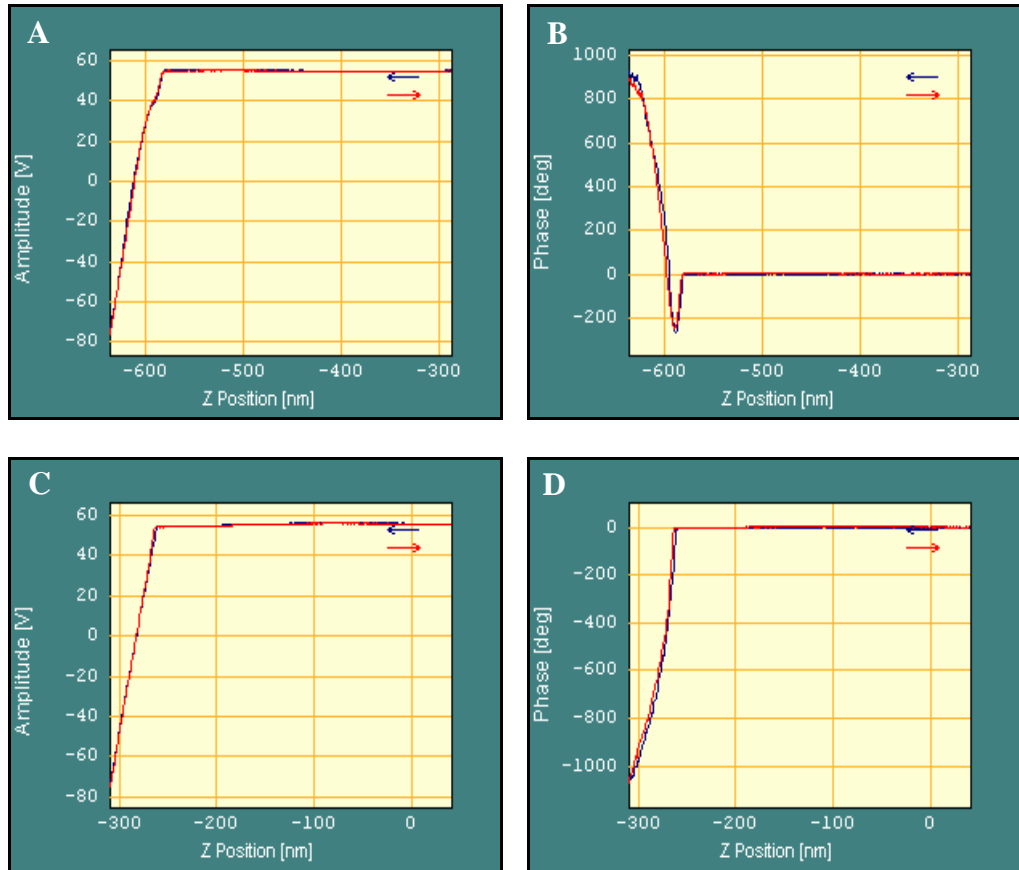
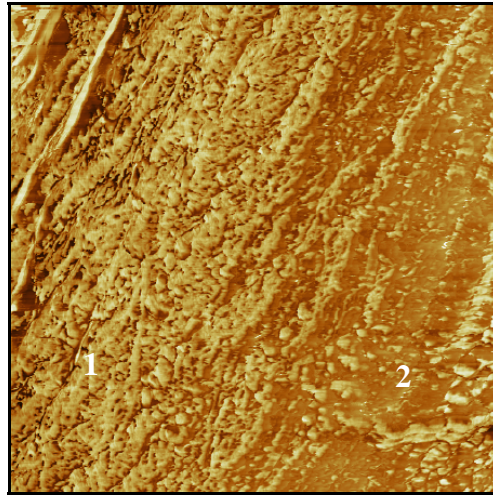
**Figure 4.34** A  $5\mu\text{m} \times 5\mu\text{m}$  image of orange dyed cotton fibres imaged using a modified hydrophilic tip: (A) topography, (B) phase and (C) 3D rendered topography, with Z-scale  $615.3\text{nm}$  and scale bar  $1\mu\text{m}$ .

Figure 4.35 displays a DI 3000 AFM images of orange dyed fibres using a modified, hydrophobic tip in TM under ambient conditions. The images show topography (A) phase (B) and 3D rendered topography (C). Within the phase image contrast can be observed, however it appears to be topography enhanced, as it closely follows the features seen in the topography image (A). Again to further explore the nature of the phase contrast, a-p-d measurements were taken of the sample area, which are illustrated in Figure 4.36. Curves (A) and (B) display the a-p-d measurement obtained from point 1 in the phase data. Here we observe a repulsive regime acting between the hydrophobic tip and sample. However curves (C) and (D) which represent the measurement taken at point 2, shows what at first appears to be an attractive regime acting between the probe and sample, but this is difficult to judge as the curve exceeds the scale. It is perhaps clear that the phase contrast observed may not be topography induced as the two sets of a-p-d curves would display identical profiles, but they may reflect the underlying crystalline/amorphous structure of the sample surface, as observed within the undyed fibres (see Figure 4.20).

The AFM data of dyed fibres has provided evidence of distension within the microfibrils, as the observed width dimensions were greater than the undyed fibre samples. The phase data of the dyed fibres, obtained using unmodified or hydrophilic tips did not exhibit any contrast details. However, the use of hydrophobic tips did show contrast detail, perhaps reflecting the underlying crystalline surface structure of cellulose fibres.



**Figure 4.35** A  $5\mu\text{m} \times 5\mu\text{m}$  image of orange dyed cotton fibres imaged using a modified hydrophobic tip: (A) topography, (B) phase and (C) 3D rendered topography, with Z-scale  $712.3\text{nm}$  and scale bar  $1\mu\text{m}$ .



**Figure 4.36** The topmost image (orange dyed fibre obtained with hydrophobic tip) is the phase data from Figure 4.35, below which are the corresponding a-p-d curves of the two areas of interest (points 1 and 2). Curves (A) and (B) correspond to point 1 in the phase image and curves (C) and (D) correspond to point 2 within the phase image. Curves (A) and (B) display a strong repulsive profile, and what appears to be attractive profile within curves (C) and (D), but the curve exceeds the scale.

#### 4.3.3.3 ToF-SIMS analysis

ToF-SIMS analysis was performed on orange dyed cotton fibres samples and was compared to control spectra of orange dye compound itself, which was spun-cast onto silicon wafer surface at a 0.05% w/v concentration (in water). These latter experiments were performed in order to allow identification of ion fragments indicative of dye molecules from the surface of dyed fibres. (See section 2.2.3 for analysis method). At first the spun-cast dye compound sample was analysed in order to produce positive (see Table 4.3) and negative (Table 4.4) ion fragmentation peak lists, these would help to assign any peaks from the dyed fibre spectra that were indicative of the dye molecule.

Figure 4.37 displays the positive ion spectra for both the orange dye compound ( $C_{51}H_{42}Cl_2N_{16}O_{16}S_4$ ) and the orange dyed fibre, with the most important peaks labelled. The peaks in the orange dyed fibre spectra were less intense than peaks found in the dye compound spectra, due to the flat surface the pure dye on silicon wafer compared with the large uneven surface of the dye fibres. The topography of a surface will vary the local concentrations of the dye molecule at the sample surface. There was also evidence of siloxane contamination within the dyed fibre positive spectra, which were highlighted by peaks at  $m/z$  28, 29, 73 and 147. These peaks were present in the positive ion spectra for the dye compound but were attributed to the silicon wafer the dye compound was spun-cast on. As mentioned previously (see section 4.3.3.2), siloxanes are a common contaminant detected within SIMS analysis, and can arise from sample preparation or exposure to atmosphere contaminants.

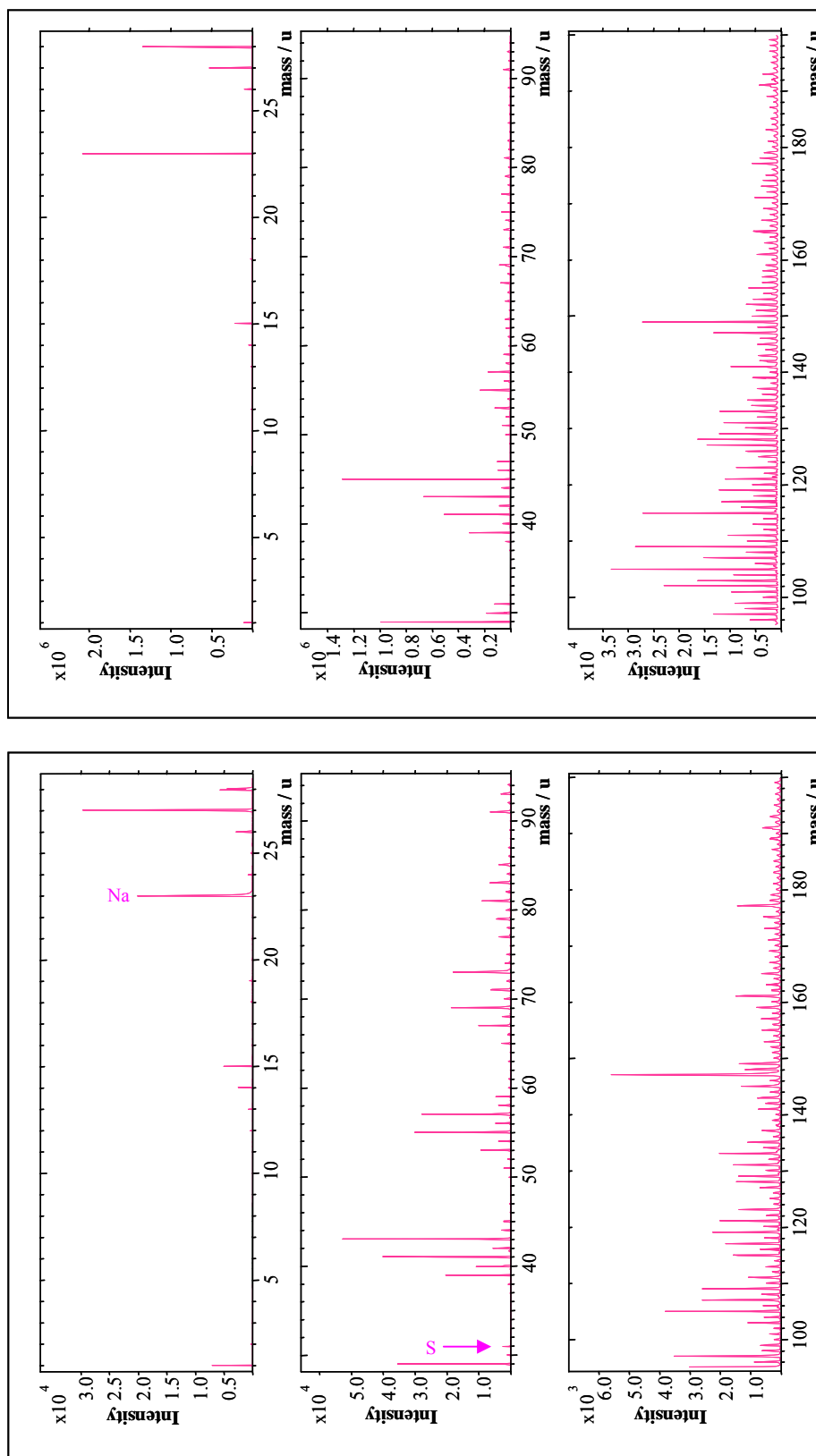


**Figure 4.37** ToF-SIMS positive ion spectra for orange dyed fibre and orange dye compound. Spectra gained using a  $\text{Ga}^+$  gun, with a scan area of  $100\mu\text{m} \times 100\mu\text{m}$  (for fibre) and  $200\mu\text{m} \times 200\mu\text{m}$  (for dye).



Figure 4.38 exhibits the negative ion spectra for the orange dye compound and the orange dyed fibres, with the important peaks labelled. Here again the negative ion peaks are less intense in the dyed fibre spectra than the dyed compound spectra.

The important positive fragment ions were identified at  $m/z$  23 and 32 within the dyed fibre positive spectra and were assigned to Na and S. S is present within the dye structure and Na is attributed to NaCl within dyebath, used to fix reactive dye compound to cellulose fibre. Its presence suggests that it was not entirely removed from the surface of the dyed fibre during the washing stage of dye processing. However, it was also observed within the dye compound positive ion spectra; this may have resulted from sodium hydroxide (NaOH) and sodium carbonate ( $\text{Na}_2\text{CO}_3$ ) which are used the dye manufacturing process. The important negative fragment ions were identified within the dyed fibre negative spectra at  $m/z$  16, 32, 35, 37, 80 and 81. These were assigned to the fragments O,  $\text{O}_2$ , Cl,  $^{37}\text{Cl}$ ,  $\text{SO}_3$  and  $\text{SO}_3\text{H}$  respectively, as they were known to be common components within the reactive dye compound.

It was unclear as to how and where the dyed fibre sample could have become contaminated with siloxane, but it again showcased the ultra-sensitivity of the analysis technique. However, this type of contamination was not observed in the EDAX spectra that were obtained for the dyed samples, only a very small amount of contaminant would need to be present to affect the spectral outcome.

The spectral analysis of the dyed cotton fibres was successful, even though the chemical structure of the dye compound was not known. It was still possible to assign and assume probable negative and positive fragment ion patterns from the dyed fibre spectra resulting from the dye compound.

m/z	Positive Fragment Ion
12	C
13	CH
14	CH <sub>2</sub>
15	CH <sub>3</sub>
18	NH <sub>4</sub>
23	Na
26	C <sub>2</sub> H <sub>2</sub>
27	C <sub>2</sub> H <sub>3</sub>
29	C <sub>2</sub> H <sub>5</sub>
32	S
37	C <sub>3</sub> H
39	C <sub>3</sub> H <sub>3</sub>
40	C <sub>3</sub> H <sub>4</sub>
41	C <sub>3</sub> H <sub>5</sub>
42	C <sub>2</sub> H <sub>2</sub> O
43	C <sub>3</sub> H <sub>7</sub>
45	C <sub>2</sub> H <sub>7</sub> N
48	C <sub>4</sub>
57	C <sub>3</sub> H <sub>6</sub> O

**Table 4.3** Characteristic positive ion peaks selected for the analysis of dyed fibres.

m/z	Negative Fragment Ion
14	N
15	NH
16	O
17	OH
25	C <sub>2</sub> H
26	CN
32	O <sub>2</sub>
33	HS
35	Cl
37	<sup>37</sup> Cl
40	CN <sub>2</sub>
41	C <sub>2</sub> HO
42	CNO
44	CO <sub>2</sub>
45	CHS
46	NO <sub>2</sub>
47	CCl
48	SO
49	SOH
59	C <sub>2</sub> Cl
60	C <sub>5</sub>
76	CSO <sub>2</sub>
77	CSO <sub>2</sub> H
80	SO <sub>3</sub>
81	SO <sub>3</sub> H

**Table 4.4** Characteristic negative ion peaks selected for the analysis of dyed fibres.

#### 4.3.4 Surface characterisation of fibre cross-sections

Fibre cross-sections embedded in resin (see section 2.1.4.3) were also examined to see if probable dye ingress sites could be viewed through the cross-section and thus aid the discovery of dye-uptake mechanisms. The cross-section were firstly examined through AFM analysis, and phase imaging by TM, to demonstrate any differences in contrast due to the presence of dye molecules across the fibres bilateral structure. This was followed by the use of ToF-SIMS to analyse the cross-section surfaces and gain qualitative chemical analysis of dye molecules within the surface of the fibre cross-section.

##### 4.3.4.1 AFM analysis

All samples were imaged using the DI 3000 AFM in air conditions using TM. Figure 4.39 displays AFM images of red dyed fibre cross-sections gained through the use of an unmodified tip. The topography (A) clearly illustrates the bilateral structure of the fibres embedded within the resin. Also within the topography it is possible to visualise the collapsed lumen within each fibre cross-section (highlighted by blue circle and see image (C)). While there was no contrast present within the phase (B) image, it did highlight the edges of the cross-sections. The lack of contrast would again suggest a uniform distribution of dye compound across the fibre cross-section, or alternatively it may indicate that the surface of the cross-sections were contaminated by the resin and became masked by the resin during the sectioning process (by microtome), which might sweep resin across the whole surface. Image (D) shows a zoomed-in section from image (A), and illustrated within this image are the fibre length (point L) and width (point W). The cross-sections were measured

across the whole image in (A), and displayed an average mean length of  $20\mu\text{m}$  and average mean cross-section width of  $10\mu\text{m}$ .

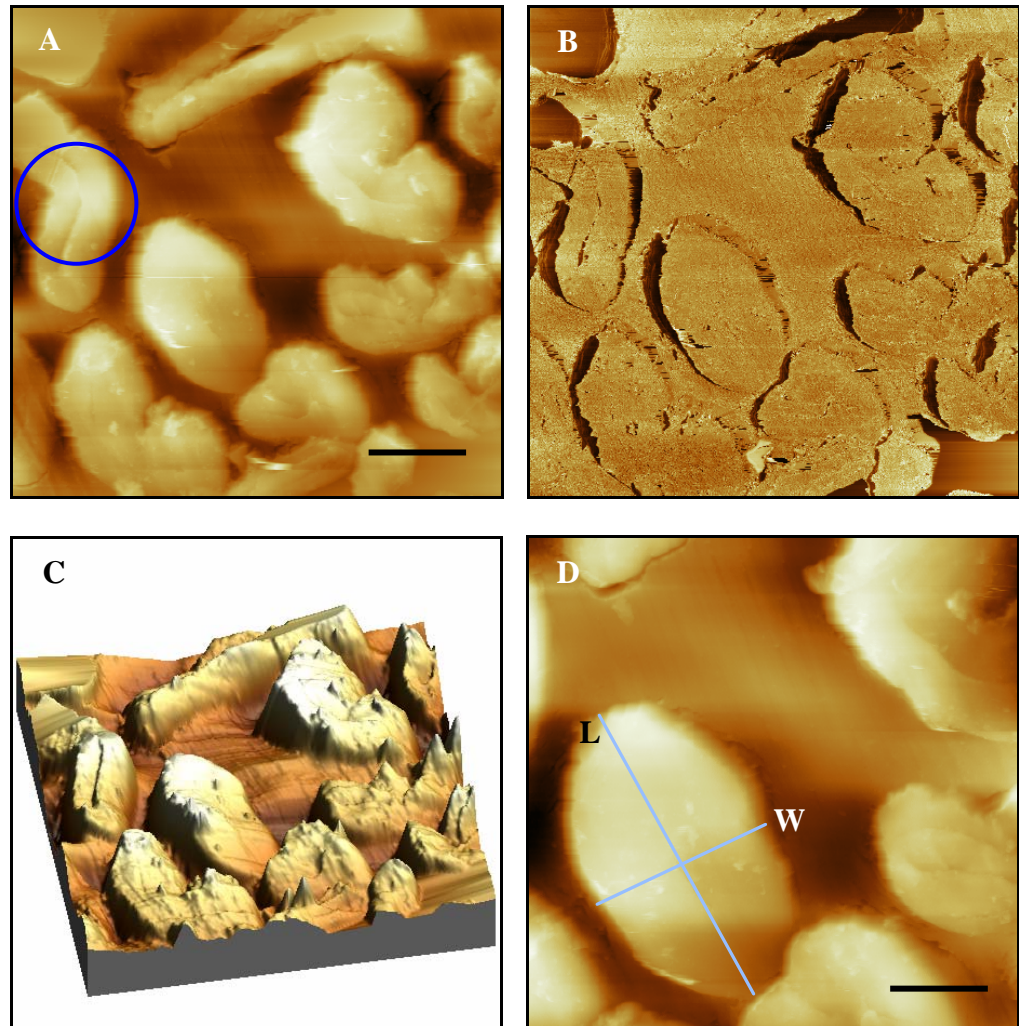


**Figure 4.39** A  $50\mu\text{m} \times 50\mu\text{m}$  image of red dyed cotton fibres embedded in resin imaged using an unmodified cantilever tip: (A) topography, (B) phase and (C) 3D rendered topography, with Z-scale  $2.4\mu\text{m}$  and scale bar  $10\mu\text{m}$ . (D) zoom-in section of (A), a  $30\mu\text{m} \times 30\mu\text{m}$  image (scale bar  $6\mu\text{m}$ ), highlighting the average mean length and width of the fibre cross-section.

Figure 4.40 displays two sets of undyed fibre AFM images gained through the use of the DI 3000 and modified cantilever tips; (A) obtained with hydrophilic tip and (B) obtained with hydrophobic tip. It is evident that the change in tip chemistry provided more contrast within the phase images. However this made only the fibre cross-section distinguishable from the resin medium in which it was embedded (most likely due to height features, such as the fibre cross-section edges). Again there was little or no contrast present within the fibre cross-section itself. A-p-d measurements of the samples were also very difficult to obtain, as the tip oscillation exceeded acceptable limits for accurate readings to be completed, due to the increased interaction between probe and sample surface. Nevertheless, the presence of the collapsed lumen within both image sets is clear.

The images displayed Figure 4.41 show greige fibre cross-sections embedded in resin. As before image set (A) were achieved through the use of a hydrophilic tip and image set (B) utilised a hydrophobic tip. However while there was very little contrast within the fibre itself, contrast was observed between the fibre edges and the embedding medium, which we ascribe to the presence of waxy cuticle layer.

AFM data of fibre cross-sections highlighted the bilateral structure of the fibres as described in literature, displaying the lumen. However, little contrast detail was observed within the phase images, most likely reflecting the presence of resin from the embedding medium within the cross-sections.

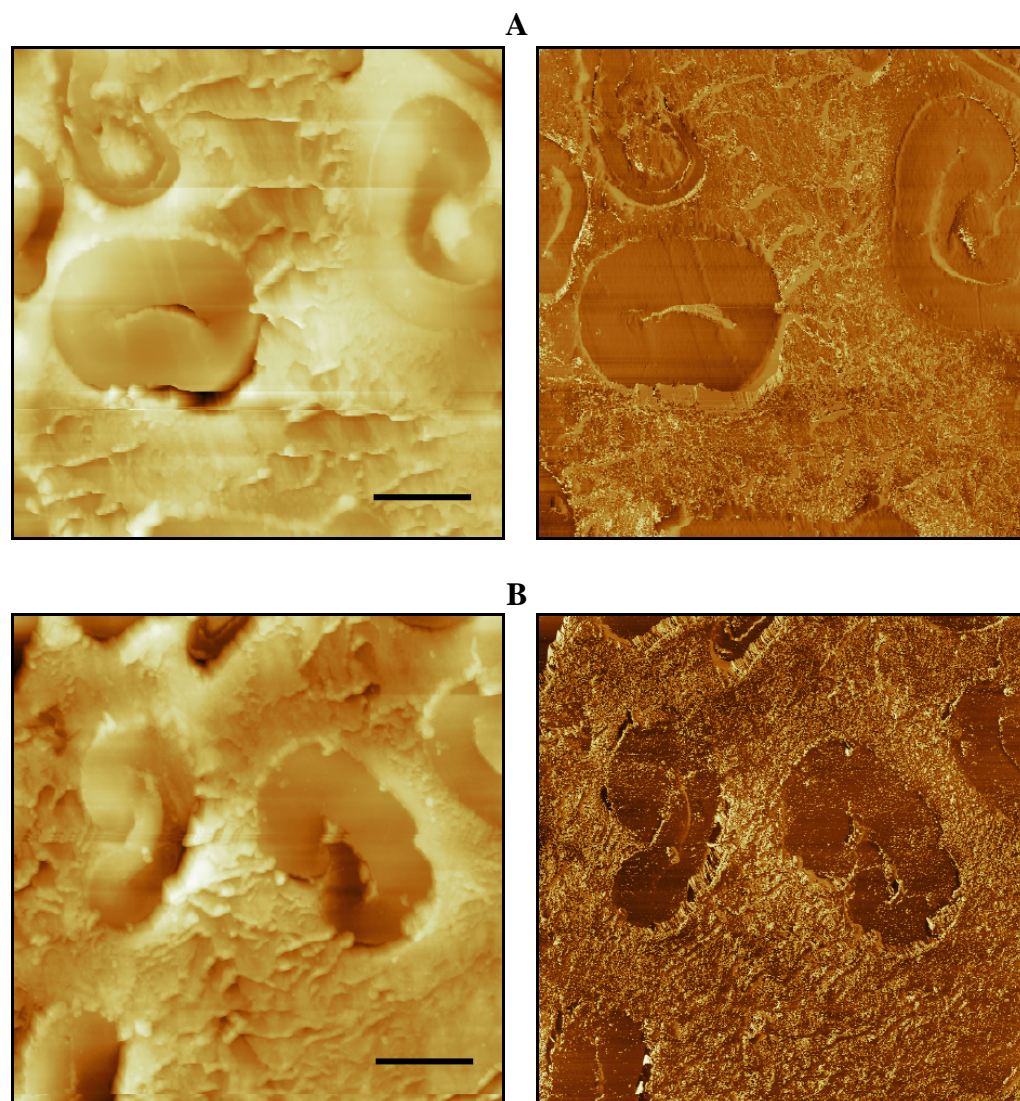


**Figure 4.40** Two AFM image data sets of undyed cotton fibres embedded in resin obtained using TM: Set (A) shows topography (left) and phase (right) imaged using a hydrophilic tip. Set (B) imaged using a hydrophobic tip; both data sets are  $40\mu\text{m} \times 40\mu\text{m}$  images with Z-scale  $2.54\mu\text{m}$  in (A) and  $2.08\mu\text{m}$  in (B) with scale bar  $10\mu\text{m}$ .

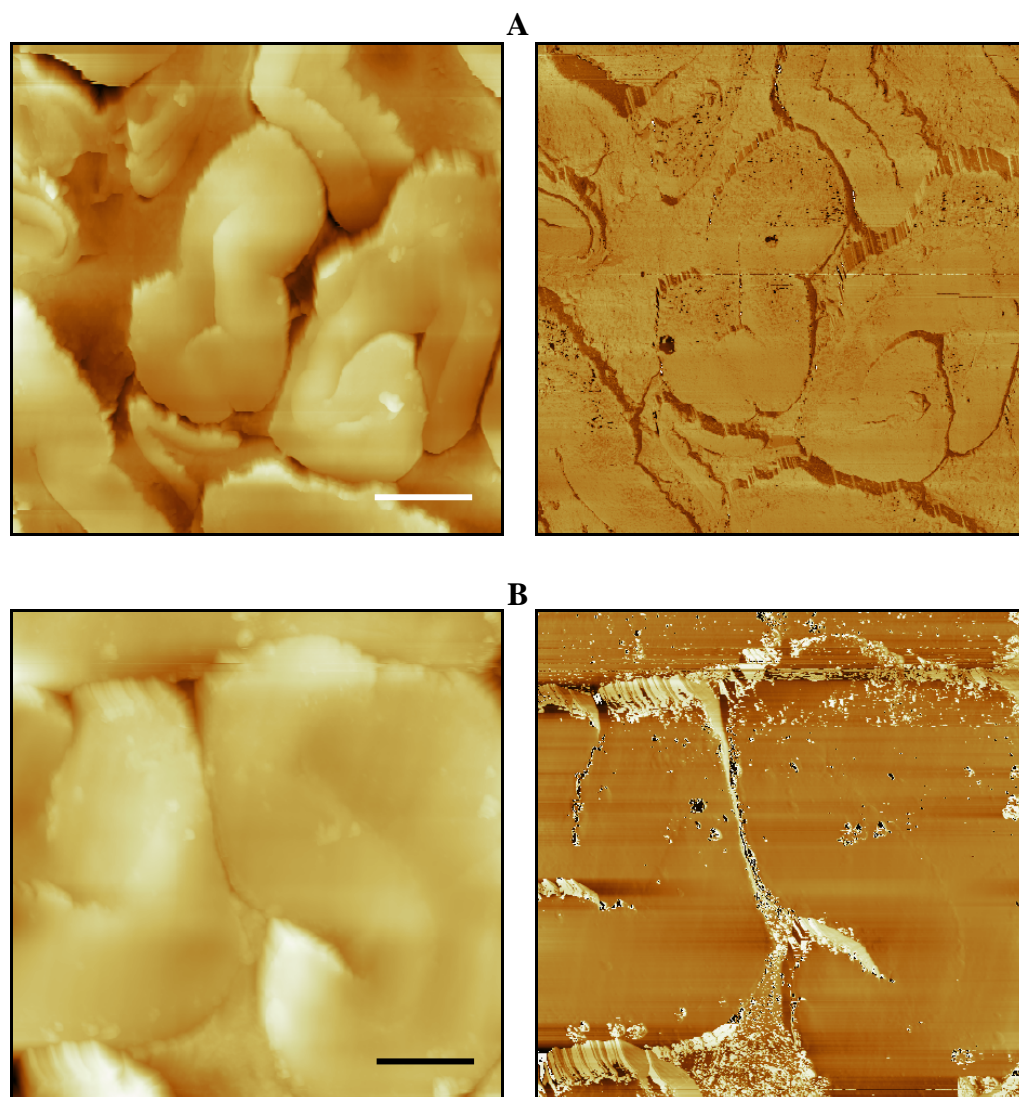


**Figure 4.41** Two AFM image data sets of greige cotton fibres embedded in resin obtained using TM: Set (A)  $32.5\mu\text{m} \times 32.5\mu\text{m}$  images, topography (left) and phase (right) with Z-scale  $3.16\mu\text{m}$  and scale bar  $6.5\mu\text{m}$ , were achieved using a hydrophilic tip. Set (B)  $20\mu\text{m} \times 20\mu\text{m}$  images were obtained using a hydrophobic tip with Z-scale  $2.27\mu\text{m}$  and scale bar  $4\mu\text{m}$ .

#### *4.3.4.2 ToF-SIMS analysis*

ToF-SIMS analysis was carried out fuchsia dyed fibre cross-sections samples which were embedded in resin. A similar analysis method to the dyed fibre samples was applied to the cross-section samples. Through the use of ToF-SIMS to analyse the cross-section surfaces within this study, it was hoped that qualitative chemical analysis information could be gained of the dye molecules within the surface of the fibre cross-section.

However during this study it became obvious that siloxane contamination of the fibre samples had become a significant hindrance in the accurate analysis of the samples, as the siloxane masked the intensity of any important peaks of interest. Spectral information on positive and negative ion peaks was first obtained from the resin medium prior to analysis of the fibre itself, in order to subtract it from the fibre cross-section spectra. However, the spectra obtained from the fibre cross-section, in both the positive (Figure 4.42) and negative (Figure 4.43) ion peaks were almost identical in intensity to the embedding medium spectra. It was determined through the use of a higher current density bombardment of the surface (to etch the embedded sample surface), that the contamination was present through the bulk fibre. The ion bombardment allowed the instrument to detect the presence of siloxane species (from the embedding medium) within the bulk of the fibre. This suggested that the embedding medium had absorbed into the fibre during sample preparation.

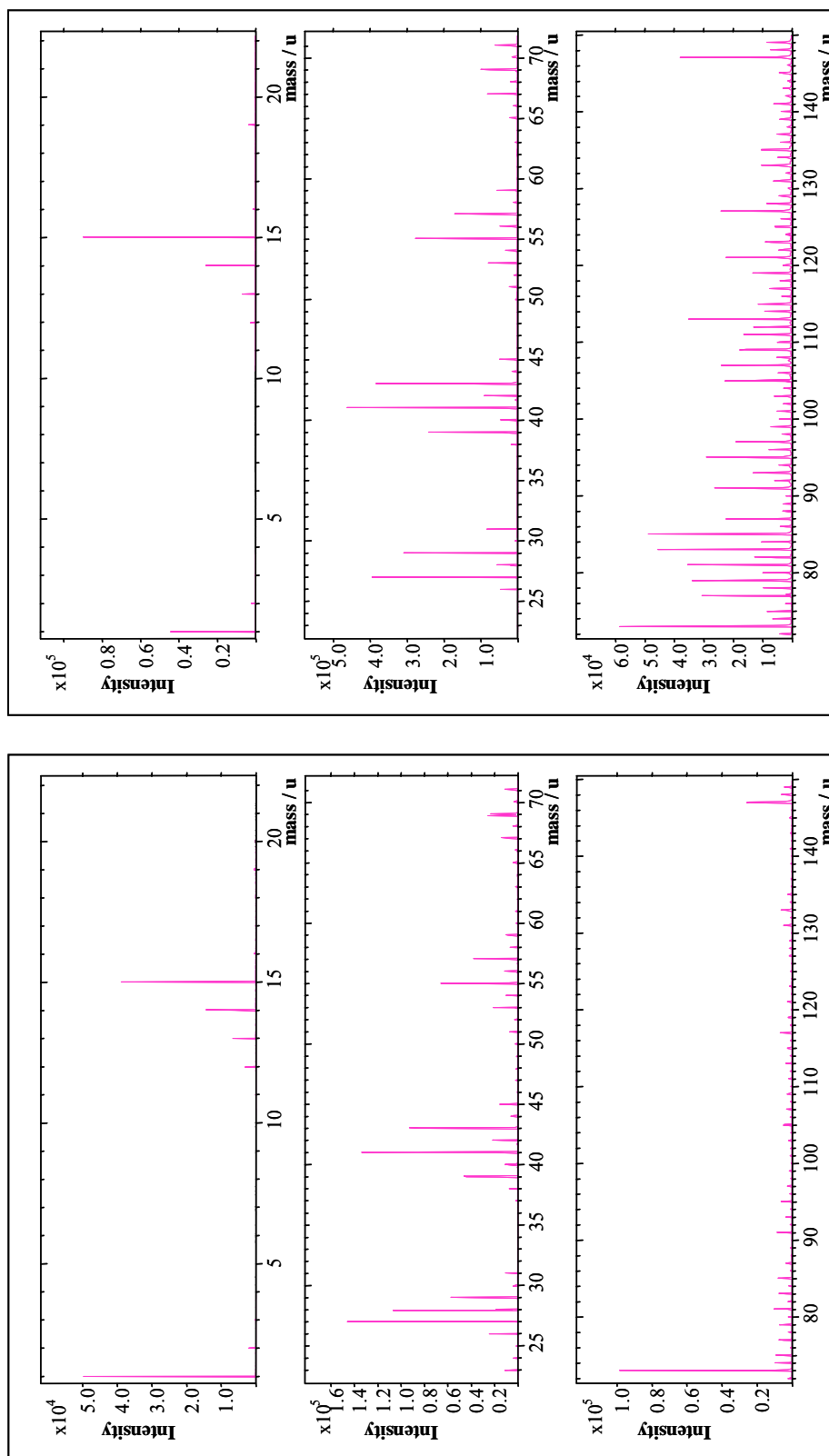


**Figure 4.42** ToF-SIMS positive ion spectra for fuchsia dyed fibre cross-sections embedded in resin using a  $\text{Ga}^+$  gun in bunched mode, with a scan area of  $200\mu\text{m} \times 200\mu\text{m}$ .

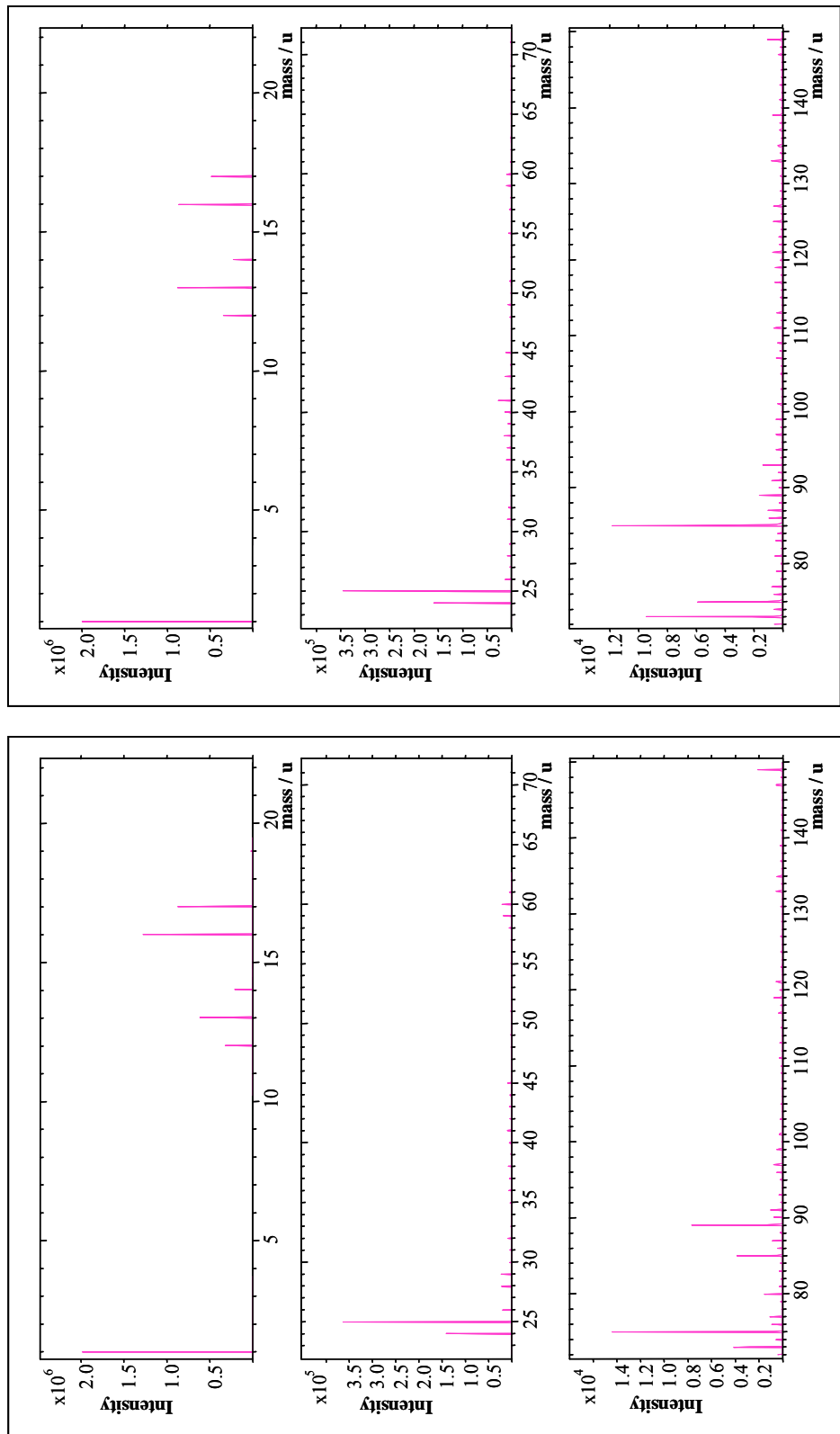


**Figure 4.43** ToF-SIMS negative ion spectra for fuchsia dyed fibre cross-sections embedded in resin using a Ga<sup>+</sup> gun in bunched mode, with a scan area of 200µm x 200µm.

The analysis of the fibre cross-sections through ToF-SIMS highlighted problems in this method of sample preparation, as contamination of samples was observed in each experiment. To gain spectral information the fibre cross-sections successfully, another form of sample immobilisation would need to be developed for analysis.

#### **4.4 CONCLUSIONS**

The results presented within this chapter illustrated the cotton fibre surface morphology with its distinctive fibrillar packing and elementary fibrils. Through the use of SEM/ESEM we were able too visualise subtle differences within the general morphology of the different cotton fibre types; greige fibres appeared to be more twisted and convoluted due to the natural fibre formation, subsequent to collapse of the lumen. In contrast the mercerised undyed fibres appeared to be less convoluted in structure along with a superficial smoother surface. While, distinctions could not be made for the dyed fibres using this technique, as undyed and dyed fibres displayed a similar structural form, the use of EDAX analysis allowed distinctions to be made through the elemental analysis of the fibre surface composition, from which dye specific elements were observed.

The AFM under various different imaging conditions showed structural details that were not visualised with the SEM. Fibres were imaged in air and liquid environment using modified cantilever tips primarily in TM, as this mode provided the most high resolution images of the samples. The examination of greige cotton fibres displayed the cuticle layer ultrastructure which was

highlighted further through phase imaging. The assessment of undyed fibres through AFM displayed very tight fibrillar packing, complimenting the data obtained through SEM. Phase images of undyed and dyed fibres obtained with hydrophobic tips showed contrast detail, highlighting possible surface crystalline structure.

Line profile measurements of the undyed fibres showed fibrillar width dimensions that agreed well with figures cited within the literature. Greige fibres had fibrillar width dimensions larger than mercerised undyed fibres resulting from the presence of cuticle layer on top of the cellulose fibre. Line profile measurements of dyed fibres showed a fibrillar dimension that was similar to greige fibres (not previously determined within literature). This may be due to the entrapment of dye molecules within the fibre matrix, during swelling of fibres within the dyebath. Fibre swelling caused hydrogen bonds between cellulose chain molecules to break, creating more movement between the chain molecules and thus allowing dye molecules to enter the fibre matrix.

Through the use of AFM, the sampling areas undoubtedly showed variations in the types of features observed within each image (microfibrils or globular uneven surface features), these were seen as characteristic of the fibrillar packing density due to the bilateral structure. AFM images of fibre cross-sections displayed the bilateral structure and collapsed lumen, but also highlighted that the samples were contaminated by the embedding medium. This was further supported by results achieved through ToF-SIMS analysis.

ToF-SIMS analysis was performed on the undyed cotton fibres samples to produce control spectra, to distinguish the data obtained from dyed cotton fibres by allowing identification of ion fragments indicative of dye molecules from the surface of dyed fibres. The positive and negative ion spectra produced characteristic cellulose ion fragments from the surface of the sample. Siloxane contaminants were observed within the spectra, but these were attributed to the adhesive tape that the undyed fibres were immobilised onto for analysis. ToF-SIMS analysis of the dyed fibres was also successful, as it was possible to assign and assume probable negative and positive fragment ion patterns from the dye compound within the dyed fibre spectra.

### **Dye-Uptake Mechanisms**

In chapters 3 and 4, the AFM was employed to characterise undyed and dyed cellulose, either within a model system (cellophane) or cotton fibres. Both undyed and dyed cellophane or cotton samples displayed the similar surface morphology (also seen with SEM) through the presence of fibrils and more irregular globular surface features. These were attributed to the variations in density of the fibrillar packing across the cotton fibre bilateral structure. It was discovered that the fibrillar width dimensions within dyed cellulose samples were larger than in the undyed cellulose samples. The data suggested that the dyeing process altered the physical structure of the cellulose within the samples most likely through swelling. This in turn would have lead to hydrogen bond breakages between cellulose chain molecules, facilitating entry of dye molecule into the fibrillar matrix. Also within the AFM study, phase images displayed contrast detail when using modified tips, which highlighted the tip sensitivity to the presence of –OH groups (from the surface of samples), as possible crystalline/amorphous regions were visualised. Tip sensitivity to –OH groups, also permitted the use of a-p-d curves measurements of a dye border cellophane sample, to successfully fingerprint dyed and undyed regions within the same sample. Other surface science techniques were also employed in the chemical investigations of dyed and undyed cellulose samples. Both EDAX and ToF-SIMS analysis successfully detected dye compound from the surface

of dyed cellulose samples. The presence of diagnostic peaks for dye compounds therefore proved that qualitative surface analysis was possible. In this chapter we move the focus of the study into identifying possible dye-uptake mechanism(s), based upon the knowledge gained in previous chapters.

## **5.1 INTRODUCTION**

There is limited knowledge of dye-uptake mechanisms within cotton fibres, as there is no single interpretation for the interaction of dyes with fibres. However, most studies agree that the dyeing-mechanism within cellulose is linked to the crystal structure<sup>119,120,122</sup>, as it is thought that dye binding occurs more predominantly in either crystalline or amorphous regions. This reason has provided the motivation for this study, by focussing on the possible crystalline/amorphous regions within cellulose, it is hoped that the most probable mechanism for dye-binding will be in some way elucidated. By improving the knowledge of dye-uptake mechanism within cellulose textiles, it is anticipated that it may help to improve dye synthesis and or dyeing methods in the future. In this chapter we utilise XPS, to aid quantification of dye compound (dye loading) on dyed cotton cellulose fibres. Also DSC analysis of dyed and undyed cotton cellulose will highlight thermal transition indicative of crystalline or amorphous structures. Lastly, AFM based studies will be presented which utilise dye functionalised tips to directly probe examine the interaction forces between dye molecules and cellulose fibre surfaces.

## 5.2 EXPERIMENTAL

The experiments detailed here examined dyed cotton cloths through the use of XPS, AFM and DSC analysis. Any experimental conditions which otherwise differ from ones previously discussed in chapter 2 are stated with the figure or data in question.

### 5.2.1 Samples

All cotton cloth samples examined within this study were manufactured at DyStar UK (DyStar UK, Cheadle Hulme, UK), using an exhaustive dyeing process<sup>283</sup>. A series of cotton cloths were dyed with reactive dye, Yellow 2 (see Figure 4.1, section 4.2.2 for chemical structure), which was synthesised at DyStar UK by following an existing exhaustive dyeing method (dye and NaCl added to dyebath at 90°C dyeing for 30 minutes, then addition of sodium carbonate to dyebath and fixed for a further 60 minutes, followed by washing off period for 15 minutes with Dekol SAD 98 (a detergent)). Each cloth within the series had one factor of a single dyeing stage altered prior to dyeing with Yellow 2. The samples which were analysed by XPS included three cloths with increasing dye content: 1%, 4% and 9% w/v concentration (optimum w/v concentration is 4%), which for the purpose of this thesis shall be referred to as *build-up* cloth samples. Analysis was also carried out on two other cloths in which the salt (sodium chloride, NaCl) content of the dyebath was altered: 35g/L and 140g/L. The normal optimum salt content for a dyebath is 65g/L, and these cloths shall be referred to within this chapter as *salt-load* cloths. All samples were compared with an undyed cloth sample. The cloth samples analysed by DSC were also supplied by DyStar UK (identical to samples used

in chapter 4) and were dyed using Yellow 2 reactive dye. AFM analysis using dye-functionalised tips was carried out on undyed and dyed cellophane samples (as used in chapter 3), as these samples posed less problems than cotton fibres, with respect to imaging.

## **5.2.2 Sample preparation and analysis**

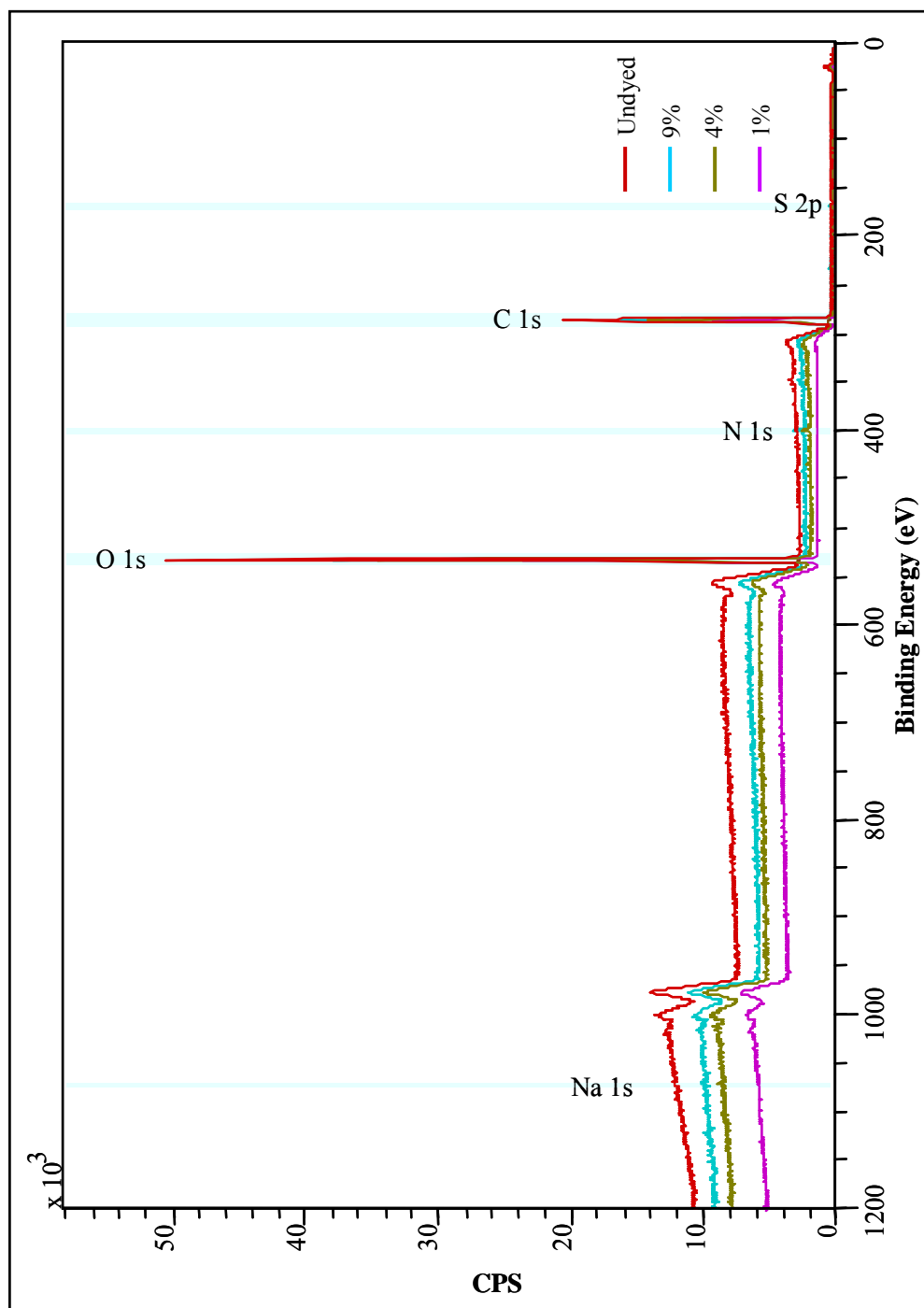
All sample preparation and analysis methods for the cotton cloths are detailed within section 2.3.3 for XPS analysis, section 2.5.3 for DSC sample preparation and analysis and section 2.1.4 for AFM analysis.

## **5.3 RESULTS AND DISCUSSION**

### **5.3.1 XPS analysis of dyed cotton**

The cotton cloth samples composed entirely of cellulose polymer would be predicted to display carbon and oxygen peaks within the XPS spectra as they are characteristic of cellulose (refer to Figure 1.1, section 1.2). This is in contrast with the dye compound, Yellow 2 which is nitrogen-rich. The nitrogen peak in the XPS spectra could therefore be used as a diagnostic peak characteristic of dye compound with the cotton sample.

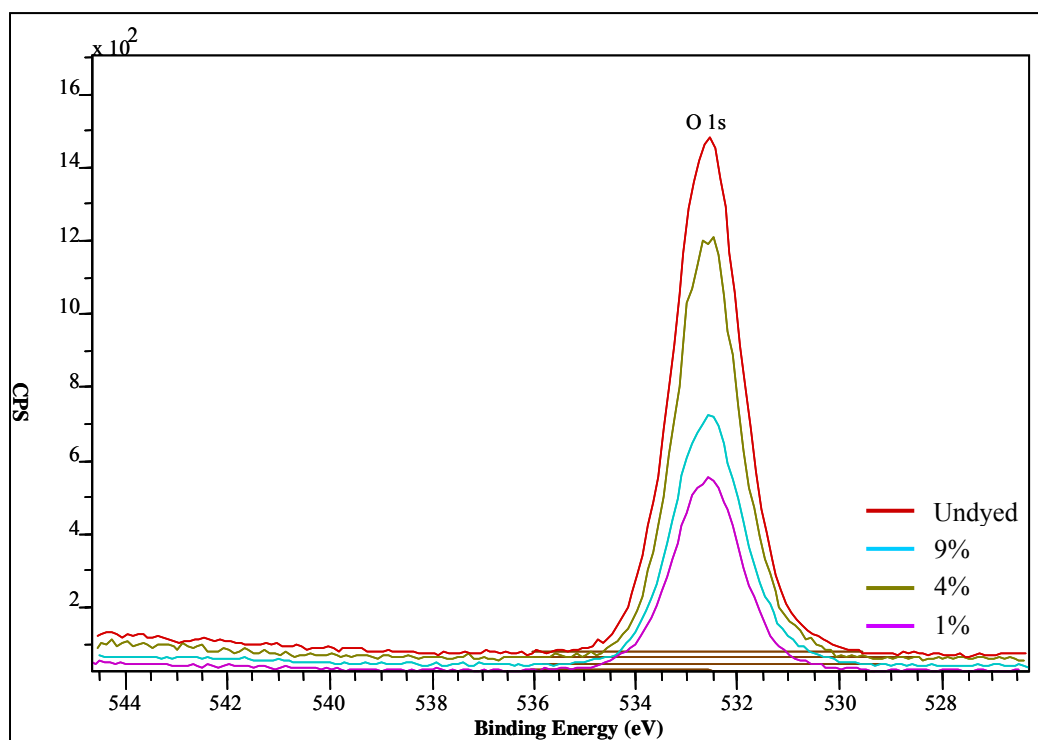
All data sets were charge corrected to the O 1s peak at 532.6eV, the reference value for oxygen atom in the C-OH environment<sup>284</sup>. This was used as an internal standard for all spectra, to correct the binding energy shift due to charging. This correction was applied to all element peaks following a background subtraction/peak deconvolution to give ‘true’ binding energy values. Peak assignment was done by reference<sup>284,285,286</sup>.



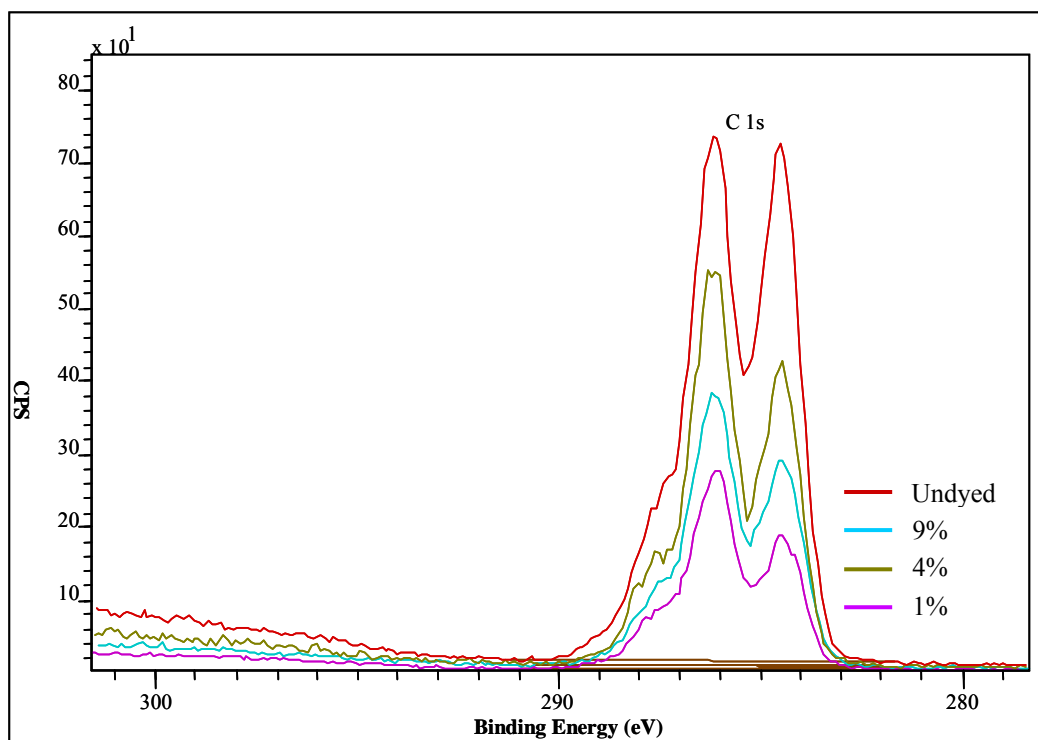
**Figure 5.1** Overlaid wide scan XPS spectra, displaying results for build-up samples compared with undyed cotton cloth.

Figure 5.1 displays typical wide scan XPS spectra recorded from the undyed cloth sample and 1%, 4% and 9% dye build-up cotton samples. The spectra shows peak intensities for oxygen 1s (O 1s atomic orbital) and carbon 1s (C 1s atomic orbital), and also highlights traces of nitrogen 1s (N 1s atomic orbital), sodium 1s (Na 1s) and sulphur 2p (S 2p) although they are difficult to see within the wide scan. The most intense peak with a binding energy value at 530eV corresponds to O 1s atomic orbital. The next binding energy value at 285eV relates to C 1s atomic orbital.

The build-up samples were also analysed using narrow scans of the important peak areas, i.e. areas of known elements (for example, C, O, N) were analysed at a higher resolution than that obtained for wide scan spectra. Figure 5.2 displays narrow scan spectra of the O 1s atomic orbital peak area, it shows spectra for all the build-up samples. The spectra show that the undyed cloth has the highest presence of O 1s relative to the other dyed samples. The next highest intensity of the O 1s orbital peak is in build-up sample, 4%, then 9% and 1% respectively. Figure 5.3 displays narrow scan spectra of C 1s, which displays a multi-component envelope. Figure 5.4 highlights the components within the C 1s envelope, which have been curve-fitted using the Gaussian-Lorentzian sum function<sup>287</sup>, with chemical shifts relative to C-C/C-H (C1), C-O for (C2), O-C-O (C3) and COO<sup>-</sup> (C4). It also follows a similar pattern of Figure 5.2, as the undyed sample displays the highest C 1s peak, followed by 4% dyed cloth, then 9% and 1%.



**Figure 5.2** Narrow scan spectra of O 1s region in build-up samples.



**Figure 5.3** Narrow scan spectra of C 1s region in build-up samples.

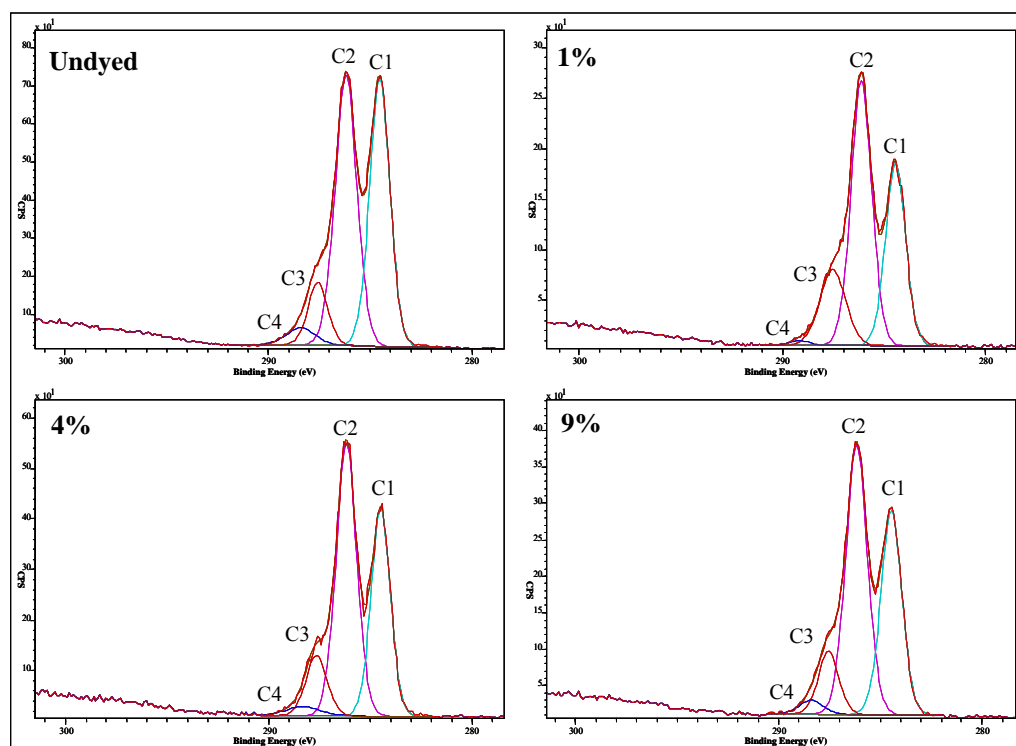


**Figure 5.4** Narrow scan spectra of C 1s envelope fitted with components.

In Figures 5.2 and 5.3, the O 1s and C 1s peaks can be attributed to the cellulose polymer; therefore it is safe to assume that undyed sample would display the highest peak concentration for these two peaks as it is composed solely of cellulose. It could be hypothesised that as dye is introduced to the fibre, the dye compound coats the surface of the fibre and masks these peaks, leading to their gradual reduction with increasing dye concentration. However within the two mentioned spectra the 4% depth dyed cloth had the next highest peak concentration of O 1s and C 1s atomic orbital after the undyed cloth, followed by 9% build-up cloth and then lastly 1%.

In the dyeing industry the optimal w/v dye compound required in the exhaust dyeing process for reactive dye compound is approximately 4%, as it provides a level dyeing into the bulk and surface of the fibre. This reason may help to explain why the 4% build-up cloth had the second highest O 1s and C 1s atomic orbital peaks after the undyed cloth sample. As optimal dyeing with 4%, may mainly dye the bulk of the fibre rather than the surface. However, it would be expected that the 1% build-up cloth would display similar peak concentrations to the undyed cloth, as it is the lowest dye concentration used within the series. However, this concentration had the biggest effect on the peak concentrations in masking their strength, this may have been due to the dye compound remaining at the surface of the cotton fibre, and not entering the bulk of the fibre. This is supported in literature by Gooding et al. who studied the kinetics and mechanism of dye-uptake in cotton cloths. They hypothesised that the dye passed from the bulk solution (dyebath) through a porous surface layer within the cloth, before passing into the bulk cloth, and adsorption onto surface sites in this porous layer blocked the passage of further dye into the cloth (see Figure 1.11, section 1.4.1). The 9% build-up cloth may have been such a high concentration that the fibres displayed both effects, that is, both bulk dye entry due to higher numbers of dye compound molecules and also surface adsorption; as excessive dye molecules would block possible porous routes into the bulk fibre by aggregating on the surface of the fibre.

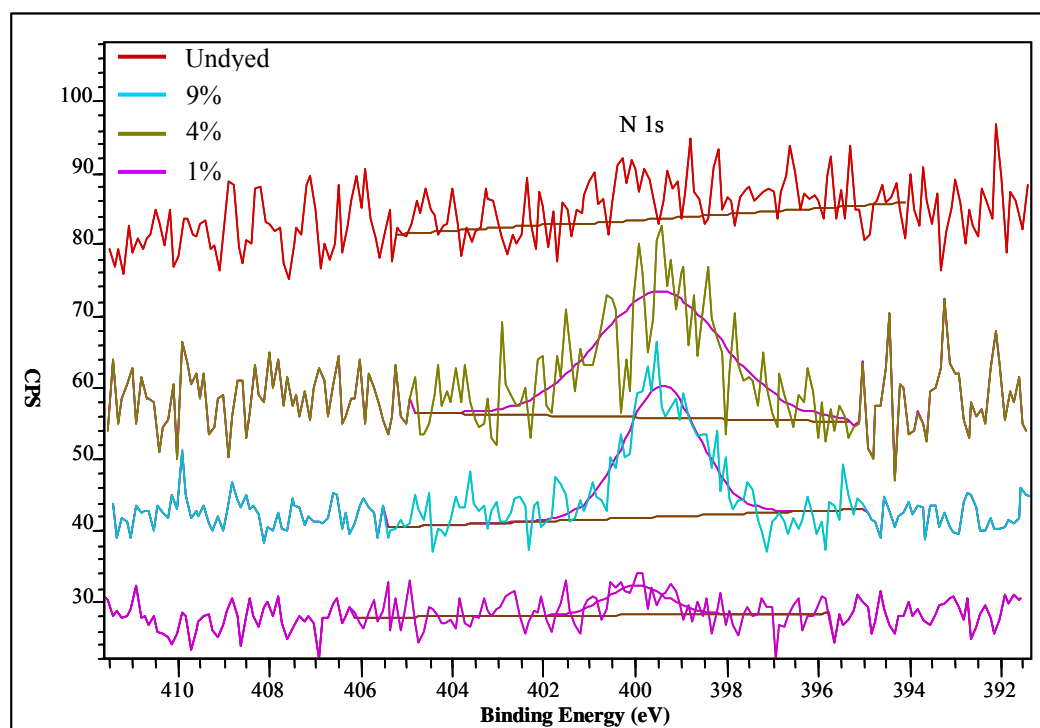


**Figure 5.5** Narrow scan spectra displaying the N 1s region.

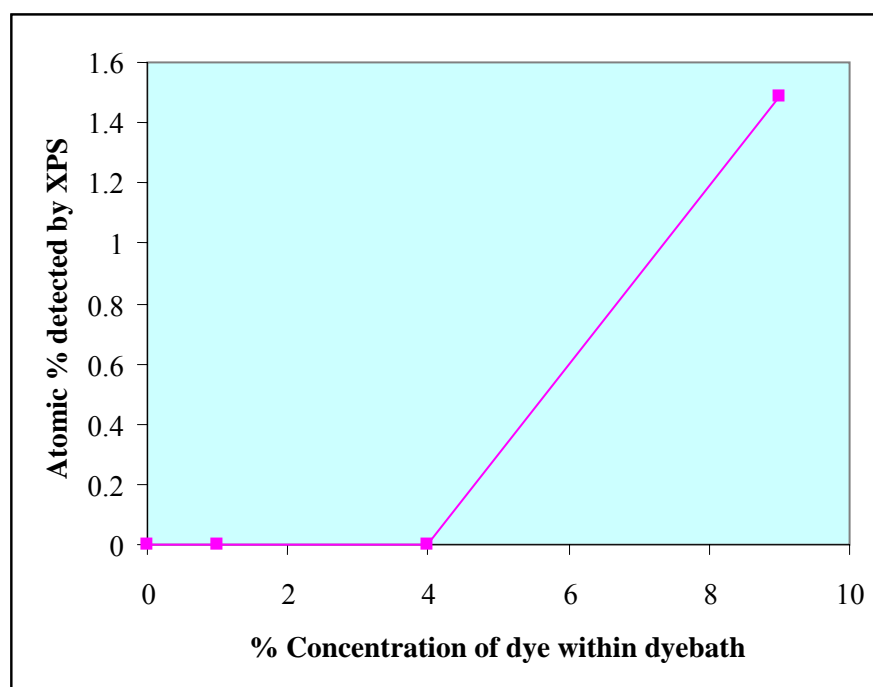


**Figure 5.6** Atomic percentage of [N] detected by XPS within build-up samples.

It is hence the surface sensitivity of XPS where the experimental sampling depth is  $<10\text{nm}^{288}$ , that reveals the surface loading of the dye in these fibres. This conclusion is supported by considering the diagnostic N 1s peak (attributed solely to the dye compound), in the narrow scan spectra displayed in Figure 5.5. The noise to peak ratio being largest for the 9% depth dyed cloth, with a percentage atomic concentration (% At. conc.) of 1.49. Which were determined through Kratos sensitivity factors, from the peak areas at FWHM. XPS therefore is able to both detect and rank the dye loading at the surface as one would expect for the bulk dyeing ratios. Figure 5.6 displays graphically the percentage atomic concentration of N detected within the build-up samples.

Element	Undyed	1%	4%	9%	35g/L	140g/L
O 1s	28.58	31.69	32.39	29.47	29.18	29.06
N 1s	0.00	0.00	0.00	1.49	1.00	1.49
C 1s	70.87	54.29	56.95	67.99	69.60	68.81
S 2p	0.37	13.1	9.84	0.74	0.22	0.58
Si 2p	0.18	0.44	0.34	0.31	0.10	0.00
Ca 2p	0.00	0.48	0.48	0.00	0.00	0.00
Na 1s	0.00	0.00	0.00	0.00	0.00	0.06

**Table 5.1** Quantification table displaying percentage atomic concentration (% At. conc.) of elements within build-up and salt-loaded samples.

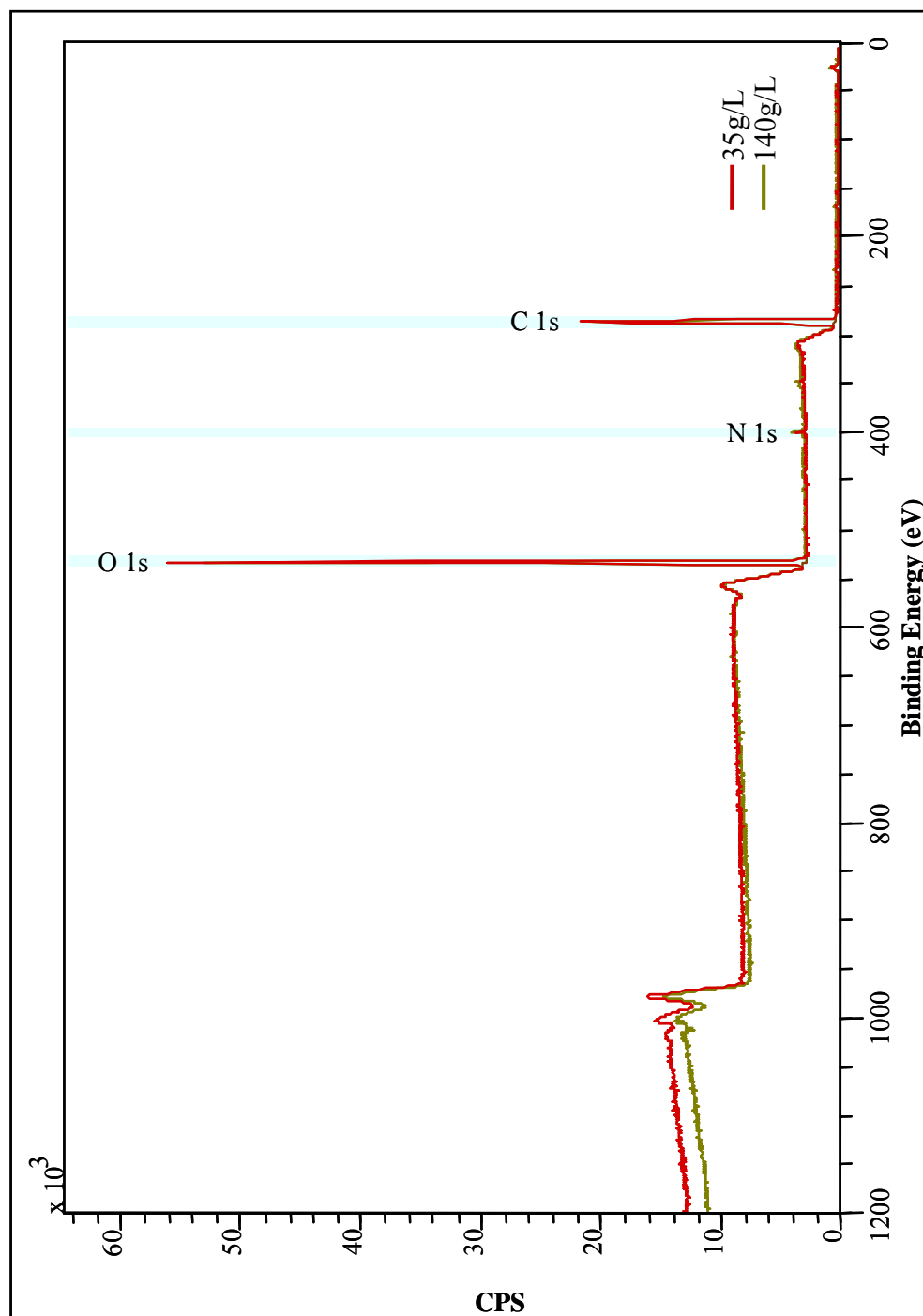


**Figure 5.7** Overlaid wide scan XPS spectra displaying salt-load cloth samples.

After examining the build-up cloths, the salt-load cloths were examined by XPS using the same experimental conditions. One sample had a low salt content, 35g/L, added to the dyebath, and the other had a high salt content (140g/L). The normal optimum salt content for exhaust dyeing process is 65g/L, and a dye concentration for both samples was 4% w/v Yellow 2 dye compound. Figure 5.7 displays the wide scan spectra for the salt-load cloths. Peaks for the O 1s, C 1s and N 1s atomic orbitals are observed at 530eV, 285eV and 398eV respectively. The red line represents the low salt content cloth (35g/L) spectra and the green line represents the high salt content (140g/L) spectra.

Figures 5.8 and 5.9 displays the narrow scan spectra of the O 1s and C 1s atomic orbital regions respectively for the salt-loaded cloths. The peaks intensity is very similar for both samples. However the high salt-loaded sample, which is represented by the green line in the spectra, is marginally higher in peak intensity to the low salt-loaded sample (see peak components in Figure 5.10). One would not expect a difference in peak intensities when the same dye concentration (4% w/v) is used in both the samples, hence the similarity in peak intensity for O 1s and C 1s atomic orbitals in both samples. The results are also comparable to the 4% depth dyed cloth in the build-up samples which display similar peak intensity.

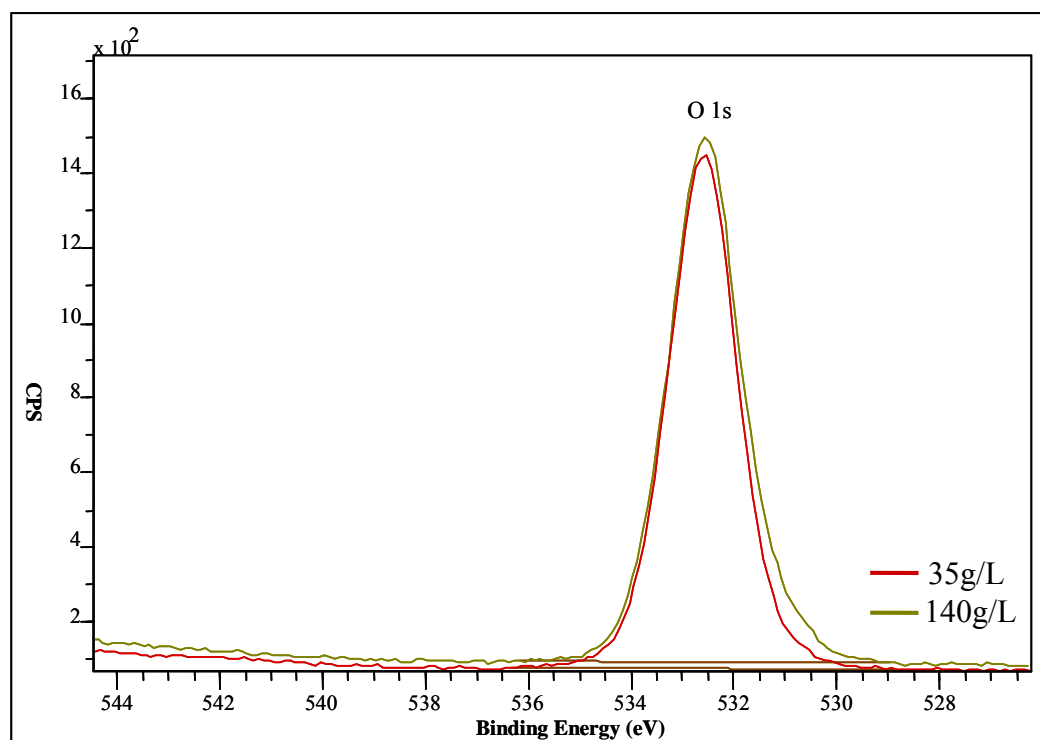


**Figure 5.8** Narrow scan spectra of O 1s atomic orbital for salt-load cloth samples.

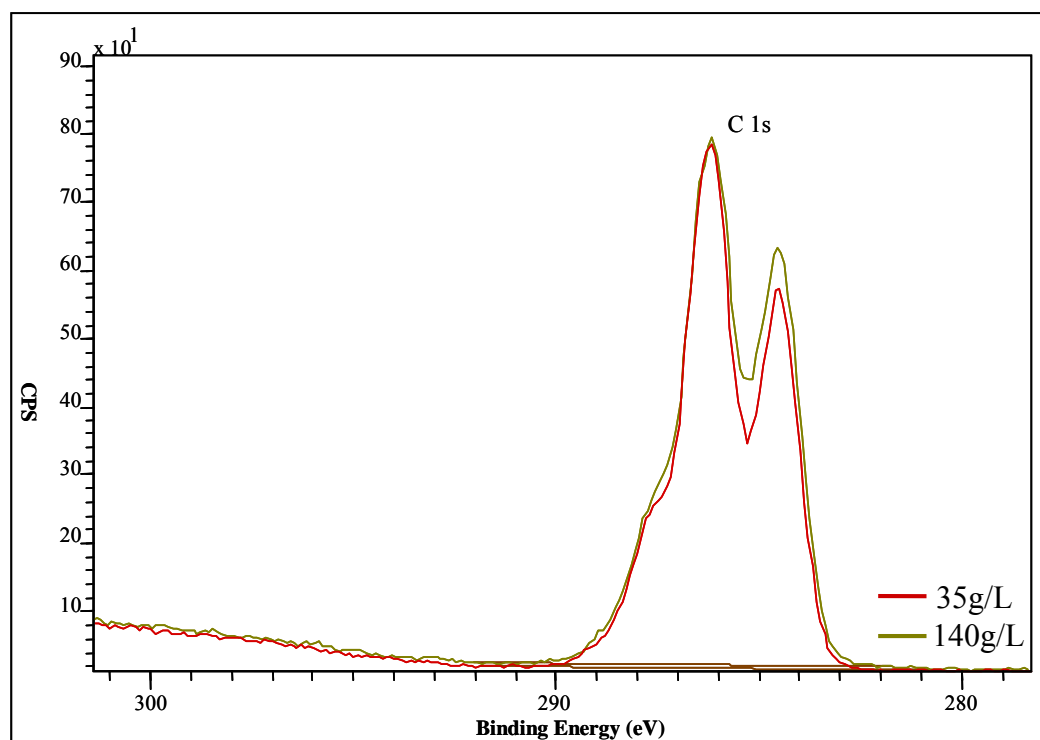


**Figure 5.9** Narrow scan spectra of C 1s atomic orbital for salt-load cloth samples.

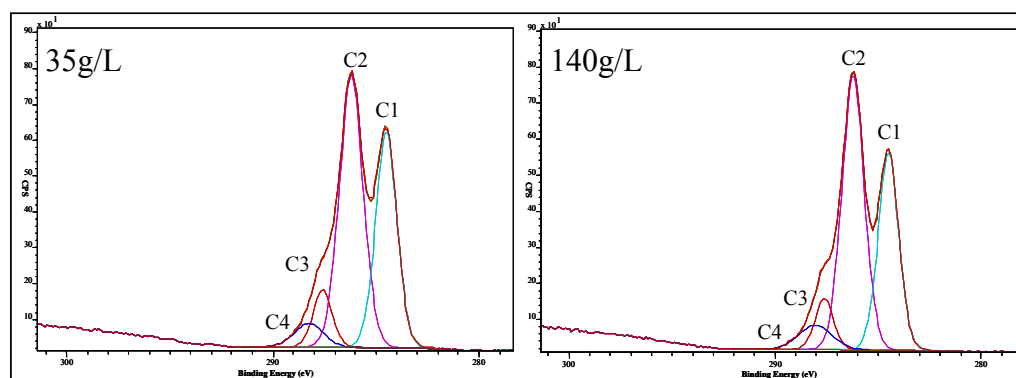


**Figure 5.10** Narrow scan spectra of C 1s envelope fitted with components for salt-load samples.

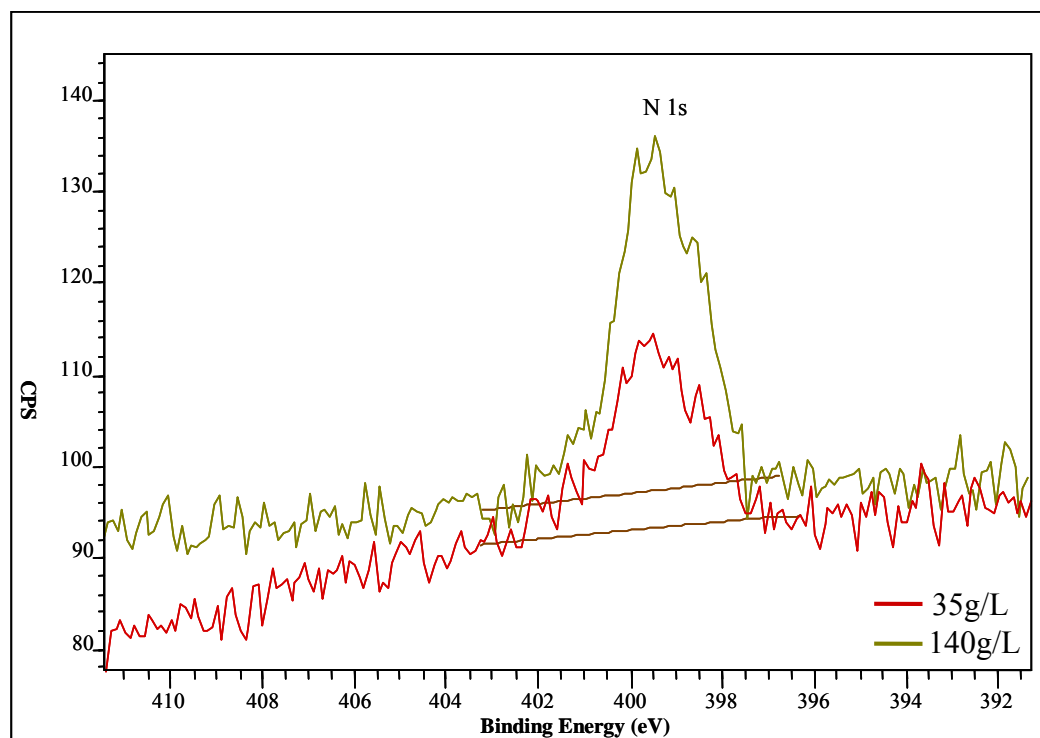


**Figure 5.11** Narrow scan spectra of N1s atomic orbital region for salt-load cloth samples.

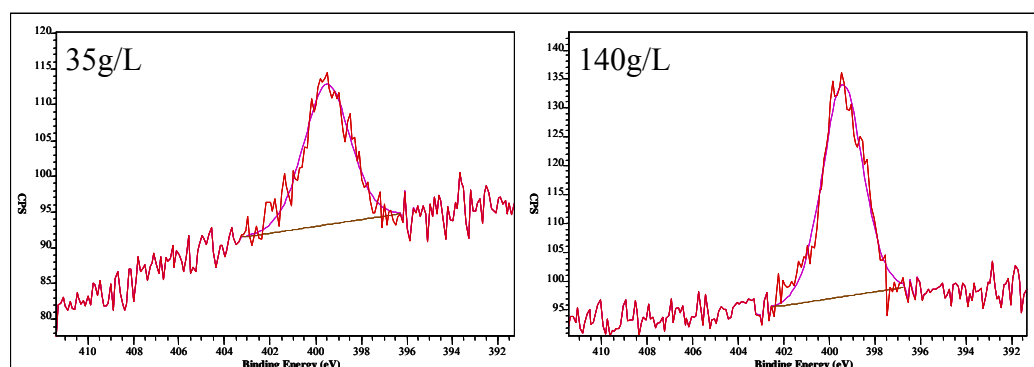


**Figure 5.11** Narrow scan spectra of N1s atomic orbital region for salt-loaded cloth samples.

It was difficult to discern any changes of dye content within the two salt-loaded samples using the O 1s and C 1s atomic orbital peak regions, as these elements are present in both the cellulose polymer, and also the dye compound. The N 1s atomic orbital region was therefore examined in both samples, as this was diagnostic to the dye compound (due to the sole occurrence of N in the dye compound). Figure 5.11 displays the narrow scan spectra for the N 1s atomic orbital region in the salt-loaded cloth samples.

It is evident from the spectra in Figure 5.11 that high salt-loaded sample displayed the highest the peak intensity for the N 1s atomic orbital (1.49% At. conc. (calculated through Kratos sensitivity factors at FWHM), see Table 5.1), and the low salt-loaded sample had weaker peak intensity (1.00% At. conc., see Table 5.1) than the high salt-load sample. These results suggest that the common salt content had a large influence on how much dye loading took place on the cloth samples. Within the exhaust dyeing process, NaCl is used to fix dye compound to the cotton cellulose substrate, but it is unclear within the

textile industry how this precisely works. Although it has been previously detailed within literature that the use of NaOH on cotton fabric during mercerisation, causes the  $\text{Na}^+$  to form an ionic association with the cellulose, resulting in a change of the crystalline structure, from cellulose I to cellulose II (a more stable crystal structure due to increased hydrogen bonding). Perhaps in the same way the  $\text{Na}^+$  from salt could also result in an ionic association with the cellulose polymer. As hydrogen bond breakages between cellulose chain molecules (thought to be amorphous regions) through swelling process in dyebath, would create more movement between the chain molecules and thus allowing  $\text{Na}^+$  molecules to enter the fibre matrix. Therefore the XPS results quantitatively show that increasing the NaCl concentration in the dyebath increases the dye-uptake in the fibres.

Figure 5.11 displays the Na 1s atomic orbital region in the salt-loaded cloth samples. The high-salt content sample (represented by green line in spectra) shows that traces of  $\text{Na}^+$  remained at the surface of the cotton fibre as signal to noise ratio was higher than the low-salt cloth sample (represented by red line within spectra). The high-salt cloth had over twice as much salt, compared with the considered 'optimum' amount, at 140g/L within the dyebath. During exhaust dyeing, the salt is removed from cloth during a 15 minute *washing-off* period. It is most likely that not all of the salt was removed from the high-salt cloth during this washing stage, as an excessive amount was used, perhaps requiring a longer washing-off period. The  $\text{Na}^+$  ion is thought to dissociate from the cellulose polymer during washing, as in mercerisation, which would leave the dye molecules trapped within the fibre matrix.

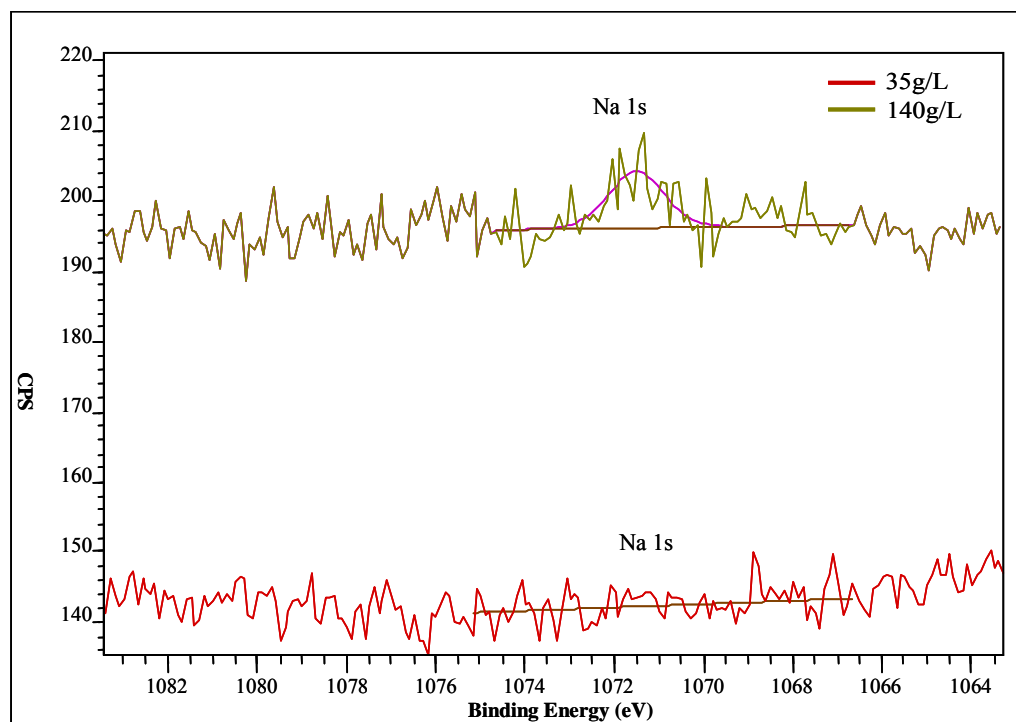


**Figure 5.11** Narrow scan of Na 1s atomic orbital region in salt-loaded cloth samples.

XPS data showed quantitative differences in the amount of dye present on the surface of the build-up cloth samples; this was deduced through the diagnostic N 1s atomic orbital peak. The data showed that there were notable differences in the surface concentration of dye, dependent on the concentration applied. Salt content had a direct influence on how much dye was loaded onto the cellulose substrate.

### 5.3.2 DSC comparison analysis

Thermal analysis of the cotton fibre samples was carried out to determine any thermal transitions, which might be characteristic of crystalline or amorphous structure (and any change in these following dyeing), as the AFM data within chapter 4 suggested the presence of both types of structure (due to density of

fibrillar packing) in the surface morphology. It is known that the pyrolysis of cellulose is a very complex chemical process and is commonly believed to involve two different mechanisms: (i) the dewatering and charring of cellulose producing H<sub>2</sub>O, CO<sub>2</sub> and solid residues and (ii) the production of the non-volatile liquid L-glucose (CH<sub>2</sub>OH occurring at C4 instead of C5, refer to Figure 1.1, section 1.2), by depolymerisation (its further cleavage produces flammable low molecular weight products).

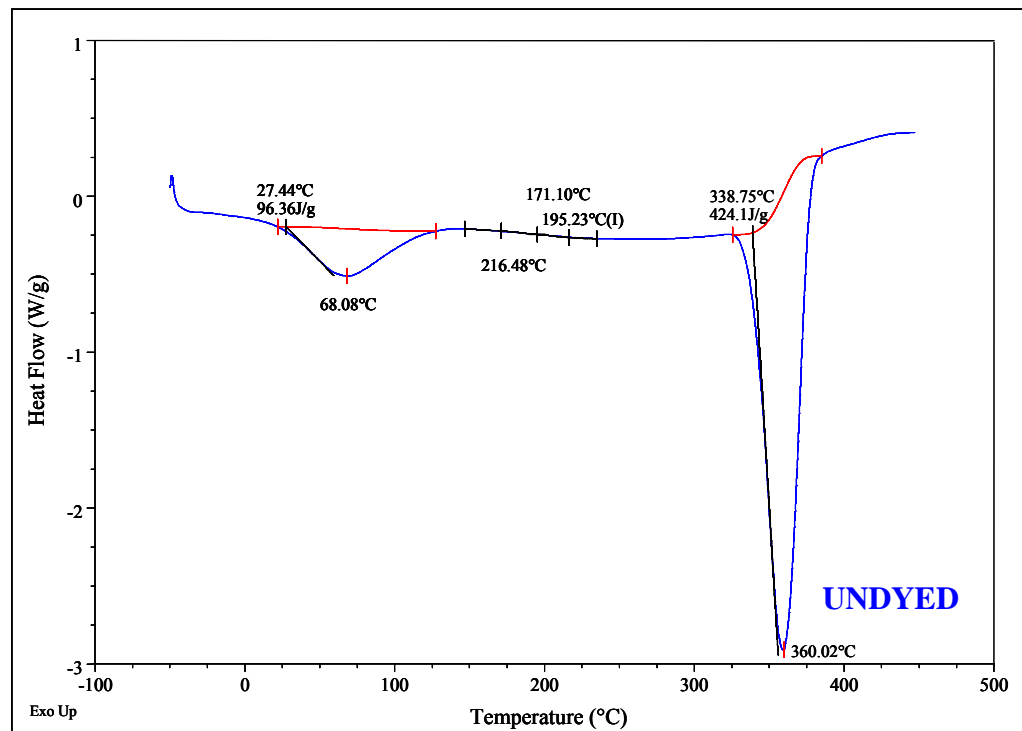


**Figure 5.12** Typical DSC curve for undyed cotton cloth sample displaying thermal transitions.

The DSC curves presented in Figure 5.12 display typical results which were obtained for the undyed and Yellow 2 dyed cotton cloth samples. Within the undyed sample the DSC curve displays many thermal transitions which include

a small endothermic peak ranging from 30 to 130°C and reaches a maximum at 68°C. This confers well with figures cited within the literature<sup>229</sup>, which attribute an endotherm peak of 80°C to the loss of adsorbed moisture. Also within the curve is the presence of another, much larger endothermic peak ranging from 330°C to 390°C with a peak maximum at 360°C. Again this confers well with literature<sup>289,230</sup>, which states a large endotherm in the 300°C to 380°C. This was ascribed to the production of non-volatile pyrolysis products, such as L-glucose (major product) and combustible gases, due to the depolymerisation of the cellulose polymer. Zhu et al. suggested that the endotherm and rapid weight loss (due to the pyrolysis) occurred mainly in amorphous regions of the cellulose polymer.

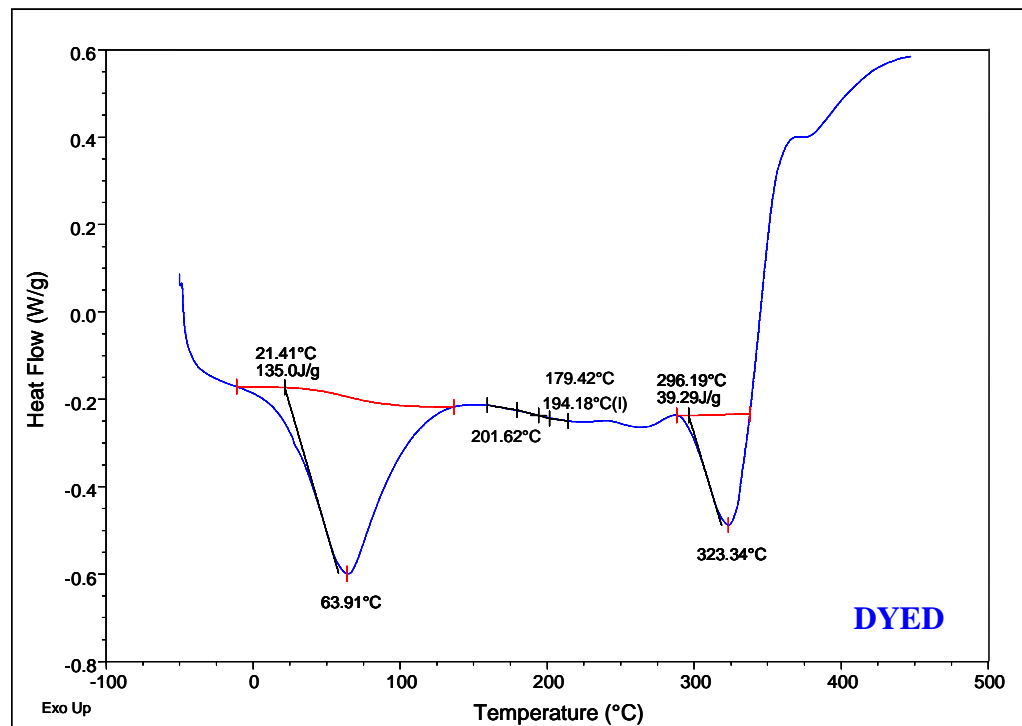


**Figure 5.13** Typical DSC curves for Yellow 2 dyed cotton cloth sample displaying thermal transitions.

In comparison to the undyed cotton cloth, the DSC curve for the Yellow 2 dyed cotton cloth in Figure 5.13 displays a slightly broader endothermic peak ranging from 0 to 135°C, with a peak maximum at approximately 64°C, similar to the endothermic peak in the undyed sample. Again this is attributed to the dehydration of adsorbed water and subsequent and depolymerisation of cellulose. An endothermic peak is observed at peak maxima 323°C after the  $T_g$ , which is again is similar to the undyed sample but at a lower temperature. This suggests a smaller amount of combustible products being produced through pyrolysis, and which may be due to the presence of increased crystallinity induced during dyeing, as the dye compound is thought to be entrapped in a slightly more stable crystalline structure than the undyed cotton sample (as previously discussed in section 5.3.1).

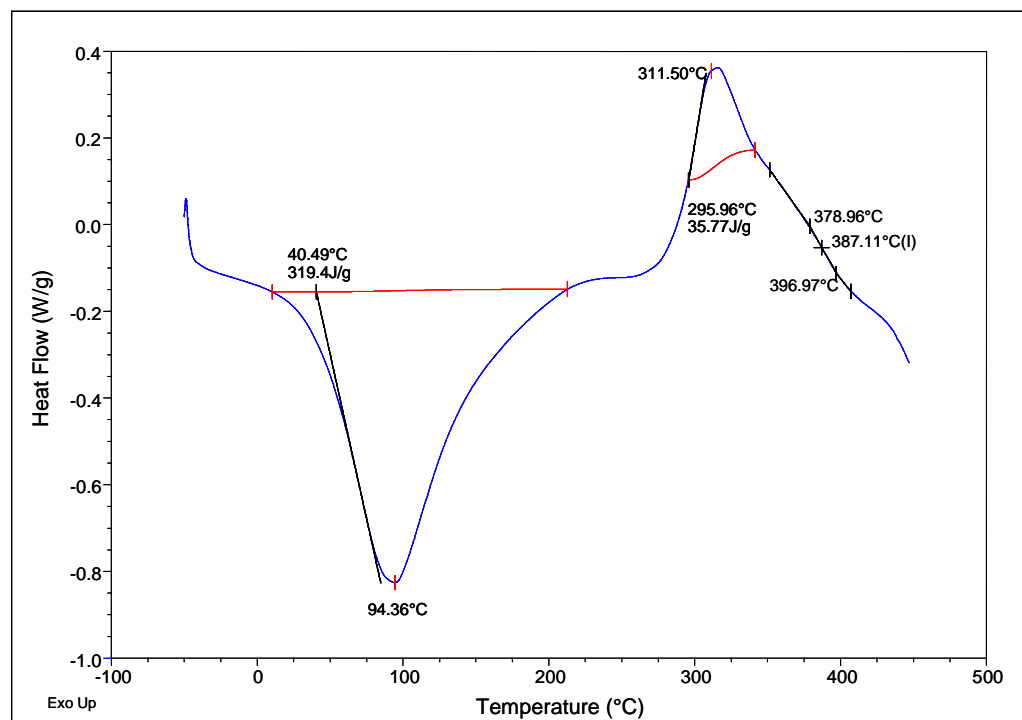


**Figure 5.14** Typical DSC curves for Yellow 2 dye compound sample displaying thermal transitions.

Figure 5.14 displays the DSC curve for the dye compound, to provide a comparison with the dyed cotton DSC curve. An endothermic peak is observed with peak maxima at 94°C, almost 30°C higher than both cotton samples with a very broad peak. This is assigned to the dehydration of the sample. Within this curve, we see an exothermic peak ranging from 290°C to 350°C with maxima at 311.50°C, which we can ascribe to the decomposition of the dye compound and combustion of volatile products. The DSC curve for the dye compound is very distinctive and has many thermal transitions occurring between 300°C and 400°C which could easily hide/mask any transitions occurring from the cellulose substrate within the dyed cotton sample. The transitions which were observed within the dye compound occur at nearly the same temperatures as the transitions observed in both cotton samples, which are highlighted by overlaying all three DSC curves, (see Figure 5.15). This would in part help to explain why little differences could be analysed between the undyed and dyed cotton samples.

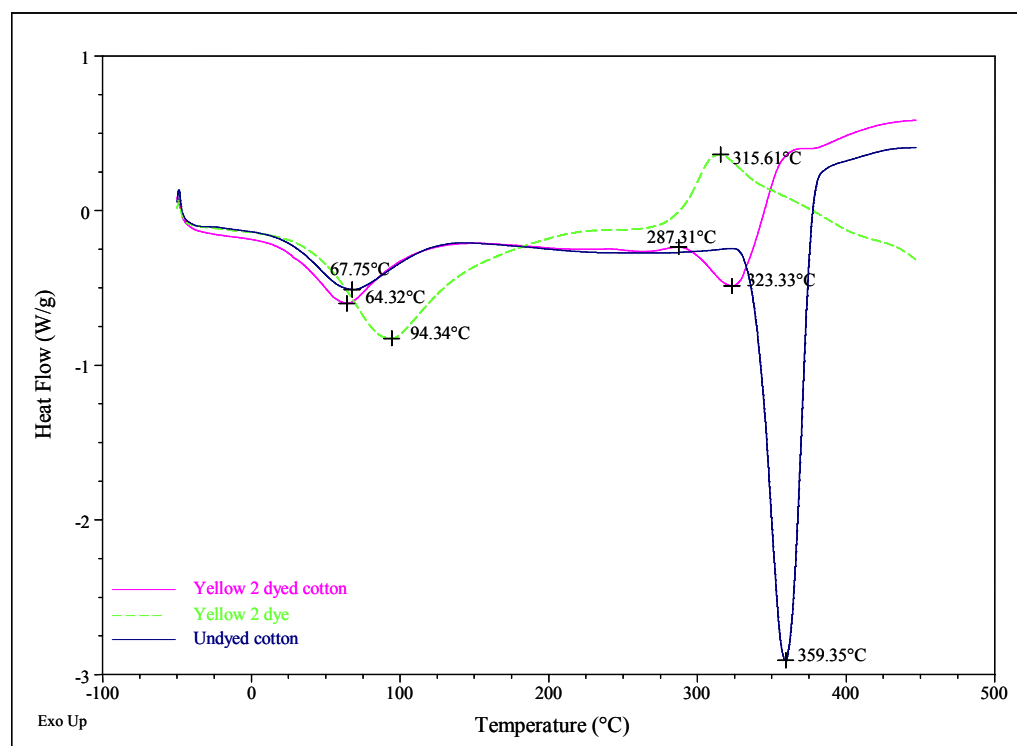


**Figure 5.15** Overlaid DSC curves for undyed, Yellow 2 dyed cloth and Yellow 2 dye compound, highlighting specific points of interest.

### 5.3.3 AFM dye-fibre interaction analysis

Within the previous AFM studies in chapters 3 and 4 we have observed phase contrast details within images using modified tips, which we suggested may reflect differences in the surface crystallinity/amorphosity of the cellulose samples. We were also able to successfully fingerprint areas of dyed and undyed cellulose in cellophane films using a-p-d curves. To further develop this approach and directly probe the dye-fibre surface interaction, preliminary AFM investigations of cellophane films using Blue 1 dye functionalised tips were performed. Using an adaptation of colloid probe AFM<sup>290,291</sup> (tips functionalised with (drug) particles to probes in order to directly measure adhesion forces occurring between the colloid probe and sample), it was hoped

that by functionalising tips with dye molecules, we could observe the nature of the interactions occurring between the dye molecules and specific regions within the cellulose surface and potentially further elucidate any potential affinity for crystalline/amorphous regions. Again due to the challenging nature of these experiments this study was carried out on cellophane films, as they posed fewer problems (with respect to surface topography) for AFM analysis.

Dye functionalised tips were produced by plasma etching using a Bio-Rad RF Plasma Barrel Etcher (Polaron Equipment Ltd, Watford, UK), for 20 seconds at 100W in an oxygen atmosphere at a pressure of  $2 \times 10^{-2}$  mbar. The ion bombardment cleaned the surfaces of cantilevers physically and chemically of any contaminants, (a method adopted from Ton-That et al.). By plasma-etching in oxygen the surface of the AFM tip is oxidised, introducing silanol groups and thus providing –OH groups for reaction with the dye in the subsequent steps. Next the oxidised tip was placed in a dyebath of 5% w/v Blue 1 dye (see Figure 3.1, section 3.2) (in water) using an adapted method of the exhaustive dyeing process, in order to deposit dye molecules onto the surface of the tip. The reactive dye, Blue 1, contained chlorotriazine groups which reacted with the –OH groups from the surface of the plasma-etched tip, to form covalent bonds, thus ‘dyeing’ the tip. The tip was then washed in water for 10 minutes to remove any excess dye from the surface; successful deposition of the tip changed the colour of the tip (usually greyish/silver in colour) to a blue colour.

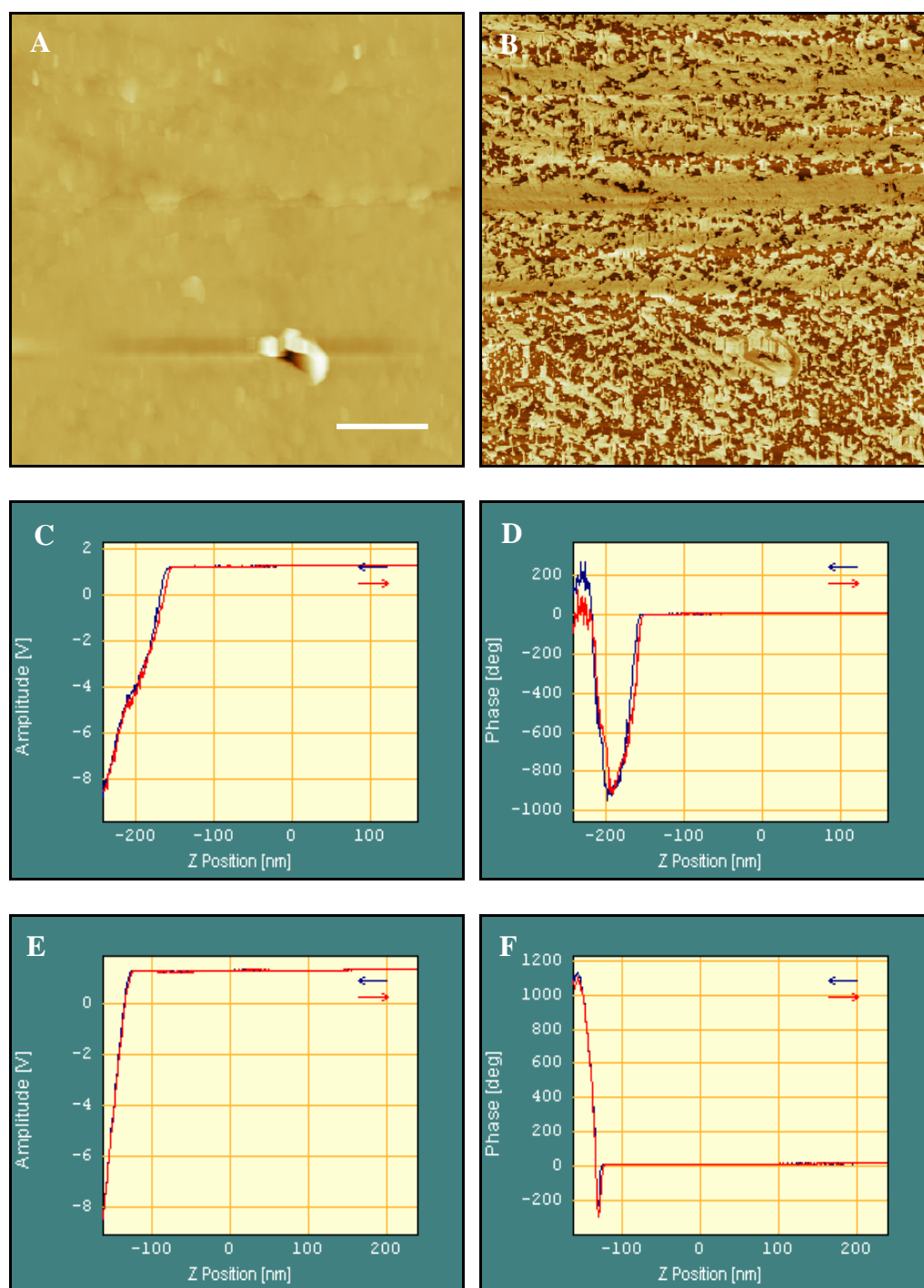


**Figure 5.16** A  $5\mu\text{m} \times 5\mu\text{m}$  DI 3000 AFM image of topography (A) and phase (B) of undyed cellophane film obtained using a Blue 1 dye-functionalised tip in TM in air, (Z-range 346.3nm and scale bar  $1\mu\text{m}$ ). Initial a-p-d curves measurements displayed in curves (C) and (D), and subsequent measurements displayed in curves (E) and (F).

Figure 5.16 displays an AFM image of undyed cellophane film (as used in chapter 3) obtained using a Blue 1 dye functionalised tip using TM in air. The topography image (A) lacks the resolution of previously displayed AFM images (as seen in chapters 3 and 4), most likely due to the successful deposition of dye onto the tip. The phase image within Figure 5.16 however displays considerable detail, which may reflect the different interactions of the dye-functionalised tip with the different crystalline/amorphous regions within the cellophane film sample. A-p-d curves measurements were obtained from the image to further investigate the nature of the interaction between the dye functionalise tip and cellulose sample surface. Ten a-p-d measurements were taken from the centre of the phase image over a few seconds. The initial a-p-d curves displayed in curves (C) and (D) displayed a strong attractive profile, which suggested a strong adhesion force between the dye functionalised tip and cellulose sample. This may have reflected the high affinity of the dye for binding sites within the sample. However the profile of the a-p-d curves changed rapidly towards the end of the recorded measurements, curves (E) and (F) display a repulsive profile, which suggests a weaker adhesion force between the dyed tip and cellulose surface. The change in profile from attractive to repulsive in the a-p-d curves, suggests a loss of dye material from the tip or contamination of the tip through the *pick-up* of material on the cellulose surface. The origin of the a-p-d profiles could have been further explained by obtaining curve measurements from the light and dark regions within the phase image, as these areas may have displayed different profiles (attractive or repulsive force between tip-sample), which would reflect possible dye-binding sites. Unfortunately, during the study it was found that dye

functionalised tips would often become damaged or break due to very strong interactions between the probe and sample surface, thus making these measurements very difficult to obtain.

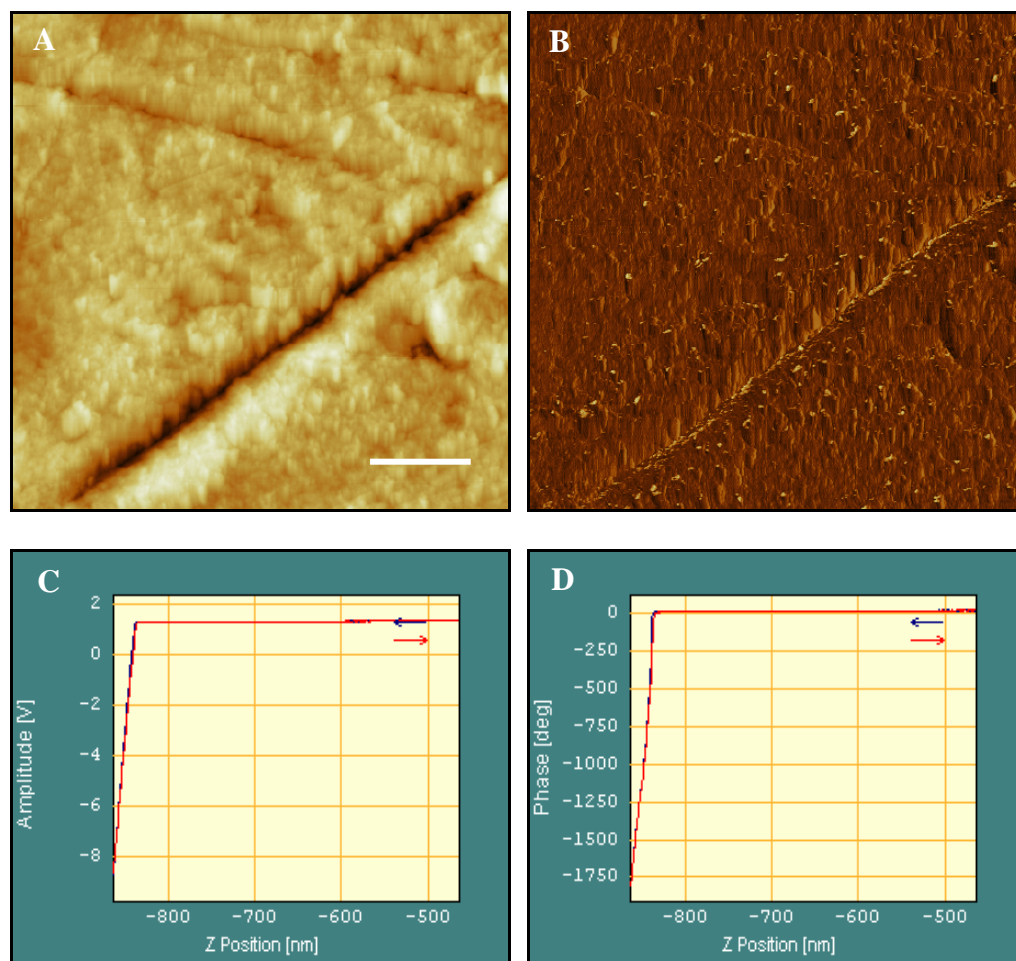


**Figure 5.17** A  $5\mu\text{m} \times 5\mu\text{m}$  DI 3000 AFM image of topography (A) and phase (B) of Blue 1 dyed cellophane film obtained using a Blue 1 dye-functionalised tip in TM in air, (Z-range 91nm and scale bar  $1\mu\text{m}$ ). A-p-d curves measurements displayed in curves (C) and (D).

Figure 5.17 displays an AFM image of Blue 1 dyed cellophane film obtained using a Blue 1 dye-functionalised tip. Again the topography image (A) lacks the resolution of previous AFM images in chapters 3 and 4, due to tip

convolution. The phase image (B) shows little contrast detail compared with the phase image obtained for the undyed cellophane sample (image (B) in Figure 5.16), this may reflect a homogenous surface chemistry due to even distribution of dye across the sample surface. Alternatively it may reflect a lack of sensitivity of the tip to the sample surface due to the removal of dye deposits from the tip during imaging. However, the a-p-d measurements obtained from the sample surface suggested that a loss of dye deposition did not occur, due to the curve profile obtained. A-p-d measurements from the phase image all displayed the same result, the typical profile displayed in curves (C) and (D) which show what appears to be the early part of an attractive profile. The possible attractive profile, again suggests an affinity of the dye molecule to the dyed sample surface, this may be due to the same functionalised groups present on both the tip and sample surface.

The AFM data obtained using dye-functionalised tips thus did show that the tip behaved differently towards the different samples, as the undyed sample displayed initial strong attractive regime acting between the probe and sample, and also great contrast detail in the phase image suggesting different tip sensitivity to possible dye binding sites. The dyed sample also displayed what appeared to be an attractive profile in the a-p-d curves but no contrast detail within the phase image, reflecting a homogenous surface chemistry due to even distribution of dye compound across the surface of the cellophane sample. However, due to very strong interactions between the tip and samples, it was difficult to obtain further a-p-d curve measurements from the light and dark regions within the phase image of the undyed sample (which may have

provided fingerprints of regions for dye affinity), as this resulted in damage or breakage of the tip.

## 5.4 CONCLUSIONS

The XPS data showed that the presence of dye compound could be quantitatively measured from the surface of the cotton fibres. Using the N 1s atomic orbital region as a diagnostic peak, the level of dye loading could be directly attributed to the concentration levels of dye within the dyebath. That is an increase in dye compound would lead to an increase of dye presence on the surface of the cotton cloth sample. The XPS data also provided strong evidence for possible dye-uptake mechanisms. We observed through the salt-loaded samples, that NaCl directly influenced the amount of dye entering the cotton fibre. An increase in salt content in the dyebath produced a dyed cotton cloth with more dye compound present at the surface. We suggest that this may have occurred by a similar mechanism thought to occur in mercerisation, where the  $\text{Na}^+$  ion ‘opens-up’ the amorphous regions in the surface of the cotton fibre and altering the crystal structure to a more stable form. In the case of the salt-load samples the  $\text{Na}^+$  from salt allowed the dye molecules to enter the fibre through the accessible amorphous regions, and thus into the bulk matrix. When the  $\text{Na}^+$  ions were removed by the washing-off period the dye molecules which entered the fibre matrix in the cotton samples were also found to remain entrapped after the washing process.

The DSC thermograms displayed many similarities between the undyed and dyed cellophane samples, the presence of shallow endothermic peaks in both

samples were attributed to a dehydration and depolymerisation of the cellulose within the samples. The undyed cotton displayed a much larger second endothermic peak (attributed to the combustion of pyrolysis products) than the dyed sample, suggesting that a smaller amount of combustible products were being produced through pyrolysis within the dyed sample. This may reflect an increased crystallinity with the dyed sample, due to the dyeing process, as the dye compound is thought to be entrapped in a slightly more stable crystalline structure than the undyed cotton. However, the dye compound DSC thermogram presented different thermal transitions occurring at similar temperatures to the transitions within the cellophane samples. This may have caused a masking of any small or overlapping transitions present within the dyed cotton sample, (that were perhaps different to the undyed sample), which in turn could have aided the comparison to the undyed sample.

Preliminary AFM investigations of cellulose samples using Blue 1 dye-functionalised tips provided a potential novel approach in elucidating the surface crystalline structure (through different regions of dye-binding/affinity) within the samples. Differences in the adhesive interactions between tip and sample were observed for the undyed and Blue 1 dyed cellophane samples. The undyed sample displayed great contrast detail within the phase image, which may have reflected the tip sensitivity to possible dye binding sites (crystalline/amorphous regions). However, strong adhesive interactions between the tip and samples caused tip damage/breakage, making it difficult to obtain a-p-d measurements (of the light and dark regions within the phase image (B) Figure 5.16). In contrast the dyed sample displayed no contrast

within the phase image, and what appeared to be an attractive profile in the a-p-d curves possibly reflecting a homogenous surface chemistry (due to even distribution of dye compound across the surface of the cellophane sample). It may be possible in the future to use stiffer tips (that are less likely to break due to strong attraction to the sample surface), to help elucidate the nature of the phase contrast detail as observed for the undyed cellophane sample. This may provide information to help understand the dye-uptake mechanism(s) in cellulose samples.

### **Final Conclusions**

The absence of a detailed molecular model for the dye-uptake mechanism(s) in cellulose based textiles, such as cotton makes it difficult to predict dye performance, and to identify key characteristics of the cotton fibre which influence dyeing. We have established that there is a current lack of fundamental information on dye-uptake mechanism(s) in cotton fibres, i.e. the existence and location of dye binding sites. However, it has been postulated that the occurrence of crystalline or amorphous regions in cellulose may play a role in such binding. Within this thesis we attempt to address these questions, by trying to gain a deeper understanding of the dyeing mechanisms through the examination of the physical and chemical characteristics of cotton itself.

The key aim of this study was therefore to provide surface morphology and physiochemical data to aid the development of dye-uptake models, to enable future research on the manufacture of more sophisticated dyes and advance dyeing techniques. Although cotton fibres have been examined previously, no other study has utilised AFM together with other complimentary surface science techniques to examine the surfaces of dyed and undyed cotton fibres to draw direct comparisons, in order to explore dye-uptake mechanism(s). As the AFM allows the user to view both dyed/undyed cotton fibres at the nanometer scale, at the outset of these studies it was thought that we could potentially

identify and image the proposed crystalline and amorphous regions within cellulose and compare their abilities to uptake dye. This hypothesis was tested within this thesis with the view to improving the existing knowledge on dye-uptake mechanism(s).

Chapters 1 and 2 provided the background information on cotton cellulose and the limited existing literature on textiles materials that had already been investigated using the experimental techniques employed within this thesis. The results presented within chapters 3 and 4, detailed and explained an understanding of the surface and chemical characteristics of dyed/undyed cellulose within a model system, and also in cotton textile fibres. The studies presented within chapter 5 provide novel information on dye-uptake, through the quantitative determination of dye coverage on cotton fibre surfaces, which interestingly was found to be dependent on the dye concentration applied and particular dyeing stages.

In chapters 3 and 4, the AFM was employed to characterise undyed and dyed cellulose, either within a model system (cellophane) or cotton fibres. Both undyed and dyed cellophane/cotton samples displayed a similar surface morphology, which was also observed through SEM. The results illustrated the cellulose fibre surface morphology with distinctive elementary and microfibrillar packing and more irregular surface features (globular). The different surface characteristics within cotton fibres were attributed to the variations in density of the fibrillar packing across the fibre bilateral structure. We discovered (through line profile measurements) that the fibrillar width

dimensions within dyed cellulose samples were larger than in the undyed cellulose samples, and were not previously highlighted within the literature. The data suggested that the dyeing process altered the physical structure of the cellulose within the samples most likely through swelling, as it was previously known that hydrogen bond breakages between cellulose chain molecules occurred during this process. The process would allow more movement between the chain molecules, facilitating the entry and entrapment of dye molecules into the fibre matrix, and hence the cellulose fibrillar width dimensions were wider than in undyed samples.

AFM under various different imaging conditions revealed structural details that were not visualised with the SEM. Imaging with chemically modified tips also displayed contrast detail within phase images. By changing the tip chemistry, the tips became sensitive to the presence of  $-OH$  groups from the surface of cellulose. It was proposed that regions of (increased) crystallinity on the surface of cellulose fibres, presented increased densities of  $-OH$  at the surface. In turn this promoted an increase in the water layer of samples, increasing capillary forces between a hydrophilic probe and sample (attractive a-p-d profile), thus inducing stronger adhesion forces. Consequently, regions of decreased crystallinity (amorphous regions) with decreased/sporadic presence of  $-OH$  groups at the cellulose surface resulted in weaker adhesion forces between hydrophilic tips and sample surface (repulsive a-p-d profile). Therefore the tip sensitivity to cellulose surface aided the visualisation of crystalline and amorphous regions. This sensitivity also aided the successful

fingerprinting of regions with varying quantities of dye (dyed to undyed) on the surface of cellulose (in cellophane).

EDAX and ToF-SIMS techniques employed in the chemical investigations of dyed and undyed cellulose samples, successfully detected dye compound from the surface of dyed cellulose samples through elemental analysis. ToF-SIMS produced qualitative data, and showed the presence of dye compound at the surface of the dyed cellophane/cotton samples. This was assisted by the reference spectra and positive/negative ion fragment peak lists, gained for undyed samples and dye compound materials, which aided the identification of dye-specific peaks within the dyed cellulose samples spectra. Crucially these indicative peaks were absent from the undyed samples. Therefore successful chemical identification of the dye compound was obtained from the surface analysis of the cellulose samples.

The DSC thermograms displayed many similarities between the undyed and dyed cellulose samples, the presence of broad endothermic peaks in both samples were attributed to a dehydration and depolymerisation of the cellulose within the samples. However, in cellophane sample, we observed exothermic peaks occurring at high temperatures (353°C and 348°C, in the undyed and dyed samples respectively); these were attributed to the decomposition of cellulose, leading to the formation and volatilisation of L-glucose and other volatile products. In the cotton samples, this thermal transition (within similar temperature ranges) was observed as an endotherm, but was also supported by literature as a decomposition of cellulose and combustion of pyrolysis

products. The undyed cotton displayed a much larger second endothermic peak than the dyed sample, suggesting that a smaller amount of combustible products were being produced through pyrolysis within the dyed sample, reflecting the increase in crystallinity within the dyed sample, due to the entrapment of dye within a more stable crystalline structure. The differences in the types of thermal transition observed in the DSC curves (in the two types of cellulose samples), were probably attributable to the different types of cellulose samples analysed, further supporting the complex nature of cellulose pyrolysis.

Both dye compounds analysed by DSC presented different thermal transitions occurring at similar temperatures to the transitions within the cellophane/cotton samples. This may have caused a masking of any small or overlapping transitions present within the dyed cellulose samples, which were perhaps different to the undyed samples. This may be possible to determine in the future by employing modulated DSC (where periodic temperature modulation is superimposed on the constant heating or cooling rate of a conventional DSC measurement), which would help to *tease-out* any small or overlapping thermal transitions (indicating differences in crystallinity between undyed and dyed cellulose), which could otherwise be missed during a controlled temperature program in normal DSC mode.

Semi-quantitative evidence of dye-uptake mechanism(s) were achieved with XPS analysis, through investigations of dye coverage on cotton fibres. Using the N 1s atomic orbital region as a diagnostic peak, the level of dye loading could be directly attributed to the concentration levels of dye within the

dyebath. That is an increase in dye compound would lead to an increase of dye presence on the surface of the cotton cloth sample. The results also showed that NaCl (used during 'fixing stage' in dyeing) directly influenced the amount of dye entering the cotton fibre. An increase in salt content in the dyebath produced a dyed cotton cloth with more dye compound present at the surface. It was proposed that this may occur by a similar mechanism as in mercerisation (using NaOH), where the Na<sup>+</sup> ions enter amorphous regions (during swelling, in the cellulose chain molecules) in the surface of the cotton fibre and altering the crystal structure to a more stable form, thus allowing dye molecules to enter the fibre through the accessible amorphous regions, (and perhaps further into the bulk fibre matrix). XPS data showed that the presence of dye compound could be quantitatively measured from the surface of the cotton fibres. Future studies using XPS by depth profiling dyed cotton sample, may elucidate the dyeing mechanism within the bulk fibre, due to a dyeing stage or dye concentration.

Finally preliminary AFM investigations with dye functionalised tips were performed to further explore the impact of the surface characteristics of cellophane on dye-textile interactions. Different adhesion profiles were observed in the undyed and dyed samples, which may have reflected the tip sensitivity to dye binding sites (crystalline/amorphous regions). However, this was difficult to ascertain due to the strong interactions between probe and sample surfaces causing tip damage/breakage. Despite this, the obtained data did show promising evidence of dye binding, as the undyed sample displayed significant phase contrast detail, suggesting a spatial variation in dye-textile

interactions. In the future it may be possible to use stiffer tips (less likely to damage/break through to strong sample interaction), to further elucidate the nature of the phase contrast detail as observed for the undyed cellophane sample. This may provide information to help understand the dye-uptake mechanism(s) in cellulose samples.

The results presented within the thesis have provided new information on the surface characteristics of the cellulose based textiles, cellophane and cotton. They have provide new insight into possible dye-uptake and dye-binding mechanism(s), and demonstrated that AFM alongside other complementary surface and bulk analytical methods can be employed to explore such processes. The knowledge obtained from these and future studies employing such surface focussed techniques will help to improve the dyes and dyeing mechanisms for the dyeing of cotton and other textiles, thus improving the quality of dyed garments offered to the consumer.

## *Acknowledgments*

---

My thanks go to my supervisors, especially Dr Stephanie Allen and Prof Clive Roberts, for their guidance and supervision during the project. Also to my industrial sponsor, DyStar UK, and in particular Dr Warren Ebenezer, whose ideas and advice were invaluable to the project.

Thank you to my family for their support. But mostly thank you to Mark for helping to keep me grounded. I could not have got through these last few years without your love, support and endless encouragement. I would also like to acknowledge a few friends who helped me to keep things in perspective, when it came to this thesis; Cedric for the much needed coffee breaks, and past colleagues in LBSA.

## REFERENCES

---

- <sup>1</sup> Shore, J., ed. Cellulosics Dyeing. *The Alden Press, Oxford*, (1995).
- <sup>2</sup> Chand, N., Tiwary, R.K. & Rohatgi, P.K. Resource structure properties of natural cellulosic fibres – an annotated bibliography. *J. Mater. Sci.*, (1988), **23**, 381-387.
- <sup>3</sup> Zugenmaier, P. Conformation and packing of various crystalline cellulose fibers. *Prog. Polym. Sci.*, (2001), **26**, 1341-1417.
- <sup>4</sup> Billmeyer, F.W. Textbook of polymer science. *John Wiley & Sons, New York*, (1984).
- <sup>5</sup> Nevell, T.P. & Zeronian, S.H., eds. Cellulose chemistry and its applications: Cellulose chemistry fundamentals. *John Wiley & Sons, New York*, (1985).
- <sup>6</sup> Hon, D.N-S. Cellulose: a random walk along its historical path. *Cellulose*, (1994), **1**, 1-25.
- <sup>7</sup> Marchessault, R.H. & Deslandes, Y. Crystalline conformation of homo- and regular heteroglucan chains. *Carbohy. Polym.*, (1981), **1**, 31-38.
- <sup>8</sup> Tuichiyev, Sh., Rashidov, D., Sultanov, N. & Kuznetsova, A.M. Study of long period structure of cellulose fibres. *Polym. Sci. U.S.S.R.*, (1974), **16**, 3001-3008.
- <sup>9</sup> Frey-Wyssling, A. & Mühlethaler, K. Die elementarfibrillen der cellulose. *Makromol. Chem.*, (1963), **62**, 25-30.
- <sup>10</sup> Emsley, A.M. & Stevens, G.C. Kinetics and mechanisms of the low-temperature degradation of cellulose. *Cellulose*, (1994), **1**, 26-56.
- <sup>11</sup> Mühlethaler, K. Fine structure of natural polysaccharide systems. *J. Polym. Sci., Part C*, (1969), **28**, 305.
- <sup>12</sup> Ha, M.-A., Apperley, D.C., Evans, B.W., Huxham, I.M., Jardine, W.G., Viëtor, R.J., Reis, D., Vian, B. & Jarvis, M.C. Fine structure in cellulose microfibrils: NMR evidence from onion and quince. *The Plant J.*, (1998), **16**, 183-190.
- <sup>13</sup> Rowland, S.P. & Roberts, E.J. Nature of accessible surfaces and acid-sensitive segments of cotton cellulose. *J. Polym. Sci.*, (1972), **10**, 2447-2461.
- <sup>14</sup> Weimer, P.J., Hackney, J.M. & French, A.D. Effects of chemical treatments and heating on the crystallinity of cellulose and their implications

for evaluating the effect of crystallinity on cellulose biodegradation. *Biotech. Bioeng.*, (1995), **48**, 169-178.

<sup>15</sup> Stöckmann, V.E. Developing a hypothesis: Native cellulose elementary fibrils are formed with metastable structure. *Biopolym.*, (2004), **11**, 251-270.

<sup>16</sup> Kondo, T. & Sawatari, C. A Fourier transform infra-red spectroscopic analysis of the character of hydrogen bonds in amorphous cellulose. *Polym.*, (1996), **3**, 393-399.

<sup>17</sup> Howsmon, J.A. & Sisson, W.A., in Ott, E., Spurlin, H.M. & Grafflin, M.W., eds. Cellulose and cellulose derivatives, 2<sup>nd</sup> edition, part 1. *Wiley-Interscience, New York*, (1954), 251.

<sup>18</sup> Herrman, K., Gerngross, O. & Abitz, W. X radiation structure research of gelatine micelle. *Z. Phys. Chem. B*, (1930), **10**, 371-394.

<sup>19</sup> Hermans, P.H. The analogy between the mechanism of deformation of cellulose and that of rubber. *J. Phys. Chem.*, (1941), **45**, 827-36.

<sup>20</sup> Mark, H., in Ott, E., Spurlin, H.M. & Grafflin, M.W., eds. Cellulose and cellulose derivatives, 2<sup>nd</sup> edition, part 1. *Wiley-Interscience, New York*, (1954), 217.

<sup>21</sup> Fringed micelle theory: Shrinkage in plastics processing. [http://www.tangram.co.uk/TI-Polymer-Shrinkage\\_in\\_plastics.html](http://www.tangram.co.uk/TI-Polymer-Shrinkage_in_plastics.html)

<sup>22</sup> Fengel, D. Ideas on ultrastructural organization of cell-wall components. *J. Polym. Sci. Part C*, (1971), **36**, 383.

<sup>23</sup> Statton, W.O. Meaning of crystallinity when judged by X-rays. *J. Polym. Sci. C*, (1967), **18**, 33.

<sup>24</sup> Wellard, H.J. Variation in the lattice spacing of cellulose. *J. Polym. Sci.*, (1954), **13**, 471-476.

<sup>25</sup> French, A.D., in Nevell, T.P. & Zeronian, S.H., eds. Cellulose chemistry and its applications: Cellulose chemistry fundamentals. *John Wiley & Sons, New York*, (1985), 84.

<sup>26</sup> Meyer, K.H. & Misch, L. Positions of atoms in the new spatial model of cellulose (on constitution of the crystallised part of cellulose IV). *Helv. Chim. Acta*, (1937), **20**, 232-244.

<sup>27</sup> Andress, K.R. The roentgen diagram of mercerised cellulose. *Z. Phys. Chem.*, (1929), **B4**, 190-206.

- <sup>28</sup> Blackwell, J., in Brown, R.M.Jr., ed. Cellulose and cellulose derivatives: The macromolecular organisation of cellulose and chitin. *Plenum Press, New York*, (1982).
- <sup>29</sup> Ellefsen, O. & Norman, N. Formation and characteristics of crystalline cellulose X modification of cellulose. *J. Polym. Sci.*, (1962), **58**, 769.
- <sup>30</sup> Kroon-Batenburg, L.M.J. & Kroon, J. The crystal and molecular structures of cellulose I and cellulose II. *Glycoconjugate J.*, (1997), **14**, 677-690.
- <sup>31</sup> Kline, E., in Ott, E., Spurlin, H.M. & Grafflin, M.W., eds. Cellulose and cellulose derivatives, 2<sup>nd</sup> edition, part 2. *Wiley-Interscience, New York*, (1954), 959-1018.
- <sup>32</sup> Stevens, M.P. Polymer chemistry: An introduction, 2<sup>nd</sup> edition. *Oxford University Press, Oxford*, (1990), 563.
- <sup>33</sup> Hebeish, A. & Guthrie, J.T. The chemistry and technology of cellulose co-polymers. *Springer-Verlag, New York*, (1981).
- <sup>34</sup> Bikales, N.M. & Segal, L. Cellulose and cellulose derivatives. *Wiley, New York*, (1971).
- <sup>35</sup> Laka, M., Chernyavskaya, S., Treimanis, A. & Faitelson, L. Preparation and properties of microcrystalline cellulose gels. *Cell. Chem. Tech.*, (2000), **34**, 217-227.
- <sup>36</sup> Efanov, M.V. Cellulose esters prepared by wood etherification. *Chem. Nat. Comp.*, (2001), **37**, 76-79.
- <sup>37</sup> Lauten, R. A. & Nyström, B. Time dependent association phenomena in dilute aqueous mixtures of a hydrophobically modified cellulose derivative and an anionic surfactant. *Coll. Surf. A*, (2003), **219**, 45-53.
- <sup>38</sup> Zhang, Y.Q., Li, J., Chen, A.M. & Huang, Y. Biodegradation of cellulose derivative/polycaprolactone blends. *Cellu. Chem. Tech.*, (2000), **34**, 51-62.
- <sup>39</sup> Morin, B.P., Breusova, I.P. & Rogovin, Z.A. Structural and chemical modifications of cellulose by graft-copolymerization. *Adv. Polym. Sci.*, (1982), **42**, 139-166.
- <sup>40</sup> Rowland, S.P. & Bertoniere, N.R., in Nevell, T.P. & Zeronian, S.H., eds. Cellulose chemistry and its applications: Chemical methods of studying supramolecular structure. *John Wiley & Sons, New York*, (1985), 112-137.

- <sup>41</sup> Kamide, K. & Saito, M. Recent advances in molecular and supramolecular characterisation of cellulose and cellulose derivatives. *Macromol. Symp.*, (1994), **83**, 233-271.
- <sup>42</sup> Bayer, E.A., Chanzy, H, Lamed, R. & Shoham, Y. Cellulose, Cellulases and cellulosomes. *Curr. Op. in Struc. Bio.*, (1998), **8**, 548-557.
- <sup>43</sup> Jarvis, M. Cellulose stacks up. *Nature*, (2003), **426**, 611-612.
- <sup>44</sup> Gümüşkaya, E. & Usta, M. Crystalline structure properties of bleached and unbleached wheat straw (*Triticum aestivum l.*) soda-oxygen pulp. *Turk. J. Agric. For.*, (2002), **26**, 247-252.
- <sup>45</sup> Koyama, M., Sugiyama, J. & Itoh, T. Systematic survey on crystalline features of algal celluloses. *Cellulose*, (1997), **4**, 147-160.
- <sup>46</sup> Atalla, R.H. The structure of cellulose: Quantitative analysis by Raman spectroscopy. *J. Appl. Polym. Sci.*, (1983), **37**, 295-301.
- <sup>47</sup> Viëtor, R.J., Newman, R.H., Ha, M.-A., Apperley, D.C. & Jarvis, M.C. Conformational features of crystal-surface cellulose from higher plants. *The Plant J.*, (2002), **30**, 721-731.
- <sup>48</sup> Nishiyama, Y., Langan, P. & Chanzy H. Crystal structure and hydrogen-bonding system in cellulose I<sub>β</sub> from synchrotron x-ray and neutron fiber diffraction. *J. Am. Chem. Soc.*, (2002), **124**, 9074-9082.
- <sup>49</sup> Proniewicz, L.M., Paluszkiwicz, C., Weselucha-Birczyńska, A., Majcherczyk, H., Barański & Konieczna, A. FT-IR and FT-Raman study of hydrothermally degraded cellulose. *J. Mol. Struc.*, (2001), **596**, 163-169.
- <sup>50</sup> Cao, Y. & Tan, H. Structural characterisation of cellulose with enzymatic treatment. *J. Mol. Struc.*, (2004), **705**, 189-193.
- <sup>51</sup> Oh, S.Y., Yoo, D.I., Shin, Y. & Seo, G. FT-IR analysis of cellulose treated with sodium hydroxide and carbon dioxide. *Carbohy. Res.*, (2005), **340**, 417-428.
- <sup>52</sup> Jandura, P., Riedl, B & Kokta, B.V. Thermal degradation behaviour of cellulose fibers partially esterified with some long chain organic acids. *Polym. Degrad. Stab.*, (2000), **70**, 387-394.
- <sup>53</sup> Hatakeyama, T., Nakamura, K & Hatakeyama, H. Vaporization of bound water associated with cellulose fibres. *Thermochim. Acta*, (2000), **352-353**, 233-239.
- <sup>54</sup> Pizzi, A. & Eaton, N. The structure of cellulose by conformational analysis. 3. Crystalline and amorphous structure of cellulose I. *J. Macromol. Sci.-Chem.*, (1985), **A22**, 139-160.

- <sup>55</sup> Gessler, K., Krauss, N., Steiner, T., Betzel, C., Sandman, C. & Saenger, W. Crystal structure of  $\beta$ -D-cellobiose hemihydrate with implications for the structure of cellulose II. *Science*, (1994), **266**, 1027-1029.
- <sup>56</sup> Sugiyama, J., Vuong, R. & Chanzy, H. Electron diffraction study on the two crystalline phases occurring in native cellulose from an algal cell wall. *Macromol.*, (1991), **24**, 4168-4175.
- <sup>57</sup> Wang, N. & Ding, E.Y. Thermal behaviour of nanocrystalline cellulose treated by acid or alkali. *Acta Polymerica Sinica*, (2004), **6**, 925-928.
- <sup>58</sup> Zauscher, S. & Klingenberg, D.J. Friction between cellulose surfaces measured with colloidal probe microscopy. *Coll. Surf.*, (2001), **178**, 213-229.
- <sup>59</sup> Kuutti, L., Peltonen, J., Pere, J. & Telemann, O. Identification and surface structure of crystalline cellulose studied by atomic force microscopy. *J. Microsc.*, (1995), **178**, 1-6.
- <sup>60</sup> Nigmatullin, R., Lovitt, R., Wright, C., Linder, M., Nakari-Setälä, T & Gama, M. Atomic force microscopy study of cellulose surface interaction controlled by cellulose binding domains. *Coll. Surf. B*, (2004), **35**, 125-135.
- <sup>61</sup> Krämer, S., Dietel, R., Haupold, G., Lukas, J., Malsch, G. & Paul, D. Characterisation of chloroacetylated/sulfonated cellulose membranes for hemodialysis by spectroscopical methods. *Acta Polym.*, (1992), **43**, 58-60.
- <sup>62</sup> Hishikawa, Y., Togawa, E., Kataoka, Y. & Kondo, T. Characterisation of amorphous domains in cellulosic materials using a FT-IR deuteration monitoring analysis. *Polym.*, (1999), **40**, 7117-7124.
- <sup>63</sup> Felix, J.M. & Gatenholm, P. Controlled interactions in cellulose-polymer composites. I: Effect on mechanical properties. *Polym. Compos.*, (1993), **14**, 449-457.
- <sup>64</sup> Hanley, S.J., Giasson, J., Revol, J.-F. & Gray, D.G. Atomic force microscopy of cellulose microfibrils: comparison with transmission electron microscopy. *Polym.*, (1992), **33**, 4639-4642.
- <sup>65</sup> Boylston, E.K., & Hebert, J.J. Fibrillar size in native cellulose. *J. Appl. Polym. Sci.*, (1980), **25**, 2105-2107.
- <sup>66</sup> Karlsson, J.O., Andersson, M., Berntsson, P., Chihani, T. & Gatenholm, P. Swelling behaviour of stimuli-responsive cellulose fibers. *Polym.*, (1998), **39**, 3589-3595.
- <sup>67</sup> Baiardo, M. Frisoni, G., Scandola, M. & Licciardello, A. Surface chemical modification of natural cellulose fibers. *J. Appl. Polym. Sci.*, (2002), **83**, 38-45.

- <sup>68</sup> Ducker, W.A., Senden, T.J. & Pashley, R.M. Measurement of forces in liquids using a force microscope. *Langmuir*, (1992), **7**, 1831-1836.
- <sup>69</sup> Zauscher, S. & Klingenberg, D.J. Normal forces between cellulose surfaces measured with colloidal probe microscopy. *J. Coll. Inter. Sci.*, (2000), **229**, 497-510.
- <sup>70</sup> Kadolph, S.J. & Langford, A.J. Textiles, 8<sup>th</sup> edition. *Prentice-Hall, London*, (1998).
- <sup>71</sup> Tortora, P.G. & Collier, B.J. Understanding textiles, 5<sup>th</sup> edition. *Prentice-Hall, London*, (1997).
- <sup>72</sup> Chaudhry, M.R. Trends in agrochemicals used to grow cotton. *Intl. Cotton Advisory Committee*, <http://icac.org>.
- <sup>73</sup> Stewart, J.M. in Mauney, J.R. & Stewart, J.M., eds. Cotton Physiology, Vol. 1: Integrated events in the flower and fruit. *The Cotton Foundation, Memphis*, (1986).
- <sup>74</sup> Segal, L. & Wakelyn, P.J., in Lewin, M. & Pearce, E.M. eds. Fiber chemistry. *Marcel Dekker, New York*, (1985), chapter 10.
- <sup>75</sup> Cotton Incorporated <http://www.cottoninc.com>.
- <sup>76</sup> Cutter, E.G. Plant anatomy, 2<sup>nd</sup> edition. *Addison-Wesley Publishing Co., Boston*, (1978).
- <sup>77</sup> Klemm, D. Comprehensive cellulose chemistry, Vol. 1. *Wiley-VCH, Weinheim*, (1998), 34.
- <sup>78</sup> Kassenbeck, P. Bilateral structure of cotton fibers as revealed by enzymatic degradation. *Text. Res. J.*, (1970), **40**, 330.
- <sup>79</sup> Woods, H.J. Physics of fibers. *Chapman and Hall, London*, (1963).
- <sup>80</sup> Johnson, D.J., in Happey, F., ed. Applied fibre science, Vol. 3: High-temperature stable and high-performance fibres. *Academic Press, London*, (1979), chapter 3.
- <sup>81</sup> Pušić, T., Grancarić, A.M., Soljačić, I. & Ribitsch, V. The effect of mercerization on the electrokinetic potential of cotton. *Col. Tech.*, (1999), **115**, 121-124.
- <sup>82</sup> Manchester Engineers and inventors. <http://www.manchester2002-uk.com/celebs/engineers4.html>.

- <sup>83</sup> Zhou, L.M., Yeung, K.W., Yuen, C.W.M. & Zhou, X. Effect of mercerisation and crosslinking on the dyeing properties of ramie fabric. *Col. Tech.*, (2003), **119**, 170-176.
- <sup>84</sup> Warwicke, J.O. & Wright, A.C. Function of sheet of cellulose chains in swelling reactions on cellulose. *J. Appl. Polym. Sci.*, (1967), **11**, 659.
- <sup>85</sup> Okano, T. & Sarko, A. Mercerisation of cellulose 2. Alkali cellulose intermediates and a possible mercerisation mechanism. *J. Appl. Polym. Sci.*, (1985), **30**, 325-332.
- <sup>86</sup> Nishimura, H. & Sarko, A. Mercerisation of cellulose III. Changes in crystallite sizes. *J. Appl. Polym. Sci.*, (1987), **33**, 855-866.
- <sup>87</sup> Cowling, E.B. & Brown, W., in Gould, R.F., ed. Advances in chemistry, series 95. *Am. Chem. Soc., Washington D.C.*, (1969), 152.
- <sup>88</sup> Gomes, R.S., Wilson, P.N., Coates, W.E. & Fox, R.W. Cotton (*Gossypium*) plant residue for industrial fuel. An economic assessment. *Indust. Crop. Prod.*, (1997), **7**, 1-8.
- <sup>89</sup> Proto, M, Supino, S. & Malandrino, O. Cotton: a flow cycle to exploit. *Indust. Crop. Prod.*, (2000), **11**, 173-178.
- <sup>90</sup> Weis, K.G., Jacobsen, K.R. & Jernstedt, J.A. Cytochemistry of developing cotton fibres: A hypothesized relationship between motes and non-dyeing fibres. *Field Crops Res.*, (1999), **62**, 107-117.
- <sup>91</sup> Maxwell, J.M., Gordon, S.G. & Huson, M.G. Internal structure of mature and immature cotton fibres revealed by scanning probe microscopy. *Text. Res. J.*, (2003), **73**, 1005-1012.
- <sup>92</sup> Takács, E., Wojnárovits, L., Földaváry, Cs., Hargittai, P., Borsa, J. & Sajó, I. Effect of combined gamma-irradiation and alkali treatment on cotton-cellulose. *Rad. Phys. Chem.*, (2000), **57**, 399-403.
- <sup>93</sup> Siffert, B. & Metzger, J.-M. Study of the interaction of titanium dioxide with cellulose fibers in an aqueous medium. *Coll. Surf.*, (1991), **53**, 79-99.
- <sup>94</sup> Gilbert, C. & Kokot, S. FT-IR and FT-Raman spectroscopy of processed cotton fibres – a chemometric study. *Mikrochim. Acta*, (1997), **14**, 185-186.
- <sup>95</sup> Ji, S., Lu, Y., Li, J., Wei, G., Liang, X. & Zhu, Y. A  $\beta$ -tubulin-like cDNA expressed specifically in elongating cotton fibers induces longitudinal growth of fission yeast. *Biochem. Biophys. Res. Comm.*, (2002), **296**, 1245-1250.

- <sup>96</sup> Harmer, S.E., Orford, S.J. & Timmis, J.N. Characterisation of six alpha-expansin genes in *Gossypium hirsutum* (upland cotton). *Mol. Genet. Genom.*, (2002), **268**, 1-9.
- <sup>97</sup> John, M.E. Cotton crop improvement through genetic engineering. *Crit. Rev. Biotech.*, (1997), **17**, 185-208.
- <sup>98</sup> Wilkins, T.A., Rajasekaran, K. & Anderson, D.M. Cotton biotechnology. *Crit. Rev. Plant Sci.*, (2000), **19**, 511-550.
- <sup>99</sup> Race, E. The degradation of cotton during atmospheric exposure, particularly in industrial regions. *J. Soc. Dyers and Colour.*, (1949), **65**, 56-63.
- <sup>100</sup> Hill, D.W. Recent studies on microbial degradation of cotton. *J. Agri. Food Chem.*, (1965), **13**, 418.
- <sup>101</sup> Heir, S.W., Cornbleet, T. & Bergeim, O. The amino acids of human sweat. *J. Biol. Chem.*, (1946), **166**, 327-333.
- <sup>102</sup> Liu, Y.Q., Hu, J.L., Zhu, Y. & Yang, Z.H. Surface modification of cotton fabric by grafting of polyurethane. *Carbohy. Polym.*, (2005), **61**, 276-280.
- <sup>103</sup> Schramm, C., Binder, W.H., Tessadri, R. & Duelli, H. Modification of cotton fabrics by means of hydrolyzed TEOS-, GPTMS- and Ti((OPr)-Pr-i)(3)(acac)-solutions. *Cell. Chem. Tech.*, (2005), **39**, 303-314.
- <sup>104</sup> Princi, E., Vicini, S., Pedemonte, E., Proietti, N., Capitán, D., Segare, A.L., D'Orazio, L., Gentile, G., Polcaro, C. & Martuscelli, E. Physical and chemical characterization of cellulose based textiles modified by periodote oxidation. *Macromol. Symp.*, (2004), **218**, 343-352.
- <sup>105</sup> Reid, J.D., Mazzeno, L.W. & Ward, K. Decreasing the acid degradation of cotton sewing thread. *Text. Res. J.*, (1946), **16**, 26-31.
- <sup>106</sup> Orr, R.S., Weiss, L.C., Humphreys, G.C., Mares, T. & Grant, J.N. Degradation of cotton fibres and yarns by heat and moisture. *Text. Res. J.*, (1954), **24**, 399-406.
- <sup>107</sup> Bhat, N.V., Dharmadhikari, A.R., Wani, S.N. & Buch, V.H. Studies on hydrolytic action of lactic acid on cotton fibres. *Ind. J. Fib. Text. Res.*, (1999), **24**, 160-166.
- <sup>108</sup> Pongprayoon, T., O'Rear, E.A., Yanumet, N. & Yuan, W.-L. Wettability of cotton modified admicellar polymerization. *Langmuir*, (2003), **19**, 3770-3778.
- <sup>109</sup> Pongprayoon, T., Yanumet, N., O'Rear, E.A., Alvarez, W.E. & Resasco, D.E. Surface characterisation of cotton coated by a thin film of

polystyrene with and without a cross-linking agent. *Coll. Interf. Sci.*, (2005), **281**, 307-315.

<sup>110</sup> Liu., X.D., Nishi, N., Tokura, S. & Sakairi, N. Chitosan coated cotton fiber: preparation and physical properties. *Carbohy. Polym.*, (2001), **44**, 233-238.

<sup>111</sup> Trotman, E.R. Dyeing and chemical technology of textile fibres, 3<sup>rd</sup> ed. *Griffin and Company Ltd, London*, (1964).

<sup>112</sup> Rys, P. & Zollinger, H. Fundamentals of the Chemistry and Application of Dyes. *Wiley-Interscience, Belfast*, (1972).

<sup>113</sup> Fessenden, R.J. Organic Chemistry, 5<sup>th</sup> ed. *Brooks/Cole Publishing, California*, (1994).

<sup>114</sup> Christie, R.M. Colour Chemistry. *Royal Society of Chemistry, Manchester*, (2001).

<sup>115</sup> Peters, R.H. Textile Chemistry: The Physical Chemistry of Dyeing, vol. 3. *Elseveir, Amsterdam*, (1975).

<sup>116</sup> Tam, K.Y., Smith, E.R., Booth, J., Compton, R.G., Brennan, C.M. & Atherton, J.H. Kinetics and mechanism of dyeing processes: The dyeing of cotton fabrics with a Procion Blue dichlorotriazinyl reactive dye. *J. Coll. Interf. Sci.*, (1997), **186**, 387-398.

<sup>117</sup> Bahrini, Z. & Burkinshaw, S.M. A study of the dyeing of cotton with commercial dichlorotriazinyl reactive dyes. *Dye. Pigm.*, (1995), **27**, 169-182.

<sup>118</sup> Burkinshaw, S.M. & Gotsopoulos, A. Pretreatment of cotton to enhance its dyeability: Part 2 Direct dyes. *Dye. Pigm.*, (1999), **42**, 179-195.

<sup>119</sup> Zohdy, M.H., El-Naggar, A.M. & Marie, M.M. Effect of copper treatment on the dyeability of gamma irradiated acrylic fabrics with different dyestuffs. *Mater. Chem. Phys.*, (1999), **61**, 237-243.

<sup>120</sup> Broadbent, A.D., Thérien, N. & Zhao, Y. Comparison of the thermal fixation of reactive dyes on cotton using infrared radiation or hot air. *Ind. Eng. Chem. Res.*, (1998), **37**, 1781-1785.

<sup>121</sup> Crawshaw, J. & Cameron, R.E. A small angle X-ray scattering study of pore structure in Tencel<sup>®</sup> cellulose fibres and the effects of physical treatments. *Polym.*, (2000), **41**, 4691-4698.

<sup>122</sup> Hearle, J.W.S. & Peters, R.H. Fibre Structure. *Butterworths, London*, (1963).

- <sup>123</sup> Ferreira, L.F.V., Garcia, A.R., Freixo, M.R. & Costa, S.M.B. Photochemistry on surfaces – solvent matrix effect on the swelling of cellulose – an emission and absorption study of adsorbed Auramine-O. *J. Chem. Soc. Faraday Trans.*, (1993), **89**, 1937-44.
- <sup>124</sup> Kai, A. & Mondal, I.H. Influence of substituent of direct dye having bisphenylenebis (azo) skeletal structure on structure of nascent cellulose produced by *Acetobacter xylinum* .1. Different influence of Direct Red 28, Blue 1 and 15 on nascent structure. *Int. J. Biol. Macrom.*, (1997), **20**, 221-231.
- <sup>125</sup> Mondal, I.H. & Kai, A. Structure of nascent microbial cellulose I. Effects of methyl and methoxy groups of Direct Blue 1 and 53 on nascent microbial cellulose. *Polym. J.*, (1998), **30**, 78-83.
- <sup>126</sup> Daescu, C. & Hadaruga, D. Substantivity of azoic coupling components 'azotols'. *Dye. Pigm.*, (1999), **40**, 235-41.
- <sup>127</sup> Timofei, S., Schmidt, W., Kurunczi, L. & Simon, Z. A review of QSAR for dye affinity for cellulose fibres. *Dye. Pigm.*, (2000), **47**, 5-16.
- <sup>128</sup> Krichevskij, G.E. *Zh. Vses. Khim. O-va*, (1981), **26**, 381-389.
- <sup>129</sup> Zollinger, H. *Color Chemistry: Synthesis, Properties and Applications of Organic Dye and Pigments*. Wiley-VCH, Weinheim, (1987).
- <sup>130</sup> Gooding, J.J., Compton, R.G., Brennan, C.M. & Atherton, J.H. The dyeing of nylon and cotton cloth with azo dyes: Kinetics and mechanism. *J. Coll. Interf. Sci.*, (1996), **180**, 605-613.
- <sup>131</sup> Binnig, G., Quate, C. & Gerber, C. Atomic Force Microscopy. *Phys. Rev. Lett.*, (1986), **56**, 930-933.
- <sup>132</sup> Binnig, G. & Rohrer, H. Scanning tunnelling microscopy. *Helv. Phys. Acta*, (1982), **55**, 726-735.
- <sup>133</sup> Thundat, T., Zheng, X. Y., Sharp, S.L., Allison, D.P., Warmack, R.J., Joy, D.C. & Ferrell, T.L. Calibration of atomic force microscope tips using biomolecules. *Scan. Microsc.*, (1992) **6**: 903-910.
- <sup>134</sup> Keller, N.J. & Chi-Chung, C. Imaging steep, high structures by scanning force microscopy with electron beam deposited tips. *Surf. Sci.*, (1992), **268**, 333-339.
- <sup>135</sup> Dai, H.J., Hafner, J.H., Rionzler, A.G., Colbert, D.T. & Smalley, R.E. Nanotubes as nanoprobes in scanning probe microscopy. *Nature*, (1996), **384**, 147-150.

- <sup>136</sup> McPherson, A., Malkin, A.J., Kuznetsov, Y.G. & Plomp, M. Atomic force microscopy applications in macromolecular crystallography. *Acta Cryst.*, (2001), **D57**, 1053-1060.
- <sup>137</sup> Hafner, J.H., Cheung, C.L., Wooley, A.T. & Mieber, C.M. Structural and functional imaging with carbon nanotubes. *Prog. Biophys. Mol. Biol.*, (2001), **77**, 73-110.
- <sup>138</sup> Allen, S., Davies, M.C., Roberts, C.J., Tendler, S.J.B., & Williams, P.M. Atomic force microscopy in analytical biotechnology. *Trends in Biotech.*, (1997), **15**, 101-105.
- <sup>139</sup> Lindsay, S.M., Lyubchenko, Y.L., Tao, N.J., Li, Y.Q., Oden, P.I., Derose, J.A. & Pan, J. Scanning-tunnelling-microscopy and atomic-force microscopy studies of biomaterials at a liquid-solid interface. *J. Vac. Sci. Technol. A-Vac. Surf. Films*, (1993), **11**, 808-815.
- <sup>140</sup> Lal, R. & John, S.A. Biological applications of atomic force microscopy. *Am. J. Physiol.*, (1994), **266**, C1-C21.
- <sup>141</sup> Ikai, A. ATM and AFM of bio/organic molecules and structures. *Surf. Sci. R.*, (1996), **26**, 261-332.
- <sup>142</sup> Martin, Y., Williams, C.C. & Wickramasinghe, H.K. Atomic force microscope force mapping and profiling on a sub 100-Å scale. *J. Appl. Phys.*, (1987), **61**, 4723-4729.
- <sup>143</sup> Lüthi, R., Meyer, E., Howald, I., Haefke, H., Anselmetti, D., Dreier, M., Rüetsche, M., Bonner, T., Overney, R.M., Fromer, J. & Güntherodt, H.-J. Progress in non-contact dynamic force microscopy. *J. Vac. Sci. & Tech. B*, (1994), **12**, 1673-1676.
- <sup>144</sup> Albrecht, T.R., Akamine, S., Carver, T.E. & Quate, C.F. Frequency modulation detection using high-Q cantilevers for enhanced force microscope sensitivity. *J. Appl. Phys.*, (1991), **69**, 668-673.
- <sup>145</sup> Magonov, S.N. & Whangbo, M.H. In Surface Analysis with STM and AFM. *VCH Publisher, New York*, (1996).
- <sup>146</sup> Zhong, Q., Innis, K., Kjoller, V.B. & Elings, V. Fractured polymer silica fibre surface studied by tapping mode atomic force microscopy. *Surf. Sci. Lett.*, (1993), **290**: L688-L692.
- <sup>147</sup> Hansma, P.K., Cleveland, J.P., Radmacher, M., Walters, D.A., Hillner, P.E., Bezanilla, M., Fritz, M., Vie, D., Hansma, H.G., Prater, C.B., Massie, J., Fukunage, L., Gurley, J. & Elings, V. Tapping mode atomic force microscopy in liquids. *Appl. Phys. Lett.*, (1994), **64**, 1738-1740.
- <sup>148</sup> Veeco. A practical guide to SPM at <http://www.veeco.com> .

- <sup>149</sup> Burnham, N.A. & Colton, R.J. Measuring the nanomechanical properties and surface forces of materials using an atomic force microscope. *J. Vac. Sci. Tech. A*, (1989), **7**, 2906-2913.
- <sup>150</sup> Hoh, J.C., Cleveland, J.P., Prater, C.B., Revel, J.-P. & Hansma, P.K. Quantized adhesion detected with the atomic force microscope. *J. Am. Chem. Soc.*, (1992), **114**, 4917-4919.
- <sup>151</sup> Gibson, C.T., Watson, G.S., Mapledoram, L.D., Kondo, H. & Myhra, S. Characterisation of organic thin films by atomic force microscopy – applications of force vs. distance analysis and other modes. *Appl. Surf. Sci.*, (1999), **144-145**, 618-622.
- <sup>152</sup> Weisenhorn, A.L., Hansma, P.K., Albrecht, T.R., & Quate, C.F. Forces in atomic force microscopy in air and water. *Appl. Phys. Letts.*, (1989), **54**, 2651-2653.
- <sup>153</sup> Cappella, B. & Dietler, G. Force-distance curves by atomic force microscopy. *Surf. Sci. Rep.*, (1999), **34**: 1-104.
- <sup>154</sup> Schmitz, I., Schreiner, M., Friedbacher, G. & Grasserbauer, M. Phase imaging as an extension to tapping mode AFM for the identification of material properties on humidity-sensitive surfaces. *Appl. Surf. Sci.*, (1997), **115**, 190-198.
- <sup>155</sup> Putman, C.A.J., Van der Werf, K.O., De Grooth, B.G., Van Hulst, N.F., Greve, J. & Hansma, P.K. A new imaging mode in atomic force microscopy based on the error signal. *Proc. SPIE*, (1992), **1639**, 198-204.
- <sup>156</sup> Danesh, A., Chen, X., Davies, M.C., Roberts, C.J., Sanders, G.H.W., Tendler, S.J.B., Williams, P.M. & Wilkins, M.J. The discrimination of drug polymorphic forms from single crystals using atomic force microscopy. *Pharma. Res.*, (2000), **17**, 887-890.
- <sup>157</sup> Danesh, A., Chen, X., Davies, M.C., Roberts, C.J., Sanders, G.H.W., Tendler, S.J.B., Williams, P.M. & Wilkins, M.J. Polymorphic discrimination using atomic force microscopy: - distinguishing between two polymorphs of the drug cimetidine. *Langmuir*, (2000), **16**, 866-870.
- <sup>158</sup> Bhushan, B., Israelachvili, J.N. & Landman, U. Nanotribochemistry – friction, wear and lubrication at the atomic scale. *Nature*, (1995), **374**, 607-616.
- <sup>159</sup> Radmacher, M. Measuring the elastic properties of living cells by the atomic force microscope. *Method Cell Biol.*, (2002), **68**, 67-90.

- <sup>160</sup> Janshoff, A., Neitzert, M., Oberdorfer, Y. & Fuchs, H. Force spectroscopy of molecular systems - single molecule spectroscopy of polymers and biomolecules. *Angew. Chem. Int. Ed.*, (2000), **39**, 3213-3237.
- <sup>161</sup> Garcia, R. & Perez, R. Dynamic atomic force microscopy methods. *Surf. Sci. Rep.*, (2002), **47**, 197-301.
- <sup>162</sup> Magonov, S.N. & Reneker, D.H. Characterization of polymer surfaces with atomic force microscopy. *Annu. Rev. Mater. Sci.*, (1997), **27**, 175-222.
- <sup>163</sup> Shao, Z., Mou, J., Czajkowsky, D.M., Yang, J. & Yaun, J.Y. Biological atomic force microscopy: what is achieved and what is needed. *Adv. Phys.*, (1996), **45**, 1-86.
- <sup>164</sup> Kasas, S., Thomson, N.H., Smith, B.L., Hansma, P.K., Miklossy, J. & Hansma H.G. Biological applications of the AFM: from single molecules to organs. *Int. J. Imag. Syst. Tech.*, (1997), **8**, 151-161.
- <sup>165</sup> Zhang, Y.Y., Sheng, S.T. & Shao, Z.F. Imaging biological structures with the cryo atomic force microscope. *Biophys. J.*, (1996), **71**, 2168-2176.
- <sup>166</sup> Sheng, S.T., Gao, Y., Khromov, A.S., Somlyo, A.V., Somlyo, A.P. & Shao, Z.F. Cryo-atomic force microscopy of unphosphorylated and thiophosphorylated single smooth muscle myosin molecules. *J. Bio. Chem.*, (2003), **278**, 39892-39896.
- <sup>167</sup> Jones, R, Pollock, H.M., Geldart, D., & Verlinden, A. Inter-particle forces in cohesive powders studied by AFM: Effects of relative humidity, particle size and wall adhesion. *Powder Tech.*, (2003), **132**, 196-210.
- <sup>168</sup> Gunning, A.P., Mackie, A.R., Wilde, P.J. & Morris V.J. Atomic force microscopy of emulsion droplets: Probing droplet-droplet interactions. *Langmuir*, (2004), **20**, 116-122.
- <sup>169</sup> Chen, X., Davies, M.C., Roberts, C.J., Tendler, S.J.B., Williams, P.M., Davies, J, Dawkes, A.C. & Edwards, J.C. Interpretation of tapping mode atomic force microscopy data using amplitude-phase-distance measurements. *Ultramicroscopy*, (1998), **75**, 171-181.
- <sup>170</sup> Scott, W.W. & Bhushan, B. Use of phase imaging in atomic force microscopy for measurement of viscoelastic contrast in polymer nanocomposites and molecularly thick lubricant films. *Ultramicroscopy*, (2003), **97**, 151-169.
- <sup>171</sup> Möller, C., Allen, M., Elings, V., Engel, A. & Müller, D.J. Tapping-mode atomic force microscopy produces faithful high-resolution images of protein surfaces. *Biophys. J.*, (1999), **77**, 1150-1158.

- <sup>172</sup> Su, C., Huang, L., Kjoller, K. & Babcock, K. Studies in tip wear processes in tapping mode<sup>TM</sup> atomic force microscopy. *Ultramicroscopy*, (2003), **97**, 135-144.
- <sup>173</sup> Berquand, A., Mazeran, P-E. & Laval, J-M. Influence of volume and surface properties on phase contrast in tapping mode atomic force microscopy. *Surf. Sci.*, (2003), **523**, 125-130.
- <sup>174</sup> Chen, X., Davies, M.C., Roberts, C.J., Tendler, S.J.B., Williams, P.M. & Burnham, N.A. Optimizing phase imaging via dynamic force curves. *Surf. Sci.*, (2000), **460**, 292-300.
- <sup>175</sup> Hanley, S.J., Giasson, J., Revol, J.F., & Gray, D.G. Atomic force microscopy of cellulose microfibrils: comparison with transmission electron microscopy. *Polym.*, (1992), **33**, 4639-4642.
- <sup>176</sup> Kuutii, L., Peltonen, J., Pere, J., & Teleman, O., Identification and surface-structure of crystalline cellulose studied by atomic force microscopy. *J. Microsc.*, (1995), **178**, 1-6.
- <sup>177</sup> Thalhammer, S. & Heckl, W.M. Atomic force microscopy for high resolution imaging of collagen fibrils – a new technique to investigate collagen structure in historic bone tissues. *J. Archaeo. Sci.*, (2001), **28**, 1061-1068.
- <sup>178</sup> Titcombe, L.A., Huson, M.G., & Turner, P.S. Imaging the internal cellular structure of merino wool fibres using atomic force microscopy. *Micron*, (1997), **28**, 69-71.
- <sup>179</sup> Gibson, C.T., Myhra, S., Watson, G.S., Huson, M.G., Pham, D.K., & Turner, P.S. Effects of aqueous exposure on the mechanical properties of wool fibre analysis by atomic force microscopy. *Text. Res.*, (2001), **71**, 573-581.
- <sup>180</sup> Lee, I., Evans, B.R., & Woodward, J. The mechanism of cellulase action on cotton fibers: evidence from atomic force microscopy. *Ultramicroscopy*, (2000), **82**, 213-221.
- <sup>181</sup> Miller, L.D., Putthanarat, S., Eby, R.K., & Adams, W.W. Investigation of the nanofibrillar morphology in silk fibers by small angle X-ray scattering and atomic force microscopy. *Int. J. Bio. Macrom.*, (1999), **24**, 159-165.
- <sup>182</sup> Rebouillat, S., Peng, J.C.M, & Donnet, J.B. Surface structure of Kevlar<sup>®</sup> fiber studied by atomic force microscopy and inverse gas chromatography *Polym.*, (1999), **40**, 7341-7350.
- <sup>183</sup> Swift, J.A. & Smith, J.R. Microscopical investigations on the epicuticle of mammalian keratin fibres. *J. Microsc.*, (2001), **204**, 203-211.
- <sup>184</sup> Crossley, J.A.A., Gibson, C.T., Mapledoram, L.D., Huson, M.G., Myhra, S., Pham, D.K., Scofield, C.J., Turner, P.S., & Watson, G.S. Atomic

force microscopy analysis of wool fibre surfaces in air and under water. *Micron*, (2000), **31**, 659-667.

<sup>185</sup> Ton-That, C., Shard, A.G., Teare, D.O.H. & Bradley, R.H. XPS and AFM surface studies of solvent-cast PS/PMMA blends. *Polym.*, (2001), **42**, 1121-1129.

<sup>186</sup> Davidovits, J.V., Pho, V., Silberzan, P. & Goldmann, M. Temperature influence on the formation of silanized monolayers on silica: an atomic force microscopy study. *Surf. Sci.*, (1996), **352-354**, 369-373.

<sup>187</sup> Wei, Z.Q., Wang, C. & Bai, C.L. Surface imaging of fragile materials with hydrophobic atomic force microscope tips. *Surf. Sci.*, (2000), **467**, 185-190.

<sup>188</sup> Kajiyama, T., Tanaka, K., Ge S-R. & Takahara, A. Morphology and mechanical properties of polymer surfaces via scanning force microscopy. *Prog. Surf. Sci.*, (1996), **1**, 1-52.

<sup>189</sup> Baldwin, P.M., Frazier, R.A., Adler, J., Glasbey, T.O., Keane, M.P., Roberts, C.J., Tendler, S.J.B., Davies M.C. & Melia, C.D. Surface imaging of thermally sensitive particulate and fibrous materials with the atomic force microscope: a novel sample preparation method. *J. Microsc.*, (1996), **184**, 75-80.

<sup>190</sup> Shakesheff, K.M., Davies, M.C., Jackson, D.E., Roberts, C.J., Tendler, S.J.B., Brown, V.A., Watson, R.C., Barrett, D.A. & Shaw, P.N. Imaging the surface of silica microparticles with the atomic force microscope: a novel sample preparation method. *Surf. Sci. Letts.*, (1994), **304**, L393-L399.

<sup>191</sup> Hou, X., Ren, D., Mao, H., Lei, J., Jin, K., Chu, P.K., Reich, F. & Wayne, D.H. Application of imaging ToF-SIMS to the study of some coal macerals. *Intl. J. Coal Geol.*, (1995), **27**, 23-32.

<sup>192</sup> Vaeck, L.V., Adriaens, A. & Gijbels, R. Static secondary ion mass spectrometry: (SSIMS) part 1. Methodology and structural interpretation. *Mass Spec. Rev.*, (1999), **18**, 1-47.

<sup>193</sup> Surface Science Western: What is time-of-flight secondary ion mass spectroscopy (ToF-SIMS)? <http://www.uwo.ca/ssw/services/tofsims.html>

<sup>194</sup> Ion-ToF: Time-of-Flight Mass Spectrometer. <http://www.ion-tof.com>

<sup>195</sup> Briggs, D. Surface analysis of polymers by XPS and Static SIMS. *Cambridge University Press, Cambridge* (1998).

<sup>196</sup> Pacholski, M.L. & Winograd, N. Imaging with mass spectrometry. *Chem. Rev.*, (1999), **99**, 2977-3005.

- <sup>197</sup> Chu, P.K., Odom, R.W. & Reich, D.F. Analysis of surface particles by time-of-flight secondary ion mass spectrometry. *Mater. Chem. & Phys.*, (1996), **43**, 87-94.
- <sup>198</sup> Vickerman, J.C. & Briggs, D., eds. ToF-SIMS, surface analysis by mass spectrometry. *IM Publications & Surface Spectra Ltd, Huddersfield*, (2001).
- <sup>199</sup> Sokhan, M., Gaspar, P., McPhail, D.S., Cummings, A., Cornish, L., Pullen, D., Hartog, F., Hubbard, C., Oakley, V. & Merkel, J.F. Initial results on laser cleaning at the Victoria & Albert Museum, Natural History Museum and Tate Gallery. *J. Cult. Herit.*, (2003), **4**, 230s-236s.
- <sup>200</sup> Brack, N., Lamb, R., Pham, D. & Turner, P. Non-ionic surfactants and the wool fibre surface. *Coll. Surf.*, (1999), **146**, 405-415.
- <sup>201</sup> Bletsos, I.V., Hercules, D.M., Greifendorf, D. & Benninghoven, A. Time-of-flight ion mass spectrometry of nylons – detection of high mass fragments. *Anal. Chem.*, (1985), **57**, 2384-2388.
- <sup>202</sup> Arunyadej, S., Mitchell, R., Walton, J. & Carr, C.M. An investigation into the effect of laundering on the repellency behaviour of a fluorochemical-treated cotton fabric. *J. Text. Inst.*, (1998), **89**, 696-702.
- <sup>203</sup> Walls, J.M., ed. Methods of Surface Analysis: Techniques and Applications. *Cambridge University Press, Cambridge*, (1988).
- <sup>204</sup> Rubinson, J.F. & Rubinson, K.A. Contemporary Chemical Analysis. *Prentice-Hall Inc., Upper Saddle River*, (1998).
- <sup>205</sup> Venezia, A.M. X-ray photoelectron spectroscopy (XPS) for catalysts characterization. *Catalysis Today*, (2003), **77**, 359-370.
- <sup>206</sup> Gustafsson, J., Ciovica, L. & Peltonen, J. The ultrastructure of spruce kraft pulps studied by atomic force microscopy and X-ray photoelectron spectroscopy. *Polym.*, (2003), **44**, 661-670.
- <sup>207</sup> Degrigny, C., Tanguy, E., Le Gall, R., Zafiropulos, V. & Marakis, G. Laser cleaning of tarnished silver and copper threads in museum textiles. *J. Cult. Herit.*, (2003), **4**, 152s-156s.
- <sup>208</sup> Shao, J., Liu, J., Zheng, J. & Carr, C.M. X-ray photoelectron spectroscopic study of silk fibroin surface. *Polym. Int.*, (2002), **51**, 1479-1483.
- <sup>209</sup> Shekarriz, S., Cohen, P., Carr, C.M., Mitchell, R. & Jones, C. Surface chemical analysis of 1,2,3,4-butanetetracarboxylic acid modified cotton. *J. Mat. Sci.*, (2003), **7**, 2945-2951.

- <sup>210</sup> Frás, L., Johansson, L.-S., Stenius, P., Laine, J., Stana-Kleinschek, K., Ribitsch, V. Analysis of the oxidation of cellulose fibres by titration and XPS. *Coll. Surf. A*, (2005), **260**, 101-108.
- <sup>211</sup> Tougaard, S. & Jansson, C. Comparison of validity and consistency of methods for quantitative XPS peak analysis. *Surf. Interf. Anal.*, (1993), **20**, 1013-1046.
- <sup>212</sup> Museum of Science, Boston: Scanning electron microscopy. <http://www.mos.org/sln/SEM>
- <sup>213</sup> Flegler, S.L., Heckman, J.W.Jr. & Klomparens, K.L. Scanning and transmission electron microscopy; an introduction. *W.H. Freeman and Co., New York*, (1993).
- <sup>214</sup> Electron Microscopy Sciences: Carbon coaters, sputter coaters and turbo coaters. <http://www.emsdiasum.com/microscopy/products/equipment>
- <sup>215</sup> Bai, C. Scanning Tunnelling Microscopy and its applications, 2<sup>nd</sup> edition. *Springer, Heidelberg*, (2000).
- <sup>216</sup> Annadurai, G., Juang, R.S., Lee, D.J. Use of cellulose-based wastes for adsorption of dyes from aqueous solutions. *J. Haz. Mat.*, (2002), **B92**, 263-274.
- <sup>217</sup> Zhang, Y.Z., Chen, X.L., Liu, J., Gao, P.J., Shi, D.X. Pang, S.J. Scanning tunnelling microscopy of the ultrastructure of cotton fiber. *Acta Biochim. Biophys. Sinica*, (2000), **32**, 521-523.
- <sup>218</sup> Qin, J.J, Wang, R., Chung, T.S. Investigation of shear stress effect within a spinneret on flux, separation and thermomechanical properties of hollow fiber ultrafiltration membranes. *J. Mem. Sci.*, (2000), **175**, 197-213.
- <sup>219</sup> Carrott, P.J.M., Nabais, J.M.V., Ribeiro-Carrott, M.M.L., Pajares, J.A. Scanning electron microscopy of activated carbons prepared from commercial acrylic textile fibres. *Fuel Process. Tech.*, (2000), **77-78**, 381-387.
- <sup>220</sup> Putthanarat, S., Zarkoob, S., Magoshi, J., Chen, J.A., Eby, R.K., Stone, M., Adams, W.W. Effect of processing temperature on the morphology of silk membranes. *Polym.*, (2002), **43**, 3405-3413.
- <sup>221</sup> Poza, P., Perez-Rigueiro, J., Elices, M., Lorce, J.L. Fractographic analysis of silkworm and spider silk. *Eng. Frac. Mechanics*, (2002), **69**, 1035-1048.
- <sup>222</sup> Stuart, B. Polymer analysis. *John Wiley & Sons Ltd, Chichester*, (2002).

- <sup>223</sup> Vandooren, A.A. & Muller, B.W. Purity determinations of drugs with differential scanning calorimetry (DSC) – a critical review. *Intl. J. Pharmaceutics*, (1984), **20**, 217-233.
- <sup>224</sup> Gmelin, E. Classical temperature-modulated calorimetry: A review. *Thermochim. Acta*, (1997), **305**, 1-26.
- <sup>225</sup> Coleman, N.J. & Craig, D.Q.M. Modulated temperature differential scanning calorimetry: A novel approach to pharmaceutical thermal analysis. *Intl. J. Pharmaceutics*, (1996), **135**, 13-29.
- <sup>226</sup> Cao, Y. & Tan, H. The properties of enzyme-hydrolysed cellulose in aqueous sodium hydroxide. *Carbohy. Res.*, (2002), **337**, 1453-1457.
- <sup>227</sup> Hirata, T. & Nishimoto, T. DSC, DTA, and TG of cellulose untreated and treated with flame-retardants. *Thermochim. Acta*, (1991), **193**, 99-106.
- <sup>228</sup> Tsujiyama, S.-i. & Miyamori, A. Assignment of DSC thermograms of wood and its components. *Thermochim. Acta*, (2000), **351**, 177-181.
- <sup>229</sup> Dahiya, J.B. & Rana, S. Thermal degradation and morphological studies on cotton cellulose modified with various arylphosphorodichloridites. *Polym. Int.*, (2004), **53**, 995-1002.
- <sup>230</sup> Zhu, P., Sui, S., Wang, B., Sun, K. & Sun, G. A study of pyrolysis and pyrolysis products of flame-retardant cotton fabrics by DSC, TGA and PY-GC-MS. *J. Anal. Appl. Pyrolysis*, (2004), **71**, 645-655.
- <sup>231</sup> Brandenberger, J.E. Notes on cellophane. *J. Franklin Inst.*, (1938), **226**, 797-801.
- <sup>232</sup> American Plastics Council at <http://www.americanplasticscouncil.org>
- <sup>233</sup> Daul, G.C. & Mitchell, R.L., in Bikales, N.M. & Segal, L., eds. Cellulose and cellulose derivatives. *Wiley-Interscience, New York*, (1971), 1225-1232.
- <sup>234</sup> Brasier, J. Cellophane – the deceptively versatile non-plastic. *Mater. Des.*, (1986), **7**, 65-67.
- <sup>235</sup> Guerra, N.P., Macias, C.L., Agrasar, A.T. & Castro, L.P. Development of a bioactive packaging cellophane using Nisaplin<sup>®</sup> as biopreservative agent. *Let. Appl. Microbio.*, (2005), **40**, 106-110.
- <sup>236</sup> Cowley, P.R. The experience curve and history of the cellophane business. *Long Range Plan.*, (1985), **18**, 84-90.

- <sup>237</sup> Urban, F. & White, H.L. pH changes accompanying filtration through cellophane membranes. *Proceed. Soc. Exptl. Bio. Med.*, (1932), **29**, 0606-0607.
- <sup>238</sup> Rosenfeld, M. Ultrafiltration of proteins through cellophane membranes of enhanced permeability. *Biochim. Biophys. Acta*, (1963), **75**, 241-249.
- <sup>239</sup> Monk, D.W. & Wellisch, E. Cellophane for kidney dialysis. *J. Appl. Polym. Sci.*, (1974), **18**, 2875-2885.
- <sup>240</sup> Smith, E.L. & Meara, R.H. Allergic dermatitis from sellotape. *Brit. Med. J.*, (1966), **2**, 239.
- <sup>241</sup> Iizuka, K. Three-dimensional camera phone. *Appl. Opt.*, (2004), **43**, 6285-6292.
- <sup>242</sup> Aravindanath, S., Paralikar, K.M., Betrabet, S.M. & Chaudhuri, N.K. Structural study of cellophane. *Polym.*, (1982), **23**, 823-828.
- <sup>243</sup> Furuta, T., Morikawa, Y., Ito, K. & Ise, N. Cellophane structure as studied by confocal laser scanning microscope. *Tappi J.*, (1994), **77**, 128-131.
- <sup>244</sup> Vazquez, M.I., de Lara, R., Galan, P. & Benavente, J. Modification of cellophane membranes by gamma-irradiation: Effect of irradiation doses on electrochemical parameters. *J. Mem. Sci.*, (2005), **256**, 202-208.
- <sup>245</sup> Wu, J. & Yuan, Q. Gas permeability of a novel cellulose membrane. *J. Mem. Sci.*, (2002), **204**, 185-194.
- <sup>246</sup> Cruz-Barba, L.E., Manolache, S. & Denes F. Generation of Teflon-like layers on cellophane surfaces under atmospheric pressure non-equilibrium SF<sub>6</sub>-plasma environments. *Polym. Bull.*, (2003), **50**, 381-387.
- <sup>247</sup> Martinez, A.J., Manolache, S., Gonzalez, V., Young, R.A. & Denes, F. Immobilised biomolecules on plasma functionalised cellophane. I. Covalently attached alpha-chymotrypsin. *J. Biomat. Sci. Polym. Ed.*, (2000), **11**, 415-438.
- <sup>248</sup> Frazier, R.A. Macromolecular interactions at polysaccharide surfaces. PhD thesis, University of Nottingham, (1996), 59-61.
- <sup>249</sup> Abbott, L.C., Macfaul, P., Jansen, L., Oakes, J., Lindsay Smith, J.R. & Moore, J.N. Spectroscopic and photochemical studies of xanthene and azo dyes on surfaces: cellophane as a mimic of paper and cotton. *Dye. Pigm.*, (2001), **48**, 49-56.
- <sup>250</sup> Okada, Y., Nagashima, T., Iizuka, H., Asano, M. & Morita, Z. Color variation of cotton dyed with reactive Cu-complex azo dyes by histidine, and

- testing methods for color fastness to perspiration. *Dye. Pigm.*, (1997), **33**, 239-250.
- <sup>251</sup> Hihara, T., Okada, Y. & Morita, Z. Photo-oxidation and –reduction of vat dyes on water-swollen cellulose and their lightfastness on dry cellulose. *Dye. Pigm.*, (2002), **53**, 153-177.
- <sup>252</sup> Sugane, A., Watanabe, A., Okada, Y. & Morita, Z. The stability of monochlorotriazinyl reactive dyes on cellulose films in aqueous alkaline solutions containing peroxide bleaching agents. *Dye. Pigm.*, (2001), **50**, 223-241.
- <sup>253</sup> McCann, M.C., Wells, B. & Roberts, K. Direct visualization of cross-links in the primary plant-cell wall. *J. Cell. Sci.*, (1990), **96**, 323-334.
- <sup>254</sup> Mark, H.F, Gaylord, N.G. & Bikales, N.M. (eds). Encyclopaedia of polymer science and technology (plastics, resins, rubbers and fibres), Vol 3. *John Wiley and Sons, New York*, (1965), 60-79.
- <sup>255</sup> Claes, M., De Gendt, S., Kenens, C., Conard, T., Bender, H., Storm, W., Bauer, T., Mertens, P & Heyns, M.M. Controlled deposition of organic contamination and removal with ozone-based cleanings. *J. Electrochem. Soc.*, (2001), **148**, G118-G125.
- <sup>256</sup> Waller, R.C., Bass, K.C. & Roseveare, W.E. Degradation of rayon tire yarn at elevated temperatures. *Ind. Eng. Chem.*, (1948), **40**, 138-143.
- <sup>257</sup> Peters, R.H. & Still, R.H., in Happey, F., ed. Applied fibre science, Vol. 2. *Academic Press, London*, (1979), 409-411.
- <sup>258</sup> Price, D., Horrocks, A.R., Akalin, M. & Farog, A.A. Influence of flame retardants on the mechanism of pyrolysis of cotton (cellulose) fabrics in air. *J. Anal. Appl. Pyrol.*, (1997), **40-41**, 511-524.
- <sup>259</sup> Franklin, W.E. Initial pyrolysis reactions in unmodified and flame-retardant cotton. *J. Macromol. Sci.-Chem.*, (1983), **A19**, 619-641.
- <sup>260</sup> Skoog, D.A., Holler, F.J. & Nieman, T. Principles of Instrumental Analysis, 5<sup>th</sup> ed. *Wadsworth, New York*. (1998), 905-908.
- <sup>261</sup> Shen, W. & Parker, I.H. A preliminary study of the spreading of AKD in the presence of capillary structures. *J. Coll. Interf. Sci.*, (2001), **240**, 172-181.
- <sup>262</sup> Henriksson, A. & Gatenholm, P. Controlled assembly of glucuronoxylans onto cellulose fibres. *Holzforschung*, (2001), **55**, 494-502.
- <sup>263</sup> Juhue, D., Gayon, A.C., Corpart, J.M., Quet, C., Delichere, P., Charret, N., David, L., Cavaille, J.Y. & Perriat, P. Washing durability of cotton coated

with a fluorinated resin: An AFM, XPS, and low frequency mechanical spectroscopy study. *Text. Res. J.*, (2002), **72**, 832-843.

<sup>264</sup> Swiech, T. & Frydrych, I. Cotton dyed fabric appearance as a result of raw material quality parameters. *Fibres & Text. In Eastern Europe*, (1999), **7**, 35-38.

<sup>265</sup> Kang, T.J. & Kim, S.C. Objective evaluation of the trash and color of raw cotton by image processing and neural network. *Text. Res. J.*, (2002), **72**, 776-782.

<sup>266</sup> Akinc, U. A practical approach to lot and setup scheduling at a textile firm. *IIE Transactions*, (1993), **25**, 54-64.

<sup>267</sup> Anis, P. & Eren, H.A. Examining the effectiveness and the environmental impact of rinsing in reactive dyeing. *AATCC Rev.*, (2001), **1**, 24-29.

<sup>268</sup> Vinodgopal, K. & Kamat, P.V. The hydroxyl radical mediated oxidation of textile dye effluent. A comparison of photocatalytic, sonolytic and radiolytic methods. *Abst. Paper. Am. Chem. Soc.*, (1997), **214**, 110.

<sup>269</sup> Bakshi, D.K., Gupta, K.G. & Sharma, P. Enhanced biodecolorization of synthetic textile dye effluent by *Phanerochaete chrysosporium* under improved culture conditions. *World J. Microbio. Biotech.*, (1999), **15**, 507-509.

<sup>270</sup> Rakoczi, F. Multistage ozone treatment of dye waste. *Ozone-Sci. Eng.*, (1991), **13**, 11-21.

<sup>271</sup> Lorimer, J.P., Mason, T.J., Plattes, M., Phull, S.S. & Walton, D.J. Degradation of dye effluent. *Pure and Appl. Chem.*, (2001), **73**, 1957-1968.

<sup>272</sup> Akbari, A., Remigy, J.C. & Aptel, P. Treatment of textile dye effluent using a polyamide-based nanofiltration membrane. *Chem. Eng. Process.*, (2002), **41**, 601-609.

<sup>273</sup> Robinson, T., Chandran, B. & Nigam, P. Removal of dyes from a synthetic textile dye effluent by biosorption on apple pomace and wheat straw. *Water Res.*, (2002), **36**, 2824-2830.

<sup>274</sup> Nettles, J.E. Handbook of chemical specialities. *Wiley Interscience, London*, (1983).

<sup>275</sup> Lewin, M. & Sello, S.B., eds. Handbook of fibre science and technology, Vol.1 Chemical Processing. *Marcel Dekker, New York*, (1983).

<sup>276</sup> Peters, R.H. Textile Chemistry, Vols. 1 & 2. *Elsevier, London*, (1967).

- <sup>277</sup> Haller, R. Nageli's micellar theory as a hypothesis in the research of chemical and physical alterations of cotton fiber, in particular the colour processes. *Kolloid-Z.*, (1917), **20**, 127-145.
- <sup>278</sup> Taylor, J.M. & Mears, P. Synthetic fibres in the dyehouse – the manufacturer's role. *J. Soc. Dyers and Colour.*, (1991), **107**, 64-69.
- <sup>279</sup> Mühlethaler, K. Ultrastructure and formation of plant cell walls. *Annual Rev. Plant Physio.*, (1967), **18**, 1-24.
- <sup>280</sup> Mitchell, R., Carr, C.M., Parfitt, M., Vickerman, J.C. & Jones, C. Surface chemical analysis of raw cotton fibres and associated materials. *Cell.*, (2005), **12**, 629-639.
- <sup>281</sup> Koga, K. & Zeng, X.C. Imaging point defects in a liquid environment: A model AFM study. *Phys. Rev. B*, (1999), **60**, 14328-14333.
- <sup>282</sup> Eccles, A.J. & Steele, T.A. Routine problem solving with the SIMS chemical microscope. *Intl. J. Adh. Adh.*, (2001), **21**, 281-286.
- <sup>283</sup> Mokhtari, J., Phillips, D.A.S. & Taylor, J.A. Synthesis and evaluation of a series of trisazo hetero bi-functional reactive dyes for cotton. *Dye. Pigm.*, (2005), **64**, 163-170.
- <sup>284</sup> Moulder, J.F., Stickle, W.F., Sobol, P.E. & Bomben, K.D. Handbook of x-ray photoelectron spectroscopy: a reference book of standard spectra for identification and interpretation of XPS data. *Physical Electronics, Minnesota*, (1995).
- <sup>285</sup> Briggs, D. & Seah, M.P. Practical surface analysis: Auger and X-ray photoelectron spectroscopy, 2<sup>nd</sup> edition, Vol. 1. *Wiley, Chichester*, (1994).
- <sup>286</sup> National Institute of Standards and Technology online database at <http://srdata.nist.gov/xps/>.
- <sup>287</sup> Scienta ESCA3000 Users' Manual, Scienta, Uppsala, Sweden.
- <sup>288</sup> Briggs, D. Surface analysis of polymers by XPS and static SIMS. *Cambridge University Press, Cambridge*, (1998).
- <sup>289</sup> Hirata, T. & Nishimoto, T. DSC, DTA, and TG of cellulose untreated and treated with flame-retardants. *Thermochim. Acta*, (1991), **193**, 99-106.
- <sup>290</sup> McNamee, C.E., Pyo, N., Tanaka, S., Kanda, Y. & Higashitani, K. Imaging of a soft, weakly adsorbing, living cell with a colloid probe tapping atomic force microscope technique. *Coll. Surf. B*, (2006), **47**, 85-89.
- <sup>291</sup> Tsukada, M., Irie, R., Yonemochi, Y., Noda, R., Kamiya, H., Watanabe, W. & Kauppinen, E.I. *Powd. Tech.*, (2004), **141**, 262-269.